Precise jet measurements and search for supersymmetric particles with the CMS experiment

Dissertation

zur Erlangung des Doktorgrades

an der Fakultät für Mathematik, Informatik und

Naturwissenschaften

Fachbereich Physik

der Universität Hamburg

CERN-THESIS-2018-258

vorgelegt von

Marek Niedziela

Hamburg

2018

Gutachter der Dissertation:	Dr. Christian Sander Prof. Dr. Peter Schleper
Zusammensetzung der Prfungskommission:	Dr. Christian Sander Prof. Dr. Peter Schleper Prof. Dr. Dieter Horns Prof. Dr. Gudrid Moortgat-Pick Dr. Christian Schwanenberger
Vorsitzender der Prfungskommission:	Prof. Dr. Dieter Horns
Datum der Disputation:	23.08.2018
Vorsitzender Fach-Promotionsausschusses Physik:	Prof. Dr. Wolfgang Hansen
Leiterin des Fachbereichs Physik:	Prof. Dr. Michael Potthoff
Dekan der Fakultt fr Mathematik, Informatik und Naturwissenschaften:	Prof. Dr. Heinrich Graener

Abstract

Searches for physics beyond Standard Model (SM) are one of the main goals of the CMS experiment at the Large Hadron Collider (LHC). Among the investigated theories is Supersymmetry (SUSY), which would manifest in a production of new particles. As the LHC is a hadron collider, it is expected that colored SUSY particles would be produced in abundance if they were light enough. The decays of these new particles would manifest in a production of jets. A good understanding of the properties of the jets is crucial to interpret searches targeting such scenarios.

In this thesis, the measurement of the jet energy resolution in data and in simulation, and a search for supersymmetry in multijet events with missing transverse momentum are presented.

The measurement of the jet energy resolution was performed on data collected at the center of mass energy of $\sqrt{s} = 13$ TeV at the CMS experiment in 2016. The method employed uses the balance of the transverse momentum in dijet events to compute the data to simulation ratios of the jet energy resolution, which are used as a correction factor in simulation. Furthermore, similar scale factors are calculated for the non-gaussian part of the jet response.

A search for supersymmetry in events with jets and missing transverse momentum is performed on the same data as the measurement of the jet energy resolution. The main focus of the work presented in this thesis was the estimation of the background arising from QCD multijet events. The method, that was used, called *rebalance and smear*, predicts the QCD contribution to the SM backgrounds based on a jet resolution model.

The observed number of events agree with the Standard Model background predictions and no evidence for supersymmetry has been observed. The upper limit on the production cross sections and exclusion curves for SUSY particles for different simplified models (SMs) are calculated. The production of gluinos with masses in a range of 1800-1960 GeV were excluded for masses of the lightest supersymmetric particle (LSP)up to values of 1 TeV for different simplified models at 95% confidence level. The top, bottom and light squarks with masses below 960, 1050 and 1450 GeV, respectively, were also excluded for masses of LSP below 400 GeV for the considered simplified models.

Kurzzusammenfassung

Die Suche nach Physik jenseits des Standardmodells ist eines der wichtigsten Ziele des Forschungsprogramms des CMS-Experimentes am LHC. Supersymmetrie (SUSY), welche zur Entstehung neuer Teilchen führen würde, ist eine der vielversprechendsten Ideen. Es wird erwartet, dass die Produktion von farbgeladenen SUSY-Teilchen zu Ereignissen mit Jets und fehlender, transversaler Energie führt. Daher ist ein gutes Verständnis der Eigenschaften von Jets essentiell um Suchen nach solchen Szenarios zu interpretieren.
Der Inhalt dieser Arbeit kann in zwei Teile aufgeteilt werden. Im ersten Teil wird die Messung der Energieauflösung von Jets in Daten und in Simulationen vorgestellt. Die Messung wurde mittels in 2016 am CMS-Detektor gesammelten Daten mit einer Schwerpunktsenergie von $\sqrt{s} = 13$ TeV durchgeführt. Die verwendete Methode nutzt die Ausgeglichenheit das transversalen Impulse in Ereignissen mit zwei Jets. Das Resultat der Messung ist das Verhältnis der Energieauflösung von Jets zwischen Daten und simulierten Ereignissen, welches als Korrekturfaktor für Simulationen verwendet werden kann. Des weiteren werden ähnliche Skalierungsfaktoren für die nicht-Gaussischen Komponenten der Jet-Messung bestimmt, welche im folgenden Teil dieser Arbeit verwendet werden.
Im zweiten Teil der Arbeit wird eine Suche nach Ereignissen mit Jets und fehlender, transversaler Energie vorgestellt. Die Suche wurde mittels der gleichen Daten, welche zur Bestimmung der Jetenergieauflösung verwendet wurden durchgeführt. Der Fokus dieser Arbeit liegt auf der Vorhersage des Untergrundes durch Ereignisse mit mehreren Jets aus der starken Wechselwirkung. Die verwendete Methode, welche sich "rebalance and smear" nennt, sagt den Anteil an QCD-Ereignissen des SM-Untergrundes anhand eines Modells der Jetenergieauflösung voraus. Das Prinzip der Methode wird erläutert und Unterschiede zu früheren Implementierungen werden vorgestellt.
Die beobachtete Anzahl von Ereignissen stimmt mit der Standardmodelvorhersage überein und kein Anzeichen von Supersymmetrie wird beobachtet. Eine oberes Ausschlussgrenze für den Wirkungsquerschnitt von SUSY-Teilchen und Ausschlussgrenzen in mehreren vereinfachten Modellen wurden bestimmt. Die Produktion von Gluinos mit Massen zwischen 1800-1960 GeV wurden für Modelle mit leichtesten Supersymmetrischen Teilchen (LSP) mit einer Masse unter 1 TeV für verschiedene vereinfachte Modelle mit einem Konfidenzintervall von 95% ausgeschlossen. Ebenfalls wurden Top-, Bottom- und leichte Squarks mit Massen unter 960, 1050 bzw. 1450 GeV für Modelle mit LSPs unter einer Masse von 400 GeV ausgeschlossen.

Contents

1 Introduction **1**

2 Theory **3**
2.1 The Standard Model of particle physics . . . 3
2.1.1 The matter particles . . . 3
2.1.2 Fundamental interactions . . . 4
2.1.3 Higgs mechanism . . . 7
2.2 Limitations of the Standard Model . . . 9
2.3 Supersymmetry . . . 10
2.3.1 Minimal Supersymmetric Standard Model . . . 11
2.3.2 Simplified models . . . 11

3 Detector **15**
3.1 The Large Hadron Collider . . . 16
3.2 Hadron collider physics . . . 18
3.2.1 Coordinate system . . . 18
3.2.2 Luminosity . . . 19
3.2.3 Kinematic quantities . . . 20
3.3 The Compact Muon Solenoid . . . 20
3.3.1 The solenoid . . . 22
3.3.2 Inner tracking system . . . 22
3.3.3 Calorimetry . . . 24
3.3.4 Muon system . . . 28
3.3.5 Trigger system . . . 29

4 Simulation of particle collisions **31**
4.1 Simulation steps . . . 31
4.2 Event generators . . . 33
4.3 Detector simulation . . . 33

5 Object reconstruction **35**
5.1 Particle flow . . . 35
5.2 Muon . . . 36
5.3 Electron . . . 37
5.4 Jet . . . 37
5.4.1 Jet clustering algorithms . . . 37
5.5 Jet energy corrections . . . 40
5.5.1 Jet energy calibration . . . 40
5.6 B-tagging of jets . . . 42
5.7 Missing transverse momentum . . . 44

6 Jet transverse momentum resolution measurement **47**
6.1 MC-Truth response . . . 47

6.2 Dijet Asymmetry . . . 49
6.2.1 Realistic dijet events in data and Monte Carlo simulation . . . 50
6.3 Samples and Event Selection . . . 50
6.3.1 Dataset and threshold . . . 50
6.3.2 Event cleaning . . . 51
6.3.3 Event selection . . . 52
6.4 Asymmetry width . . . 52
6.5 Corrections for additional jet activity . . . 54
6.6 Particle level imbalance . . . 54
6.7 Extension of the asymmetry method at higher pseudorapidities . . . 56
6.8 Jet resolution data to simulation ratios . . . 57
6.9 Systematic uncertainties . . . 58
6.9.1 Combination of systematic uncertainties . . . 62
6.10 Results . . . 65
6.11 Outlook . . . 67
6.12 Non-gaussian tail resolution measurement . . . 70
6.12.1 Dataset and simulation samples . . . 70
6.12.2 Fractional tail contribution . . . 71
6.12.3 Additional jet activity extrapolation . . . 73
6.12.4 Data to simulation ratios of response tail fractions . . . 74
6.12.5 Outlook . . . 74

7 Search for supersymmetry 75
7.1 Decay channels . . . 75
7.2 Event selection . . . 76
7.3 Triggers . . . 77
7.4 Event cleaning . . . 78
7.5 Search variables . . . 79
7.5.1 Aggregate search regions . . . 80
7.6 Backgrounds . . . 82
7.6.1 Lost-lepton background . . . 82
7.6.2 Hadronically decaying τ lepton background . . . 83
7.6.3 $Z \to \nu\bar{\nu}$ background . . . 84

8 Rebalance and smear 87
8.1 Rebalance and smear . . . 88
8.1.1 Trigger efficiencies and seed sample selection . . . 88
8.1.2 Simulation samples . . . 89
8.1.3 Rebalancing . . . 90
8.1.4 Smearing . . . 93
8.1.5 Response templates . . . 93
8.1.6 Validation of the method . . . 95
8.2 The final prediction and systematic uncertainties . . . 98
8.3 Results comparison . . . 103
8.3.1 $\Delta\phi$ extrapolation method . . . 104
8.3.2 Discussion of QCD background evaluation results . . . 106

9 Results of the supersymmetry search 109

10 Conclusions **117**

A Jet transverse momentum resolution **121**
A.1 Additional jet activity correction 121
A.2 Additional jet activity correction for forward extension 131

B Rebalance and smear **142**

C Supersymmetry search **145**
Bibliography 151

1 Introduction

Since the beginning of civilization, humans, fascinated with the world they found themselves in, felt the desire to understand and describe it. Ancient philosophers were taking first steps towards a logical understanding of nature. Already around the 5^{th} century BCE, Leucippus and Democritus proposed that matter is composed of indivisible particles called *atomos*, an idea that reappeared in the works of numerous scholars throughout subsequent history. The correspondence between the atomos postulated by Democritus and modern elementary particles is perhaps far-fetched. However, it is fascinating to look at modern day science from a broader perspective and see that our knowledge is a result of a continuous development over millennia.

The 19^{th} and 20^{th} centuries brought enormous advancement in the understanding of the building blocks of matter, which culminated in the 1970s in the formulation of the Standard Model (SM) of particle physics. This theory not only managed to describe the observations of particles at the time of its formulation, but also predicted new particles and phenomena which were discovered after its completion. While it describes the observed matter and its interactions very well, it leaves some questions unanswered, like what is the nature of Dark Matter, or why the mass of the Higgs boson is as improbably small as 125 GeV. One of the main objectives of modern particle physics is finding the possible solutions to these problems and testing them in experiments. One of the proposed extensions of the Standard Model, which provides an answer to some of the open questions and can be tested experimentally, is Supersymmetry (SUSY), which predicts new particles with masses around the TeV scale. Supersymmetry introduces a superpartner for each of the Standard Model particles. Among other features it provides candidates for Dark Matter, solves the hierarchy problem and hints at a possibility of a unification of the three fundamental forces.

The elementary particles and their interactions can be investigated in collider experiments, in which particles are accelerated to high energies and collided with a stationary target or other highly energetic particles. The largest and most powerful particle accelerator to date is the Large Hadron Collider located at CERN, which accelerates two proton beams to a center of mass energy of 13 TeV. The beams are collided in the several points at which the experiments are located. One of the experiments is conducted at the CMS detector. Studies presented in this thesis were based on the data collected in 2016 by the CMS detector.

To find evidence for Supersymmetry, it is necessary to understand the Standard Model predictions and the objects measured at high energy particle physics experiments. One particularly important class of objects are the so-called jets, which are the result of showering and hadronization of elementary particles produced in the particle collision. A good understanding of the properties of jets is fundamental for all measurements performed at collider experiments. One such property is the jet energy resolution, which can be measured by investigating the transverse momentum imbalance of the γ/Z+jet and dijet systems. Jet resolution depends fundamentally on the intrinsic response of the detectors, as well as on the algorithm used to reconstruct the jet. The first measurement of the jet transverse momentum resolution performed on the 13 TeV data collected in 2016 at the CMS detector is presented in this thesis. The measurement is performed on dijet events

because they are produced with large cross section, which allows for a large dataset. The high integrated luminosity of the used dataset allowed the measurement of the resolution in finer intervals of pseudorapidity compared to 7 and 8 TeV analyses, reflecting granular variations in the response over the geometry of the CMS detector. Furthermore, it allowed for a measurement of the non-gaussian component of the jet energy response, providing a more complete understanding of the jet response.

The comprehensive understanding of jet energy resolution is utilized in the search for supersymmetry presented in the second part of this thesis. The presented analysis, based on the same 2016 CMS data, is targeting fully hadronic multijet events with large missing transverse momentum and b-tagged jets in the final state. The analysis is a direct successor of the analysis performed on 2015 CMS data, and further of the analyses which did not include b-tagged jets in the final state, performed on 7 and 8 TeV datasets. There are several significant changes introduced in the analysis presented in this thesis compared to its direct ancestor. Firstly, the 2016 analysis includes at least 2 jets and transverse momentum $H_T \geq 300$ GeV, compared to $N_{jets} \geq 3$ and $H_T \geq 500$ GeV in the 2015 analysis. The lowering of the N_{jets} selection improves the sensitivity of the analysis to squark pair production, and lowering the H_T selection improves the sensitivity of the study to scenarios with small mass differences between the lightest supersymmetric particle and the squark or gluino. Secondly, finer intervals in H_T and $\not{H}_T$ are used, which leads to an increase in the sensitivity across the board. The last change, perhaps most important in the context of this thesis, is the inclusion of the rebalance and smear as the main QCD background estimation method. The QCD background, even though it is not a dominant background in the analysis, is particularly difficult to model, as the missing transverse momentum in the QCD events arises primarily from the mismeasurement of the energy of jets. The rebalance and smear method, a version of which was used in 7 and 8 TeV studies, relies on a good understanding of the jet-p_T response. The 2016 implementation of rebalance and smear has improved modeling of the missing transverse momentum at the particle level, which was achieved by modifying the rebalancing procedure.

This thesis presents the measurement of the jet energy resolution, the non-gaussian jet energy response tails, and the estimation of the QCD background for the SUSY search using the rebalance and smear method, and is organized as follows:

A short descriptions of the Standard Model and supersymmetry are provided in chapter 2. The LHC and the CMS experiment along with their design are discussed in chapter 3. Then, the event simulation, along with the Monte Carlo event generators, is briefly discussed in chapter 4. Following this is a description of the physics object reconstruction in chapter 5. The measurements of jet energy resolution and non-gaussian tail response are presented in chapter 6. The search for supersymmetry is introduced in chapter 7, including the search strategy and discussion of non-QCD backgrounds and the techniques used to estimate them. The rebalance and smear QCD multijet background estimation method is presented in chapter 8. The results of the search for supersymmetry, including comparisons with the results of other CMS and ATLAS searches for SUSY, are presented in chapter 9. Finally, chapter 10 provides the summary of the work presented in this thesis.

2 Theory

The *Standard Model* (SM) of particle physics describes elementary particles and interactions between them. It has been formed in the second part of 20th century, the first step in its development being the unification of electromagnetic and weak interactions by Salam, Glashow and Weinberg [1, 2]. Later came the incorporation of Higgs mechanism into the electroweak interaction [3–5]. The last step was the development of the theory of strong interactions, the quantum chromodynamics (QCD). In the following sections the Standard Model, its shortcomings and possible extensions will be discussed. More details on these topics can be found in extensive literature, e.g. [6].

2.1 The Standard Model of particle physics

The Standard Model of particle physics is a quantum field theory which incorporates quantum mechanics and special relativity. It describes the matter, represented by *fermions* with spin 1/2, three of the main interactions: electromagnetic, weak and strong, mediated by the gauge *bosons* with spin 1, and the Higgs boson, the only scalar elementary particle in the Standard Model, which is responsible for generating masses of weak bosons, quarks and charged leptons. In a field theory, the dynamics of the physical system can be fully described by a *Lagrangian density* $\mathcal{L}$, which is used to define the action

$$A = \int \mathcal{L} \mathrm{d}^4\mathrm{x}. \tag{2.1}$$

The interactions terms in the lagrangian $\mathcal{L}$ are obtained by assuming local invariance under gauge transformations. The gauge group of the SM is

$$SU(3)_C \otimes SU(2)_L \otimes U(1)_Y, \tag{2.2}$$

where $U(1)_Y$ represents the electromagnetic interaction acting on weak isospin Y, $SU(2)_L$ represents the isospin symmetry and the weak interaction of left-handed (L) particles and $SU(3)$ is the color symmetry and represents the strong interaction.

The unit system used throughout this thesis and generally in particle physics is the *natural unit convention*. It assumes that the *reduced Planck constant* $\hbar$ and the speed of light c are equal to unity:

$$\hbar = c = 1. \tag{2.3}$$

This convention uses the same units for energy, mass and momentum of the particles.

2.1.1 The matter particles

There are 12 fermions described within SM, summarized in table 2.1. Each of the fermions has an antiparticle which has the same mass but the quantum numbers with opposite signs. Fermions are grouped into quarks and leptons.

	fermions		
	1^{st} generation	2^{nd} generation	3^{rd} generation
leptons	ν_e	ν_μ	ν_τ
	e	μ	τ
quarks	u	c	t
	d	s	b

Table 2.1: Fermions of the Standard Model.

Quarks There are six quarks in the SM. They carry a color charge and thus interact strongly. They are grouped in three generations (see table 2.1), with the up-type quarks ($u,\ c,\ t$) carrying $+2/3$ electric charge and down-type quarks ($d,\ s,\ b$) carrying $-1/3$ electric charge.

Leptons The SM contains 6 leptons. Same as quarks, they are grouped into three generations. Each generation carries its own lepton number, namely electron number L_e for the 1^{st}, muon number L_μ for the 2^{nd} and tau number L_τ for the 3^{rd} generation. Three of the leptons ($e,\ \mu$ and τ) have electrical charge of -1, and three, the corresponding neutrinos, are neutral.

Fermions carry a weak isospin T. Within each generation of fermions there are left-handed (L) isospin doublets with isospin $T = \pm 1/2$ and right-handed (R) isospin singlets with $T = 0$. The left- and right-handedness refers to different states of *chirality*. For massless particles chirality is equal to helicity which is the projection of the particles spin onto its momentum.

Masses of the fermions vary significantly and this so-called mass hierarchy is not understood within the SM. The neutrinos have masses $m_\nu < 2$ eV, while the mass of electron is $m_e = 510.998928(11) \cdot 10^3$ eV and the mass of the heaviest fermion, the top quark t, is $m_t = 173.1(0.6) \cdot 10^9$ eV (all masses taken from [7]).

2.1.2 Fundamental interactions

The interactions between SM particles are usually split into 3 categories, the electromagnetic, weak and strong. The electromagnetic and weak interactions are described with a unified electroweak theory. So far, the attempts to add the theory of gravity to the Standard Model have failed. The fundamental forces are carried by the so-called gauge bosons. The interactions of the Standard Model are summarized in figure 2.1 and described below:

The electromagnetic interaction is mediated by photon γ and couples to the electric charge. The photon is massless and has no electric charge, which makes the range of the electromagnetic interaction infinite. *Quantum Electrodynamics* (QED) is the theory describing interactions between all charged particles and photons. All processes within QED can be described using a Feynman diagram presented in figure 2.2. The interactions with photon always leave the flavor of the particles unchanged. The strength of the

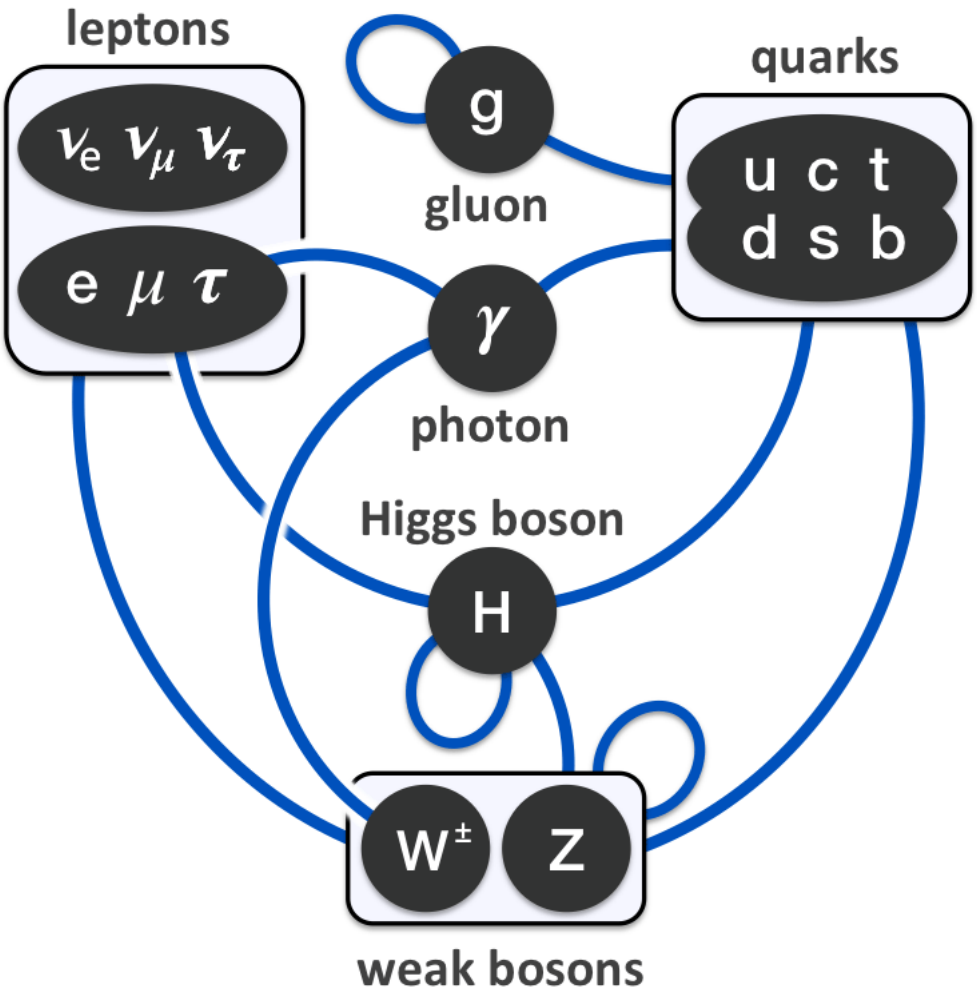

Figure 2.1: Summary of the particle content of the Standard Model. Blue lines represent interactions. Taken from [8].

interaction is given by the running coupling α_{em}, which is increasing with energy (and decreasing with distance). A sketch of the dependence of α_{em} on energy is presented in figure 2.2. The decrease of the coupling with increasing distance is caused by the *screening* effect, which reduces the effective charge of the charged particle seen by the photon at large distances due to *vacuum polarization*. More details are discussed in [6, 9].

The weak interaction is mediated by three bosons, W^1, W^2 and W^3, which couple to the weak isospin ($SU(2)$ quantum number) and to hypercharge ($U(1)$ quantum number). In the electroweak theory the linear combinations of the charged $W^{1,2}$ bosons form the W^+ and W^- bosons, and the linear combination of the neutral W^3 with the neutral B form the Z and γ bosons. The weak bosons are massive, with the mass of the Z boson $m_Z = 91.1876 \pm 0.0021$ GeV and of the W boson $m_{W^\pm} = 80.379 \pm 0.012$ GeV [7]. This causes the weak interaction to be suppressed at energies below the masses of $Z/W^\pm$ bosons.

The elementary Feynman diagrams of the weak interaction are presented in figure 2.3. The first two from the left are the *neutral current* and *charged current* interactions, re-

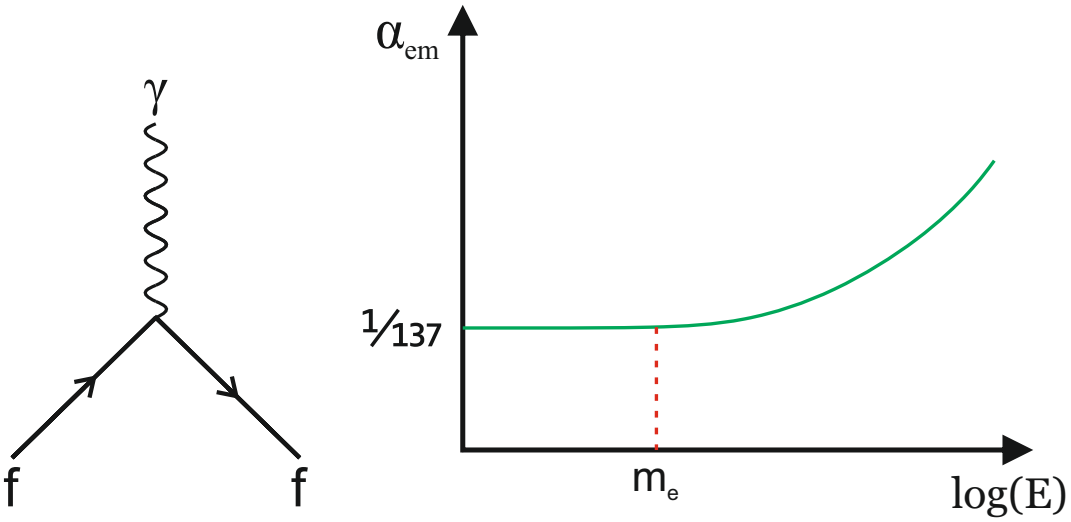

Figure 2.2: (left) Generalized QED Feynman diagram. The interaction with photon does not change the flavor of the fermion. (right) A sketch of the effective QED coupling constant as a function of energy.

spectively, and the remaining two are triple and quadric gauge boson interactions. The neutral current interaction is mediated by the Z boson and does not change the flavor of the fermion, much like in the case of the photon interaction. The charged current interactions, mediated by either W^+ or W^- bosons, change the charge of the fermion by $\Delta Q = \pm 1$ and its flavor, namely it changes the up-type into down-type quarks, and charged leptons into neutrinos, and vice-versa. Because the weak-eigenstates and mass-eigenstates of the fermions are different, $W^\pm$ bosons can couple to fermions from different generations, however, such processes have significantly lower probabilities. The couplings of possible transitions between up- and down-type quarks are summarised in the CKM matrix [10,11]. In the Standard Model the lepton numbers are conserved, however the observation of the neutrino oscilations [12, 13] contradicts this assupmtion. An analog of the CKM matrix for leptons is the Pontecorvo-Maki-Nakagawa-Sakata (PMNS) matrix [14, 15].

The weak interaction violates parity, which has been first observed and properly interpreted in an experiment by Wu [16, 17]. The violation of P symmetry means that the weak interaction is not symmetric under spatial reflections. The $W^\pm$ bosons couple only to left-handed fermions and right-handed antifermions, and Z has a different coupling strength to L and R states.

The electromagnetic and weak interactions are described by a unified theory of *electroweak interaction*, introduced by Salam, Glashow and Weinberg [1, 2]. Above the energies of several 100 GeV the strengths of electromagnetic and weak interactions are of the same order of magnitude. This has been confirmed in e^+e^- collisions at the PETRA experiment at DESY [18] and at the LEP experiment at CERN [19]. The unfied theory predicted the existance of the neutral Z boson. The first experimental evidence of its existence came from the measurement of the neutral currents (interaction mediated by the Z boson) in Gargamelle experiment at CERN [20,21], and the $W^\pm$ and Z bosons were later discovered at the SPS collider at CERN [22, 23].

The strong interaction is mediated by massless gluons which couples to particles carrying *color charge*. The gluon itself carries the color charge, which means that it can interact

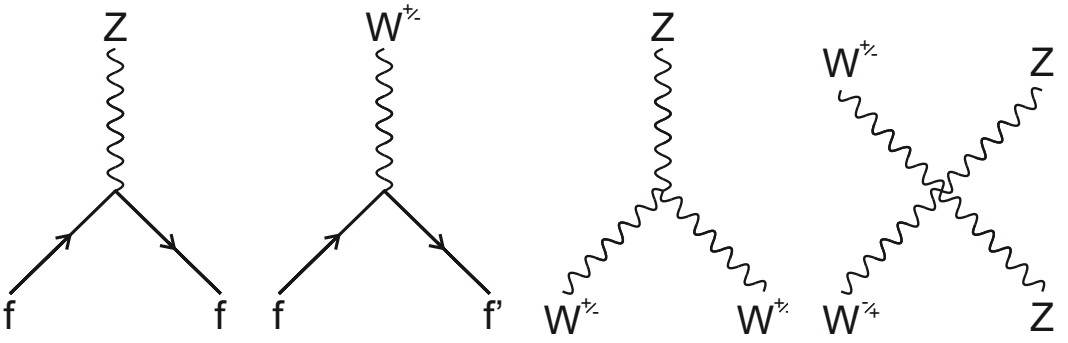

(a) Neutral current (b) Charged current (c) Triple gauge interaction (d) Quartic gauge interaction

Figure 2.3: Fundamental Feynman diagrams of the weak interaction.

with other gluons. The strong interaction is described by the *Quantum Chromodynamics* theory.

There are three linearly-independent color states, commonly referred to as *red, blue* and *green* and three respective anti-colors. Quarks carry one color, meaning that a quark can have three different color states, and gluons carry one of eight linear combinations of the fundamental colors and anticolors. The theory of the strong interaction emerged as an explanation for the existence of particles like Δ^{++}, a bound state of three u quarks with parallel spins, which seemed to violate the Pauli-principle. The solution to this problem, proposed independently by Greenberg [24] and Han and Nambu [25], was the introduction of additional quantum number which would later be called *color*. The vector gauge boson proposed by Han and Nambu, later called *gluon*, was observed for the first time at the PLUTO detector at DESY [26, 27].

Bound, colorless states of quarks or antiquarks are called *hadrons*. These can be divided into *baryons*, which are build out of three quarks (antiquarks) of different colors (anticolors), and *mesons*, which consist of a pair of quark and antiquark carrying color and its anticolor respectively. The quarks creating the hadrons and defining their quantum numbers are called *valence quarks*. The valence quarks exchange gluons, which in turn can interact with other gluons or create quark-antiquark pairs (*sea quarks*). The quarks and gluons inside of the hadrons are collectively called *partons*.

The strength of the strong force, as a consequence of the self-interaction of gluons, increases with distance. As a consequence, states with color cannot exist as free objects and will generate new coloured particles if separated from the bound state. This phenomenon is known as *color confinement*, and is responsible for the typical dimension of colourless objects of around 10^{-15} m. On the contrary, at small distances, which correspond to high energies, the strength of the strong coupling decreases and coloured particles behave as free particles. This phenomenon, known as *asymptotic freedom*, has been proven by Gross, Politzer and Wilczek in [28, 29]. An important consequence of the color confinement is that a creation of quark or gluon creates a cascade of hadrons, which are then detected in high-energy experiments and then collected into objects called *jets*.

2.1.3 Higgs mechanism

The theories discussed above do not provide any explanation for one crucial observable: the mass of fermions or weak bosons. Direct incorporation of mass terms into the SM

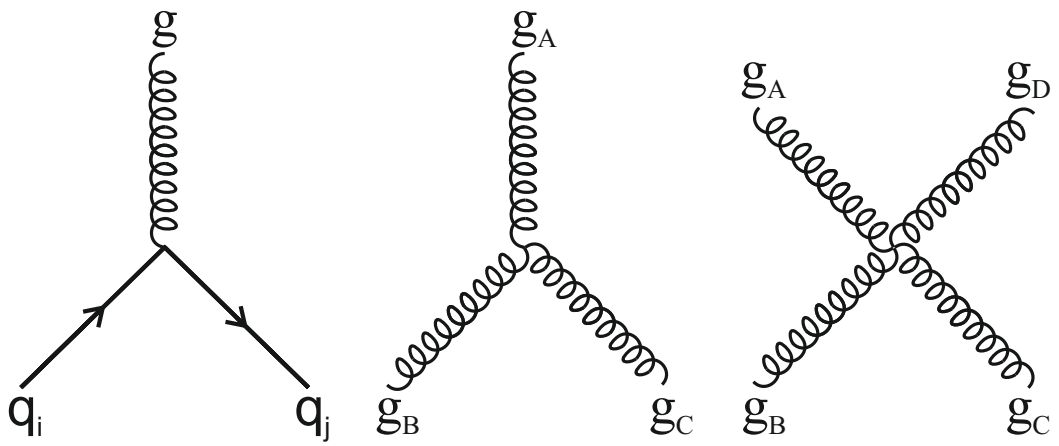

Figure 2.4: Fundamental Feynman diagrams of the strong interaction.

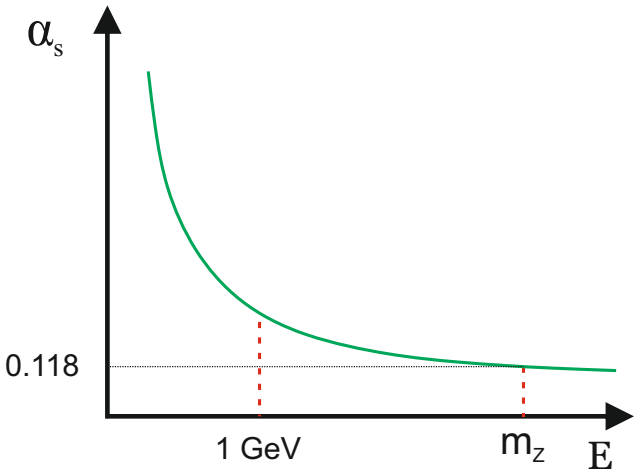

Figure 2.5: A schematic of the strong coupling constant as a function of energy.

lagrangian violates $SU(2)_L \otimes U(1)_Y$ gauge invariance and the theory violates unitary. The solution to that problem is the so-called Higgs mechanism [3–5].

To generate masses of the particles the *Higgs filed* Φ is postulated with a quartic potential. The field Φ has non-vanishing vacuum expectation value (VEV). The expansion of the field around the VEV leads to an emergence of massive, scalar boson known today as *Higgs boson*. Insertion of the Higgs potential and kinematic terms into the SM lagrangian results in mass terms of $W^{\pm}$ and Z bosons. Importantly, the lagrangian with Higgs contribution remains invariant under electroweak gauge transformations. The masses of fermions can be generated by coupling to the Higgs field (*Yukawa coupling*). More detailed discussion is presented in most of classical quantum field theory textbooks like [6].

In 2012 Atlas and CMS experiments at LHC, CERN announced the discovery of a scalar particle with a mass $m_H \approx 125$ GeV [30, 31]. The particle is in many ways compatible with the Higgs boson described above and remains one of the biggest interests of both CMS and Atlas collaborations.

2.2 Limitations of the Standard Model

The Standard Model has been very successful not only in describing what was already known when it was constructed, but also in predicting phenomena discovered many years after its completion, with latest examples the discovery and measurements of Higgs boson. There are, however, certain measurements or observations which are either incompatible, or not addressed by the Standard Model. A selection of such problems is presented below.

Dark matter and dark energy According to Λ Cold Dark Matter model (ΛCDM), the so-called Standard Model of cosmology, the matter and energy described by the Standard Model make up only 4.9% of the total energy of the universe [32, 33]. The 27% is coming from the so-called *dark matter* (DM) and remaining 68% from the *dark energy* (DE). "Dark" refers to the fact that neither DM nor DE have been directly observed. However, there are plenty of measurements that implicate that they do indeed exist. The observations of rotation curves of galaxies suggest that there is a substantial amount of matter and energy in them that is not visible but interacts gravitationally [34, 35]. Same conclusion comes from the observation of weak gravitational lensing [36]. This suggests that DM is electrically neutral and interacts only weakly and gravitationally. The only SM candidates that fits these criteria are neutrinos, but they cannot make up for the whole mass of dark matter [37].

Matter-antimatter asymmetry At the early, hot stages of the history of the Universe matter and antimatter were at equilibrium [38]. When the Universe cooled down almost all particles and antiparticles annihilated, however, as can be observed today, some amount of matter remained. Exactly why such an asymmetry between number of matter and antimatter particles is observed is not understood, and the SM does not provide the answer to that question. The CP violation in the SM is too weak to account for the observed baryon asymmetry.

Unification of couplings In the Standard Model weak and electromagnetic forces are unified into one theory. It is postulated that further unification of electroweak interaction with strong force should be possible, creating the so-called *Grand Unified Theory* (GUT). However, this would require the couplings of all three interactions to become equal at same energy scale. In the Standard Model this unification of coupling strength is not predicted [39].

Gravity One of the fundamental forces, gravity, is completely unaccounted for in the Standard Model. Furthermore, so far the efforts to describe the gravity using quantum field theory have failed.

Hierarchy problem One of the open questions of modern physics is why the fundamental forces differ so significantly: for example the gravity is incomparably weaker than the three remaining forces. One of the manifestations of this *hierarchy problem* is the observed mass of the Higgs boson. Briefly, the loop corrections to m_H are of the order of the Planck scale, which is of the order of $\mathcal{O}(10^{19})$ GeV. An excessive fine-tuning would be required for such huge corrections to cancel out and result in the measured Higgs mass of ≈ 125 GeV.

There are many extensions to the Standard Model currently investigated both theoretically and experimentally. Among them are *Grand Unified Theories*, which introduce

a higher order SU(5) or SO(10) symmetry groups, *Extra dimensions*, or *String theory*, by many considered to be a step towards "the theory of everything". These models will not be discussed in this thesis. Instead, a model called *Supersymmetry* (SUSY) will be presented in next section, and later in chapters 7-9 a search for particles predicted by it will be presented.

2.3 Supersymmetry

Supersymmetry is the largest possible extension of the Poincaré group [40]. In general, it postulates an additional symmetry between fermions and bosons, under which laws of physics are invariant. Work on SUSY began in 1970s, with the renormalization features of the supersymmetric quantum field theories presented by Wess and Zumino in [41], which consequently led to first applications of SUSY in particle physics. Supersymmetry gathered more attention when the *Minimal Supersymmetric Standard Model* (MSSM), the first realization of SUSY that solved the hierarchy problem, was presented by Dimopoulos and Georgi at the beginning of the 1980s [42]. A good introduction to supersymmetry is provided in [43, 44].

Supersymmetry introduces an additional symmetry between bosons and fermions. The generator of the symmetry transformation Q acts like a ladder operator on spin of the particle. It follows the Lie algebra and changes the value of spin by 1/2, which can be understood as turning bosons into fermions and fermions into bosons:

$$Q|\text{fermion}\rangle \propto |\text{boson}\rangle \qquad Q|\text{boson}\rangle \propto |\text{fermion}\rangle. \tag{2.4}$$

The new particles created using the Q operator, called *sparticles*, have modified spin, but other quantum numbers and mass remain unaffected. This already implies that the new symmetry has to be broken to justify the fact that no light SUSY particles with masses equal to the known SM particles have been observed. Supersymmetry has to be constrained as it violates for example the baryon number B and lepton number L conservation. The consequence of this violations would be the instability of the proton, while it is known to be stable, with lifetime $\tau > 10^{34}$ years [45]. To ensure conservation of B and L a new conserved, multiplicative quantum number is introduced, the R-parity:

$$R = (-1)^{3(B-L)+2S}, \tag{2.5}$$

where S is the spin. For SM particles R-parity value is $R = +1$ while for SUSY particles it is $R = -1$. Introduction of R-parity is not the only way to ensure baryon number conservation in SUSY [44], however the other ways will not be discussed here.

The conservation of R-parity has some practical consequences for experimental searches: it ensures that the sparticles are produced in pairs, and that the *lightest supersymmetric particle* (LSP) has to be stable. Additionally a stable LSP serves as a perfect candidate for dark matter. Furthermore, R-parity conserving supersymmetry provides solutions to some of the problems listed in section 2.2. Couplings of the fundamental interactions in SUSY converge when extrapolated to the GUT scale, hinting at the possibility of unification of all forces. Additionally it provides a solution to the hierarchy problem. In case of unbroken supersymmetry the corrections to Higgs mass m_H from SM particles and their SUSY partners cancel out exactly. In case of broken SUSY this is still possible for new particles with masses at the order of $\mathcal{O}(1\text{TeV})$. The condition that SUSY particles cannot be too heavy is called *naturalness*.

names	particles	spin
quarks (×3)	$(u_L,\ d_L)\ u_R,\ d_R$	$\frac{1}{2}$
squarks (×3)	$(\tilde{u}_L,\ \tilde{d}_L)\ \tilde{u}_R,\ \tilde{d}_R$	0
leptons (×3)	$(\nu_L,\ e_L)\ e_R$	$\frac{1}{2}$
sleptons (×3)	$(\tilde{\nu}_L,\ \tilde{e}_L)\ \tilde{e}_R$	0
gluon	g	1
gluino	$\tilde{g}$	$\frac{1}{2}$
W bosons	$W^{\pm},\ W^0$	1
wino	$\tilde{W}^{\pm},\ \tilde{W}^0$	$\frac{1}{2}$
B boson	B^0	1
bino	$\tilde{B}^0$	$\frac{1}{2}$
Higgs	$(H_u^+,\ H_u^0)\ (H_d^0, H_d^-)$	0
higgsinos	$(\tilde{H}_u^+,\ \tilde{H}_u^0)\ (\tilde{H}_d^0, \tilde{H}_d^-)$	$\frac{1}{2}$

Table 2.2: Particle content of MSSM. Based on [43].

2.3.1 Minimal Supersymmetric Standard Model

The number N of supersymmetry transformations is arbitrary. The SUSY model with $N = 1$ is the Minimal Supersymmetric Standard Model (MSSM). This realization of supersymmetry introduces a supersymmetry partner for each of the SM particles, with a separate superpartner for left- and right-handed fermions. The particle content of the MSSM is summarized in table 2.2. The symbols of the superpartners are same as for the corresponding SM particles but with a tilde above them, and the naming convention is as follows: the *fermions* partners, *sfermions*, gain a prefix *s*, e.g. *top* guark partner is *stop squark*, and gauge boson partners, *gauginos*, gain a *-ino* suffix, so for example a superpartner of W boson is *wino* $\tilde{W}$. The bino, winos and higgsinos mix to form the electric neutral mass eigenstates called *neutralinos* $\chi^0_{1,2,3,4}$ and charged *charginos* $\chi^{\pm}_{1,2}$.

2.3.2 Simplified models

Due to R-parity conservation SUSY particles are produced in pairs. The processes with highest possible cross-sections are pair production of gluinos and squarks [46–50]. The possible decays of the produced sparticles depend on the specific SUSY model used, however, many SUSY and non-SUSY models predict very similar topologies. These similarities allow for model-independent interpretation of search results. *Simplified models* [51] provide a framework for presentation of search results and were used in the interpretation of the search [52] discussed in chapters 7-9.

In a simplified model a set of particles and a sequence of their production and decays is defined. The naming scheme of the particles used within the simplified model framework has been adapted from the constrained MSSM (CMSSM). The simplified models assume the production process of the primary particles considered. Primary particles undergo a chain of decays or decay directly into neutral, invisible *Lightest Supersymmetric Particle* (LSP). In the simplified models discussed in [52] the LSP is the neutralino χ^0_1 and the

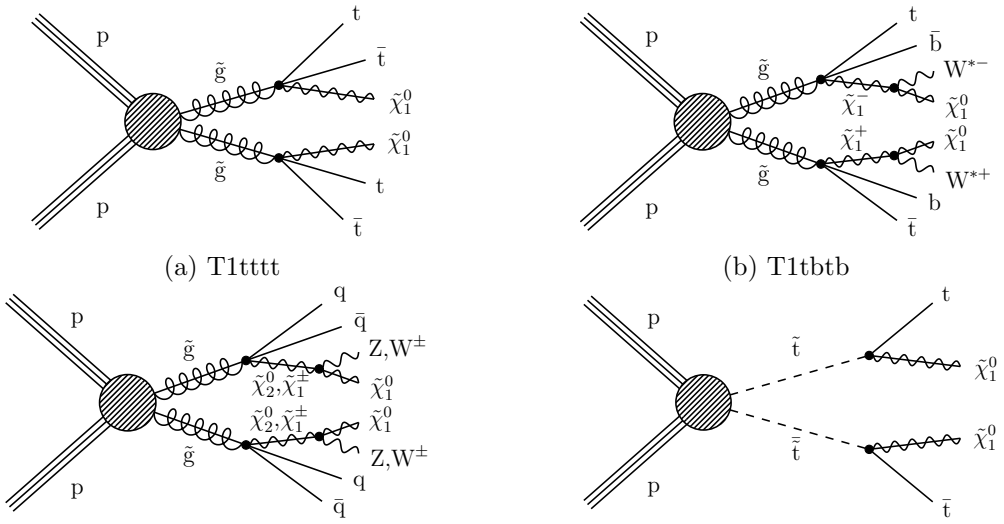

(a) T1tttt (b) T1tbtb

(c) T5qqqqVV (d) T2tt

Figure 2.6: Feynmann diagrams of some of the simplified model signal scenarios considered in search for supersymmetry particles described in chapters 7-9. Taken from [52].

possible intermediate particles are the charginos $\chi_1^\pm$ and heavier neutralino χ_2^0.

Five types of models are considered in [52]. Examples are presented in figure 2.6 and the models considered are listed below.

T1tttt, T1bbbb, T1qqqq T1 models assume pair production of virtual gluinos $\tilde{g}$. In T1tttt scenario, presented in figure 7.1a, the gluino decays into top quark-antiquark pair and a neutralino $\tilde{g} \to t\bar{t}\chi_1^0$. T1bbbb and T1qqqq are similar with the exchange of $t\bar{t}$ to bottom or light-flavor quark-antiquark pairs.

T1tbtb In the T1tbtb, presented in figure 7.1b, the gluinos decay as $\tilde{g} \to t\bar{b}\chi_1^-$ or its charge conjugate. The charginos $\chi_1^\pm$ decay into $W^\pm$ boson and LSP χ_1^0. The chargino and neutralino are assumed to be nearly mass degenerate, which represents the fact that they are expected to appear within the same SU(2) multiplet [53]

Mixed model An additional model is consider which mixes, with varying branching ratios, all T1 models listed above.

T2tt, T2bb, T2qq T2 models assume production of squark-antisquark pairs. In T2tt, presented in figure 7.1d, top squark-antisquark pair is produced, which decay directly into their SM partner and LSP. Similarly, T2bb and T2qq assume pair production of bottom and light-flavored squark-antisquark pairs, respectively.

T5qqqqVV T5 models assume gluino pair production. In T5qqqqVV, presented in figure 7.1c, gluinos decay into light quark-antiquark pair and either next-to-lightest neutralino χ_2^0 or charginos $\chi_1^\pm$. The neutralino decays into Z boson and the LSP $\chi_2^0 \to Z\chi_1^0$ and charginos decay into a W bosons and the LSP $\chi_1^\pm \to W^\pm\chi_1^0$.

The choice of the investigated models is dictated by the expectation that certain SUSY particles will have low masses due to naturalness. This can be motivated as follows. The minimization of the Higgs potential in MSSM yields a relation for the mass of Z boson

$$m_Z^2 = -2(m_{H_u}^2 + |\mu|^2) + ... \tag{2.6}$$

where H_u is the first Higgs doublet and μ is related to the Higgs potential vacuum expectation value and is the higgsino mass term in the MSSM superpotential. In MSSM mass of the H_u is expected to be close to the mass of SM Higgs boson, which implies from 2.6 that $|\mu| \lesssim 200$ GeV and corresponds to small higgsino masses. At the one-loop level the highest correction to the Z mass is expected to come from the stops, which limits their mass to $m_{\tilde{t}} \lesssim 400$ GeV. Furthermore, the corrections from winos limit their mass to $m_{\tilde{W}} \lesssim 1$ TeV. Consequently also neutralinos are expected to be light, as they are linear combinations of neutral higgsinos, neutral wino and bino. The mass of the stop gets a correction from the gluinos, which also gives an estimated relation between gluino and stop masses $m_{\tilde{g}} \lesssim 2m_{\tilde{t}}$.

3 Detector

Particle accelerators have become a primary tool in searches for new particles and in measurements of the parameters of the Standard Model. The analyses presented in this thesis are based on the data collected at the *Compact Muon Solenoid* (CMS) detector, which is one of the experiments located at the *Large Hadron Collider* (LHC, [54], [55]), the most powerful particle accelerator to date. The LHC is a proton-proton (pp) collider operated by the *European Organisation for Nuclear Research* (CERN) in Geneva, and is located in the former tunnel of the *Large Electron-Positron collider* (LEP). The aerial view of CERN area is presented in figure 3.1.

The Section 3.1 of this chapter presents an introduction to the LHC program, Section 3.2 introduces the basic detector concepts and finally Section 3.3 presents the design and performance of the CMS detector.

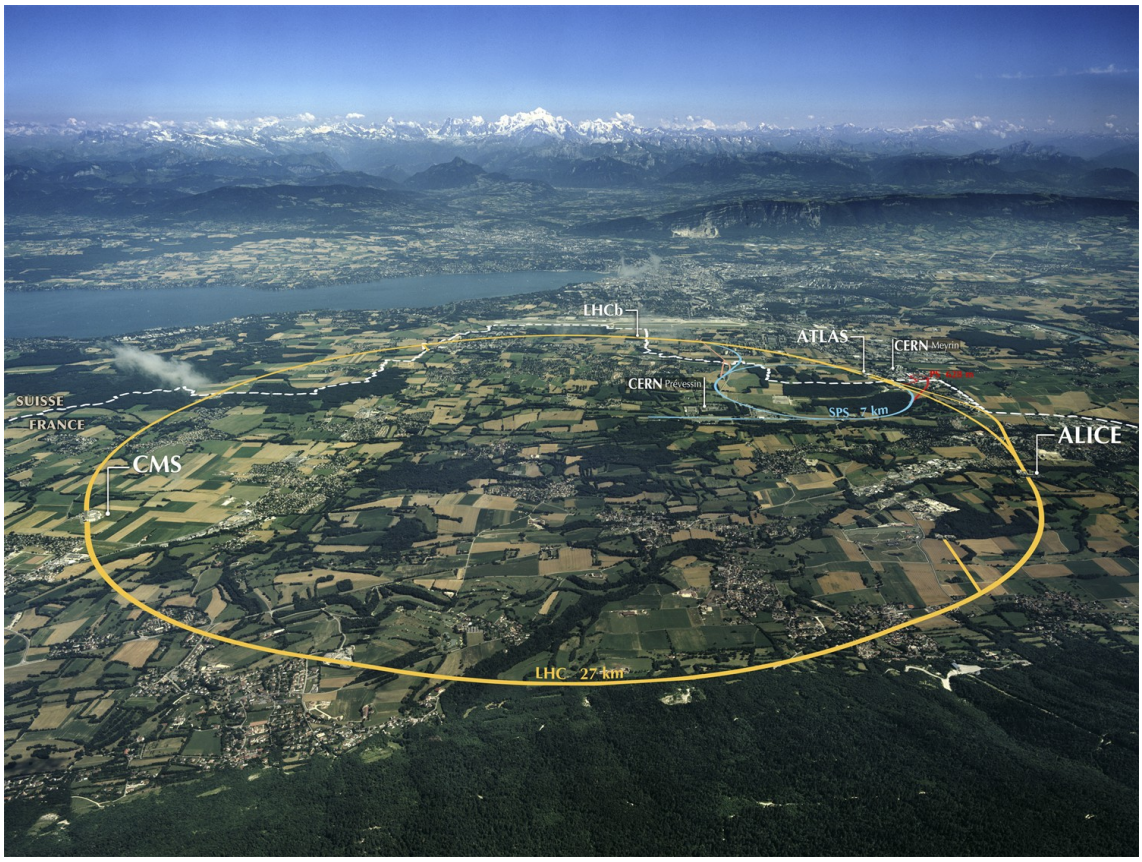

Figure 3.1: Aerial view of the CERN, with accelerator complex and experiments marked. Taken from [56].

3.1 The Large Hadron Collider

The LHC is a ring accelerator with circumference of 26.7 km, located in the vicinity of Geneva, at depth ranging from 45 m to 170 m below surface. It is composed of two rings, in which two counter-rotating beams of protons or heavy ions (mostly lead, but there was a single run with xenon ions) are accelerated. The beams are crossed in the interaction points where the experiments are located.

The maximal number of proton bunches is 2808; however in the year 2016 the maximal number achieved was 2220, and the number of protons per bunch during that year was approximately 1.18×10^{11}. Protons are accelerated using 16 superconducting radio frequency cavities (RF), with the field gradients up to 5.5 MV/m. The RF cavities are operated at the frequency of 40 MHz, which corresponds to the same frequency of the bunch crossings at the interaction points (IP) and the time separation between the bunches of 25 ns. The bunches are steered using dipole magnets and focused using quadrupole and sextuple magnets, all of them superconducting. Both the RF cavities and the magnets are operated at temperatures of around 1.9K. As already mentioned, time separation between the bunches is 25 ns, which corresponds to 7.5 meter between the bunches. At the crossing point, the bunches are approximately 8 cm long and have 20μm radius.

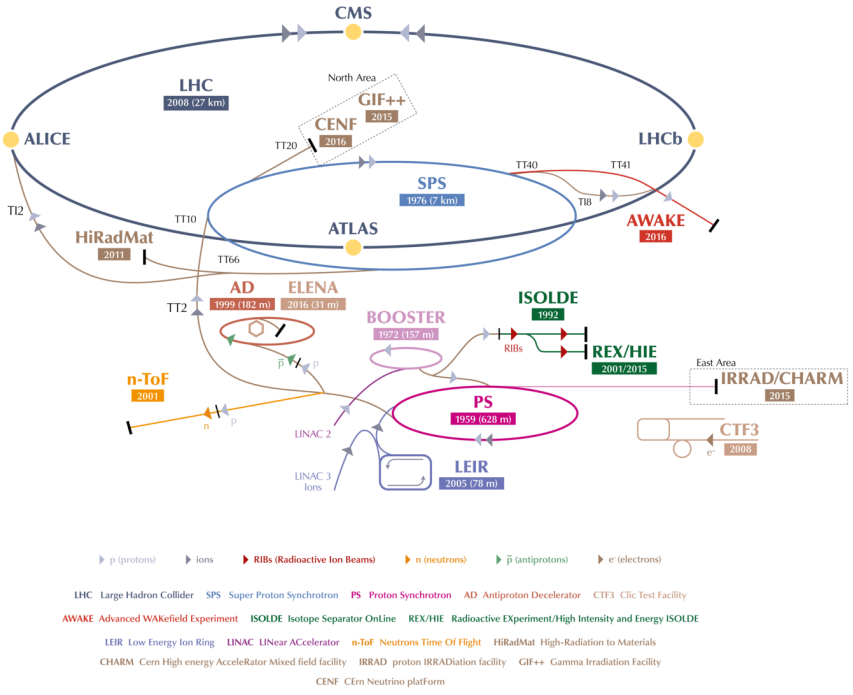

Figure 3.2: Schematic view of the CERN accelerator complex. For each machine the year of first operation and in brackets circumference for ring accelerators are stated. Below, the names are explained. Protons are pre-accelerated in *Linac4*, the *Proton Synchrotron Booster*, the *Proton Synchrotron*, and the *Super Proton Synchrotron*. Taken from [57].

Before being injected into the LHC, proton bunches are accelerated to 450 GeV in a

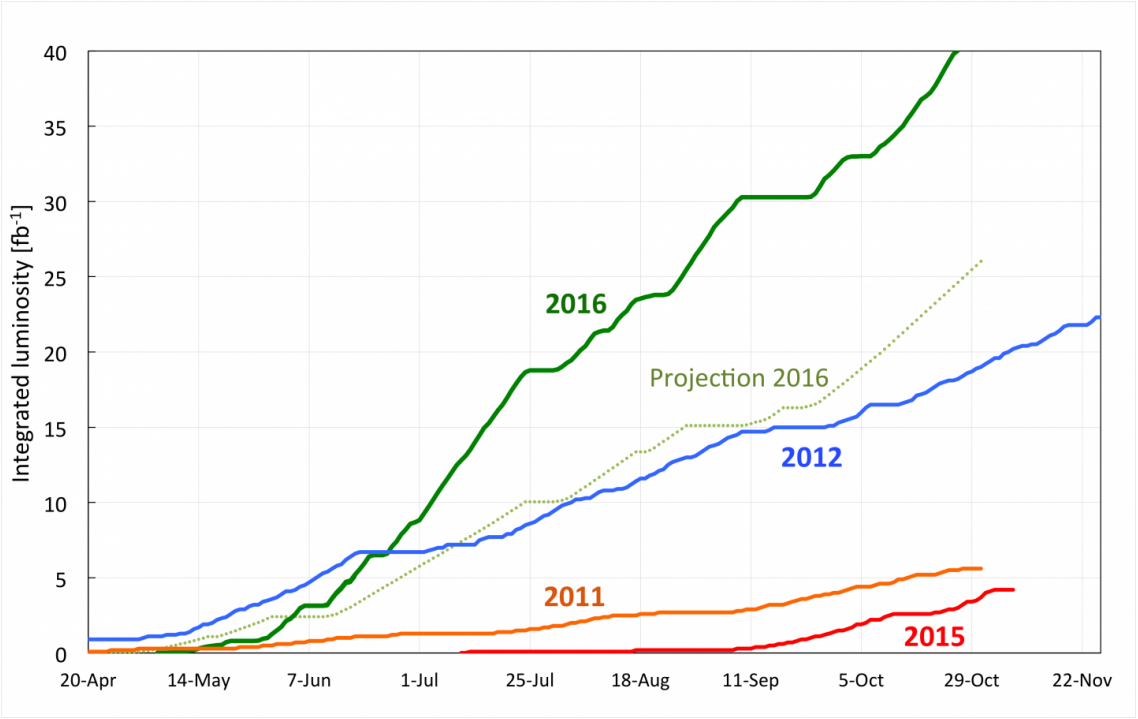

Figure 3.3: The integrated luminosity of pp collisions in LHC in 2016, compared to performance in previous years and the projected value for the same year. Taken from [60].

chain of various accelerators. The CERN accelerator complex is shown in figure 3.2 and the pre-acceleration steps are listed in the description of that figure. After injection, it takes approximately one hour to accelerate the beams to 6.5 TeV and to form the so-called stable beams, which means beams that can be collided.

The design centre-of-mass energy of the LHC is 14 TeV. During tests conducted in 2008, some dipoles were losing superconductivity when subjected to high currents. The fix for this condition would require a substantial amount of time, and it was decided that delivery of 13 TeV collisions in 2015 is preferred to postponing the entire experiment to adjust the dipole magnets [58]. On the other hand, the luminosity, which will be explained in next section, reached values of $1.5 \times 10^{34}\text{cm}^{-2}\text{s}^{-1}$ in the year 2016, which corresponds to the design value [59] [60], and reached the values of $2.06 \times 10^{34}\text{cm}^{-2}\text{s}^{-1}$ in the year 2017 [61]. The integrated luminosity, which corresponds to the total number of registered events, exceeded in 2016 the anticipated value by $\approx 60\%$, reaching value of 40fb^{-1} while only 25fb^{-1} was expected. The figure 3.3 shows the integrated luminosity of pp collisions up to the end of run 2016.

The Standard Model cross sections of inelastic pp scattering and some exclusive processes are shown in figure 3.4. It is interesting to note the increase of the cross sections of some processes at 13 TeV compared to 7 and 8 TeV values. The ratios of gg, qg and $q\bar{q}$ parton luminosities at $\sqrt{s} = 7, 8, 13$ TeV are presented in figure 3.5. The plot shows the parton luminosities, so the luminosity of a collision of given partons from the colliding protons, as a function of the final state invariant mass M_X. It can be seen that for an interaction of two gluons, even at low M_X the luminosity at $\sqrt{s} = 13\text{TeV}$ is twice as high as at $\sqrt{s} = 8\text{TeV}$.

3.2 Hadron collider physics

In this section, the basic quantities used in the discussion of hadron collider physics will be introduced. The choice of the coordinate system and kinematic variables presented below is discussed in detail in [63].

3.2.1 Coordinate system

A right-handed coordinate system with its origin at the nominal interaction point is used in this thesis, as well as generally within CMS collaboration. In Cartesian coordinates, the x-axis points towards the center of the LHC ring, the y-axis points upwards in the direction of the surface, and the z-axis is pointed counter-clockwise viewed from above, along the proton beam. In the polar coordinate system, the radial distance r and the azimuthal angle ϕ are defined in the xy plane, with $\phi = 0$ corresponding to the x-axis.

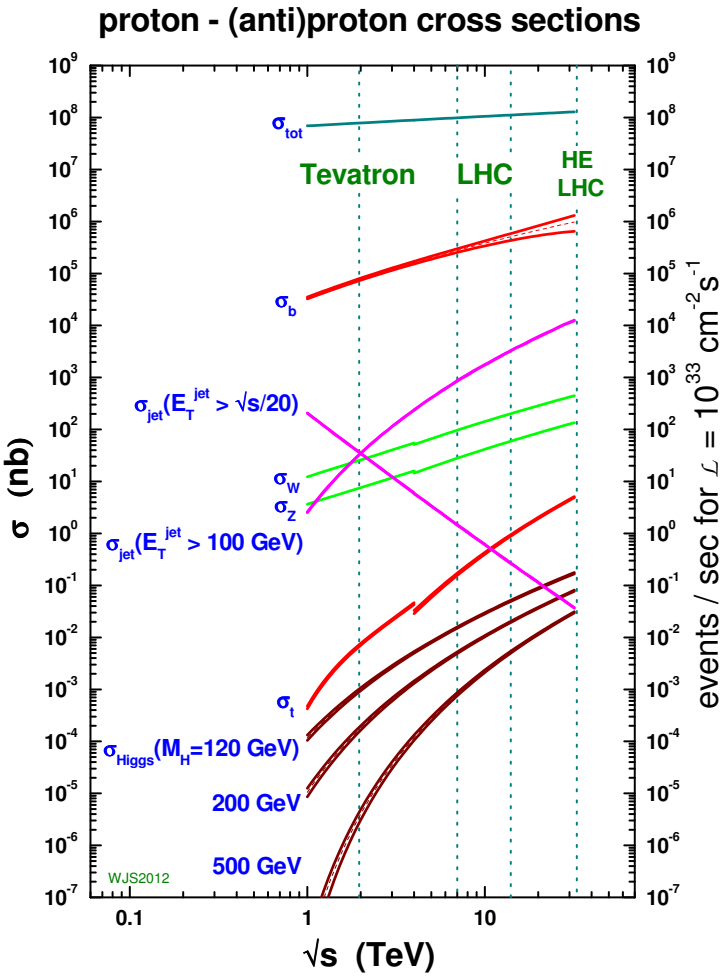

Figure 3.4: Cross sections of important exclusive processes for pp ($\sqrt{s} > 4$TeV) and $p\bar{p}$ scattering ($\sqrt{s} < 4$TeV) shown as a function of $\sqrt{s}$. The dotted line corresponds to $\sqrt{s} = 13$ TeV. Taken from [62].

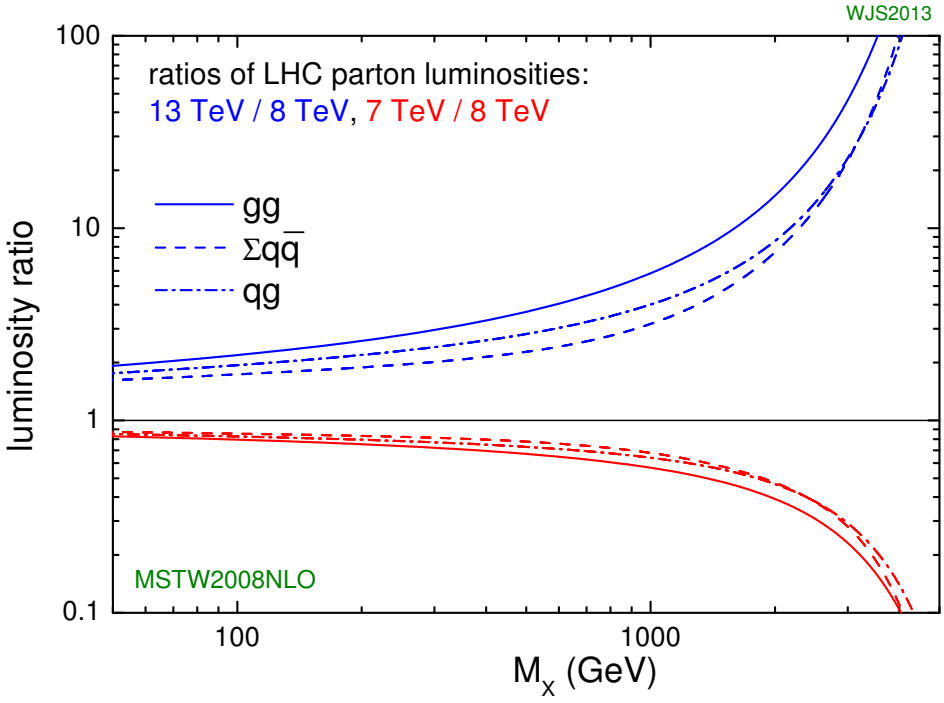

Figure 3.5: Ratios of parton luminosities. Taken from [62].

The polar angle θ is defined with respect to the z-axis and is used to define how forward the measured particles are.

3.2.2 Luminosity

The number of expected events of a given process is defined as a product of the cross section of the considered process and the integral $L = \int \mathcal{L} dt$ of the instantaneous luminosity $\mathcal{L}$ over time. The luminosity $\mathcal{L}$ characterises the experimental conditions and, as defined in [64], is given by the following equation

$$\mathcal{L} = \frac{\gamma f k_B N_p^2}{4\pi \varepsilon_n \beta^*} F, \tag{3.1}$$

where γ is the Lorentz factor, f is the revolution frequency, k_B is the number of bunches, N_p is the number of particles per bunch, ε_n is the normalized transverse emittance, β^* is the betatron function at the interaction point, and F is the form factor correction due to bunch crossing angle. The emittance ε_n describes the spatial parameters of the beam. The betatron function, also called amplitude function, is connected with the focusing power of the magnets. The lower the value of β^*, the smaller cross section of the beam at the interaction point, which can be translated into a higher probability of a proton-proton interaction. As the number of events grows linearly with time, accelerators are designed to achieve a high luminosity $\mathcal{L}$.

3.2.3 Kinematic quantities

The hard (high-momentum) interaction in a hadron collider occurs between partons, which carry only a fraction $x_i, i \in 1, 2$ of the protons momentum. As a result, the center-of-mass frame of the interacting partons has an unknown boost along the z-axis with respect to the laboratory (detector) frame. This imposes certain choices regarding the kinematic variables, which will be discussed briefly.

The parton four-momenta are given by

$$p_1 = \frac{\sqrt{s}}{2}(x_1, 0, 0, x_1) \tag{3.2}$$

$$p_2 = \frac{\sqrt{s}}{2}(x_2, 0, 0, -x_2), \tag{3.3}$$

where $\sqrt{s}$ is the centre-of-mass energy of the pp collision and x_i are the momentum fractions of both partons. Given the above four-momenta, the centre-of-mass energy of the parton interaction $\sqrt{\hat{s}}$ is given by $\hat{s} = x_1 x_2 s$, and its invariant mass is $M = \sqrt{x_1 x_2 s}$. The relation between momentum transfer Q (equal to invariant mass $M = Q$), momentum fraction x and the so-called rapidity $y = \frac{1}{2} ln(x_1/x_2)$ is shown in figure 3.6. The definition and importance of rapidity will be discussed at the end of this subsection.

Unfortunately, due to a technical limitation, the full four-momenta of the produced particles cannot be measured, which means that also the boost of the final state cannot be measured. Instead, the quantity called transverse momentum p_T is used in physics analyses. It is the component of the particles four-momentum in the plane perpendicular to the z-axis. This component is equal in the detector's and parton's center-of-mass frames. Weakly interacting particles, such as neutrinos, will escape the detector undetected, which will cause a transverse momentum imbalance in the event. This imbalance is denoted as *missing transverse momentum* $\not{E}_T$, and is defined as negative of the vector sum of the momenta of all N measured particles:

$$\not{E}_T = -\sum_{i=1}^{N} \vec{p}_{T,i}. \tag{3.4}$$

$\not{E}_T$ serves as a proxy of a sum of momenta of all undetected particles.

Number of particles produced is approximately constant per interval of rapidity y, which makes it a useful variable. However, y can not be measured, thus a quantity called pseudorapidity η is introduced

$$\eta = -ln\left[\tan\left(\frac{\theta}{2}\right)\right]. \tag{3.5}$$

In the relativistic limit, pseudorapidity becomes equal to rapidity. $\eta = 0$ corresponds to $\theta = 0$ and $|\eta| \to \infty$ points along z-axis.

3.3 The Compact Muon Solenoid

The CMS experiment [65] is a general purpose detector designed to take advantage of the multi-TeV energy and high luminosity delivered by the LHC. Typically for collision experiments, its design is cylindrical, with layers of different detector components positioned around the beam-line. The detector measures 14.6 m in diameter and 21.6 m in length,

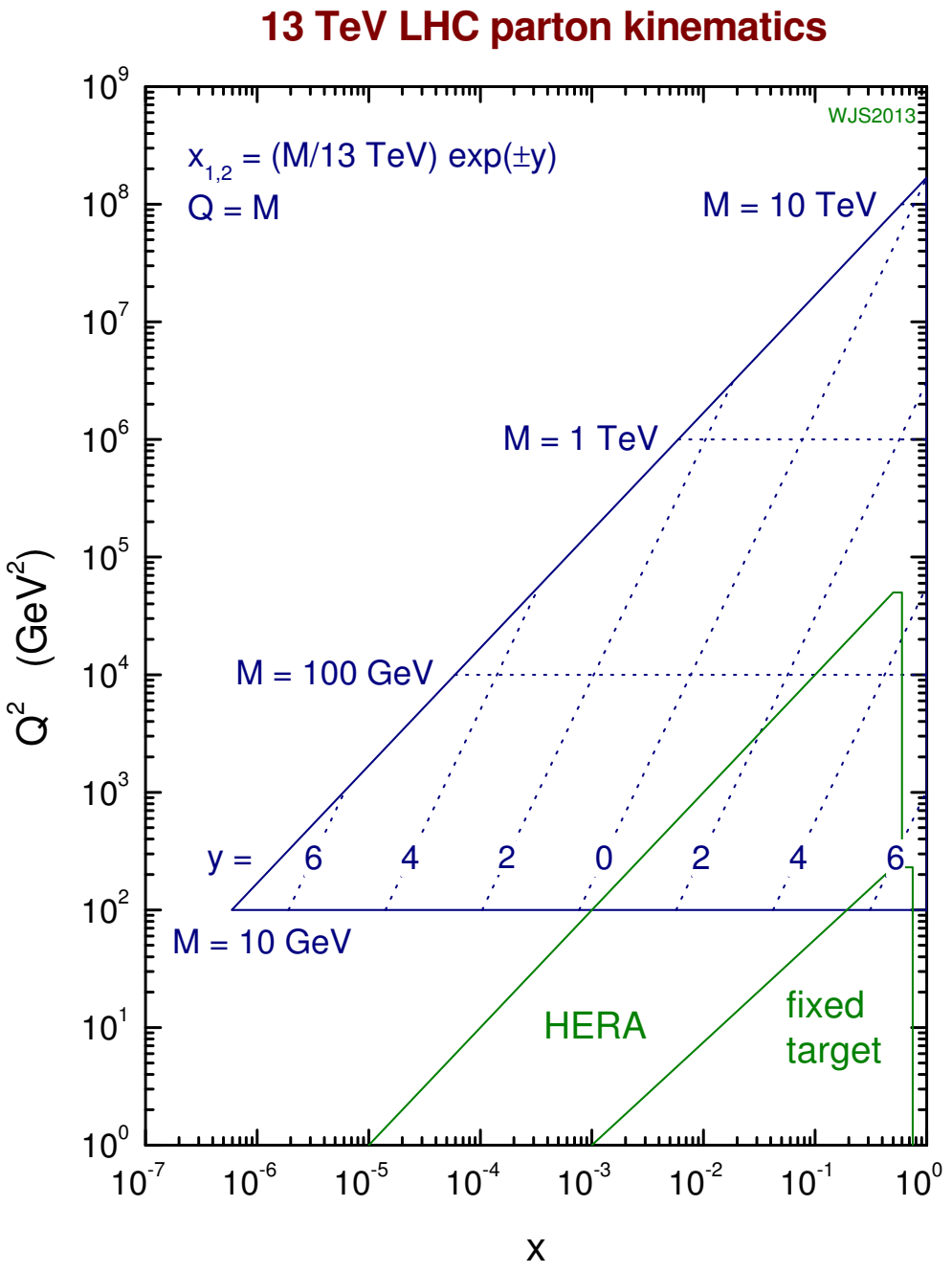

Figure 3.6: The kinematic reach of the LHC at $\sqrt{s} = 13$ TeV compared to the reach of the HERA(Hadron Electron Ring Accelerator, an electron-proton collider located at DESY in Hamburg, Germany). The relation between the momentum transfer Q and the momentum fraction x of the parton is shown, along with the rapidity y of the event. LHC reaches 3 orders of magnitude higher in Q^2 than HERA, allowing for productions of heavier particles. Taken from [62].

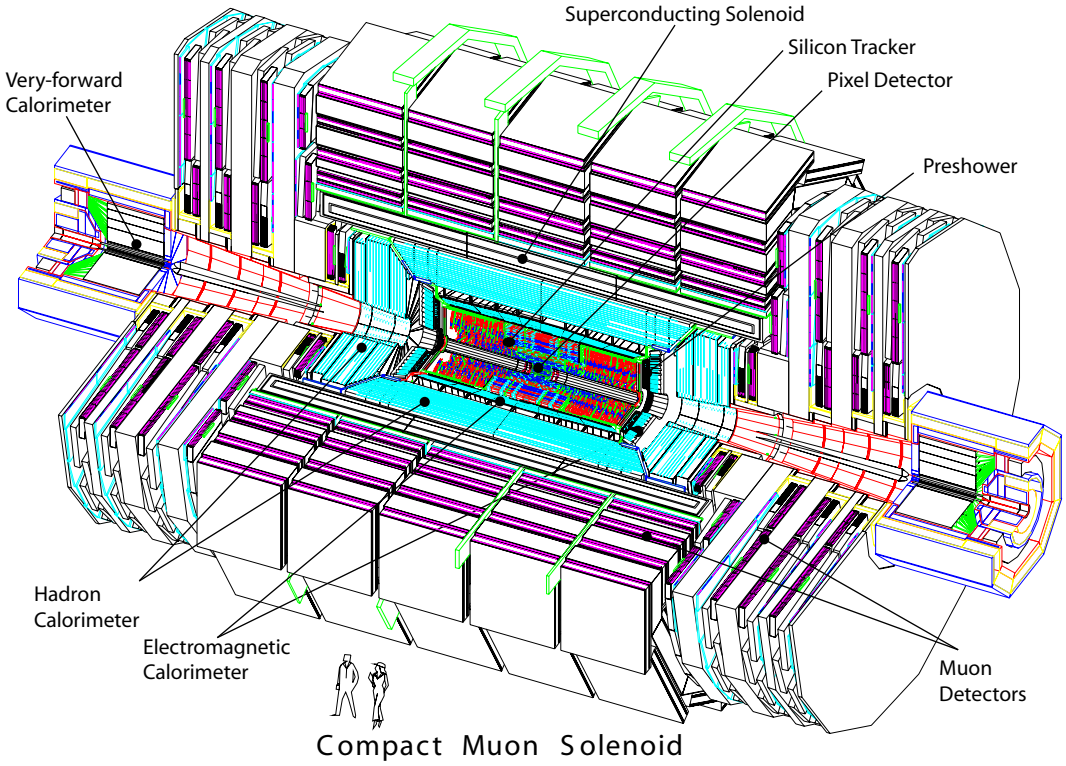

Figure 3.7: The exploded view of CMS detector. [65].

with the total weight of 14 000 tons. A scheme of the detector is presented in figure 3.7. In the following subsections, the detector components and trigger system will be discussed.

3.3.1 The solenoid

The superconducting solenoid magnet is one of the key components of the CMS detector. It provides a homogeneous magnetic flux of 3.8 T inside of it, and it surrounds the tracking and calorimetry systems. It allows for precise measurement of the charged particles momenta and the sign of their charge via measurement of the curvature of their tracks in the tracking system. The solenoid is 12.5 m long and has a inner bore of 5.9 m. The design magnetic flux inside of the solenoid is 4 T, however to maximize the longevity of the system it is operated at a lower field of 3.8 T.

To measure the momenta of the muons outside of the solenoid, an iron return yoke is used, which closes the magnetic field lines.

3.3.2 Inner tracking system

The tracking system is the innermost part of the CMS detector and is built using silicon based semiconductor sensors. It measures the trajectories of charged particles, which are used in the calculation of the charge and the momentum of the particles, as well as for the calculation of the impact parameter of the vertex, allowing for discrimination between primary and secondary vertices.

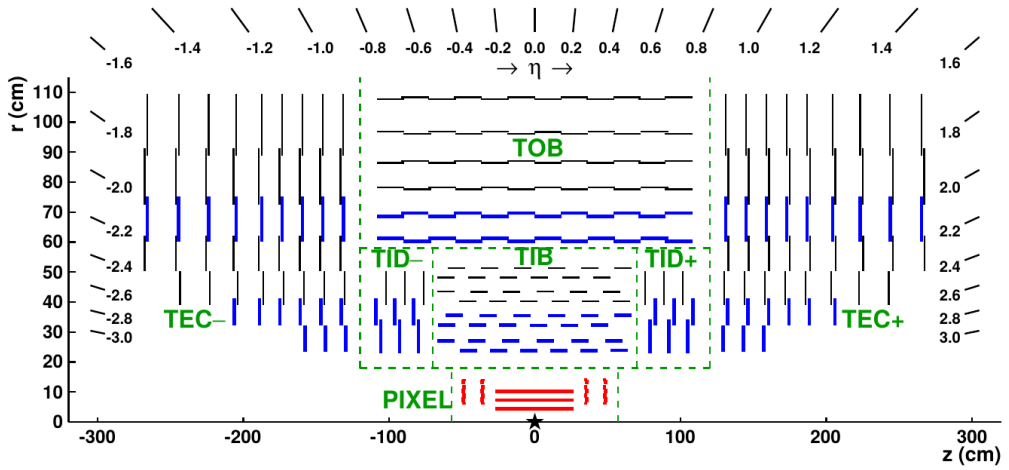

Figure 3.8: Layout of the inner tracker system, up to 2016, in the r-z plane. PIXEL and components of the silicon strip tracker are marked. Taken from [66].

The pixel detector

The particle flux varies with the distance from the interaction point. It is the highest closest to interaction point, with $\approx 10^7$ particles/s at $r = 10$ cm, which imposes the use of a pixel detector. It is composed of three cylindrical layers and two end disks on each side. The layers are positioned at 4.4 cm, 7.3 cm and 10.2 cm away from the interaction point, and the end disks, extending from 6 cm to 15 cm in radius, are positioned at $|z| = 34.5$ cm and 46.5 cm. The pixel size of 100×150 μm^2 results in an occupancy of about 10^{-4} per pixel per bunch crossing. There are $\approx 66 \times 10^6$ pixels allowing for a hit-position resolution of $10 - 20$ μm, therefore ensuring good separation of narrowly spaced trajectories. The layout of the whole tracking system is presented in figure 3.8.

In 2017 the pixel detector has been replaced with a new, upgraded system [67], designed to withstand higher luminosities and $\bar{\text{PU}}$ exceeding 50. Among others the changes include new geometry of the detector (4 layers positioned at $r = 3.0$ cm, 6.8 cm, 10.2 cm and 16.0 cm), redesigned end disks). However, new physics search and jet resolution measurement presented in this thesis use data collected prior to the pixel upgrade.

The silicon strip tracker

At the distance of $r = 20 - 55$ cm the particle flux drops, allowing the use of silicon strip detectors with the minimum strip size of 10 cm $\times$ 80 μm, which gives an occupancy of $\approx 2 - 3\%$ per crossing. This part of the detector is named track inner barrel(TIB) and consists of 4 layers. In the outermost part of the tracker, track outer barrel (TOB), the particle flux is low enough to enable the use of wider strips of 25 cm $\times$ 180 μm. To ensure the coverage at pseudorapidity up to $|\eta| = 2.5$, the tracker endcap (TEC) and tracker inner disc (TID) are mounted perpendicular to the beam line. The silicon strip detector has more than 15 000 individual strip sensors, it extends to a radius of 1.1 m and is 5.6 m long.

Combined information from pixel and strip detectors allows for precise reconstruction of tracks over pseudorapidity range $|\eta| < 2.5$. For particles with $p_T > 0.9$ GeV the average track-reconstruction efficiency in the central region ($|\eta| < 0.9$) is 94%, and at higher pseudorapidity it is 86%. In the barrel region, muons with momentum $p_T = 100$ GeV have a

relative resolution of 2.8% in p_T and 30 and 10 μm in longitudinal and transverse impact parameter respectively. For vertices reconstructed using at least 50 tracks the primary vertex resolution is 10 μm in $r-\phi$ plane and 12 μm in z direction [66].

3.3.3 Calorimetry

Calorimeters are designed to measure energy deposits of high-energy particles traveling through the detector material. Electrons and photons initiate an electromagnetic cascades by creating, via bremsstrahlung and pair production, electrons and photons with lower energies. Below a certain energy, photons and electrons dissipate the energy via ionisation and the photo-effect, consequently stopping the development of the shower. Hadrons (strongly interacting particles) produce further hadrons through a process called hadronisation, creating the hadronic shower. Around 90% of the hadrons produced are pions. Neutral pions decay into two photons, which initiate an electromagnetic shower, contributing to the electromagnetic fraction f_{em} of the particles energy. The charged secondaries dissipate energy through ionisation, excitation and interactions with nuclei. Around 20-40% of energy is carried by neutrons or absorbed in nuclei recoils and is not detected.

Calorimeters are usually characterized by the ratio of electromagnetic e and hadronic h calorimeter response $\langle e/h \rangle$. It can be determined using the ratio of detector response to pions π and electrons e:

$$\frac{\pi}{e} = \frac{e f_{em} + (1 - f_{em})h}{e}, \tag{3.6}$$

where f_{em} is the electromagnetic fraction for pions, which depends on the energy.

The relative energy resolution σ_E/E of the calorimeter can be parametrized as

$$\left(\frac{\sigma_E}{E}\right)^2 = \left(\frac{S}{\sqrt{E}}\right)^2 + \left(\frac{N}{E}\right)^2 + C^2, \tag{3.7}$$

where N represents the noise term, which dominates the uncertainty at low energies and originates from electronic noise. The stochastic term S represents statistic variations such as fluctuations in the shower development. At large energies the constant term C becomes dominant. It originates mainly from non-uniformity of the detector, calibration uncertainty and radiation damage of the active material used in the detector.

Electromagnetic Calorimeter The electromagnetic calorimeter (ECAL) [65, 68] hermetically surrounds the tracking system and is a homogeneous (the entire volume is sensitive) detector[1] build out of 61 200 lead-tungstate ($PbWO_4$) crystals in the barrel part and an additional 7324 crystals in each of the endcaps. The advantage of using a homogeneous design is that all charged particles are visible, which results in a good statistical precision. However, such detectors are expensive and they allow only limited segmentation, which translates into limited spatial resolution. The task of the ECAL is to measure the energy deposits of electrons and photons. $PbWO_4$ crystals have been chosen for their short radiation length X_0[2], Molière radius R_M[3] and low light decay time [68]. The biggest

[1] Except the Preshower (PS), which is a sampling calorimeter, in which absorber is sandwiched with signal generating material.

[2] X_0 corresponds to 7/9 of the mean free path of photon for pair production or a mean distance at which electron loses $1/e$ of it's energy.

[3] Within a cylinder of radius R_M on average 90% of the showers energy will be deposited.

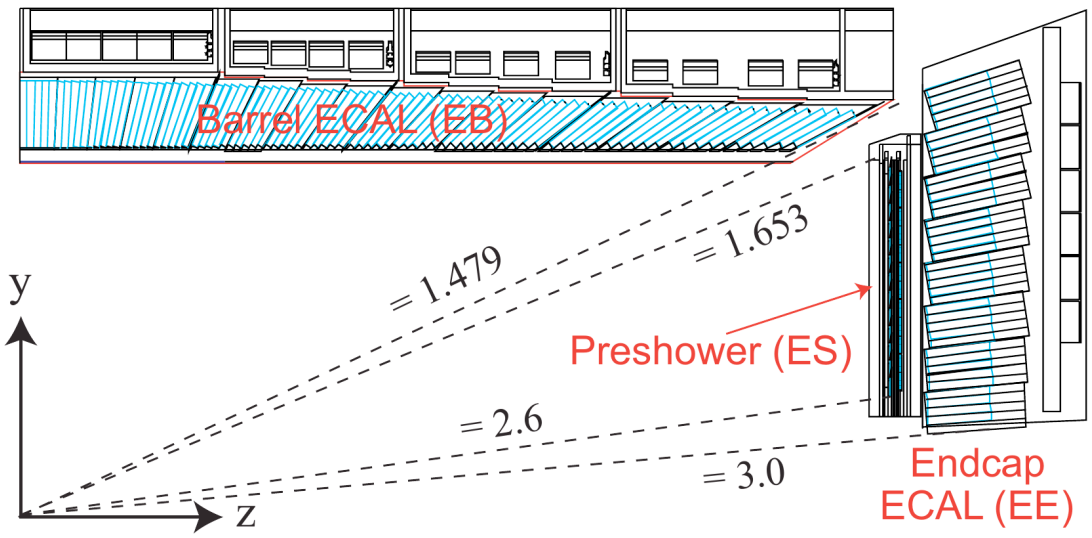

Figure 3.9: Layout of one quarter of the ECAL detector. [65].

disadvantage of these crystals is their low light yield, which has been compensated by the use of large-area silicon avalanche photodiodes.

As seen in figure 3.9, the ECAL is divided in 3 sections:

Barrel ECAL(EB) Covers the pseudorapidity range $|\eta| < 1.479$. The crystals (blue rectangles in figure 3.9) are 230 mm long, which corresponds to 25.8 radiation lengths X_0. The light produced is collected by photodiodes.

Preshower (ES) A disk-shaped detector installed in front of the Endcap ECAL. It covers pseudorapidity range $1.653 < |\eta| < 2.6$. The main purpose of ES it the detection of neutral pions and improvement of position determination of electrons and photons. It is a sampling calorimeter, where the active material, in this case a silicon strip detector, is interleaved with passive absorber layers. It is much more finely grained than the endcap. It was intended to resolve photons from neutral pions and generally to improve the spatial resolution, beneficial for resolving deposits originating from particles close to one another. However, the identification and separation powers are significantly impaired by parasitic signals. As a result, the energy deposits in the preshower are added to the closest endcap clusters. [69]

Endcap ECAL(EE) The endcap ECAL consists of a disk-shaped subdetectors made of 220mm long crystals $PbWO_4$. The scintillation light is collected by phototriodes. It extends the coverage to $|\eta| = 3.0$.

The length of the barrel and endcap crystals corresponds to approximately 24-26 radiation lengths, enough to contain over 98% of energies of the photons and electrons with momenta up to 1 TeV. The transverse size of the crystals in the barrel and endcap matches the Moliére radius of the material used, making it possible to resolve hadron and photon deposits only 5 cm apart from one another [69]. This feature improves the particle identification capabilities and is one of attributes making the CMS detector well suited to benefit from *Particle flow* algorithm. The performance of the ECAL has been tested with

electron beams [70, 71] and the relative energy resolution without the magnetic field has been measured as

$$\left(\frac{\sigma_E}{E}\right)^2 = \left(\frac{2.8\%}{\sqrt{E}}\right)^2 + \left(\frac{12\%}{E}\right)^2 + (0.3\%)^2. \tag{3.8}$$

Hadronic Calorimeter The hadronic calorimeter (HCAL) [64,65,72] in combination with ECAL creates a full calorimetry system, allowing for measurement of jets and missing transverse energy. It is composed of four modules: the hadron barrel (HB), hadron endcap (HE), hadron outer (HO) and hadron forward (HF) calorimeters (see figure 3.10).

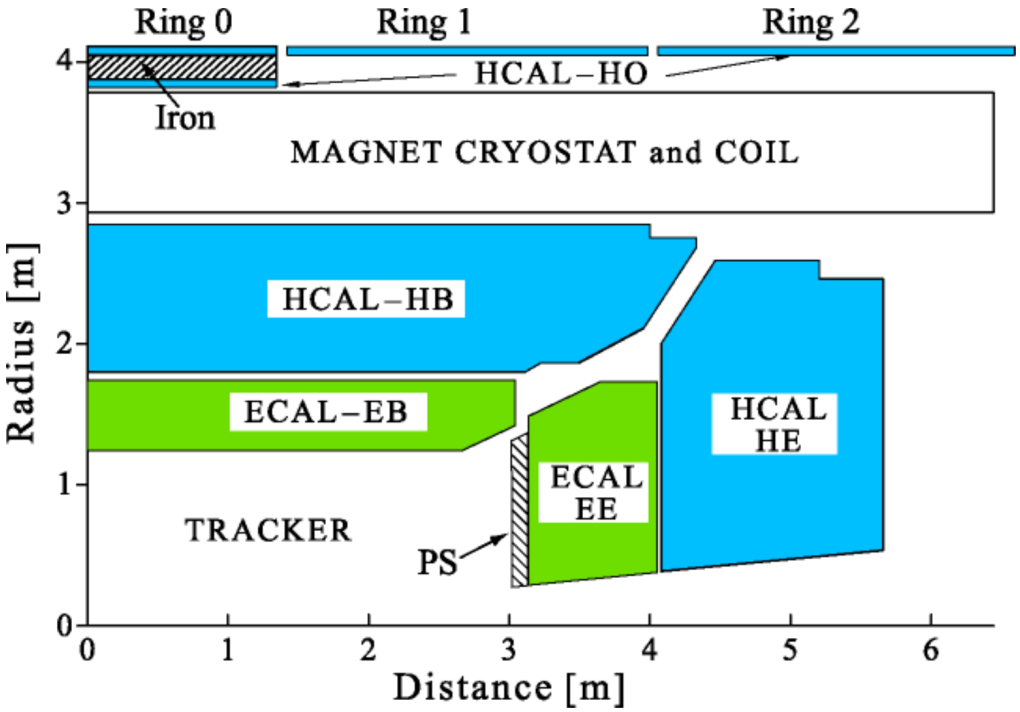

Figure 3.10: Layout of one quarter of the ECAL and HCAL detectors. [73].

The HCAL is a sampling calorimeter, with brass alloy serving as the absorber and plastic scintillators as an active material. In such a detector only part of the shower is visible, which results in lower statistical precision compared to homogeneous design. On the other hand sampling detectors are much cheaper and allow for a good transverse and longitudinal segmentation. Brass has been chosen because of its short interaction length and non-magneticity.

Hadronic Barrel Calorimeter(HB): The HB calorimeter covers a pseudorapidity range up to $|\eta| = 1.392$ and is completely contained within the magnet. The innermost and outermost layers of the absorber are made of stainless steel for structural strength; the remaining 15 layers are made of brass. The scintillator tiles are organized into cells with a size of $\Delta\phi \times \Delta\eta = 0.087 \times 0.087$. The depth of HB calorimeter in terms of interaction terms λ_I ranges from $5.8\lambda_I$ at $\eta = 0$ to $10.6\lambda_I$ at $|\eta| = 1.3$.

Hadronic Outer Calorimeter(HO) The HO consists of scintillator tiles mounted outside of the solenoid. It uses the magnet as additional absorber material, increasing the thickness to at least $11.8\lambda_I$.

Hadronic Endcap Calorimeter(HE) The HE extends the eta coverage to $|\eta| = 3.0$. Up to $|\eta| = 1.6$ it uses same granularity as HB, above the cells size is $\Delta\phi \times \Delta\eta = 0.175 \times 0.175$.

Hadronic Forward Calorimeter(HF) The HF is a disk shaped detector installed around the beam pipe approximately 11 meters away from the interaction point. It uses steel as the absorber interleaved with quartz fibres. The signal is coming from the Cherenkov light emitted by charged particles passing through quartz and is channelled to the photomultipliers. The HF covers a pseudorapidity between $|\eta| = 3.0$ and $|\eta| = 5.0$ and is organized into 450 towers in one forward module.

The performance of the HCAL has been tested with particle beams with energies from 2 to 350 GeV [73] and the combined energy resolution of the ECAL and HCAL is parametrised by

$$\left(\frac{\sigma_E}{E}\right)^2 = \left(\frac{94.3\%}{\sqrt{E}}\right)^2 + (8.4\%)^2. \tag{3.9}$$

For pions with energy E = 50 GeV this parametrization gives an uncertainty of 16%. The calorimeters of the CMS detector are a crucial component for efficient reconstruction of particles which are later clustered into jets. The high segmentation and resolution of the ECAL combined with hermeticity of the HCAL allow for good identification of photons and high energy resolution of charged and neutral hadrons.

3.3.4 Muon system

The outermost part of the CMS detector is the muon system. It consists of three types of gaseous detectors installed in an iron frame, which also serves as a return yoke for the magnetic field. The measurement of the muons' momenta is based on the combined information from the inner tracker and muon system. For muons with momenta up to 200 GeV, the measurement in the muon system is strongly influenced by multiple scattering and radiation losses in the material before the first muon station: for these muons the best measurement is given by the inner tracker. However, for high momentum muons the information from the muon system improves the resolution significantly (See [65]).

The layout of the muon system is shown in figure 3.11. Different detector types have been used in the various radiation environments:

Drift tube chambers (DT): In the barrel region $|\eta| < 1.2$, where the neutron induced background is small and muon rates are also small, drift tube (DT) chambers have been used. They are organized in four layers (*stations*), installed between radii $r = 4.0m$ to $r = 7.0m$ in such a way, that the high-p_T muon will always cross at least 3 muon stations. Each station has a ϕ precision better than 100μm in position and 1 mrad in direction.

Cathode strip chambers (CSC): In the endcap region the muon rates and radiation are high, and the magnetic field is high and non-homogeneous. Cathode strip chambers are used in that region due to their high radiation resistance and fast response. They cover the η range $0.9 < |\eta| < 2.4$. CSC is a multi-wire proportional chamber detector, with anode wires and cathode strips. The signal on the strips is fast and is used in Level-1 triggering;

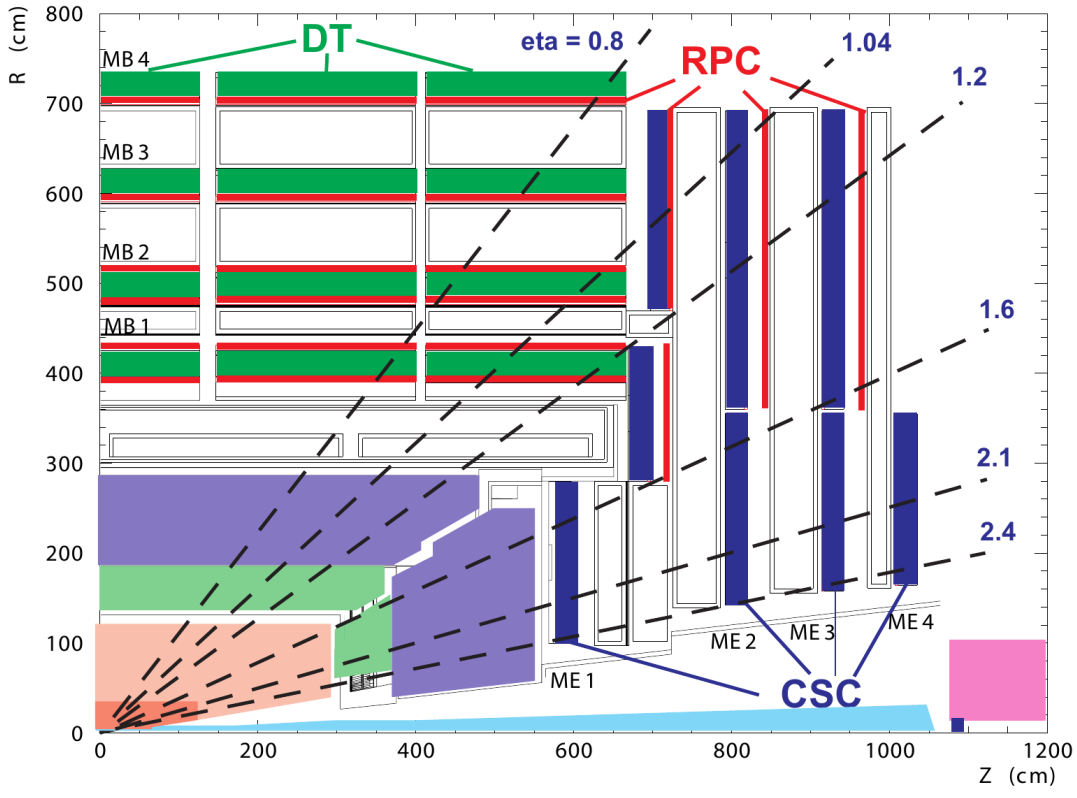

Figure 3.11: Layout of one quarter of the muon system. [65].

however, the spatial resolution of the hit is coarser than in drift tube chamber. The typical resolution provided by the chamber is 200μm and angular resolution is ≈ 10mrad.

Resistive plate chambers (RPC): RPC detectors are used to complement drift tube and cathode strip chambers for pseudorapidities up to $|\eta| = 1.6$. These are gaseous parallel plate detectors which provide an excellent time resolution; however, the spatial resolution is inferior compared to the CSC and DT detectors. The RPC are used for trigger system.

Muon identification efficiency is around $95 - 99\%$ high, except in the transition region $|\eta| \approx 1.2$ between the barrel and endcap detectors. The momentum resolution for muons with $p_T < 100$GeV ranges from $1 - 2\%$ in the barrel region to $\approx 6\%$ in the endcap and for $p_T > 100$GeV is is below 10%.

3.3.5 Trigger system

The high luminosity of the LHC means that events with a very low cross section can be observed, but also means that the event rate will be extraordinarily high. The bunch crossing rate with 25ns time separation is 40 MHz, and a single event corresponds to approximately 1 MB of data, which makes it impossible to record every event. Thus an event selection system has to be employed to preselect interesting collisions and reduce the volume of the recorded data [65]. The CMS trigger system consists of two main parts, the Level-1 trigger and High-Level trigger:

Level-1 (L1) trigger: The full resolution data about each event is stored in buffers while the reduced-granularity and reduced-resolution data is provided to the Level-1 trigger. Within the time of 3.2μs the simplified data from the calorimetry and muon systems is transferred to the L1 trigger hardware, where the decision is made whether to keep the data, and that decision is delivered back to the front-end electronics where buffered data is discarded or transferred further. The L1 decision is based on the so-called *trigger primitive* objects such as photons, electrons or jets above certain E_T and p_T thresholds and on global objects like missing transverse energy. The event rate after L1 trigger is reduced to less than 100 kHz.

High-Level trigger (HLT): After an event has passed the L1 trigger selection, it is forwarded to the High-level Trigger system. The selection at HLT is based on the full information from the detector and using simplified reconstruction techniques similar to reconstruction performed later when processing data for use in physics analyses. HLT is software based, which allows for modification even during the data taking. The event rate is reduced to the order of 100 Hz.

4 Simulation of particle collisions

The outcome of a collision of particles such as protons, as in case of the LHC, is very complicated, to say the least. The collision of the protons is in fact an interaction between two partons, gluons or quarks, that carry only a fraction of the protons momentum. Particles that are created as a result of the interaction of these partons decay further into more particles which carry fraction of the initial partons momentum, and then they hadronize, creating a cascade of particles that interact with the detector material. On top of that, during a single bunch crossing more than one proton collision happens, which means that in a single event actually the outcome of several collisions is observed.

The simulation of high energy particle collisions is a very important tool in a variety of applications, varying from the interpretation of the results of the experiments, to the prediction of the behavior of detectors being designed or optimization of the search strategies. It relies on *Monte Carlo* (MC) techniques, which use a sampling of random numbers in order to make a prediction of a considered value. The brief description of the simulation process and utilized software is provided below.

4.1 Simulation steps

A simulation of high energy collision follows several steps, overview of which is presented in figure 4.1. The steps are described below.

Hard process The collision of two protons is in fact an interaction between two partons. This interaction is usually referred to as the *hard process*. The interaction is described by the type of partons that interact (gluons or quarks), the fraction $x_{a,b}$ of the protons momentum that the partons carry, and the momentum transfer Q^2 between the two partons. Using the factorization theorem [75] the probability of a $2 \to X$ process can be transcribed as

$$\sigma = \sum_{a,b} \int_0^1 dx_a \int_0^1 dx_b \int f_a(x_a, Q^2) f_b(x_b, Q^2) d\sigma_{ab\to X}(Q^2) \tag{4.1}$$

where $\sigma_{ab\to X}$ is the cross-section of a given process $2 \to X$, and $f_a,\ f_b$ are the *parton distribution functions* (PDFs) of the partons a and b. PDFs can be determined experimentally at deep inelastic scattering experiments. Most precise measurements of the PDFs have been performed at the HERA collider at DESY[1] [80].

Parton shower The particles produced in the hard process emit a cascade of softer particles, referred to as *parton shower* or *final-state radiation* (FSR). This evolution is usually described by a probabilistic shower algorithm. The same effect can be observed for the initial partons before the hard process. The shower produced from these *initial* partons is called *initial-state radiation* (ISR).

[1] At HERA the PDFs were measured up to $Q^2 = 1$ GeV^2. However, knowing PDF at some initial Q^2, it is possible to calculate it at a different scale using the DGLAP evolution equation [76–79]

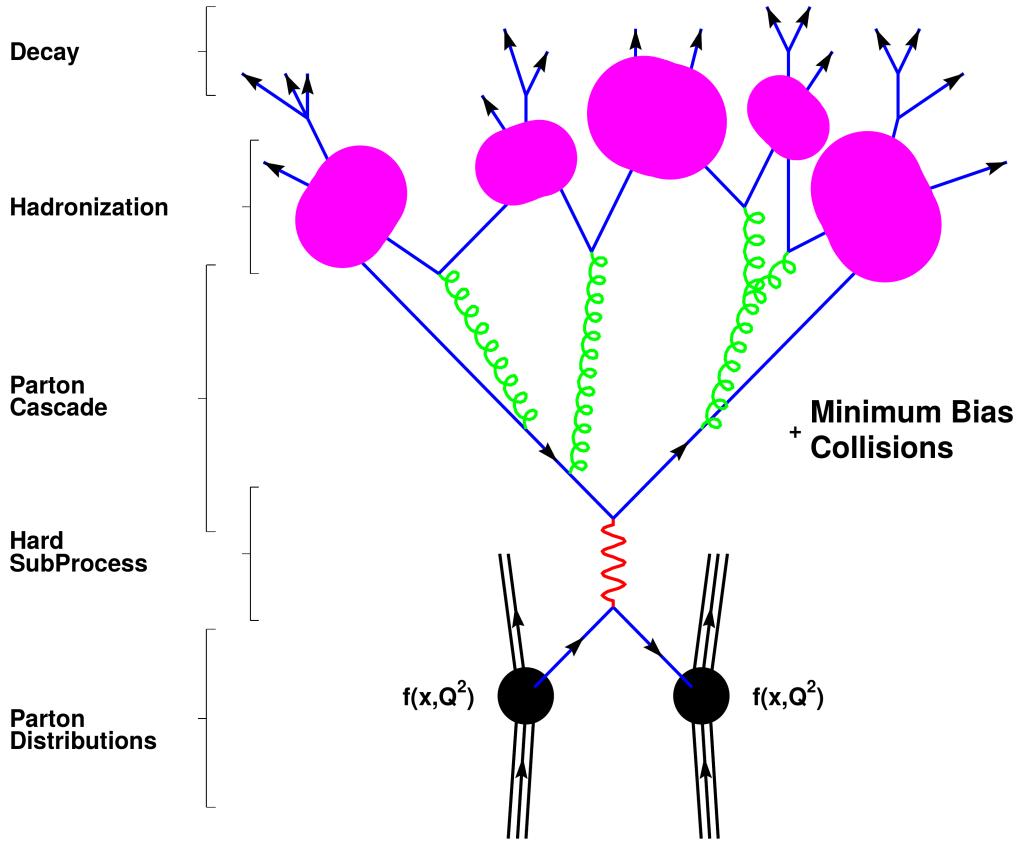

Figure 4.1: Schematic of the steps of the event simulation. Taken from [74].

Hadronization The process of showering continues until the produced particles have energies low enough to form color neutral states. The transition from partons to hadrons is referred to as *hadronization*. At this step of the simulation energies are too low to apply perturbation theory. Hadronization is characterized using two types of models. *String models* [81] assume that the color potential depends linearly on the distance between the particles in the shower, and *cluster models* [82,83] assume that at some intermediate mass scales of few GeV quarks and antiquarks form clusters that decay directly into lighter clusters, and below that scale they hadronize via a two-body decay.

Decay The hadrons formed in the previous step are usually unstable with lifetimes $c\tau \lesssim 10$ mm. The decay of these hadrons into stable particles are modeled based on experimental and theoretical knowledge about such processes. The particles produced at this step of the simulation are referred to as *generator-level* or simply *gen* particles.

Underlying event Additional interactions within the protons or the interactions of the remnants of the protons after the hard interaction can produce further hadrons which contribute to the observed events. Such contributions are broadly referred to as *underlying event* (UE)

4.2 Event generators

The steps described in previous section are calculated using various software called *event generators*. There are several event generators utilized in high energy physics, some of which are described below.

MadGraph5 [84] `MadGraph` is a leading-order (LO) and next-to-leading order (NLO) $2 \to n$ matrix element generator. It provides a precise description of multiparton processes. It can generate any tree-level process, however, usually events are generated with $n \leq 6$, since the generation procedure is time-consuming. Because it does not include showering and underlying event calculation, it has to be interfaced with other event generators, like `Herwig++` or `Pythia`, using the so-called MLM procedure [85].

Powheg [86–88] `Powheg` is a next-to-leading order (NLO) $2 \to 2$ process matrix element generator. Similar to `MadGraph`, it has to be interfaced with other generators, like `Herwig++` or `Pythia`, since it does not include showering and underlying event simulation. The NLO computations provide improved QCD modeling.

pythia 8 [89, 90] `Pythia` is a so-called *multi-purpose generator*, meaning that it can simulate the whole event including all steps described in section 4.1. It is designed to simulate hadrons and same-generation leptons collisions. The $2 \to 2$ hard process matrix elements are calculated at LO. Hadronization is simulated via the string model. Additionally, `Pythia` can be interfaced with other generators to perform only the showering, hadronization and decay steps of the simulation.

HERWIG [91] `HERWIG` is a multi-purpose generator. It is designed to simulate lepton-lepton, lepton-hadron and hadron-hadron collisions. `HERWIG` uses angular ordering in generation of parton showers, which provides correct treatment of the coherence of soft radiation.

4.3 Detector simulation

To predict the signal measured by the detector a *full simulation* is performed using `GEANT4` software [92–94]. This step includes modeling the interactions of the particles with the detector material, both sensitive and inert, and the behavior of the read-out electronics. Because this step is very resource-consuming, a simplified method, called *fast simulation* [95], has been developed.

The output of the detector simulation is stored in the same format as the collision data. The next step of the processing of simulated sample is the object reconstruction, discussed in the following chapter.

5 Object reconstruction

Particles produced in proton-proton collisions interact with the detector, and the signature which they produce can be used not only to measure their transverse momentum and energy, but also to identify them. The identification of the particles is performed by combining the signals measured in the various detector systems and by using them in the *Particle Flow* (PF) algorithm [69].

In this chapter the reconstruction and identification of particles measured by CMS detector is described. First the Particle Flow algorithm is discussed in section 5.1. Then, the reconstruction of the muons is described in section 5.2 and of the electrons in section 5.3. The discussion of reconstruction of jets, jet energy corrections and the *b-tagging* procedure are presented in sections 5.4, 5.5 and 5.6 respectively.

5.1 Particle flow

Modern detectors for measurement of high-energy particles are build according to a cylindrical, multi-layered design. These layers, described in chapter 3, are designed to measure specific particles or their specific properties. This allows for a reconstruction of the physics objects based on the signals collected with the different subdetectors:

- *jets* consist mainly of photons and hadrons, whose energy can be reconstructed from energy deposits measured by the calorimeters.
- *electrons* and *isolated photons* can be reconstructed based on the ECAL measurements in combination with the tracking detector.
- heavy flavor *jet tagging* can be performed using the information from the tracker, in particular, the most inner pixel detector.
- *muons* can be reconstructed using the muon chambers in combination with the tracking detector.

The identification of these objects can be significantly improved by combining the signals from different detector parts using the *particle-flow algorithm*. It was first developed by the ALEPH experiment at LEP [96] and is planned to be used at future lepton colliders, like e.g. ILC or CLIC [97, 98]. A detector feature crucial for a successful implementation of the PF algorithm is the spatial granularity of the sub-components of the detector. A too coarse detector leads to merging of the signals induced by different particles, especially in the case of electromagnetic and hadronic showers in the calorimeters. The first step of the event reconstruction is the identification of the tracks in the tracking system and calorimeter clusters.

Tracks are rendered using the iterative algorithm [99, 100]. The procedure starts with a selection of a seed trajectory, which usually includes two or three hits in the pixel detector, and is required to pass some quality criteria, e.g. it should extrapolate close to the interaction point. Then the trajectory is extended to all hits measured in the successive

layers. The trajectories are extended by one layer at a time, up until the outermost layer is reached. To decrease the number of considered trajectories, at each layer some quality criteria are applied to reject the least physical ones. The tracks kept for further analysis have to be reconstructed using at least 8 hits, to originate from a few mm away form the beam axis, to have the momentum of at least 0.9 GeV and have no more than one hit missing along the path. A similar procedure is applied in the muon system, resulting in muon tracks.

Calorimeter clusters are the basic calorimetry objects and are calculated separately for each subcomponents of the calorimeter: ECAL barrel, ECAL endcap, HCAL barrel, HCAL endcap, HCAL forward, HCAL outer and two preshower layers. The clustering starts with a *cluster seed*, which consists of the cells with an energy deposit above a certain threshold and larger than the neighboring cell deposits. Then, the *topological clusters* are formed by adding to the seed cluster the cells that have a common side or corner with the seed. The energy of these cells has to be larger than two standard deviations above the noise level.

Typically, a particle traveling through the detector leaves a signal that consists of the objects described above. Depending on the type of the particle, its signature might include a charged particle track, several calorimeter clusters and a muon track. These objects are combined using a so-called link algorithm. The inner tracks are extrapolated to the calorimeter system, and if they match a cluster, they are linked together. Additionally, to account for bremsstrahlung, tangents of the trajectories are also extrapolated to the clusters. Clusters within ECAL and HCAL are also matched. Finally, the muon tracks are combined with inner tracking system trajectories.

The particle flow algorithm analyses collections of matched reconstructed objects and interprets them. Each time a particle is identified, its signal is removed from the further analysis. First, the muons are reconstructed, followed by identification of the electrons along with the clusters originating from bremsstrahlung. The remaining high quality tracks are compared with the clusters they are matched to. If the energy measured using the calorimeter agrees with the momentum measured using the track, the object is identified as a charged hadron. Based on the remaining deposits in the ECAL and HCAL photons and neutral hadrons are identified. If there is no HCAL deposit, or if it is smaller than 15% of the total energy in the cone of radius $R \leq 0.15$ around the cluster, the particle is identified as a photon. If there are deposits in the HCAL, these are interpreted as neutral hadrons.

The particles identified using the PF algorithm are called *particle flow candidates* and they are used to construct more complex objects like jets and to calculate quantities like the missing energy $\not{E}_T$. Quality criteria applied to electrons and muons used in the analysis presented in chapters 7-9 are described in sections 5.3 and 5.2 respectively. The reconstruction, calibration and flavor tagging of the jets are discussed in section 5.4.

5.2 Muon

The muon reconstruction is based on the inner tracker and muon system trajectories. The muon tracks based only on reconstruction from muon system inputs are called *standalone-muon tracks*. They are then extrapolated and fitted with tracks reconstructed from the inner tracker system, forming the *global-muon track*. For high transverse momentum muons, the global tracks have a superior resolution compared to inner tracker trajectories.

If the muon has low momentum, it may occur that it does not result in a track being reconstructed in the muon system. However, it should still generate single hits in the muon detector which can be matched to the inner tracks and may form the *tracker muon*. The muon identification is limited to $|\eta| < 2.4$, which corresponds to the muon system η range.

Muon candidates considered in search for supersymmetry [52] discussed in this thesis have more strict requirements on the matching between the tracker and the muon-detector trajectories [101] compared to the standard PF muons. Additionally, they have to pass an isolation requirement. It is based on the variable I, defined as the scalar sum of transverse momentum of charged hadron, neutral hadron and photon candidates in a cone of radius $R = \sqrt{(\Delta\phi)^2 + (\Delta\eta)^2}$ around the muon direction. The radius of the cone depends on the transverse momentum of the muon and is defined as:

$$R(p_T) = \begin{cases} 0.2 & \text{if } p_T \leq 50 \text{ GeV} \\ 10 \text{ GeV}/p_T & \text{if } p_T \in (50, 200) \text{ GeV} \\ 0.05 & \text{if } p_T \geq 200 \text{ GeV} \end{cases}$$

where p_T is the transverse momentum of the muon. The isolation requirement for muons is $I < 0.2$.

5.3 Electron

Most of the electron energy is measured in the ECAL. However, because of the bending in the magnetic field, electron deposits in the ECAL are spread in ϕ, and due to bremsstrahlung it emits photons tangent to its trajectory. To properly identify all of the clusters originating from the considered electrons a specialized technique called *Gaussian Sum Filter* (GSF) is employed [102]. This algorithm not only identifies clusters caused by bremsstrahlung, but also estimates the fraction of the energy lost by the electron due to it. In order to enhance the quality of reconstructed electrons used in [52], they are required to pass additional requirements on the ECAL to HCAL energy deposits ratio and on the lateral shape of the ECAL shower [103]. Furthermore, they have to pass an isolation criteria of $I < 0.1$, where I is defined in the same way as for muons.

5.4 Jet

A collimated stream of particles, produced as a result of evolution of parton showers (see chapter 4), is reconstructed as an object called *jet*. Choosing a proper definition of the jet, that encapsulates the evolution of the partons they originate from, is essential for the measurements and searches performed on the data collected in high energy physics experiments. In the following section few definitions of the jets will be discussed, and in section 5.5 a procedure of correcting the jet transverse momentum will be presented.

5.4.1 Jet clustering algorithms

A jet clustering algorithm defines the procedure of combining individual particles into a jet. The algorithm is required to properly address the effects of collinear splittings of the particles, a feature called *collinear safety*, and the emissions of soft particles, which is denoted as *infrared safety*. In perturbive QCD calculations the soft and collinear divergences

cancel exactly via Bloch, Nordsieck [104] and Konoshita, Lee and Nauenberg [105,106] theorems. As a result, the jet algorithms are required to be insensitive to collinear and soft splitting, a feature referred to as *IRC safety*.

A detailed overview of the definitions of jets and their practical implications is provided in [107]. Below, a brief description of the two most common types of jet algorithms, the *cone algorithms* and the *sequential recombination algorithms*, is presented.

Cone Algorithms are historically the first jet algorithms, intended for application in e^+e^- experiments [108]. Cone jets are typically defined using a geometric and an energy parameter. In the first definition, the geometric parameter defines the opening angle δ of the cone, and the energy parameter ϵ defines the amount of the event energy which should be contained within that cone. Currently, an updated version of the algorithm is used, known as *iterative cone algorithm*. In this algorithm, a seed particle is chosen, and the momenta of all particles in a circle of size R in the $\phi - \eta$ plane around that particle are summed. The procedure is repeated with the newly summed momenta serving as the new seed until the jet is stable. The constituents of the stable jet are removed from the collection of particles and the procedure is repeated again to find another jet. In this algorithm the original angle δ is replaced by the dimensionless jet radius R, and ϵ is replaced with a transverse-momentum threshold of the jet. A procedure defined in this way is not collinear safe. This problem is fixed in the *seedless cone* algorithms, in which each subset of particles is checked if it forms a stable cone. This procedure is not very practical for application in CMS, as the number of possible subsets of all particles grows exponentially. The *SISCone* algorithm, presented in [109], significantly reduces the computation time, however it is still more time consuming than the sequential recombination algorithms.

Sequential recombination algorithms were also developed for e^+e^- experiments, and the first implementation was presented by the JADE collaboration in [110, 111]. In these methods, a metric is introduced, defining the distance d_{ij} between two particles i and j. Additionally, for hadron colliders, a distance d_{iB} between a particle i and the beam is also introduced. A metric, invariant under longitudinal boost, is given by

$$d_{ij} = \min(k_{T,i}^{2p}, k_{T,j}^{2p}) \frac{\Delta R_{ij}^2}{R^2}, \tag{5.1}$$

$$d_{iB} = k_{T,i}^{2p}, \tag{5.2}$$

where ΔR_{ij} is the distance between particles i and j in the $\phi - \eta$ plane, R serves as an angular cut-off and p is a parameter which defines the properties of the algorithm. The first step of the procedure is the calculation of all possible d_{ij} and d_{iB} in order to find the minimal distance d_{min}. If d_{min} is some d_{ij} and it is below some *jet resolution threshold* d_{cut}, the particles i and j are merged together and form a new particle, and the procedure is repeated from the beginning. If d_{min} is some d_{iB}, particle i is declared as jet, removed from the list of particles and the first step is repeated. The algorithm ends when there are no particles left.

The choice of the p parameter defines the behavior of the algorithm. The inclusive k_T algorithm [112] uses $p = 1$, which results in clustering of jets around soft particles. Because of that it is necessary to include some minimal p_T for a jet. Also, k_T jets are likely to be geometrically irregular, complicating the detector calibration. On the other

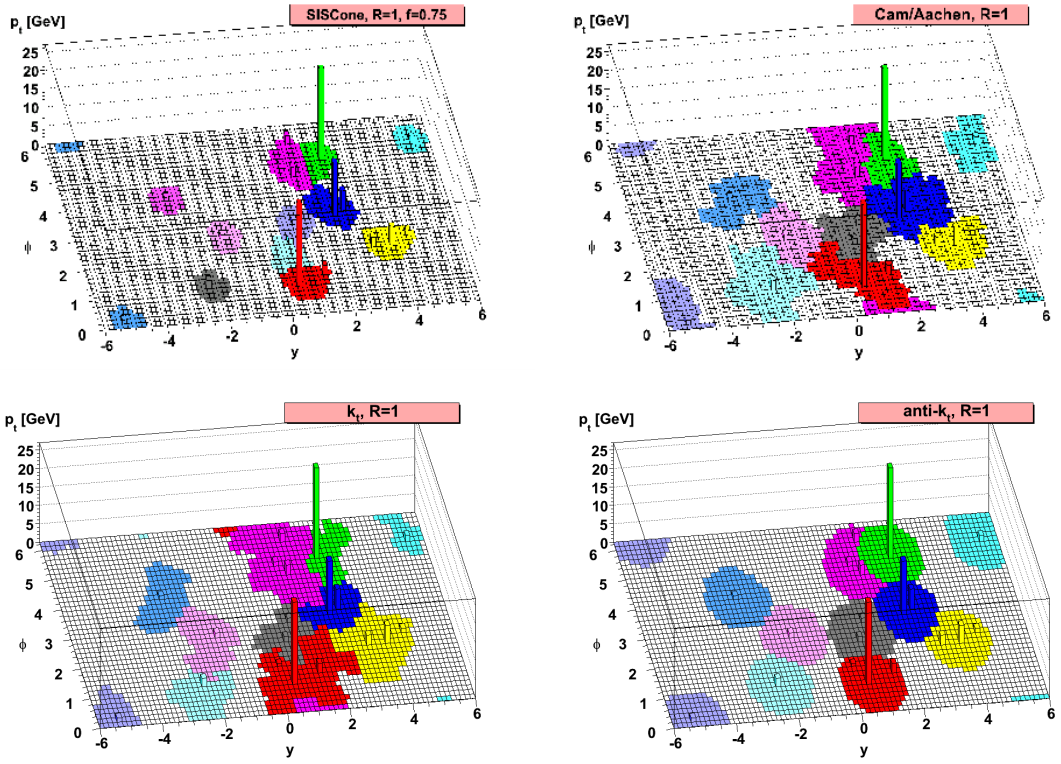

Figure 5.1: Visual representation of the preformance of different clustering algorithms on a parton-level Herwig [117] generated event. Taken from [52]

hand, the algorithm is IRC safe. The *Cambridge-Aachen* (CA) algorithm [113–115] uses $p = 0$. In this algorithm particles with smallest distance $\Delta R_{i,j}$ are clustered. It produces irregular jets, but is considered suitable for the studies of jet substructure. CA algorithm is also IRC safe. The *anti-k_T* algorithm [116] uses $p = -1$ and is the most commonly used algorithm in the CMS analyses. It starts the clustering from the hardest particles and is rather insensitive to soft objects. It is an IRC safe algorithm which produces circular jets which are easier to calibrate.

A visual representation of the performance of different jet clustering algorithms is presented in figure 5.1. At the CMS experiment the anti-k_T algorithm is used. The typical cone size used for the 7 and 8 TeV analyses was $R = 0.5$ and for the 13 TeV it is $R = 0.4$. Thus, the jets used for 13 TeV analyses are denoted as AK4 jets. It is important to include some further classifications of the jets.

PF Jets If the jets are reconstructed using the PF candidates, they are called *Particle Flow Jets* (PF Jets). PFJets are the default jets used in CMS analyses. They exhibit superior performance due to the generally improved resolution of the PF candidates over e.g. calorimeter-only based objects. To limit contributions from pileup, the so-called *charged hadron subtraction* (CHS) technique is employed. The CHS removes charged hadrons which originate from vertices other than the primary one from the collection of the particles considered in the clustering algorithm. The resulting jets are denoted as PFCHS jets. An alternative approach to correct for the pileup contribution to jets is the *Pile Up Per Particle Identfication* (PUPPI) [118]. This algorithm calculates a weight for

each PF candidate, which describes how likely the particle is to originate from pileup.

Calo Jets The jets clustered using only the calorimeter deposits are called *Calo Jets*. Although these jets have inferior resolution compared to PF jets, they are used in some situations. For example Calo jets are used in the L1 trigger calculations, as the PF reconstruction is not performed at that stage.

Additionally, jets can be reconstructed using not only detector level, but also generator level objects. Such jets are referred to as *particle jets* or *generator jets* and are widely used in studies, for example in studies of the properties of jets.

5.5 Jet energy corrections

The momentum of a jet measured with the detector and reconstructed using a given algorithm will not, in general, be equal to the momentum of the jet at the particle level. Even the momentum of the particle-level jet will not be equal to the one of the original particle, but this relation will not be investigated in this work. A relation between the measured and particle-level jet momenta can be investigated using the *jet response*, which is defined in this thesis as the ratio of the momentum measured in the detector to the momentum of the corresponding generator jet. However, given the constrains imposed by the design of the detector, *jet transverse-momentum response* $\mathcal{R}$ is used, defined as

$$\mathcal{R} = \frac{p_T}{p_T^{particle}} \tag{5.3}$$

where p_T is the transverse momentum of a jet and $p_T^{particle}$ is the transverse momentum of the particle level jet matched to a detector jet. Neutrinos are not included in the clustering of the jets. For the studies of the calorimeter jet response also the muons are excluded from the clustering because their momentum is measured using tracker and muon system. However, for the purpose of the studies of the particle flow jet transverse momentum, muons are not excluded from the jets [119]. The average value of response $\langle\mathcal{R}\rangle$ is denoted as *jet energy scale* and it should be equal to unity $\langle\mathcal{R}\rangle = 1$. The standard deviation of $\mathcal{R}$ distribution is the relative *jet transverse-momentum resolution*.

5.5.1 Jet energy calibration

Due to effects like non-linear detector response, pileup and detector noise, the jet energy scale requires adjustment. To ensure that $\langle\mathcal{R}\rangle = 1$ *Jet Energy Corrections* (JEC) have to be derived. In CMS the calculation of the JEC employs a factorized procedure [120] schematically presented in figure 5.2. The steps of the procedure are discussed below.

L1 offset correction is the first step of the correction procedure. It is designed to remove the contribution of particles not originating from the hard scattering, for example from pileup events or electronic noise, from the energy of the jet. The magnitude of the effect can be estimated as a function of the offset energy density ρ [121,122], jet area A, jet p_T and pseudorapidity η. The offset energy ρ is defined as the median of the energies measured in each $\eta-\phi$ cell. The use of the median instead of the mean guarantees that the high-p_T jets do not influence the estimate. The jet area is calculated by adding randomly distributed infinitely soft particles to the event and performing the jet clustering. The area A of the jet is given by the fraction of the soft particles that were clustered with it. The correction

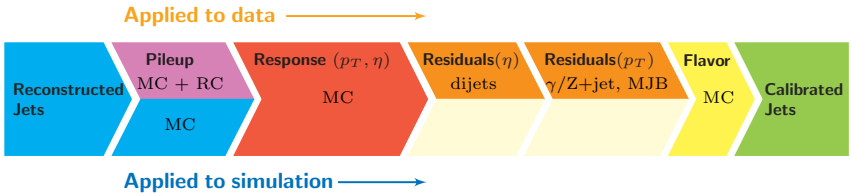

Figure 5.2: Consecutive stages of JEC, for data and MC simulation. All corrections marked with MC are derived from simulation studies, RC stands for random cone, and MJB refers to the analysis of multijet events. . Taken from [120].

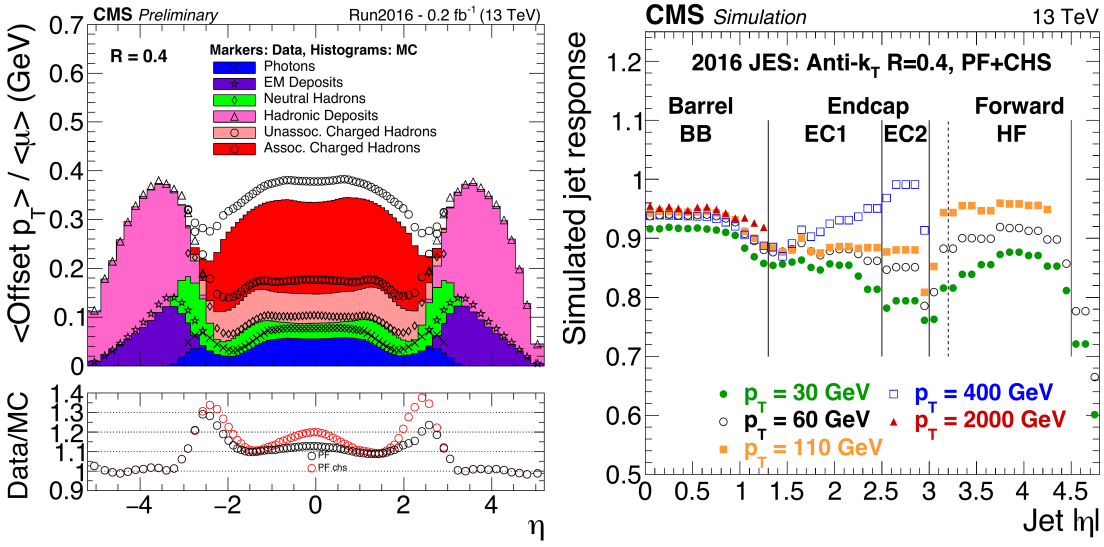

Figure 5.3: The average offset per additional pileup interaction μ in data and in simulation (left) and MC-truth response corrections for different values of jet p_T (right). Taken from [124].

is derived using simulated samples by comparing the p_T of jets with and without pileup contribution. The corrections for differences between data and simulation are derived from the so-called zero-bias events. The pileup offset can be identified by calculating the average transverse momentum of the PF candidates in a randomly placed cone. The offset corrections, along with the data to simulation ratio, are presented in the left plot in figure 5.3. The different sources of the offset are presented in the histogram.

L2L3 MC-truth corrections are derived from simulated samples by comparing the p_T of matched reconstructed and particle level jets. This correction is derived after the L1 offset is applied. The simulated QCD multijet events used for the derivation of L2L3 MC-Truth correction were generated with the `Pythia 8` event generator [89, 90] tuned with CUETP8M1 [123], and the detector simulation was performed by using `Geant4` [94]. The correction is calculated as the mean of the jet response R derived in intervals of p_T and $|\eta|$. The jets used in the calculation of the response are required to be matched with a distance parameter $\Delta R < 0.2$, and the particle level jets do not include the energy contributions from neutrinos. MC-truth correction, for five values of jet p_T, as a function of $|\eta|$, are presented in left plot in figure 5.3. The ranges of different subdetector parts are marked on the plot.

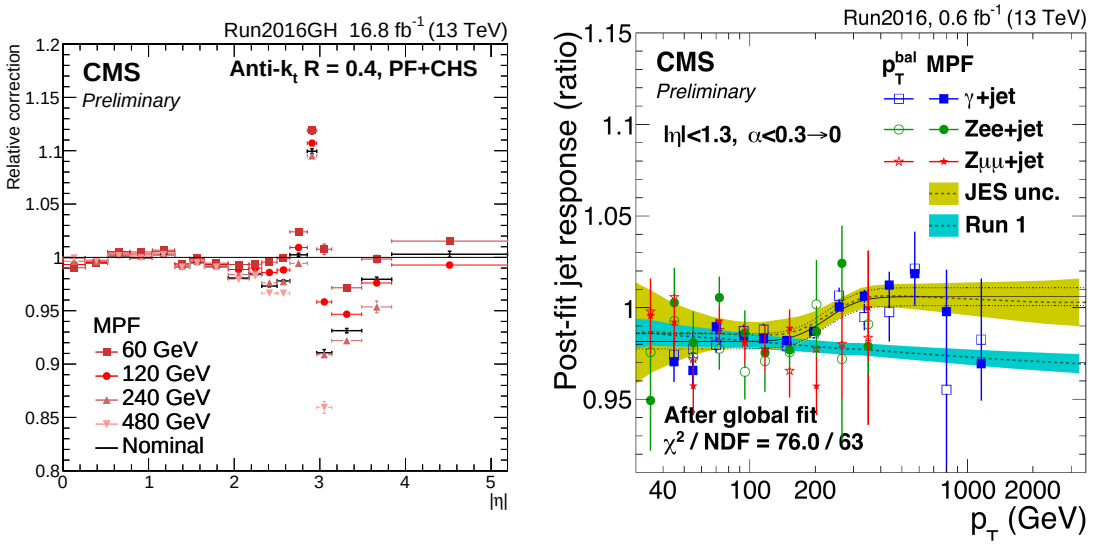

Figure 5.4: The $|\eta|$ dependent L2 (left) and p_T dependent L3 (right) residual corrections. Taken from [124].

L2L3 Residual corrections are intended to correct for the small differences between the jet responses in simulation and in data and are in fact two separate corrections called L2 and L3 residuals. The L2 Residuals are derived using the so-called *dijet events* with two jets which are back-to-back in ϕ and have p_T considerably higher than remaining jets in the event. These corrections are η dependent and the method is intended to correct the jet energy scale (JES) of the probe jet with respect to the JES of the reference jet, where the reference jet is chosen to be in the barrel region $|\eta| < 1.3$. The method uses two techniques: the first one is based on the p_T balance between the two leading jets; the other is based on the missing transverse momentum projection fraction (MPF). The L2 corrections are presented in the left plot of figure 5.4, The procedure is presented in detail in [120, 125]. The L3 residuals are derived using Z/γ+jet events, in which the momentum of the Z boson or photon γ is used as a proxy of the particle level p_T of the jet. The method exploits the fact that the Z/γ and the jet are balanced at the particle level and the momentum of the γ or the leptons from the Z boson decay have small uncertainties. The L3Res corrects the jet absolute scale and is p_T dependent. The values of the L3 corrections are presented in the right plot of figure 5.4.

The uncertainties of the jet energy corrections are an important source of systematic uncertainties in many analyses. This includes the measurement of the data to simulation jet energy resolution ratio discussed in chapter 6 and the rebalance and smear QCD background estimation method presented in chapter 8. The uncertainties as a function of p_T and $|\eta|$ with the different sources separated are presented in figure 5.5.

5.6 B-tagging of jets

Jets originating from the hadronization of the b quark, called b-jets, are present in many physics processes. Bottom quarks are for example produced in decays of top quark $t \to W^+b$ and are present in many final states predicted by BSM models. Some of the simplified

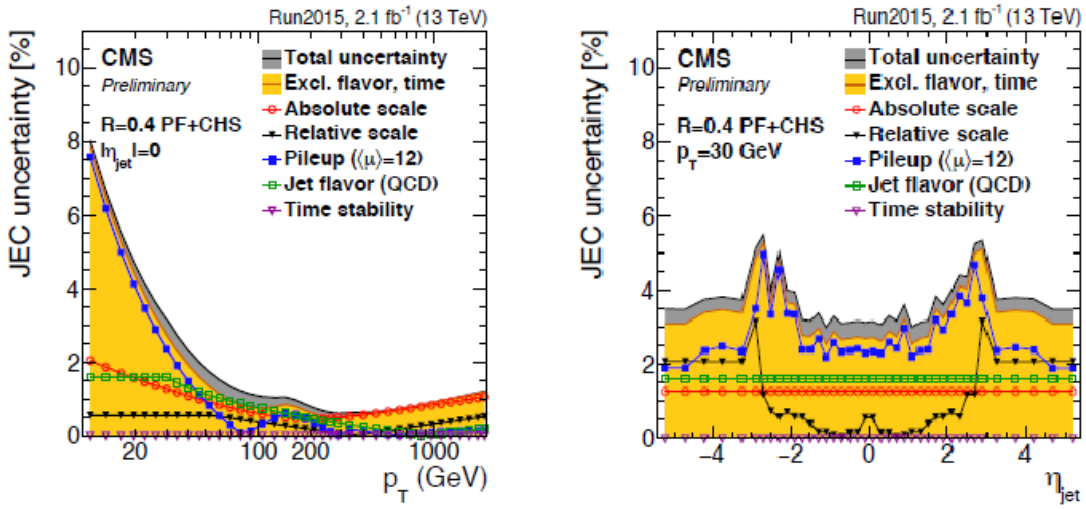

Figure 5.5: The uncertainty of the jet energy corrections as a function of p_T (left) and $|\eta|$ (right). Taken from [124].

models considered in the SUSY search presented in this thesis also predict production of b quarks. Therefore, an accurate identification of the b-jets is crucial for numerous measurements conducted at LHC, ranging from precise measurements of standard model properties, like the mass of the top quark [126–128], studies of the properties of the Higgs boson, e.g. decays of Higgs boson into b quark-antiquark pair [129–133] and many beyond standard model searches, like searches for SUSY [52, 134–136].

The b-jet identification [137–140], usually referred to as *b-tagging*, is possible due to the relatively large lifetime of B hadrons, which is around $c\tau = 500\mu$m. The large lifetime results in a reconstruction of an additional *secondary vertex*, which is displaced with respect to the interaction point. Moreover, b-jets are likely to contain soft leptons which are a product of semi-leptonic decays of B mesons.

The identification of the b-jets in the CMS experiment is performed using the *b-tagging algorithms* which calculate a discriminator value for each jet in the event. The discriminator d indicates how much a jet resembles a b-jet, and usually is normalized to take the values between 0 and 1. In the case of CSV algorithm discussed below, the $d = 0$ means that jet is very unlikely to be originating from a b quark, and $d = 1$ means that it almost certainly does originate form a b quark. A jet is tagged as a b-jet, if its discriminator is above a certain threshold value of the discriminator called *working point*.

Using simulated events the efficiency of the b-tagging and misidentification probability can be calculated. The efficiency is the fraction of true b-jets[1] that have the discriminator d value above the discriminator threshold, and the misidentification probability is defined as the probability that a non b-jet is tagged. Three working points are typically used which correspond to 10%, 1%, 0.1% misidentification probability. They are named *loose, medium* and *tight* working points respectively.

The most commonly used b-tagging algorithm in the analyses of the $\sqrt{s} = 13$TeV data collected at the CMS experiment is the so-called *Combined Secondary Vertex version 2* (CSVv2) algorithm [139], based on the CSV algorithm [138] used for 7 and 8 TeV analyses [138]. The discriminator is calculated using a neural network which takes as an input information about the secondary vertex, provided by Inclusive Vertex Finder

[1] In simulated events a true b-jet contains at least one B hadron.

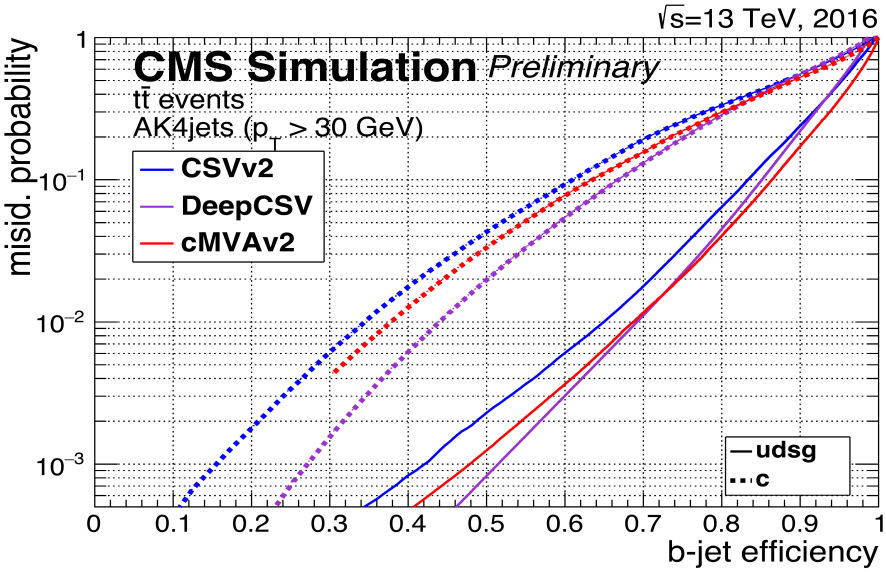

Figure 5.6: The efficiency versus misidentification probability of three different b-tagging algorithms, CSVv2, DeepCSV and cMVAv2. Taken from [142].

(IVF) [141], and displaced tracks. A modified version of CSVv2 is the *DeepCSV* [142], which uses the same input variables but uses a different learning algorithm. The other algorithm used for 13 TeV CMS measurements is the *combined Multivariate Algorithm version 2* (cMVAv2) [139], which uses *Boosted Decision Tree* BDT [143] and inputs from CSVv2 and *Jet Probability* (JP) [138] methods. The performance of the discussed b-tagging algorithms is shown in figure 5.6. The plot shows how large the misidentification probability is for a given efficiency.

5.7 Missing transverse momentum

The momenta of the products of a collision of two protons are balanced in the plane transverse to the beam. However, the sum of the transverse momenta of all measured particles will not be equal to zero because neutrinos escape the detector undetected. The mismeasurements of the momenta of the particles will also induce some amount of transverse momentum imbalance. Furthermore, many models beyond SM predict the existence of weakly interacting neutral particles, which can contribute to the momentum imbalance.

A precise measurement of the missing transverse momentum is important, for example, for searches for new physics, like the SUSY search discussed in chapters 7-9. It is also important in measurements where neutrinos are expected in the final states. The missing transverse momentum is calculated as

$$\vec{\not{E}}_T = -\sum_{i=PFcand.} \vec{p}_T^{\,i}, \tag{5.4}$$

where the sum is over the transverse momenta $\vec{p}_T^{\,i}$ of all particle flow candidates. In fact, the missing transverse momentum, calculated using the above equation is the so-called *raw-*$\not{E}_T$, as it does not include corrections applied to the reconstructed objects. The jet energy corrections are accounted for by the *type-I corrections* [144–146] which replace the raw jets with corrected ones. The type-I corrected missing transverse momentum is

calculated using

$$\vec{\not{E}}_T^{\,corr} = -\sum_{i=PFcand.} \vec{p}_T^{\,i} - \sum_{j=jets} (\vec{p}_T^{\,j,JEC} - \vec{p}_T^{\,j,raw}), \tag{5.5}$$

where $\vec{p}_T^{\,j,JEC}$ and $\vec{p}_T^{\,j,raw}$ are the JEC-corrected and uncorrected jet transverse momenta, and the second sum is over all jets. The additional correction for the pileup offset of the $\vec{\not{E}}_T^{\,corr}$ is called *type-II correction*. It is based on the assumption that the contribution of the neutral pileup particles is proportional to charged pileup. Using CHS the contribution of the charged pileup particles to the transverse momentum imbalance is calculated, and based on that estimate also the contribution from neutral pileup is calculated. However, if both type-I and type-II corrections are applied, some of the neutral particles are corrected for twice. This contribution is considered to be negligible and is ignored.

6 Jet transverse momentum resolution measurement

A good understanding of jets and their properties is crucial for many measurements and searches performed within the CMS collaboration. Events with jets in the final state are used in such fundamental analyses as measurement of the strong coupling α_s [147] or of the weak mixing angle θ_W [148], but also in searches for physics beyond SM, e.g. a search for supersymmetry in multijet events with missing transverse momentum [52].

The resolution of jet transverse momentum plays a significant role in many analyses. In the measurement of jet cross sections, (e.g. [149]), it is necessary to describe migration effects. Jet migration[1] is an effect, in which a jet with a particle level transverse momentum p_T^{truth} below a given threshold p_T^{bin} is reconstructed with a p_T^{reco} above that threshold $p_T^{\text{reco}} > p_T^{\text{bin}}$. For a measurement that is binned in p_T it is important to understand how many jets will migrate between the search intervals due to resolution effects. In the aforementioned supersymmetry search [52] jet resolutions are used to determine the background originating from QCD multijet events. The estimation of that background is discussed in detail in chapter 8. A good understanding of the jet response allows to predict the background where one or more jets are significantly mismeasured, which leads to fake missing transverse energy.

In this chapter *jet response* will be discussed and a measurement of the ratio of the jet transverse momentum p_T in data and in simulation will be presented. This measurement was documented in [150], written by author. The method utilizes the momentum conservation in the dijet events, and has been implemented before in CMS [151], [120]. A similar method using γ+jets has also been used in the past [120]. The work was mainly based on doctoral theses by M. Schröder [152] and K. Goebel [153], which presented the measurement of jet transverse momentum resolution in CMS data collected at 7 TeV and 8 TeV center of mass energies respectively.

6.1 MC-Truth response

Particle-level jets can be accessed in simulated data samples. They are represented by the generator-level jets. This allows for a direct access to the response distribution, which in this case is referred to as *MC-truth response*. In this thesis response distributions were prepared using QCD multijet sample generated with MadGraph and showered with Pythia. The tune used was `CUETP8M1`.

For the calculation of the response the two leading, i.e. with highest p_T, generator jets were matched to detector-level jets by minimizing the distance in η-ϕ plane $\Delta R = \sqrt{\Delta\eta(g,d)^2 - \Delta\phi(g,d)^2}$, where g and d denote generator- and detector-level jets respectively. The jet is not matched if $\Delta R \leq \Delta R_{max} = 0.25$.

Response $\mathcal{R}$ depends on the momentum and pseudorapidity of the jet. There are several reasons for that dependence. As described in the section 3.3.2, 3.3.3, the resolution and response of the detector subsystems depend on the energy of the jet.

[1] Migration can be defined for any variable describing any physical object, for example transverse energy or mass of an electron.

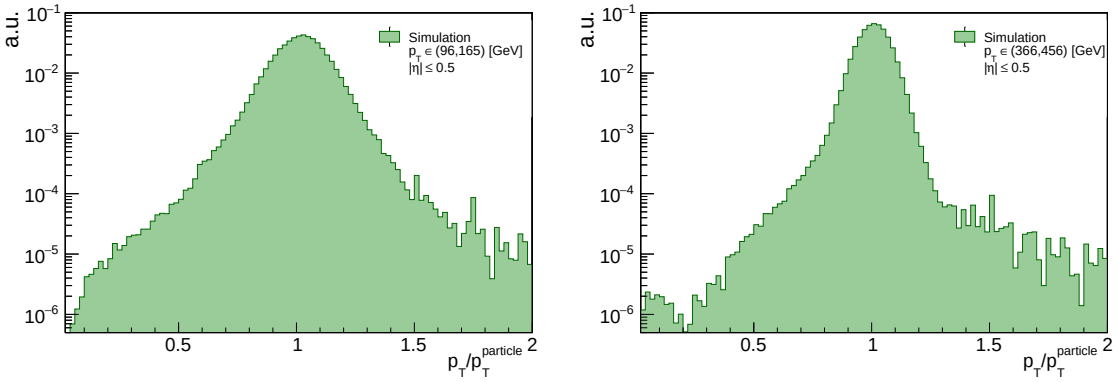

Figure 6.1: Jet response histogram for $|\eta| \leq 0.522$, $p_T \in (96, 165)$[GeV] (left) and $p_T \in (366, 456)$[GeV] (right).

An example of response histogram are presented in figure 6.1. Both the QCD cross-section and pile-up weights have been applied to the simulation sample used to prepare these plots. As may be seen in figure, the response consists of two contributions: the Gaussian-like core and the *non-Gaussian* part denoted as *tails*, mainly visible in the low response region. Tails are usually of order $\mathcal{O}(10^{-3} - 10^{-2})$ of the bulk.

There are mainly two effects that result in the fluctuation of the response around the mean value. First is the intrinsic resolution of the subdetectors, and the second one is the performance of the Particle Flow and jet clustering algorithms. Electronic noise and pile-up also contribute to the reconstructed momentum of the jet, increasing its expected value. This offset is corrected for using jet energy calibration. More details about the subdetector systems have been summarized in section 3. Some aspects of the energy and momentum measurement at the calorimeters, tracking detector and PF algorithm have been presented in [69, 73, 151].

The resolution of the p_T in tracking is mainly caused by the limited precision of measuring the curvature of the track. At high values of p_T it is mainly due to finite hit precision uncertainty, while at low p_T it is caused by multiple scattering. Overall, the precision of the track measurement deteriorates with increasing momentum. However, the opposite effect can be observed in the calorimeters, where the uncertainty decreases with increasing p_T. At low momentum the measurement is highly influenced by electronic noise and pileup, in intermediate momentum range, the leading cause of mismeasurement are fluctuations in showering, and at high p_T inhomogeneities and miscalibration of both calorimeters play the leading role. In the barrel region ($\eta \leq 0.8$) the ECAL has an uncertainty of the measurement of the energy of electrons better than 2% [154] and of the photons ranging $1.1 - 2.4\%$ [155]. In endcap for both photons and electrons the uncertainty increases up to 5%. On the other hand the HCAL resolution is significantly lower, e.g. for a 50GeV pion it is around 18% [73]. There are plenty of reasons for a decrease of precision compared to ECAL. The response of this subdetector to hadrons is lower than to electrons, and the electromagnetic fraction is not constant property of showering. Additionally, the HCAL is a sampling detector, in which the shower is not fully visible because only part of the detector is active, and which are in general less precise. The ECAL is a homogeneous detector, in which same material serves as absorber and active medium. In such a detector all charged particles in the shower are visible. Furthermore, jets contain several hadrons, and their showers can overlap.

Fortunately the impact of low resolution of HCAL on the final jet momentum measure-

ment is constrained by PF algorithm. Charged particles and photons, momenta of which are measured by combining tracker and ECAL information, carry ca. 85% of the energy of the jet. However, the HCAL contribution gets sizeable in two cases. First is the forward region, where no tracking is provided, and second is at very high p_T, when the calorimetry resolution is better than that of the tracking.

The other source of mismeasurement of the jets p_T is the particle flow algorithm, for which again different processes dominate the uncertainty in different momentum ranges. At low p_T track identification efficiency is the most significant source of uncertainty, while at high p_T the uncertainties of single hadron response corrections take over.

The choice of the jet clustering algorithm along with its parameters also impact the jet p_T resolution. Some of the particles might be too soft or too separated geometrically from the shower to be clustered into the jet, but also it might happen that the particles from the underlying event get clustered into a jet.

The effects behind the formation of the non-gaussian tails are different from the ones described above. Jets that contribute to these have been severely mismeasured. One class of jets for which this might happen include ones formed by a heavy flavour quark decaying semi-leptonic, where a fraction of momentum is carried by a neutrino ν that escapes the detector undetected. Other effects include: shower leakage, which means that not all energy has been deposited in instrumented regions; punch through effect, when due to rather small interaction length of ≈ 6 nuclear interactions at small η, some particles escape the calorimeter; finally malfunctions of detector elements.

6.2 Dijet Asymmetry

As introduced earlier in section 5.5 the jet transverse momentum resolution corresponds to the width of the distribution of the response $\mathcal{R}$. Jet response can be accessed directly in simulation and is used to calculate MC-Truth resolution, this information however is not available in data. The information about JER has to be accessed in an indirect way. This is achieved by employing the dijet asymmetry method. In this method, the events with at least two jets are selected, and the asymmetry $\mathcal{A}$ is defined for the two leading jets by

$$\mathcal{A} = \frac{p_T^1 - p_T^2}{2p_T^{ave}}, \qquad p_T^{ave} = \frac{1}{2}(p_T^1 + p_T^2) \tag{6.1}$$

where p_T^1 and p_T^2 denote momentum of the leading and sub-leading jet, and the p_T^{ave} is the average momentum of the dijet system. Assuming that the asymmetry follows a normal distribution, the mean deviation can be calculated using

$$\sigma_{\mathcal{A}} = \Big|\frac{\partial \mathcal{A}}{\partial p_T^1}\Big|\sigma(p_T^1) \oplus \Big|\frac{\partial \mathcal{A}}{\partial p_T^2}\Big|\sigma(p_T^2). \tag{6.2}$$

Furthermore, assuming that jets are balanced at a particle level and have been measured in similar conditions, namely they have been in the same η region, the mean values of the momenta $\langle p_T^1 \rangle = \langle p_T^2 \rangle = \langle p_T \rangle$ and respective uncertainties $\sigma(p_T^1) = \sigma(p_T^2) = \sigma(p_T)$ are equal. Substituting these in 6.2 gives the relation between jet response width $\sigma(p_T)$ and asymmetry width $\sigma_{\mathcal{A}}$

$$\frac{\sigma(p_T)}{\langle p_T \rangle} = \sqrt{2}\sigma_{\mathcal{A}}. \tag{6.3}$$

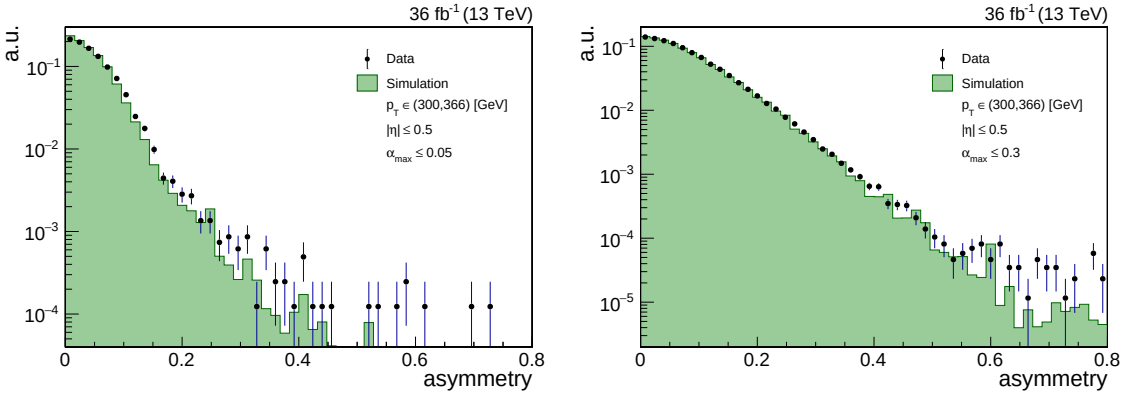

Figure 6.2: Histogram of absolute value of asymmetry $|\mathcal{A}|$ in data and simulation, for $p_T \in (300, 366)$, $|\eta| \leq 0.522$ and two intervals of additional jet activity, $\alpha \leq 0.05$ on the left and $\alpha \leq 0.3$ on the right.

The methods using this relation have been applied at the Tevatron experiments [156] [157], at ATLAS [158], and also at CMS on 7TeV [152] [151] and 8TeV data [153] [120].

6.2.1 Realistic dijet events in data and Monte Carlo simulation

The ideal dijet topology, for which eq. 6.1 and 6.3 have been derived, is not realized in nature. The balance between the partons is distorted due to a momentum transfer to additional partons before or after the hard interaction, denoted *Initial State Radiation* ISR and *Final State Radiation* FSR respectively. To parametrize the introduced imbalance of a dijet system, an *additional jet activity* is introduced, which is defined as the ratio of the third leading jet momentum p_T^3 to the average momentum of the dijet system p_T^{ave}

$$\alpha = \frac{p_T^3}{p_T^{ave}}. \tag{6.4}$$

The impact of this additional hadronic activity can be shown on figure 6.2. As seen on the plot, an additional imbalance introduced by ISR/FSR jets increases the width of the asymmetry, which would lead to a bias in the measurement if left untreated. The impact of α and a method of correcting for it will be discussed with more detail in section 6.5.

As described in section 6.1 jet resolution depends on p_T and η. Asymmetry inherits that dependence, thus $\sigma_{\mathcal{A}}$ has to be measured in intervals of these variables. However, instead of using intervals of p_T of the leading jet, the average momentum p_T^{ave} has to be used. This is due to the fact that the jet-p_T spectrum is steeply falling with momentum, which in case of binning in p_T would mean that more jets with low p_T^{gen} would migrate into given interval than jets with high p_T^{gen}, introducing a bias towards jets with higher resolution. Using p_T^{ave} allows for reduction of such bias.

6.3 Samples and Event Selection

6.3.1 Dataset and threshold

In the presented analysis multijet events from pp collisions recorded with CMS detector at $\sqrt{s} = 13$ TeV were used. The used data sample correspond to an integrated luminosity of 36.8 fb^{-1}. The events are selected using a set of triggers which are based on the average

Trigger	Offline threshold (GeV)
HLT_DiPFJetAve40	51
HLT_DiPFJetAve60	74
HLT_DiPFJetAve80	96
HLT_DiPFJetAve140	165
HLT_DiPFJetAve200	232
HLT_DiPFJetAve260	300
HLT_DiPFJetAve320	366
HLT_DiPFJetAve400	456
HLT_DiPFJetAve500	569

Table 6.1: Triggers used for dijet selection in data with their thresholds.

Trigger (forward)	Offline threshold (GeV)
HLT_DiPFJetAve60_HFJEC	72
HLT_DiPFJetAve80_HFJEC	95
HLT_DiPFJetAve100_HFJEC	118
HLT_DiPFJetAve160_HFJEC	188
HLT_DiPFJetAve220_HFJEC	257
HLT_DiPFJetAve300_HFJEC	354

Table 6.2: Forward triggers used for dijet selection in data with their thresholds. These triggers work from $\eta = 2.5$ and are used for $\eta \geq 2.8$.

momentum of the leading jets p_T^{ave}, as defined in 6.1. Two sets of triggers were used, standard dijet triggers and forward dijet triggers, intended for use at higher pseudorapidity η regions, where a slightly modified version of the procedure is applied. This *Forward Extension* will be described in section 6.7. Both sets of triggers, along with their thresholds, are listed in tables 6.1 and 6.2

6.3.2 Event cleaning

Some defects in the performance of the detector or in the reconstruction algorithms might result in a significantly misreconstructed jets. Several *cleaning filters* have been applied on the data to remove events that might suffer from these problems:

Good vertex: At least one high quality vertex is required to be present in the event. A vertex is recognized as good if it is located not further away from the nominal point than 24 cm in z direction and 2 cm in xy plane. It is also required to have at least 4 tracks pointing towards it.

Beam halo: Vacuum in the beam pipe is not perfect, which results in protons interacting sometimes with residual gas. Interactions like that produce muons parallel to the beam, which can be identified in the CSC of endcap disks (*CSC tight halo*). An alternate version of the beam halo filter (*Global tight halo*) is also applied. It uses also information from calorimeters and checks for characteristic patterns of halo muon interactions, like out-of-time hits and long η size in barrel.

Noise in calorimeters: If a particle hits the electronics, wiring or generally instrumentation of the calorimeters, it can result in an anomalous signal from that part of detector. The pulse shape and timing information are used to identify noise originating from such events (*HBHE noise filter*). There is also a separate filter dedicated to rejecting events with isolated noise activity in the calorimeter (*HBHE Isolated noise filter*).

Dead ECAL cells: Due to malfunctioning read-out electronics or crystals, around 1.2% of ECAL cells are not working. If a jet is aligned with such a channel, the energy of that cell can be still estimated from trigger primitives. This method however has a narrower application range, and if the estimated energy is close to the saturation energy, it most likely means that it was strongly underestimated.

To remove contamination from $t\bar{t}$ and W+jets events, it is required that no isolated muons or electrons with $p_T > 15$ GeV and $\eta < 2.4$ are present. Additionally, quality criteria for jets are applied, namely the electromagnetic fraction of the energy of the jets above 15 GeV is required to be below 90%.

6.3.3 Event selection

As explained in section 6.2.1, realistic dijet events will not be imbalanced only due to resolution effects. To ensure that events resembling dijets are selected, and thus the equation 6.3 holds, several selection criteria have to be applied. Events with at least two jets with $p_T > 30$ GeV are selected. Leading jets are required to be approximately back-to-back in the transverse plane

$$\Delta\phi(p_T^1, p_T^2) > 2.7. \tag{6.5}$$

This criterion suppresses contribution of events that are strongly imbalanced. Another selection to reduce same contribution is the cut on additional jet activity α

$$\alpha < 0.3. \tag{6.6}$$

As mentioned earlier, to ensure validity of the assumptions made to derive equation 6.3, namely $\langle p_T^1 \rangle = \langle p_T^2 \rangle$ and $\sigma(p_T^1) = \sigma(p_T^2)$, events are binned in intervals of average momentum p_T^{ave} and absolute value of the pseudorapidity $|\eta|$. p_T^{ave} bin edges correspond to trigger thresholds summarized in tables 6.1 and 6.2, and η bins are chosen to reflect the geometry of the detector. Using trigger thresholds as bin edges ensures that each bin is populated by events triggered by one trigger path. In case of η binning, both leading jets are required to be in the same $|\eta|$ interval, meaning that they have been measured using the same detector subsystems. Events are also recorded in bins of α. This binning is inclusive, meaning each bin contains events with $\alpha \in (0, \alpha_{max})$. Values of α_{max}, p_T and $|\eta|$ bin edges are listed in the table 6.3.

6.4 Asymmetry width

The jet transverse momentum resolution was defined as standard deviation of the gaussian part of the $\mathcal{R}$ distribution. The same definition applies to the width of the asymmetry distribution $\sigma_{\mathcal{A}}$. Assuming that the asymmetry follows a normal distribution, its standard deviation would be equal to the width parameter of a Gaussian function fitted to the

histogram. This method of calculating $\sigma_{\mathcal{A}}$ was used in 7 TeV measurement [152]. However, starting from the 8 TeV measurement, presented in [153], alternative method of calculating $\sigma_{\mathcal{A}}$ has been adopted, where the root mean square of the distribution with respect to $\mathcal{A} = 0$ is calculated:

$$\sigma_{\mathcal{A}} = \sqrt{\frac{1}{\sum_i y_i} \sum_i y_i \mathcal{A}_i^2}, \tag{6.7}$$

where y_i is the frequency of the asymmetry value $\mathcal{A}_i$ and the sum covers 98.5% of the whole distribution, starting from zero. This method proves to be more stabile, especially in p_T and η intervals with low events yield. The uncertainty of $\sigma_{\mathcal{A}}$ is given by

$$\Delta\sigma_{\mathcal{A}} = \frac{\sigma_{\mathcal{A}}}{\sqrt{2n_{eff}}}, \tag{6.8}$$

where n_{eff} is the number of effective entries in the range specified for equation 6.7. Effective entries for an unweighted histograms is simply number of entries. For weighted

$\lvert\eta\rvert$	0, 0.522, 0.783, 1.131, 1.305, 1.740, 1.930, 2.043, 2.322, 2.5, 2.853
$\lvert\eta\rvert$, forward extension	0, 1.131, 1.305, 1.740, 1.930, 2.043, 2.322, 2.5, 2.853, 2.964, 3.139, 5.191
p_t^{ave}(GeV), (central)	51, 74, 96, 165, 232, 300, 366, 456, 569, 1500
p_t^{ave}(GeV), (forward)	72, 95, 118, 188, 257, 354, 1500
α_{max}	0.05, 0.1, 0.15, 0.2, 0.25, 0.3

Table 6.3: Bin boundaries of the asymmetry distributions. Forward triggers are used for $\eta \geq 2.853$.

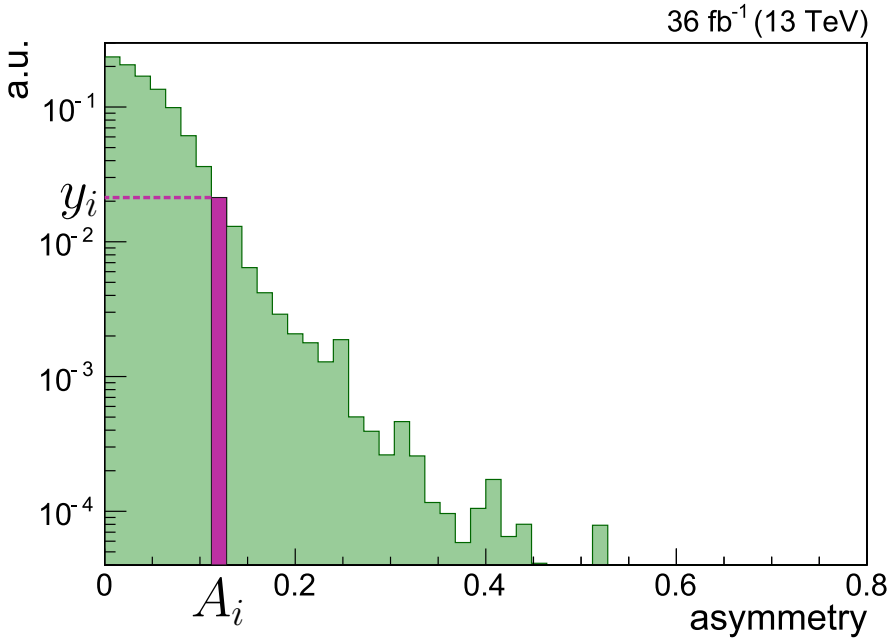

Figure 6.3: The example of asymmetry distribution with the frequency y_i and asymmetry value A_i, used in equation 6.7, highlighted.

histogram it is the number of unweighted events that would be necessary to get a histogram of same statistical power as the weighted histogram.

To ensure that the non-Gaussian contribution doesn't bias the measurement, the width has to be calculated only in range where asymmetry $\mathcal{A}$ is Gaussian. This is done by excluding 1.5% of points with highest $\mathcal{A}$ values.

6.5 Corrections for additional jet activity

Equation 6.3 holds for an ideal dijet. However, as shown in figure 6.2, contribution from additional jets, originating in e.g. from soft radiation or hard process, increases the measured asymmetry width. To compensate for that effect an extrapolation procedure is employed. For each $|\eta|$ and p_T^{ave} interval the measured widths $\sigma_{\mathcal{A}}(\alpha_{max})$ are extrapolated to $\alpha \to 0$ assuming linear behaviour,

$$\sigma_{\mathcal{A}}(\alpha_{max}) = a\alpha_{max} + b \tag{6.9}$$

and the y-intercept b of the fitted function represents the width without additional hadronic activity. The linear dependence of the asymmetry width on α_{max} has not been derived from first principles. However, as can be seen from figure 6.4, the linear assumption is very well justified empirically. Fit uncertainty of parameter b is used as the statistical uncertainty of extrapolated width $\sigma_{\mathcal{A}}(\alpha_{max} \to 0)$. The correlation between asymmetries in different α_{max} intervals is addressed by minimizing

$$\chi^2 = dy^T C^{-1} dy, \tag{6.10}$$

where $dy = y_{measured} - y_{predicted}$ and C is the covariance matrix, defied as

$$C_{ij}(\sigma_{\mathcal{A}_i}, \sigma_{\mathcal{A}_j}) = (\Delta\sigma_{\mathcal{A}_i})^2 \frac{\sigma_{\mathcal{A}_i}}{\sigma_{\mathcal{A}_j}} \frac{n_i}{n_j} \tag{6.11}$$

where $n_{i,j}$ denote number of events in i-th and j-th α_{max} bin. The result of such extrapolation is presented in figure 6.4.

6.6 Particle level imbalance

The dijet events, both in data and in simulation, are not perfectly balanced at the particle level. This can be seen from the blue plot in figure 6.4, which represents the extrapolation of the widths of asymmetry distributions measured using generator level jets.

The origin of this *particle level imbalance* (PLI) is e.g. initial and final state radiation. Due to the fact that only the detector effects on the resolution of jets are meant to be measured, the PLI contribution has to be subtracted from the extrapolated detector level widths. This is achieved using the following expression

$$\sigma_{JER} = \sqrt{\sigma^2_{JER,tot} - \sigma^2_{PLI}} \tag{6.12}$$

where both $\sigma_{JER,tot}$ and σ_{PLI} are widths extrapolated to $\alpha \to 0$ for detector level and generator level jets respectively.

The resolutions acquired in that way are presented in figure 6.5. The function fitted is the so-called NSC function

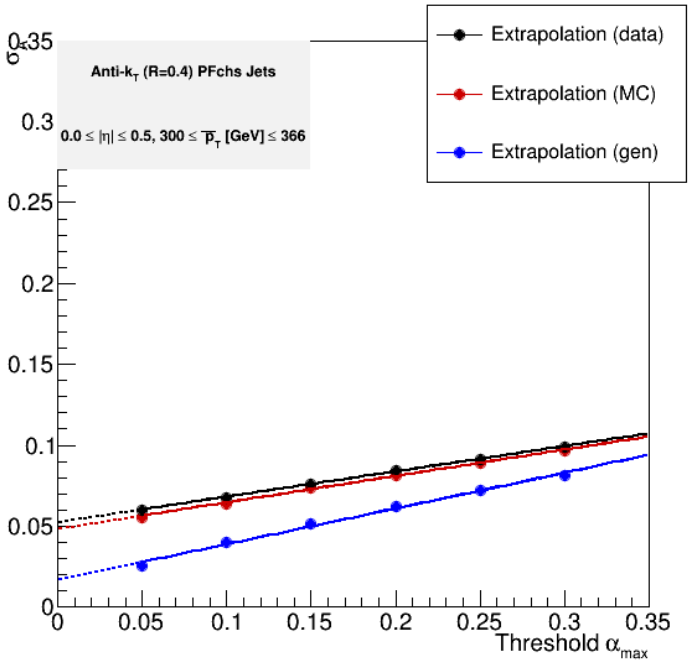

Figure 6.4: Plots of the fits to asymmetry widths as a function of additional hadronic activity α_{max}. The black points and line represent data points, red color represents detector level simulation and blue represents truth level simulation.

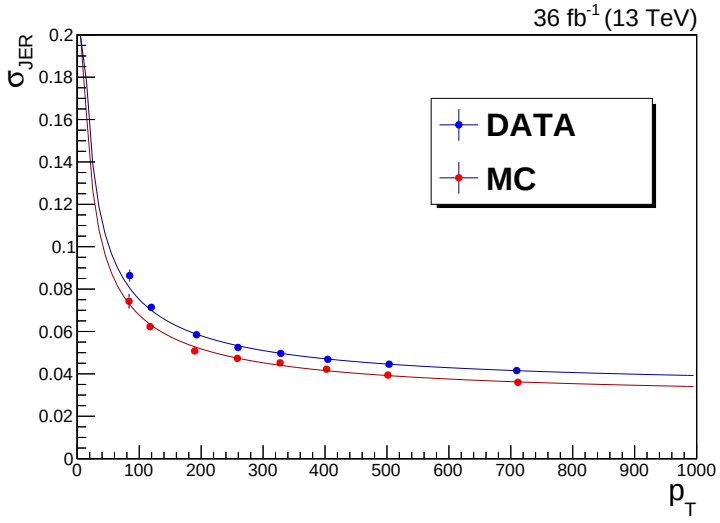

Figure 6.5: Jet resolutions for data and monte-carlo simulation (MC) as a function of p_T for $|\eta| \in (0, 0.522)$

$$\sigma(p_T) = \sqrt{\frac{N^2}{p_T^2} + \frac{S^2}{p_T} + C^2}, \tag{6.13}$$

introduced already in equation 3.7. These functions are used to derive one of the systematic uncertainties which will be described in a further part of this chapter.

6.7 Extension of the asymmetry method at higher pseudorapidities

The asymmetry method described above uses events with both jets in the same $|\eta|$ region, which allows the use of the simplified equation 6.3. However, in the forward pseudorapidity intervals jets tend to have lower momentum p_T, which means that they are triggered using highly prescaled trigger paths, which leads to low event count in these measurement intervals. In order to improve the statistics at higher pseudorapidities a modified asymmetry method was implemented, which will be referred to as *forward extension*.

In this modified method the assumption that both jets are observed in the same pseudorapidity intervals is dropped. This means that $\langle p_T^1 \rangle = \langle p_T^2 \rangle = \langle p_T \rangle$ assumption is kept, but uncertainties of the jets are not equal $\sigma(p_T^1) \neq \sigma(p_T^2)$. In that case the resolution of one of the jets, referred to as the reference jet, has to be known to calculate the resolution of the second jet, which will be referred to as the probe jet. The equation 6.2 acquires the following form

$$\frac{\sigma(p_T^{probe})}{\langle p_T \rangle} = \sqrt{4\sigma_{\mathcal{A}}^2 - \left(\frac{\sigma(p_T^{ref})}{\langle p_T \rangle}\right)^2}, \tag{6.14}$$

where $\sigma_{\mathcal{A}}$ is the width of asymmetry distribution constructed using events for which one of the leading jets is in a predefined reference region $|\eta_{ref}|$ for which the resolution $\frac{\sigma(p_T^{ref})}{\langle p_T \rangle}$ is known, and the other one is in the probe region $|\eta_{probe}|$ for which the resolution $\frac{\sigma(p_T^{probe})}{\langle p_T \rangle}$ is measured.

The choice of the reference region is arbitrary. It is preferred to be well populated, which is why it is chosen to be $|\eta_{ref}| \in (0, 1.131)$. The intervals in η for the forward extension are defined in table 6.3.

The procedure of subtracting the reference region resolution is executed in two steps. First is to measure asymmetry distribution using a standard method for the reference region $|\eta| \in (0, 1.131)$ and to calculate the resolutions for that pseudorapidity interval. Then the NSC function (6.13) is fitted to these measured resolutions. The resulting function is presented in figure 6.6. The second step of the procedure is to subtract the reference region resolution from the forward extension measurements for $|\eta| \geq 1.131$ using the NSC function obtained in the first step of the procedure.

After the correction for the reference region resolution the PLI contribution is subtracted, which is done same way as for the standard asymmetry method. The resolution obtained this way are presented on figure 6.7.

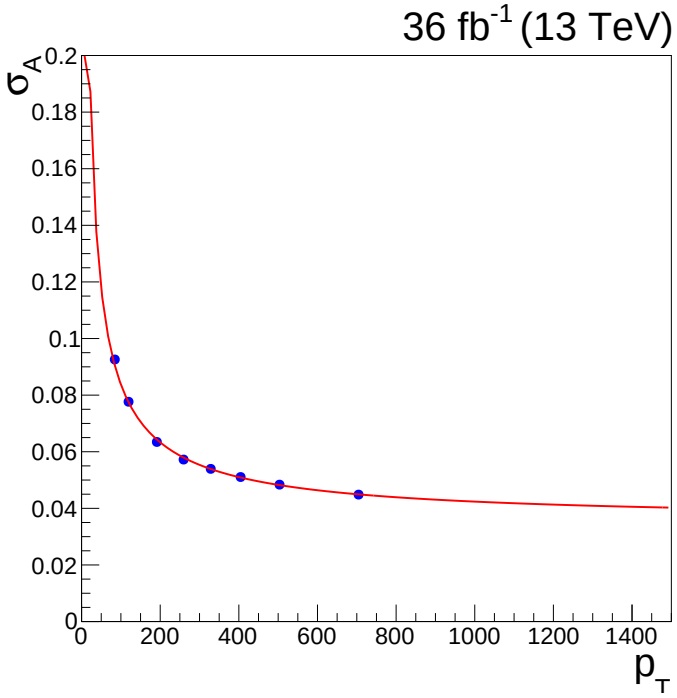

Figure 6.6: Jet resolutions for data as a function of p_T for the forward extension reference region $|\eta| \in (0, 1.131)$. The fitted NSC function is used to subtract reference region resolution from the forward extension measurements for $|\eta| \geq 1.131$ as prescribed by equation 6.14.

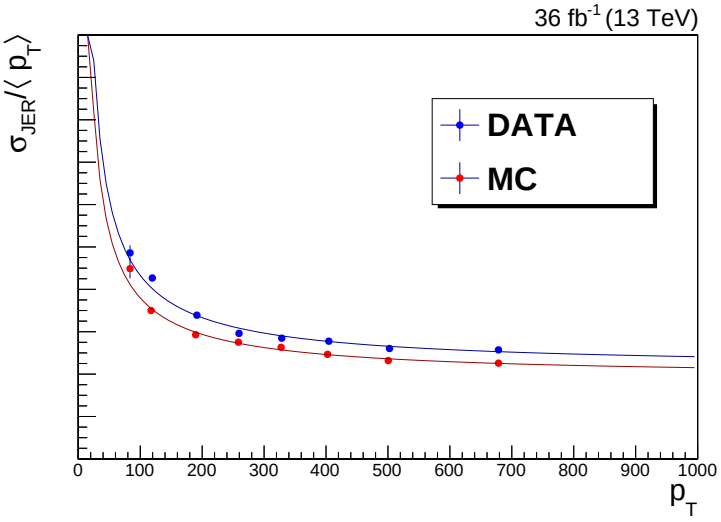

Figure 6.7: Relative jet resolutions for data and monte-carlo simulation (MC) as a function of p_T for $|\eta| \in (1.305, 1.740)$ calculated using forward extension.

6.8 Jet resolution data to simulation ratios

The last step of calculating the jet resolution data to simulation ratios, commonly referred to as *jet resolution scale factors*, is to divide the resolutions obtained in previous steps and to average them in each pseudorapidity interval. This is conducted separately for

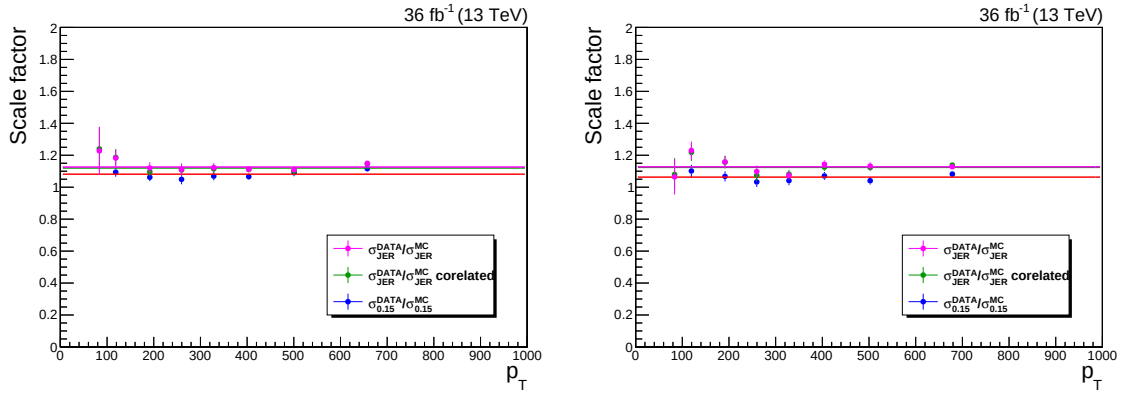

(a) Standard method

(b) Forward extension

Figure 6.8: Ratios of jet resolutions for data and monte-carlo simulation (MC) as a function of p_T for $|\eta| \in (1.305, 1.740)$ calculated using standard method (left plot) and forward extension (right plot). For that pseudorapidity interval both results are consistent within statistical uncertainties.

the resolutions obtained using the standard asymmetry method and its forward extension. The example of the result of such procedure for both methods for $|\eta| \in (1.305, 1.740)$ are presented side by side in figure 6.8 (green points). Additionally to the nominal procedure, scale factors are calculated for a simplified extrapolation to $\alpha \to 0$ in which correlations between the points are not treated (the magenta points and fit) and without extrapolation, taking the asymmetry widths for $\alpha_{max} = 0.15$ (blue points). Interestingly, results of the nominal procedure and the one with simplified fit agree very well. However, the big advantage of using the nominal procedure is that there is no need of calculating a systematic uncertainty originating from the correlation between the points.

6.9 Systematic uncertainties

Additionally to the statistical uncertainties there are certain systematic effects that might be influencing the result. The sources of these uncertainties will be discussed in this section.

All systematic uncertainties, except the ones originating from the p_T dependence of scale factors and the difference between standard method and forward extension, are calculated by varying the method in a certain aspect and measuring the shift of the data-to-simulation ratios compared to nominal measurement

$$\delta SF(Data/MC) = SF(Data/MC)_{modified} - SF(Data/SF)_{nominal}. \tag{6.15}$$

PU reweighting The pileup distributions in data are calculated with a nominal minimum bias cross section of 69.4 mb. To calculated the influence of the choice of min-bias cross section, the calculations are repeated for a cross section varied to 72.4 mb (PU up) and 66.0 mb(PU down). These distributions are used to reweight simulation so that it matches the pileup conditions observed in data.

Particle-level imbalance As described in section 6.6, the measured resolution is corrected for the imbalance at particle level. To estimate the systematic uncertainty on PLI, the

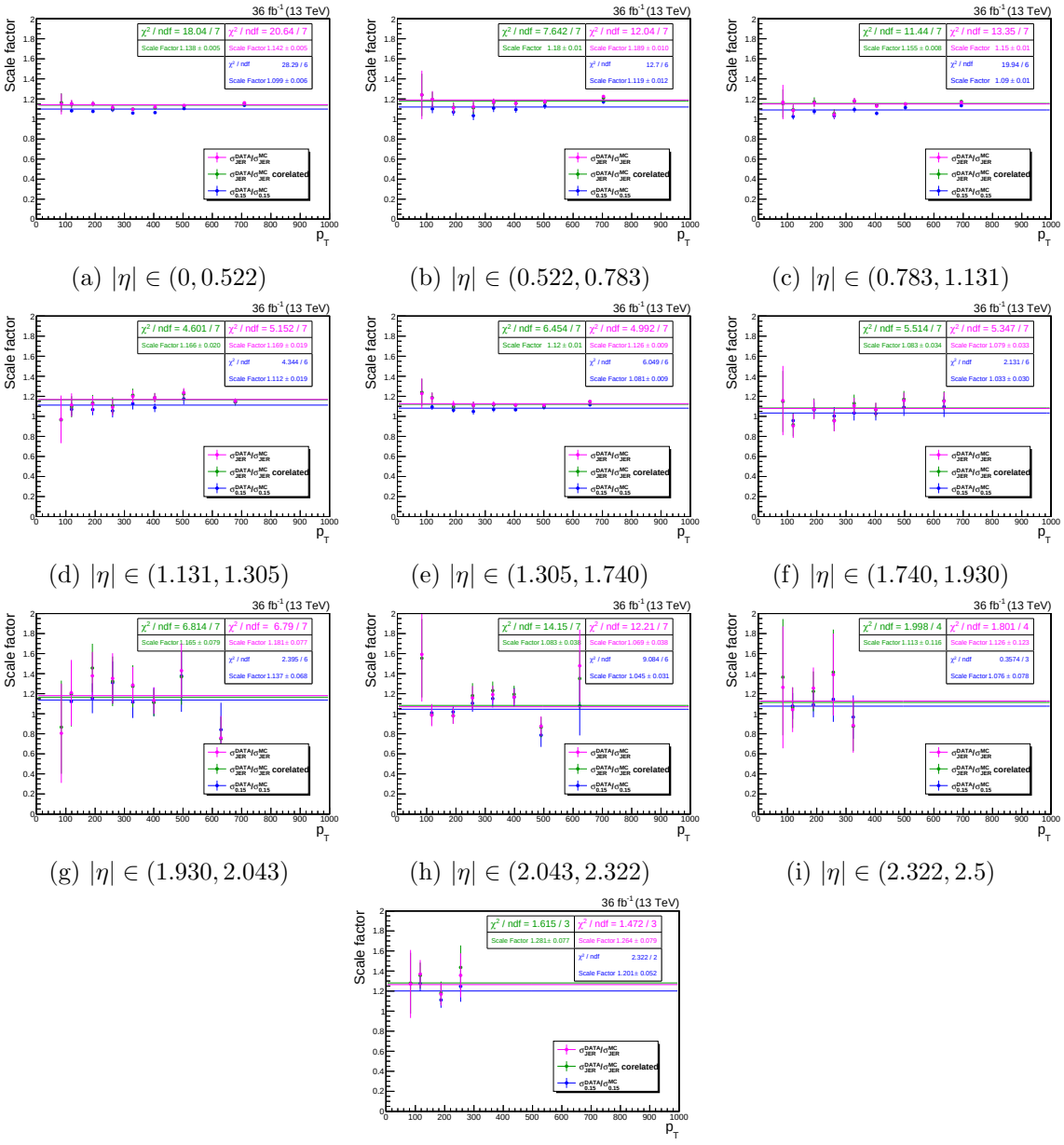

(a) $|\eta| \in (0, 0.522)$ (b) $|\eta| \in (0.522, 0.783)$ (c) $|\eta| \in (0.783, 1.131)$

(d) $|\eta| \in (1.131, 1.305)$ (e) $|\eta| \in (1.305, 1.740)$ (f) $|\eta| \in (1.740, 1.930)$

(g) $|\eta| \in (1.930, 2.043)$ (h) $|\eta| \in (2.043, 2.322)$ (i) $|\eta| \in (2.322, 2.5)$

(j) $|\eta| \in (2.5, 2.853)$

Figure 6.9: Ratios of jet resolutions for data and monte-carlo simulation (MC) as a function of p_T, for all $|\eta|$ intervals, calculated using standard method. On each plot three measurements are presented: green points are results obtained using the correlated fit which is the nominal method used, the magenta points represent the results obtained using a simple linear fit which does not treat the correlations between inclusive α_{max} intervals. The blue points, used as a cross check, present the results for which, instead of performing the extrapolation, the asymmetry widths for $\alpha_{max} = 0.15$ are used in the calculation.

σ_{PLI} is shifted by 25% up and down

$$\sigma_{\mathrm{JER}} = \sqrt{\sigma^2_{\mathrm{JER,tot}} - f \cdot \sigma^2_{\mathrm{PLI}}}\,, \tag{6.16}$$

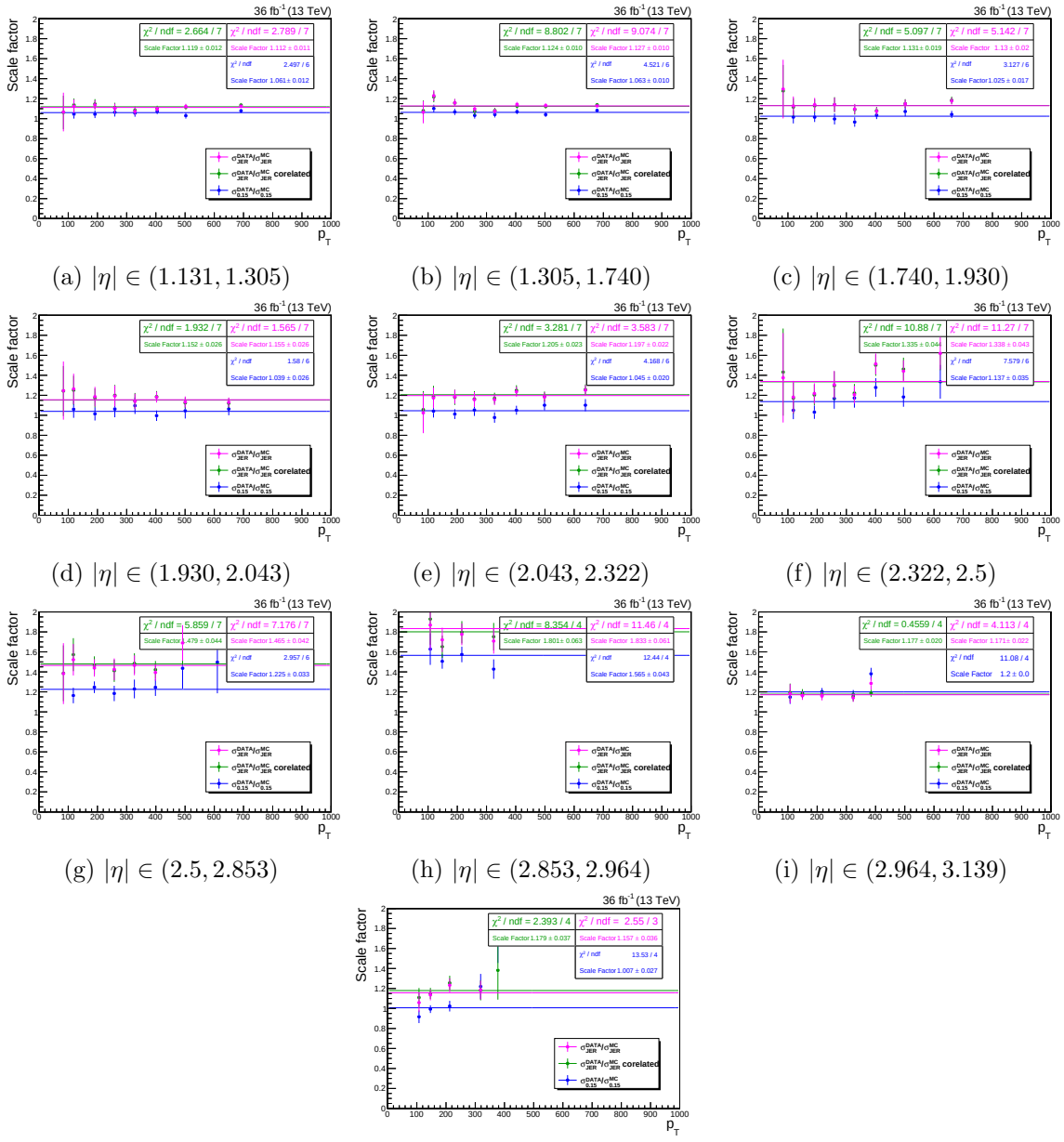

(a) $|\eta| \in (1.131, 1.305)$ (b) $|\eta| \in (1.305, 1.740)$ (c) $|\eta| \in (1.740, 1.930)$

(d) $|\eta| \in (1.930, 2.043)$ (e) $|\eta| \in (2.043, 2.322)$ (f) $|\eta| \in (2.322, 2.5)$

(g) $|\eta| \in (2.5, 2.853)$ (h) $|\eta| \in (2.853, 2.964)$ (i) $|\eta| \in (2.964, 3.139)$

(j) $|\eta| \in (3.139, 5.191)$

Figure 6.10: Ratios of jet resolutions for data and monte-carlo simulation (MC) as a function of p_T, for all $|\eta|$ intervals, calculated using forward extension. On each plot three measurements are presented: green points are results obtained using the correlated fit which is the nominal method used, the magenta points represent the results obtained using a simple linear fit which does not treat the correlations between inclusive α_{max} intervals. The blue points, used as a cross check, present the results for which, instead of performing the extrapolation, the asymmetry widths for $\alpha_{max} = 0.15$ are used in the calculation.

with $f = 0.75, 1.25$ respectively.

Jet energy scale Jet energy scale is corrected using calibration factors. To estimate the uncertainty originating from that jet energy scale, these correction factors are varied up and down by their uncertainties.

α-range The extrapolation technique described in section 6.5, which is used to account for additional hadronic activity, has not been theoretically derived and is based purely on empirical observation. The method is based on a assumption that the width of asymmetry distribution scales linearly with additional jet activity α. However, $p_T > 15$ GeV cut used in the measurement translates into $\alpha_{min} = 15\text{GeV}/p_T^{ave}$. To access lower α values the jet p_T cut is changed from 15 GeV to 10 GeV. In this way the linear assumption is tested for lower α values.

Non-gaussian tails As described in section 6.4, for the calculation of the asymmetry distribution 1.5% of highest asymmetry points are rejected. It is possible that the tail contributions in data and simulation do not cancel out. To test that effect the truncation point is changed to 5%.

Standard-Forward methods differences Due to the fact that the scale factors calculated using standard method and forward extension do not agree within the statistical uncertainties in some of the pseudorapidity intervals, a non-closure uncertainty is calculated by taking the half of the difference between the obtained results:

$$\sigma_{\text{ST-FE diff}} = (\sigma_{\text{JER,FE}} - \sigma_{\text{ST}})/2. \tag{6.17}$$

p_T dependence In the calculation the scale factors are assumed not to depend on p_T. This is mostly due to the fact that the calculation is limited by statistical uncertainties, which are too high to measure precisely the dependence of the scale factors on transverse momentum. To test the validity of the assumptions, the resolution in data and simulations are fitted separately and the ratio of the fits is used as a cross check with the constant scale factors. The following function is fitted to simulation

$$f(p_T) = \sqrt{\frac{N^2}{p_T^2} + \frac{S^2}{p_T} + C^2}, \tag{6.18}$$

with $p_T = p_T^{ave}$. If the scale factors did not depend on momentum, there should be a single correction to the above function to all parameters N, S and C, that would be equal to the constant data to simulation resolution ratio. However, this is not true and some p_T-dependence of the scale factors can be observed. To measure that effect, the data is fitted with the following formula

$$f(p_T) = \sqrt{\frac{(k_{NS} \cdot N)^2}{p_T^2} + \frac{(k_{NS} \cdot S)^2}{p_T} + (k_C \cdot C)^2}, \tag{6.19}$$

where parameters N, S and C are taken from the fit to simulation and are fixed, and parameters k_{NS} and k_C are allowed to change. Both fits are presented on figure 6.5 and 6.7 for standard method and forward extension respectively. The ratio of the fitted functions is compared with the constant scale factors on figure 6.11. The uncertainty is calculated as the difference between the NSC fits ratio and constant scale factor at the p_T corresponding to the lowest measured point. Due to large fluctuations of the difference for

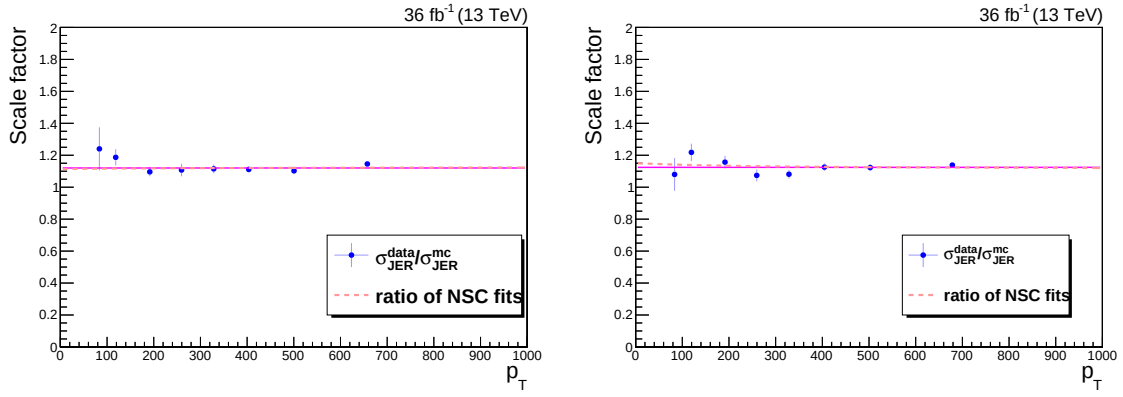

(a) Standard method (b) Forward extension

Figure 6.11: Jet resolution scale factors for standard method (left) and forward extension (right) compared with the ratio of the NSC fits to data and simulation resolutions for $|\eta| \in (1.305, 1.740)$. The difference between the constant fit and the NSC functions ratio at the p_T corresponding to the lowest measured point is displayed in the legend. This value is used in the calculation of the systematic uncertainty.

the consecutive η bins, the average of the calculated uncertainties in three regions, defined by the ranges in $\eta \in (0, 1.131, 2.853, 5.2)$, is calculated.

6.9.1 Combination of systematic uncertainties

All uncertainties for standard method and forward extension are listed in tables 6.4 and 6.5 respectively. The systematic uncertainties, except for the FE-ST difference, are summed in quadrature

$$\sigma(syst) = \sum_{i \neq FE-ST} \sigma_i^{syst}. \tag{6.20}$$

The total uncertainties with each of the sources are plotted on fig 6.12 for both standard method and forward extension. The main source of uncertainty is the p_T-dependence. The rather conservative approach in calculating this uncertainty was chosen because some analyses rely mainly on low momentum jets, for which the effect of the p_T dependence is the strongest. For both methods the total uncertainty is highest for the transition region $|\eta| \in (2.322, 2.964)$ and the systematic uncertainties fluctuate the most in that interval. This is again due to low number of events entering these intervals and the dynamically changing geometry of the detector.

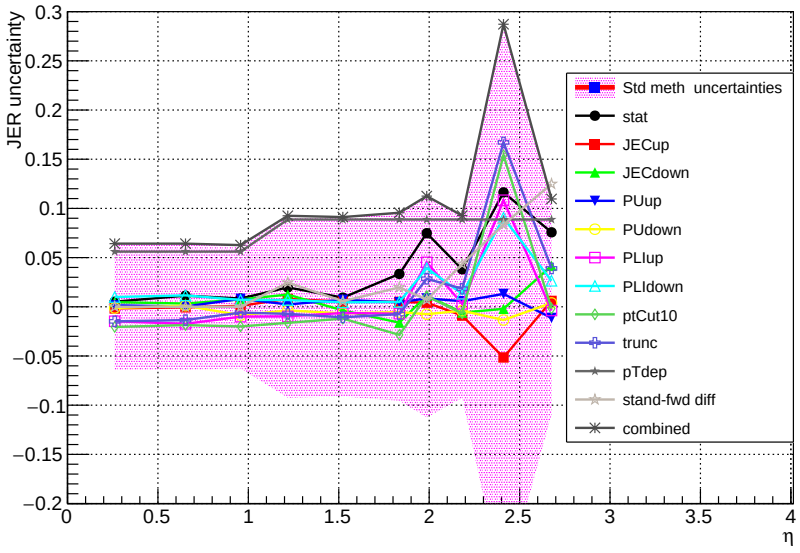

(a) Standard method

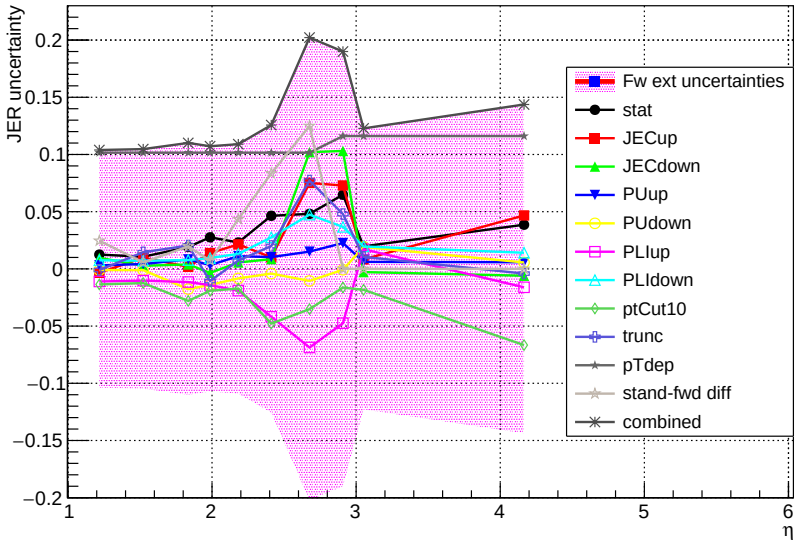

(b) Forward extension

Figure 6.12: Break-up of the sources of the uncertainties of the jet transverse momentum data to simulation ratios.

Table 6.4: All systematic uncertainties for the standard method scale factors

$\|\eta\|$ range	Scale	statUnc	JECup	JECdown	PUup	PUdown	PLIup	PLIdown	ptCut10	trunc.	pTdep	combined
0-0.522	1.1595	0.0052	0.0017	0.0047	0.0015	0.0012	0.0147	0.0099	0.0205	0.0148	0.0561	0.0642
0.522-0.783	1.1948	0.0113	0.0005	0.0033	0.0003	0.0011	0.0173	0.0116	0.0186	0.0135	0.0561	0.0642
0.783-1.131	1.1464	0.0084	0.0010	0.0075	0.0081	0.0085	0.0100	0.0070	0.0200	0.0059	0.0561	0.0627
1.131-1.305	1.1845	0.0197	0.0080	0.0124	0.0024	0.0037	0.0097	0.0069	0.0163	0.0072	0.0887	0.0925
1.305-1.740	1.1229	0.0093	0.0053	0.0037	0.0071	0.0067	0.0063	0.0045	0.0120	0.0107	0.0887	0.0912
1.740-1.930	1.0804	0.0334	0.0050	0.0161	0.0046	0.0054	0.0070	0.0049	0.0285	0.0074	0.0887	0.0956
1.930-2.043	1.1332	0.0748	0.0042	0.0113	0.0085	0.0075	0.0452	0.0393	0.0108	0.0285	0.0887	0.1125
2.043-2.322	1.1081	0.0381	0.0089	0.0059	0.0057	0.0040	0.0029	0.0132	0.0067	0.0184	0.0887	0.0927
2.322-2.5	1.1549	0.1163	0.0515	0.0021	0.0131	0.0134	0.1083	0.0905	0.1541	0.1671	0.0887	0.2872
2.5-2.853	1.2534	0.0757	0.0060	0.0416	0.0113	0.0039	0.0038	0.0264	0.0018	0.0390	0.0887	0.1096

Table 6.5: All systematic uncertainties for the forward extension scale factors

$\|\eta\|$ range	Scale	statUnc	JECup	JECdown	PUup	PUdown	PLIup	PLIdown	ptCut10	trunc.	pTdep	combined
1.131-1.305	1.1354	0.0125	0.0034	0.0097	0.0031	0.0010	0.0110	0.0075	0.0136	0.0010	0.1016	0.1039
1.305-1.740	1.1342	0.0106	0.0098	0.0027	0.0042	0.0011	0.0103	0.0071	0.0124	0.0145	0.1016	0.1047
1.740-1.930	1.1198	0.0191	0.0018	0.0039	0.0083	0.0177	0.0115	0.0077	0.0280	0.0204	0.1016	0.1101
1.930-2.043	1.1475	0.0276	0.0138	0.0035	0.0033	0.0140	0.0142	0.0095	0.0191	0.0106	0.1016	0.1072
2.043-2.322	1.1951	0.0231	0.0214	0.0056	0.0111	0.0083	0.0190	0.0131	0.0172	0.0072	0.1016	0.1090
2.322-2.5	1.3220	0.0464	0.0101	0.0085	0.0103	0.0041	0.0418	0.0275	0.0478	0.0200	0.1016	0.1257
2.5-2.853	1.5032	0.0481	0.0751	0.1020	0.0151	0.0105	0.0687	0.0474	0.0352	0.0772	0.1016	0.2022
2.853-2.964	1.7788	0.0648	0.0729	0.1031	0.0226	0.0008	0.0475	0.0367	0.0163	0.0479	0.1161	0.1900
2.964-3.139	1.1869	0.0197	0.0083	0.0028	0.0061	0.0192	0.0172	0.0196	0.0183	0.0105	0.1161	0.1228
3.139-5.191	1.1922	0.0386	0.0467	0.0060	0.0058	0.0056	0.0161	0.0141	0.0666	0.0041	0.1161	0.1437

Table 6.6: The combined data to simulation resolution scale factors with full uncertainties

$\|\eta\|$ range	ScaleF	ST	FE	StatUnc	SystUnc	ST-FEdiff	fullSyst	fullUnc
0-0.522	1.1595	1.1595	0.0000	0.0052	0.0642	0.0000	0.0642	0.0645
0.522-0.783	1.1948	1.1948	0.0000	0.0113	0.0642	0.0000	0.0642	0.0652
0.783-1.131	1.1464	1.1464	0.0000	0.0084	0.0627	0.0000	0.0627	0.0632
1.131-1.305	1.1609	1.1845	1.1354	0.0161	0.0982	0.0246	0.1012	0.1025
1.305-1.740	1.1278	1.1229	1.1342	0.0099	0.0979	0.0057	0.0981	0.0986
1.740-1.930	1.1000	1.0804	1.1198	0.0263	0.1028	0.0197	0.1047	0.1079
1.930-2.043	1.1426	1.1332	1.1475	0.0512	0.1099	0.0072	0.1101	0.1214
2.043-2.322	1.1512	1.1081	1.1951	0.0306	0.1008	0.0435	0.1098	0.1140
2.322-2.5	1.2963	1.1549	1.3220	0.0814	0.2064	0.0835	0.2227	0.2371
2.5-2.853	1.3418	1.2534	1.5032	0.0619	0.1559	0.1249	0.1997	0.2091
2.853-2.964	1.7788	0.0000	1.7788	0.0648	0.1900	0.0000	0.1900	0.2008
2.964-3.139	1.1869	0.0000	1.1869	0.0197	0.1228	0.0000	0.1228	0.1243
3.139-5.191	1.1922	0.0000	1.1922	0.0386	0.1437	0.0000	0.1437	0.1488

6.10 Results

The data to simulation ratios are calculated by combining the result of the calculation of standard method and forward extension. For $|\eta| \leq 1.131$ only the standard method is used, and for $|\eta| \geq 2.853$ only forward extension is used. For the intermediate eta range, where the forward and standard method overlap, the scale factors are calculated using weighted average, with the weights calculated using

$$weight = \frac{1}{\sigma^2_{stat} + \sigma^2_{syst}}. \tag{6.21}$$

Statistical and systematic uncertainty calculated with Eq. 6.20 are averaged. Then the total uncertainty is calculated as

$$\sigma(total) = \sqrt{\sigma^2_{stat} + \sigma^2_{syst} + \sigma^2_{FE-ST}}. \tag{6.22}$$

The data to simulation ratios of the jet energy resolutions are presented in table 6.6. The standard method, forward extension and combined ratios with full uncertainties are presented in figure 6.13. Standard method and forward extension agree well in region $|\eta| \in (1.131, 2.322)$, however the disagreement for the last two overlapping intervals is the reason for introducing the non-closure uncertainty. The data to simulation ratio in the pseudorapidity $|\eta| \in (2.853, 2.964)$ interval is exceptionally high, which is caused by several factors. The tracking detector extends only to $|\eta| = 2.4$, therefore for this interval there are no tracks, reducing the quality of the energy measurement. Additionally, it is a region where the coverage of endcap calorimeters ends and the coverage of forward calorimeter starts. This transition region covers several different components of the detector, which results in a lower efficiency of object reconstruction and is the reason to treat that region separately. Moreover, it is a very narrow interval, which reduces the statistical precision of both jet resolution scale factors and jet energy corrections.

In figure 6.14 the calculated data to simulation ratios are compared with the results obtained for 7 and 8 TeV data. The scale factors for all three results are in good agreement for $|\eta| \geq 1.131$. The overall higher total uncertainty of the 13 TeV measurement compared to 8 TeV result comes mostly from a more conservative approach to p_T-dependence un-

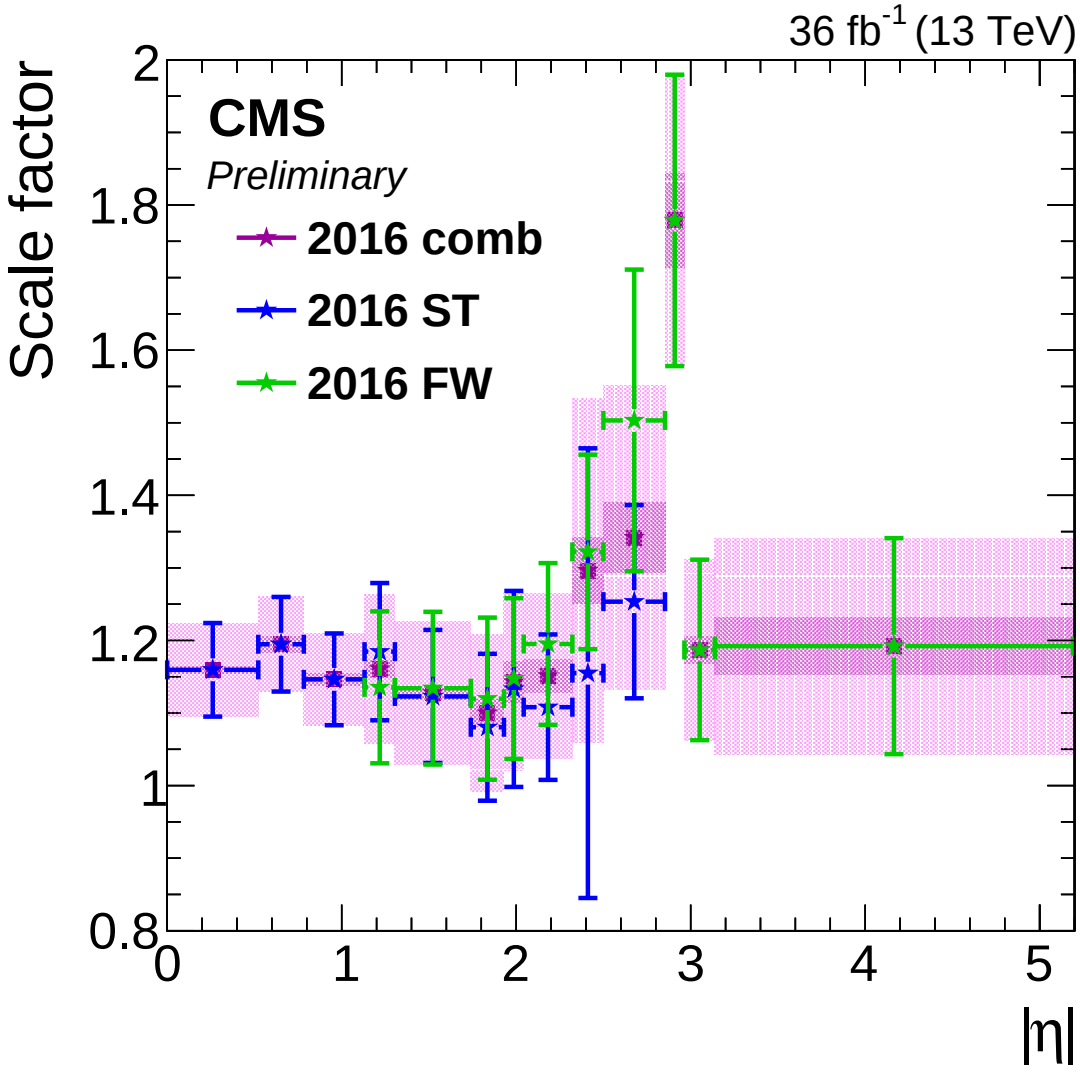

Figure 6.13: Data-to-simulation ratios for jet p_T resolutions (magenta) for results obtained with standard method, shown with blue points, with forward extension, shown with green points, and for combined results, shown with magenta shaded rectangles, the darker area represents only systematic uncertainty while the lighter color shows full uncertainty.

certainty, which increased from around 2% for 8 TeV to 6-10% for 13 TeV. For the barrel region the results for 13 TeV are visibly higher than for 7 and 8 TeV, which might have several explanations. The higher pileup conditions of 2016 data might have an influence, however the influence of changing the pileup scenario was measured to be negligible. Other effect might be deterioration of the crystals in the ECAL, which become opaque due to radiation damage. For example, the response of the endcap ECAL is expected to drop from 70% after collecting 10 fb^{-1}, to 30% after collecting 100 fb^{-1} [159].

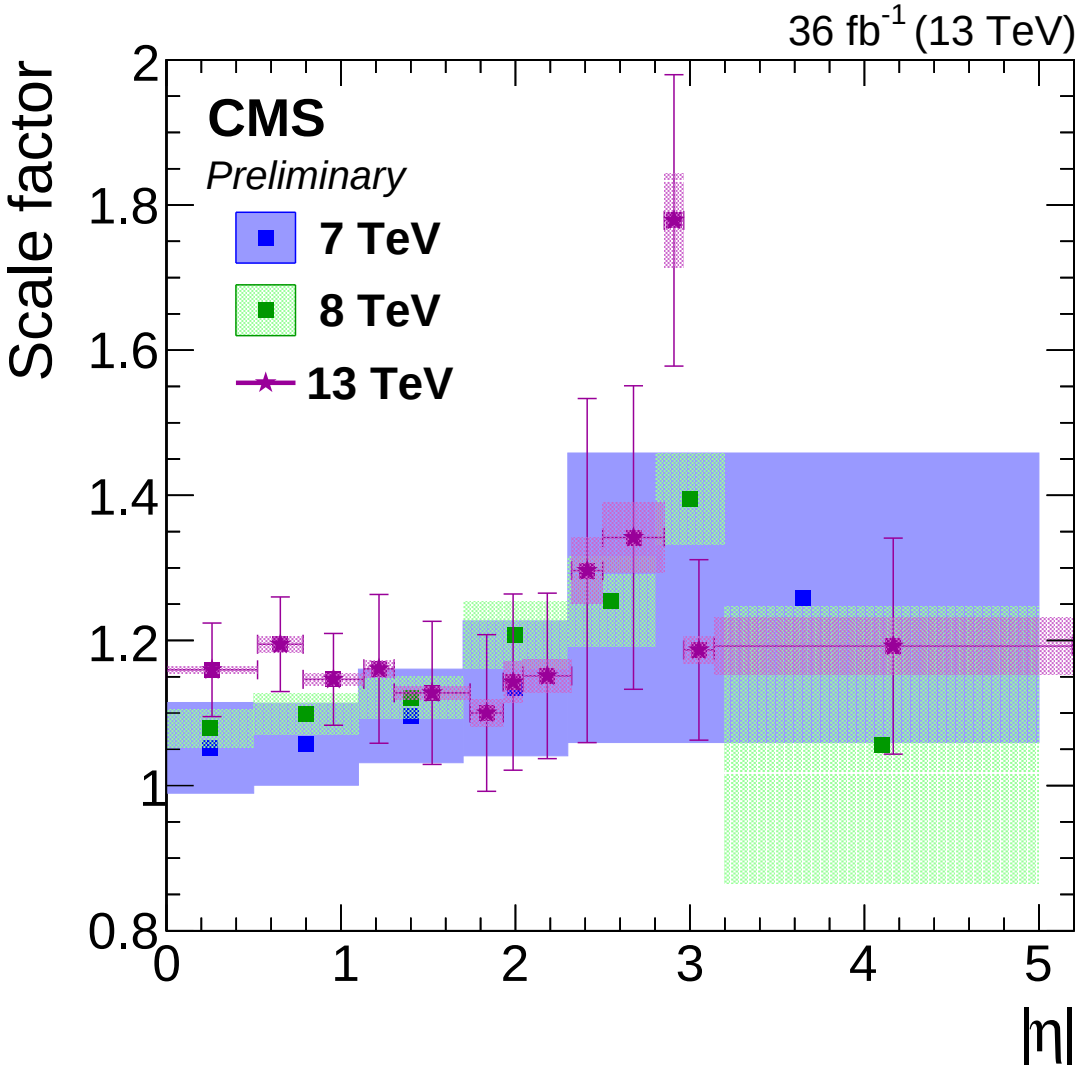

Figure 6.14: Data-to-simulation ratios for jet p_T resolutions (magenta) for results obtained for 2016 datasets at 13 TeV compared with results for 7 and 8 TeV pp collisions at the LHC. Full uncertainties are presented for all three results.

6.11 Outlook

The intervals in additional jet activity α used in the dijet method are inclusive, meaning that the intervals are defined as $\alpha \in (0, \alpha_{max})$. This introduces correlation between the measured points which has to be properly treated in the extrapolation procedure. A possible modification to the method would be to apply exclusive α intervals. For exclusive intervals of α, the linear dependence of the width of asymmetry distribution can be better motivated than in case of inclusive intervals, but the calculation of the width of the distribution requires fitting of a gaussian function, which is less stable than the root mean square used in the current implementation.

Other possible modification of the method is redefinition of the α variable. Instead of using the full momenta of the jets, $\alpha_{||}$ defined as projection of the 3$^{\text{rd}}$ jet transverse momentum on a *dijet axis*, could be used:

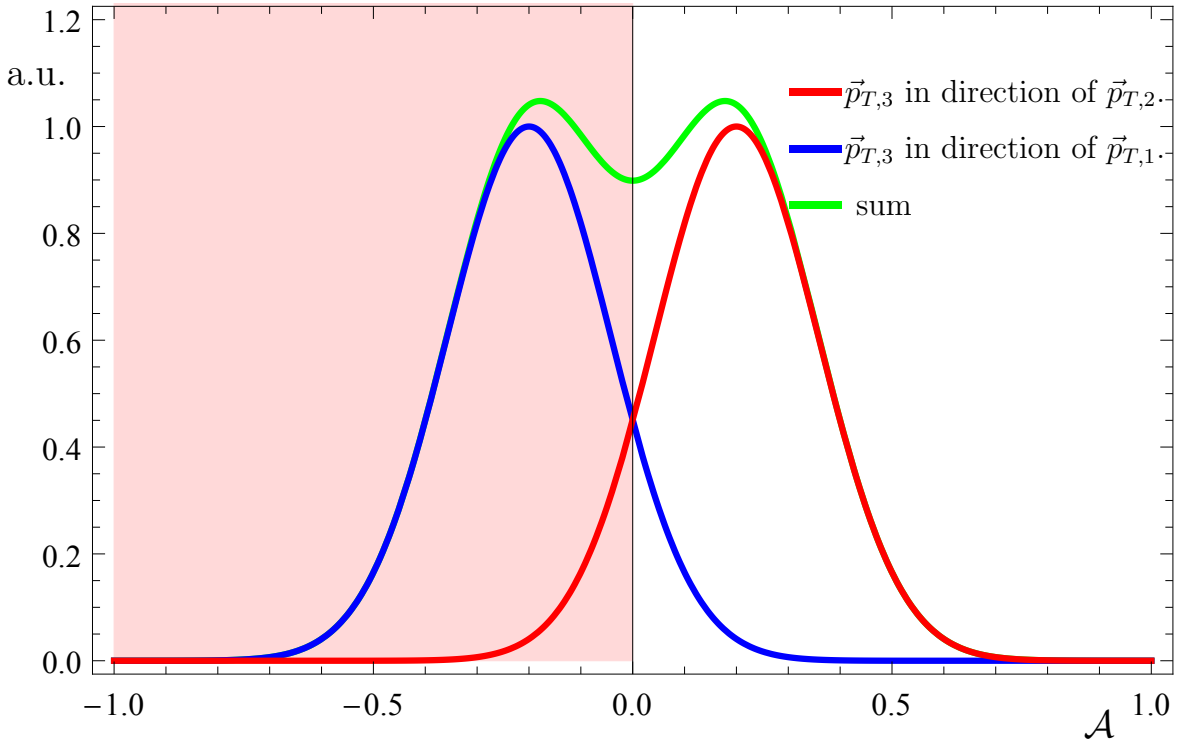

Figure 6.15: Sketch of the expected asymmetry distribution for exclusive intervals of α in case of jets ordered randomly.

$$\alpha_{\parallel} = \frac{\overrightarrow{p}_{T,3} \cdot \hat{i}}{p_{T,ave}} \qquad \hat{i} = \frac{\overrightarrow{p}_{T,1} - \overrightarrow{p}_{T,2}}{|\overrightarrow{p}_{T,1} - \overrightarrow{p}_{T,2}|}. \tag{6.23}$$

The dijet axis can be defined by the vector $\hat{i}$ obtained by subtracting the transverse momenta vectors of the leading jets. The definition of the modified α variable is illustrated in figure 6.16. The $\alpha_{\parallel}$ definition includes the component of the transverse momentum of the additional jet that introduces the imbalance in the dijet system, while it is insensitive to the part that can be seen as a boost of the whole system. Moreover, $\alpha_{\parallel}$ could have very small values, as $p_{\vec{T},3}$ can be perpendicular to the dijet axis. This not only could improve the $\alpha \to 0$ extrapolation, but also removes the problem of addressing the α-range in the systematic uncertainties. Furthermore, for a given exclusive $\alpha_{\parallel}$ interval, the asymmetry would have a non zero expected value which would manifest in a double-peak structure of the asymmetry distribution, sketched in figure 6.15. These results were calculated using simulated QCD events generated and showered with `pythia8` [160], and the response of the detector was simulated using `Geant4` [92–94].

Combination of these two modifications gives a good explanation of the linear dependence of asymmetry width on additional jet activity. The first results look promising, however more work is required. The example of the $\alpha_{\parallel} \to 0$ extrapolation is presented in figure 6.17.

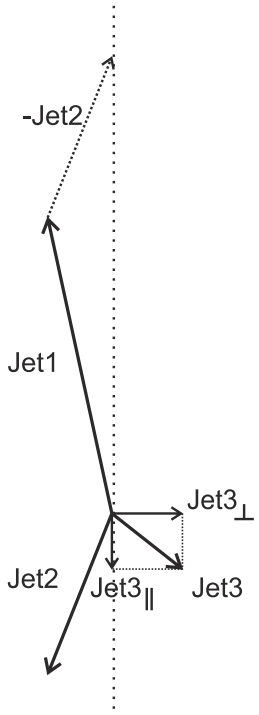

Figure 6.16: Illustration of the definition of the $\alpha_{\parallel}$.

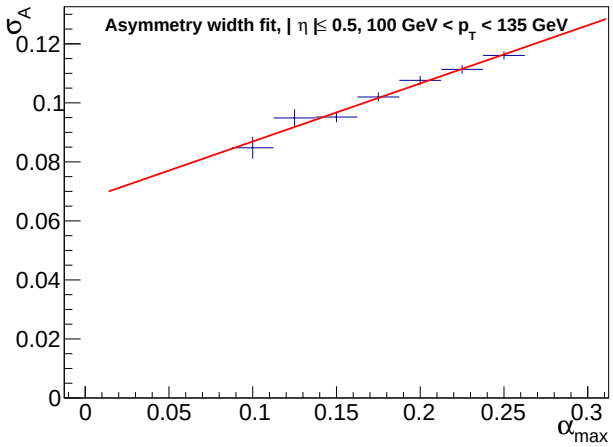

Figure 6.17: An example of the $\alpha_{\parallel} \to 0$ extrapolation for exclusive intervals of $\alpha_{\parallel}$.

Table 6.7: QCD simulation samples used in the studies of exclusive $\alpha_{\parallel}$ intervals.

Simulation sample
QCD_Pt_5to10_TuneCUETP8M1_13TeV_pythia8
QCD_Pt_10to15_TuneCUETP8M1_13TeV_pythia8
QCD_Pt_15to30_TuneCUETP8M1_13TeV_pythia8
QCD_Pt_30to50_TuneCUETP8M1_13TeV_pythia8
QCD_Pt_50to80_TuneCUETP8M1_13TeV_pythia8
QCD_Pt_80to120_TuneCUETP8M1_13TeV_pythia8
QCD_Pt_120to170_TuneCUETP8M1_13TeV_pythia8
QCD_Pt_170to300_TuneCUETP8M1_13TeV_pythia8
QCD_Pt_300to470_TuneCUETP8M1_13TeV_pythia8
QCD_Pt_470to600_TuneCUETP8M1_13TeV_pythia8
QCD_Pt_600to800_TuneCUETP8M1_13TeV_pythia8
QCD_Pt_800to1000_TuneCUETP8M1_13TeV_pythia8
QCD_Pt_1000to1400_TuneCUETP8M1_13TeV_pythia8
QCD_Pt_1400to1800_TuneCUETP8M1_13TeV_pythia8
QCD_Pt_1800to2400_TuneCUETP8M1_13TeV_pythia8
QCD_Pt_2400to3200_TuneCUETP8M1_13TeV_pythia8
QCD_Pt_3200toInf_TuneCUETP8M1_13TeV_pythia8

6.12 Non-gaussian tail resolution measurement

The jet transverse momentum response consists of two contributions: the Gaussian-like core and non-gaussian tails. The measurement of the data to simulation ratio of the jet resolution was investigating only the gaussian part of the response and asymmetry distribution. For most of the measurements conducted at CMS this is sufficient. However, a good understanding of non-Gaussian tails is necessary to fully describe the jets. The effects responsible for the formation of the tails include semi-leptonic decays of the heavy-flavor jets and instrumental effects such as shower leakage and punch through effects. Even though the tails are of the order of $\mathcal{O}(10^{-2} - 10^{-3})$ of the bulk of the jet response, they have to be accounted for in measurements in which heavily mismeasured jets play a role. An example of such an analysis is the search for supersymmetric particles presented in chapters 7-9, in which mismeasurements of jet momenta can result in a high *fake* $\not{H}_T$. The estimation of the background originating from events with such *fake* $\not{H}_T$ is presented in chapter 8.

In this chapter a rough estimation of the scale factors of the non-Gaussian response tails is presented. The procedure follows similar steps to the measurement of the scale factors of the jet resolution. It was discussed in [152], where a much more in-depth study is presented. The calculation presented in this section was conducted as a part of the *rebalance and smear* QCD background estimation method presented in chapter 8 of this thesis.

The dataset used and event selection are discussed in section 6.12.1. In section 6.12.2 the analogue of the asymmetry width for the tails, the so-called *tail fraction*, is introduced. Afterwards, in section 6.12.3 the correction for additional jet activity is presented. Finally, in section 6.12.4 the obtained data to simulation ratios are presented.

6.12.1 Dataset and simulation samples

The calculation was performed using the dataset and simulation samples listed in tables 6.8 and 6.9 rspectively. Additionally, the simulation was smeared using jet energy resolution scale factors documented in [161]. The jet energy corrections are different from the ones

used for the core measurement and resolution scale factors applied are not the ones listed in table 6.6 because the results presented for the tails were derived with an earlier version of those corrections. The smearing procedure is performed by scaling the reconstructed momentum p_T of the jet with a factor

$$c_{\mathrm{JER}} = 1 + (s_{\mathrm{JER}} - 1)\frac{p_T - p_T^{truth}}{p_T}, \tag{6.24}$$

where p_T^{truth} is the momentum of the particle-level jet matched to the scaled detector-level jet and s_{JER} is the data to simulation resolution scale factor. This procedure is performed so that the core resolution in simulation and data agree and the tails can be consistently defined and compared.

Table 6.8: Standard model QCD simulation samples used in the measurements of the jet response non-gaussian tails. All cross sections are calculated to LO.

Dataset	(fb^{-1})
`JetHT Run2016B`	5.8
`JetHT Run2016C`	2.6
`JetHT Run2016D`	4.2
`JetHT Run2016G`	7.6
`JetHT Run2016H`	8.4
Jet energy corrections: `Spring16_25nsV8p2`	

Table 6.9: Standard model QCD simulation samples used in the measurements of the jet response non-gaussian tails. All cross sections are calculated to LO.

Simulation sample	σ (pb)	(fb^{-1})
QCD_HT100to200_TuneCUETP8M1_13TeV-madgraphMLM-pythia8	27990000	0.3
QCD_HT200to300_TuneCUETP8M1_13TeV-madgraphMLM-pythia8	1717000	0.03
QCD_HT300to500_TuneCUETP8M1_13TeV-madgraphMLM-pythia8	351300	0.16
QCD_HT500to700_TuneCUETP8M1_13TeV-madgraphMLM-pythia8	31630	1.97
QCD_HT700to1000_TuneCUETP8M1_13TeV-madgraphMLM-pythia8	6802	6.68
QCD_HT1000to1500_TuneCUETP8M1_13TeV-madgraphMLM-pythia8	1206	12.54
QCD_HT1500to2000_TuneCUETP8M1_13TeV-madgraphMLM-pythia8	120.4	98.23
QCD_HT2000toInf_TuneCUETP8M1_13TeV-madgraphMLM-pythia8	25.42	239.26
Jet energy corrections: `Spring16_25nsV8p2`		

The definition of the asymmetry and the event selection are exactly same as described in sections 6.2 and 6.3.3 respectively. The triggers used are same as the ones described in section 6.3.1, however the trigger thresholds used are slightly different. This is due to the fact that different jet energy corrections were applied compared to jet response core measurements.

Due to the fact that tails constitute only tiny fraction of the asymmetry distribution they are much more susceptible to statistical fluctuations. As a result, a much coarser binning in $|\eta|$ and p_T has been used in the tail measurement. The intervals are listed in table 6.10.

6.12.2 Fractional tail contribution

As mentioned earlier, the jet response and jet asymmetry consists of the core and tails. The core follows a normal distribution, and the tails can be simply defined as the remaining,

$\|\eta\|$	0, 1.131, 2.322, 4.7
p_t^{ave}(GeV), (central)	51, 73, 95, 230, 365, 1500
p_t^{ave}(GeV), (forward)	51, 73, 95, 230, 365
α_{max}	0.05, 0.1, 0.15, 0.2, 0.25, 0.3

Table 6.10: Bin boundaries of the asymmetry distributions used for the measurements of the non-gaussian tails. Forward triggers are used for $\eta \geq 2.853$.

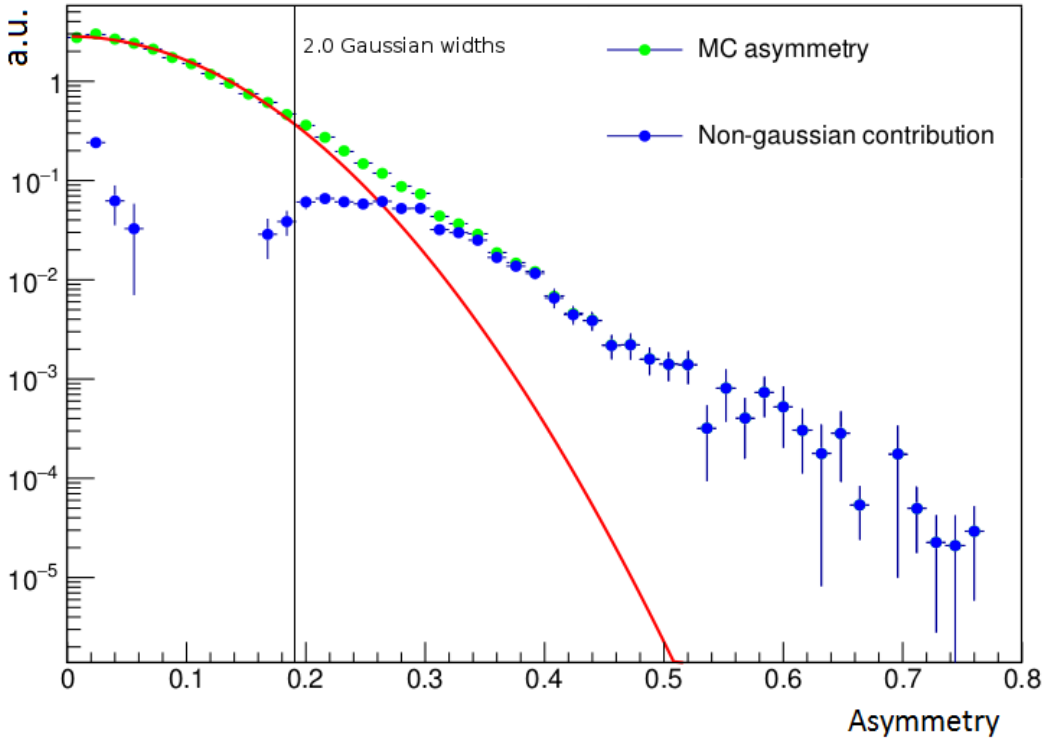

Figure 6.18: The asymmetry distribution (green points) with the tail component (blue points) and a gaussian function (red curve) fitted in the range $\mathcal{A} \in (0, 2{\cdot}\sigma_{gaus})$. The blue points were obtained by subtracting the fit from the distribution. The distribution was obtained from simulation, with $p_t^{ave} \in (366, 456)$ and $|\eta| \in (0.783, 1.131)$.

non-gaussian part of the asymmetry or the response. The definition of the tails is visualised in figure 6.18. The tail region is defined for $\mathcal{A} \geq 2.5 \cdot \sigma_{gaus}$, where σ_{gaus} is the width of the gaussian function fitted to the core of the distribution. The fitting is performed iteratively in the range $\mathcal{A} \in (0, 2{\cdot}\sigma_{gaus})$, with the fitting range updated after each iteration. The value of σ_{gaus} is initially taken to be the RMS of the distribution calculated using equation 6.7, and it was found sufficient to repeat the fitting 3 times. The tail threshold $\mathcal{A}_{tail} = 2.5{\cdot}\sigma_{gaus}$ is calculated using simulated events for the lowest $\alpha_{max} = 0.05$ interval of each of p_T and $|\eta|$ intervals, and the same threshold value is used for varying α_{max} intervals for both simulated and data asymmetry distributions.

The tails can be described using a value called *tail fraction*, defined as

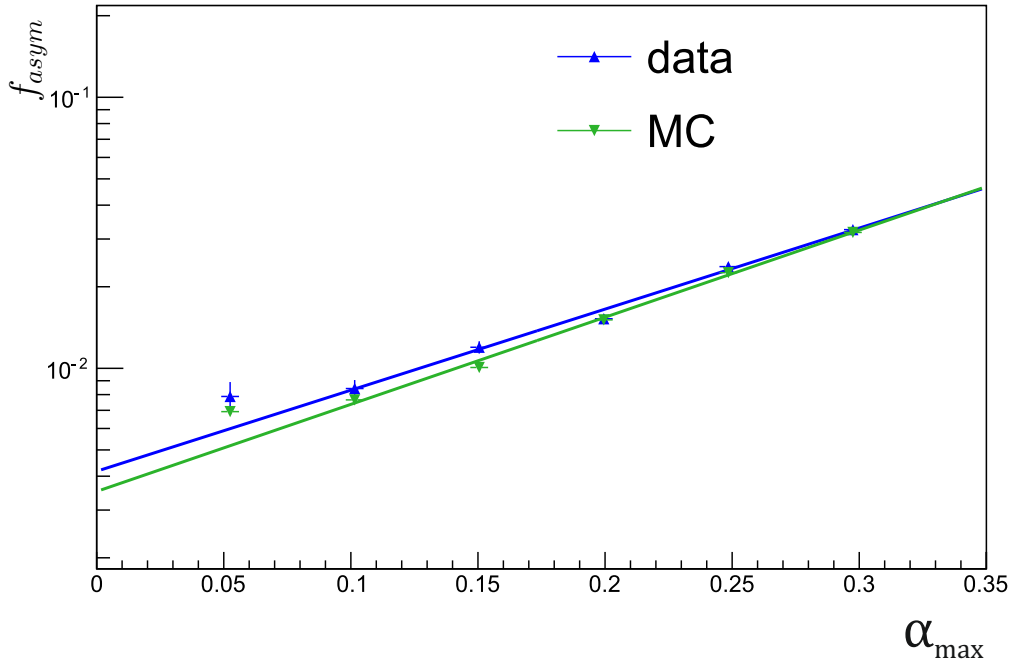

Figure 6.19: Tail fraction f_{asym} as a function of α_{max} for $p_t^{ave} \in (73, 95)$ and $|\eta| \in (0, 1.131)$. Exponential function fitted to data (blue line) and simulation (green line).

$$f_{asym} = \frac{\text{Number of events in the tail}}{\text{Number of events in total distribution}}. \tag{6.25}$$

To calculate the number of events in the tails N_{tail} the gaussian part of the asymmetry is subtracted from the distribution. To do that the distribution is fitted with a gaussian function using the same procedure as for the calculation of the tail threshold. To calculate N_{tail} the result of the subtraction (blue points in figure 6.18) is then integrated in the range $\mathcal{A} \in (\mathcal{A}_{tail}, 0.8)$. Number of events in total distribution N_{total} is an integral of the whole distribution. Using these values f_{asym} is calculated for each α_{max}, p_T and $|\eta|$ interval.

6.12.3 Additional jet activity extrapolation

Similar to asymmetry width, the tail fraction f_{asym} increases with growing α_{max}. However, as can be seen in figure 6.19, the dependence on additional jet activity is not linear but exponential. The points are fitted with function

$$f(\alpha_{max}) = b \cdot \exp(a \cdot \alpha_{max}), \tag{6.26}$$

where parameter b corresponds to the f_{asym} with no additional jet activity. The particle level imbalance (PLI), which had to be addressed in the jet energy resolution data to simulation ratio measurement (see section 6.6), is expected to cancel in the case of tail measurement.

6.12.4 Data to simulation ratios of response tail fractions

In the events which contribute to the tails of asymmetry distribution one or both jets from the dijet system were significantly mismeasured. This means that there is a high chance that these events are assigned to the wrong p_T^{ave} interval. This effect is expected to occur with same frequency in simulation and in data, which leads to a conclusion that it should cancel out. With that assumption, the scale factors of the tail fractions are calculated for each p_T and $|\eta|$ interval:

$$\rho_{tail} = \frac{f_{asym}^{data}(\alpha_{max} \to 0)}{f_{asym}^{sim}(\alpha_{max} \to 0)}. \tag{6.27}$$

The ratios calculated for different p_T intervals in each $|\eta|$ interval are averaged, and a single scale factor is derived for each pseudorapidity range. The uncertainties of the core scale factors are propagated to the tail measurement and used as a systematic uncertainty. Based on the measurement presented in [152] it is expected to be by far the dominant source of systematic uncertainties. The ratios calculated using equation 6.27 along with the statistical and systematic uncertainties are listed in table 6.11.

Table 6.11: Jet transverse momentum response tails data to simulation ratios.

η range	ratio	statistical unc.	systematic unc.
0. - 1.1	1.143	±0.052	±0.03
1.1 - 2.3	0.906	±0.056	±0.061
2.3 - 4.7	0.88	±0.18	±0.04

6.12.5 Outlook

The measurement presented in this section was a rough estimation conducted as a part of the *rebalance and smear* calculation (see chapter 8). For the future applications it is recommended to re-derive the response tail scale factors using the latest jet energy corrections (JECs) and resolution scale factors. The study was conducted in a time when the JECs were still in development and they changed significantly. This might have had an impact on the stability of the measurement of the f_{asym}. The study could be improved by conducting it using a finer binning in $|\eta|$ and full systematic uncertainties evaluation.

7 Search for supersymmetry

Searches for new physics, including searches for supersymmetry, are one of the main goals of the LHC physics program. Among them the searches for squarks and gluinos are of particular interest, as the corresponding potential cross sections at pp collisions are large. Such searches have previously been conducted for center of mass energies of 7 and 8 TeV [162–164], as well as using 13 TeV CMS data from 2015 as in [136], of which the analysis presented in this chapter is a direct successor. These searches observed no significant excesses in the search regions and set the lower limit for the gluino masses, depending on the simplified model used for the interpretation, to values between 1440 and 1600 GeV. The data collected with the CMS detector in 2016, which has significantly higher integrated luminosity compared to 2015 dataset, provides the opportunity to further extend the reach of the conducted search in the means of gluino and squark masses.

The search [52] that is presented in this chapter is performed in the fully hadronic final state, searching for R-parity conserving squark and gluino pairs production. Such events would feature jets and missing transverse momentum $\not{E}_T$ which would arise from the weakly interacting LSPs. The analysis is performed on the data corresponding to 35.9fb^{-1} collected with the CMS detector at LHC CERN in 2016.

7.1 Decay channels

For the purpose of a search for squarks and gluinos various simplified models (see section 2.3.2) are considered. In all of them the lightest neutralino $\tilde{\chi}_1^0$ is the LSP. For gluino production the models T1qqqq, T1tttt as shown in figure 7.1a, T1bbbb, T1tbtb as shown in figure 7.1b and T5qqqqVV as shown in figure 7.1c are considered. In T1qqqq, each gluino decays into a light-flavor quark-antiquark $q\bar{q}$ pair. T1bbbb and T1tttt are similar models with gluinos decaying into bottom quark-antiquark $b\bar{b}$ and top quark-antiquark $t\bar{t}$ pairs, respectively. In the T1tbtb model, shown in figure 7.1b, the gluino decays as $\tilde{g} \to \bar{t}b\tilde{\chi}_1^+$ or it's charged conjugate, and the lightest chargino $\tilde{\chi}_1^\pm$ decays further into a neutralino and off-shell W* boson $\tilde{\chi}_1^\pm \to \tilde{\chi}_1^0 W^{*\pm}$. In the T5qqqqVV scenario, shown in figure 7.1c, the gluino decays to a light quark-antiquark pair and a next-to-lightest neutralino $\tilde{\chi}_2^0$ or a chargino $\tilde{\chi}_1^\pm$. The $\tilde{\chi}_2^0$ and $\tilde{\chi}_1^\pm$ decay into an Z and W$^\pm$ bosons respectively.

Additionally, three mixed gluino scenarios are considered where gluinos can decay as $\tilde{g} \to \bar{t}t\tilde{\chi}_1^0$, $\tilde{g} \to \bar{b}b\tilde{\chi}_1^0$, $\tilde{g} \to \bar{t}b\tilde{\chi}_1^+$ or $\tilde{g} \to \bar{b}t\tilde{\chi}_1^+$, with three sets of branching ratios.

Three simplified models of squark production are considered: T2tt, T2bb and T2qq. In these scenarios the squark (antisquark) decays into a respective quark (antiquark) and neutralino $\tilde{\chi}_1^0$.

Supersymmetric particles not involved in the described processes are assumed to be infinitely massive, and the SUSY particles considered decay promptly except for the LSP, which is considered to be stable.

There are several Standard Model processes which would yield same signature as the simplified models described above. These SM backgrounds include events with top quarks, events with W or Z bosons and QCD events. The first two backgrounds will be discussed in more detail in section 7.6, and the QCD background will be discussed in chapter 8.

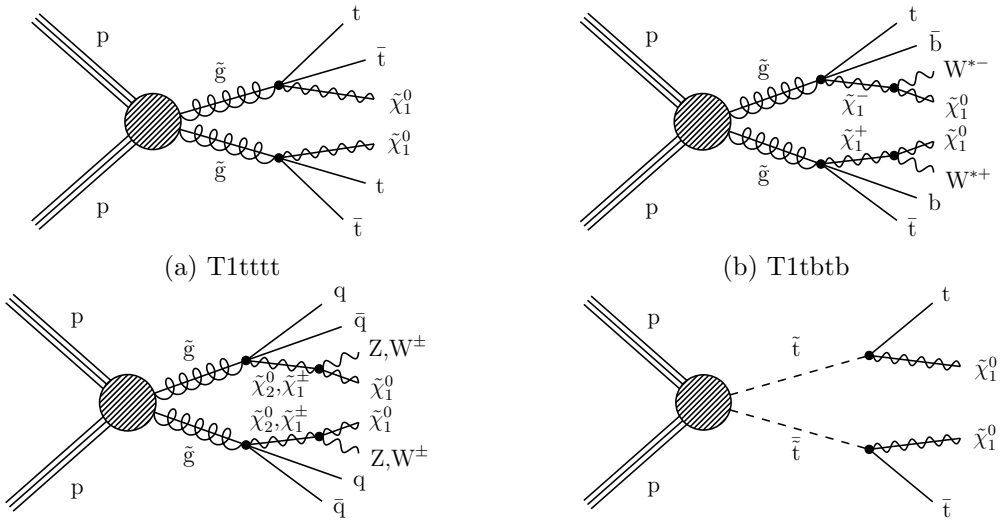

(a) T1tttt (b) T1tbtb

(c) T5qqqqVV (d) T2tt

Figure 7.1: Feynmann diagrams of some of the considered simplified model signal scenarios. Taken from [52].

7.2 Event selection

The signal models that are considered in this analysis differ by the number of expected jets, called N_{jets} here, and tagged bottom quark jets, called N_{bjet} here. To maximize the sensitivity, the so-called baseline selection criteria are applied:

$\mathbf{N_{jets} \geq 2}$ The events are required to have at least 2 jets that pass the kinematic criteria, with jets defined as Particle Flow jets with transverse momentum $p_T > 30$ GeV and pseudorapidity $|\eta| < 2.4$. Additionally, jets are required to satisfy the so-called jet identification (jet ID, [165]) criteria which are intended to reject fake, badly reconstructed and noise jets while keeping 99% of real jets.

$\mathbf{H_T > 300}$ GeV with H_T being the scalar sum of the momenta of the same jets defined as in the point above.

$\mathbf{\not{H}_T > 300}$ GeV where $\not{H}_\mathbf{T} = -\sum_{\mathbf{jets}} \vec{p}_T$ with sum over jets satisfying $p_T > 30$ GeV and $|\eta| < 5$. They also have to satisfy jet ID. It is important to underline here that the definition of jets in the calculation of the missing transverse momentum differs from the definition used in the previous two points,

Muon and Electron veto Muons are required to satisfy $p_T > 10$ GeV and $|\eta| < 2.4$. To make sure that the muons from b-hadron decays are not vetoed, muons are required to pass the isolation criteria $I < 0.2$. Electrons are required to have $p_T > 10$ GeV and $|\eta| < 2.5$. Similarly to muons electrons are required to satisfy isolation $I < 0.1$. Events with electrons or muons satisfying these requirements are vetoed.

$\mathbf{\Delta\Phi(\not{H}_T, jet_i)}$ Most of the QCD events that pass the above selection will have a significantly mismeasured jet, which will lead to a high value of $\vec{\not{H}}_\mathbf{T}$. In that case, the missing mo-

mentum vector will be aligned with the momentum vector of the mismeasured jet, which allows for an efficient discrimination of the QCD events. Events are selected if the azimuthal angle between the $\tilde{\not{H}}_{\mathbf{T}}$ and two highest-p_T jets is higher than $\mathbf{\Delta\Phi}(\not{H}_{\mathbf{T}}, \mathbf{jet_{1,2}}) > 0.5$. Additionally, for the events with 3 jets, it is required that $\mathbf{\Delta\Phi}(\not{H}_{\mathbf{T}}, \mathbf{jet_3}) > 0.3$, and for $N_{jets} \geq 4$ also $\mathbf{\Delta\Phi}(\not{H}_{\mathbf{T}}, \mathbf{jet_4}) > 0.3$.

Isolated track veto The dominant source of the SM background after applying the above selection are events with single-top, $t\bar{t}$-pair or W+jets production, in which one of the W bosons decays leptonically $W \to l\nu$. Approximately half of these events will have a W decaying into tua, which in turn decays hadronically, and half will have a W decaying into electrons or muons which are not identified or do not satisfy the isolation criteria. To reject these backgrounds, events with at least one isolated track are vetoed. The track isolation I_{tk} is defined as scalar sum of the momenta p_T of other charged tracks within a cone of radius $\Delta R = 0.3$ around the primary track normalized by the momentum of the track. In case a track has been tagged as leptonic by PF algorithm, it is identified as isolated track if it has momentum $p_T > 5$GeV and isolation $I_{tk} < 0.2$, and in case of hadronic tracks, it is required to have $p_T > 10$GeV and isolation $I_{tk} < 0.1$. Isolated track vetos can also reject signal events, so isolated tracks are vetoed only if they satisfy $m_T(\text{track}, \tilde{\not{E}}_{\mathbf{T}}) < 100$GeV, where m_T is the transverse mass of the sum of isolated track and missing energy.

7.3 Triggers

The following set of triggers were used for the selection of the events:

- HLT PFMET100 PFMHT100 IDTight,
- HLT PFMET110 PFMHT110 IDTight,
- HLT PFMET120 PFMHT120 IDTight,
- HLT PFMETNoMu100 PFMHTNoMu100 IDTight,
- HLT PFMETNoMu110 PFMHTNoMu110 IDTight,
- HLT PFMETNoMu120 PFMHTNoMu120 IDTight.

The efficiency of these triggers depends on the jet multiplicity, H_T and $\not{H}_T$ and is computed using a Bayesian neutral network (BNN, [166]). This is an alternative to measuring the efficiency of the triggers in intervals of the variables they depends on. Neural networks (NN) are functions that can map input variables into outputs. Such a network is trained with events for which the desired output is known: in particle physics analysis it is trained on sets of signal and background events. A bayesian neural network is a NN with a prior imposed on it, which solves the problem of overfitting a neural network. Overfitting occurs when the output function fits very well or exactly to the training sample, but fails to describe additional samples.

The BNN is trained on a single electron data sample for which events that pass one or more of the triggers are treated as signal, and events that fail all six of the triggers are treated as background. The single electron trigger that is used to select the training sample is fully efficient in the part of the kinematic phase-space that is considered. The result of the procedure is an estimate of the trigger efficiency

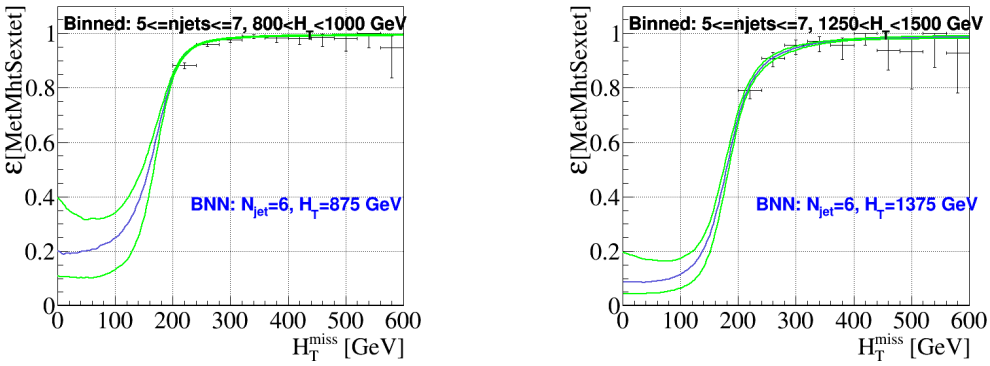

Figure 7.2: The trigger efficiency as a function of $\not{H}_T$, measured using the BNN (blue curve) and measured in bins (histograms) for $N_{jets} = 6$ and various values of H_T. The green curves represent the 1 standard deviation uncertainty of the efficiency estimate.

$$BNN = P(s|\vec{\Theta}) = \frac{p(\vec{\Theta}|s)}{p(\vec{\Theta}|s) + p(\vec{\Theta}|b)} \tag{7.1}$$

where $\vec{\Theta}$ represents the input variables, namely H_T, $\not{H}_T$ and N_{jets}, and s and b denote the events for which a trigger was fired and not fired, respectively. The output of the procedure is a set of functions rather than a single function, the standard deviation is defined as the 68% containment interval of the outputs, and the central value is calculated as the mode of them. The trigger efficiency calculated using BNN is presented in figure 7.2. The events are selected with the triggers and weighted according to the prescale of the lowest trigger that was fired, and the trigger efficiency is calculated using the BNN approach.

7.4 Event cleaning

Some events are affected by the misbehavior of the detector or by particles not originating from the analyzed collision. These kind of events are rare, however they tend to have large missing energy $\vec{\not{E}}_{\mathbf{T}}$, which means that they can enter the signal regions (see [146]). To remove these events from the selection, they are rejected based on certain *filters*, sources of which are listed below.

Beam halo The vacuum beam pipe of LHC contains some residual gas, with which protons can interact. The products of these interactions, mostly muons, are collimated along the z-axis of the detector and create the so-called *beam halo*. The signature of the signal left in the detector by these particles allows for efficient discrimination, with rejection of around 85% events in the halo-enriched simulated sample, while maintaining very low mistag rate below 0.01%.

Anomalous HCAL signals Anomalous signals within the calorimeters are identified using multiple filters. An *HBHE*[1] *noise filter* is based on geometrical patterns and pulse shape and timing of the signal. It rejects machine-induced noise that can arise, for example, in the read-out electronics. Additionally, the energy deposits in the calorimeters are combined with the hits in the tracker, and if the deposits in HCAL are isolated, they are rejected by the *HBHE isolated noise filter*.

Dead ECAL-cells In the ECAL many of the spurious and noise signals are removed on the reconstruction level, based on information from the ECAL only. However, there are some effects that are left uncorrected. Some of the ECAL towers do not provide precise read-out. This can be partially compensated using trigger primitive (TP) information, however for high energy deposits this method is not precise. To reject events where we can not depend on TP level information, an *ECAL dead cell trigger primitive* filter is used. Additionally, five ECAL endcap (EE) supercrystals(clusters of crystals) have been identified to give anomalously high energy deposits. To identify these signals, an *EE bad supercrystal* filter is applied.

Bad PF muon In the muon tracking, low-quality muons are rejected. However, the high-p_T tracks survive this procedure, and are considered as charged hadrons which enter the calculation of $\not{E}_{\mathbf{T}}$. These events are rejected using *Bad PF muon* and *Bad charged hadrons* filters.

Bad/noise jets Sometimes noise can be identified as a jet. Fortunatelly, these jets tend to have anomalously high fractions of photons and neutral hadrons. Consequently, we reject events with jets that pass $p_T > 30$ GeV and $|\eta| < 5.0$ but do not pass the loose jetID selection.

There are some additional effects that are compensated for. To make sure that high $\not{E}_{\mathbf{T}}$ is not caused by a failure in the Particle Flow algorithm, events with PF missing energy (*PFMET*) much higher than missing energy calculated using only calorimeter deposits (*CaloMET*), that is with PFMET/CaloMET> 5, are rejected.

Abnormally high energetic jets have been observed in the forward region with pseudorapidity values $|\eta| \in (3.0, 3.1)$. To reject events with such jets a thresholds on the ratio of scalar jet momentum sum H_T of jets within the tracker coverage $|\eta| < 2.4$ and in the full coverage $|\eta| < 5.0$ is set to $H_T^{5.0}/H_T^{2.4} < 2.0$.

Sometimes a muon is misreconstructed as a jet. The events with jets with $p_T > 200$ GeV for which more than half of the energy is originating from muons are rejected.

7.5 Search variables

The search intervals are defined using four variables: the number of jets N_{jet}, the number of bottom quark jets N_{bjet}, the scalar sum of jets momenta H_T and the amplitude of the vector sum of jets momenta, or missing transverse momentum, $\not{H}_T$. The intervals in jet and b-tagged jet multiplicity are as follows

[1] HBHE - HCAL barrel and and endcap

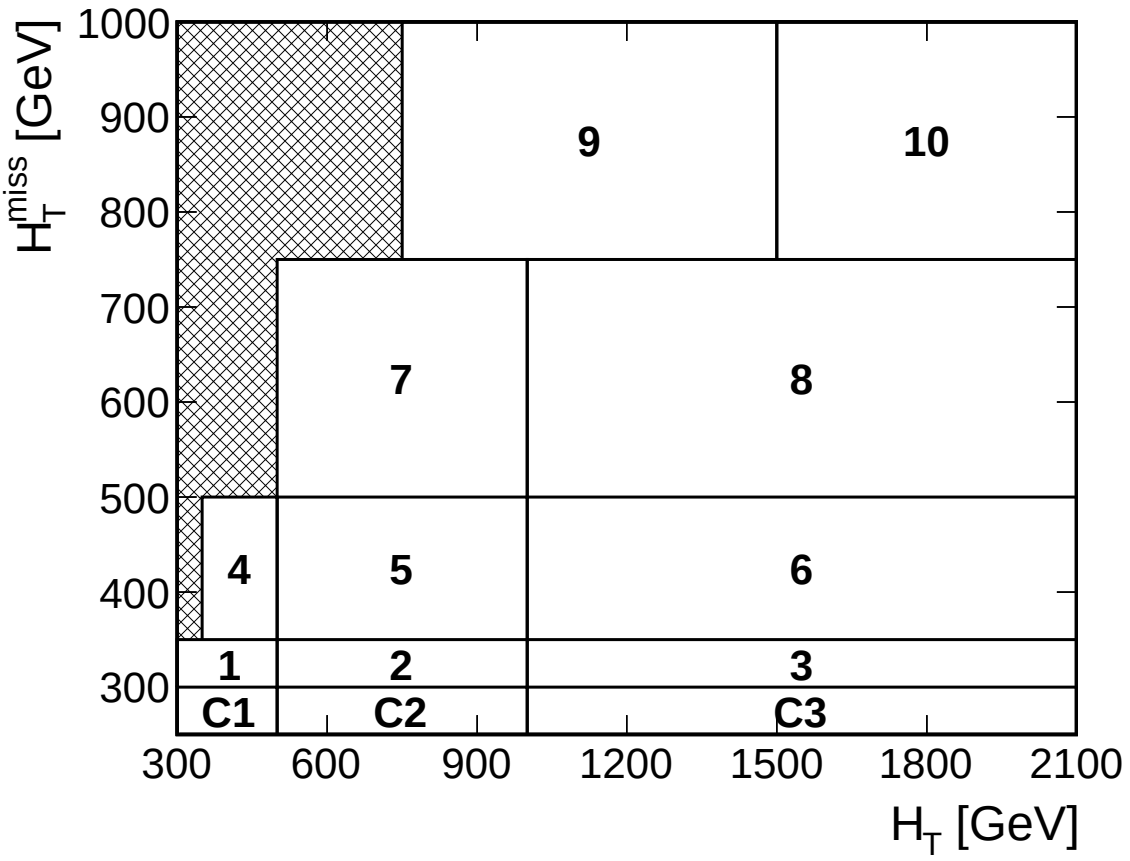

Figure 7.3: Schematic view of the H_T and $\not{H}_T$ plane showing the search intervals, labeled 1 to 10, and the QCD control bins, C1, C2 and C3, used for the evaluation of the QCD background. Figure taken from [52].

- N_{jet}: 2, 3-4, 5-6, 7-8, ≥ 9;
- N_{bjet}: 0, 1, 2, ≥ 3;

Intervals with $N_{jet} = 2$ and $N_{bjet} \geq 3$ are dropped, as it would be empty by definition. The binning in H_T and $\not{H}_T$ is presented in figure 7.3, and the intervals are listed in table 7.1. Ten kinematic regions are defined. For $N_{jet} \geq 7$ bins 1 and 4 are discarded as they are sparsely populated. Also events with large $\not{H}_T$ and small H_T are not included, as these events most likely originate from mismeasurements. The total number of search bins is 174. Additionally, 49 QCD sideband bins are defined, which are used to derive transfer factors for the QCD estimation method described in section 8.3.

7.5.1 Aggregate search regions

To provide the interpretation of the results, a likelihood fit to the complete set of search bins is made. For easier interpretation, 12 so-called *aggregate search regions* are introduced, which are defined by summing some of the nominal search intervals. Each aggregate search region is tailored to represent one of 12 particularly interesting signal topologies which are listed in table 7.2. For each of these bins the results will be interpreted as a single-bin analysis, which allows for simpler re-interpretation.

Interval	$\not{H}_T$[GeV]	H_T[GeV]
C1	250-300	300-500
C2	250-300	500-1000
C3	250-300	>1000
1	300-350	300-500
2	300-350	500-1000
3	300-350	>1000
4	350-500	350-500
5	350-500	500-1000
6	350-500	>1000
7	500-700	500-1000
8	500-700	>1000
9	>750	750-1500
10	>750	>1500

Table 7.1: Intervals in H_T and $\not{H}_T$ used to define the search bins. Intervals C1, C2 and C3 are defined for the validation of the QCD background estimate. Intervals 1 and 4 are not used for search bins with $N_{jet} \geq 7$. Taken from [52].

Region	Heavy flavor?	Parton multiplicity	Δm	N_{jet}	N_{b-jet}	H_T [GeV]	$\not{H}_T$ [GeV]
1	No	Low	Small	≥2	0	≥500	≥500
2	No	Low	Large	≥3	0	≥1500	≥750
3	No	Medium	Small	≥5	0	≥500	≥500
4	No	Medium	Large	≥5	0	≥1500	≥750
5	No	High	All	≥9	0	≥1500	≥750
6	Yes	Low	Small	≥2	≥2	≥500	≥500
7	Yes	Low	Large	≥3	≥1	≥750	≥750
8	Yes	Medium	Small	≥5	≥3	≥500	≥500
9	Yes	Medium	Large	≥5	≥2	≥1500	≥750
10	Yes	High	All	≥9	≥3	≥750	≥750
11		$\tilde{\tau}$-like	Small	≥7	≥1	≥300	≥300
12		$\tilde{\tau}$-like	Large	≥5	≥1	≥750	≥750

Table 7.2: The targeted topologies and aggregate search bins corresponding to them. Taken from [52].

7.6 Backgrounds

Backgrounds can be divided into three categories. One category consists of top quark and W+jets events, which can be subdivided into further two categories, the so-called *lost-lepton* and *hadronic* τ. Another background is the $Z \to \nu\nu$ events, referred to as *Z to invisible*. Third, background from QCD events. All backgrounds are evaluated using the so-called data-driven methods, in which the background counts are calculated from the data control regions (CRs).

In the following sections, the backgrounds originating from *lost-lepton* events(Sec. 7.6.1), hadronic-τ decays(Sec. 7.6.2) and $Z \to \nu\nu$ events (Sec. 7.6.3) will be discussed. The QCD background estimation method *rebalance-and-smear* is one of the main topics of this thesis and will be discussed in chapter 8, and the validation of the prediction with second QCD background estimate will be presented in chapter 8.3.

7.6.1 Lost-lepton background

A background from W+jets and top quark events can arise when the W boson decays leptonically $W^{\pm} \to l^{\pm}\bar{\nu}$ but the charged lepton is "lost". This can happen if electrons or muons, also originating from tau decays, are not within kinematic acceptance, are not reconstructed, or are not isolated. To calculate the event counts originating from this background, single-lepton control regions are defined, and the events from these control regions enter the search regions with a weight that represents the probability of the lepton being lost. The method is explained in detail below.

The CRs are defined with the standard triggers and selection, apart from the lepton veto and isolated track veto that are not applied. The CRs are defined separately for electrons and for muons, with exactly one electron or muon present. The transverse mass of the sum of the missing momentum $\vec{\not{E}}_T$ and the lepton has to be below approximately the mass of the W boson $m_T < 100$ GeV. This reduces possible signal contamination, while keeping majority of the SM events. The signal contamination is in most of the signal regions negligible, but for certain model points it can become as high as 60% for large values of N_{jet}, N_{b-jet}, H_T and $\not{H}_T$. This issue is addressed in the interpretation of the results.

The efficiencies of the acceptance, reconstruction and isolation of the leptons and some additional corrections, such as the m_T cut efficiency, are derived from simulation samples. These include simulations of $t\bar{t}$, W+jets, single t, exotic and QCD processes, and the same selection as to Control Regions is applied to them.

Events from the CRs enter the search regions with weights which represent the probability of the lepton with given kinematic properties to be "lost". Additional corrections are applied to account for effects like purity of the control regions and efficiency differences between data and simulation. The efficiencies depend on the search variables and kinematic properties of leptons. The sum of all weights of the events from CRs define the background predictions in each search region. The entire procedure is carried out separately for single-electron and single-muon CRs. Both results yield the prediction of lost-electron and lost-muon backgrounds. The results are consistent and averaged to obtain the final prediction.

The method can be tested on simulated sample by comparing the result of the method applied on that sample with direct prediction taken from it. Such a test is presented in figure 7.4

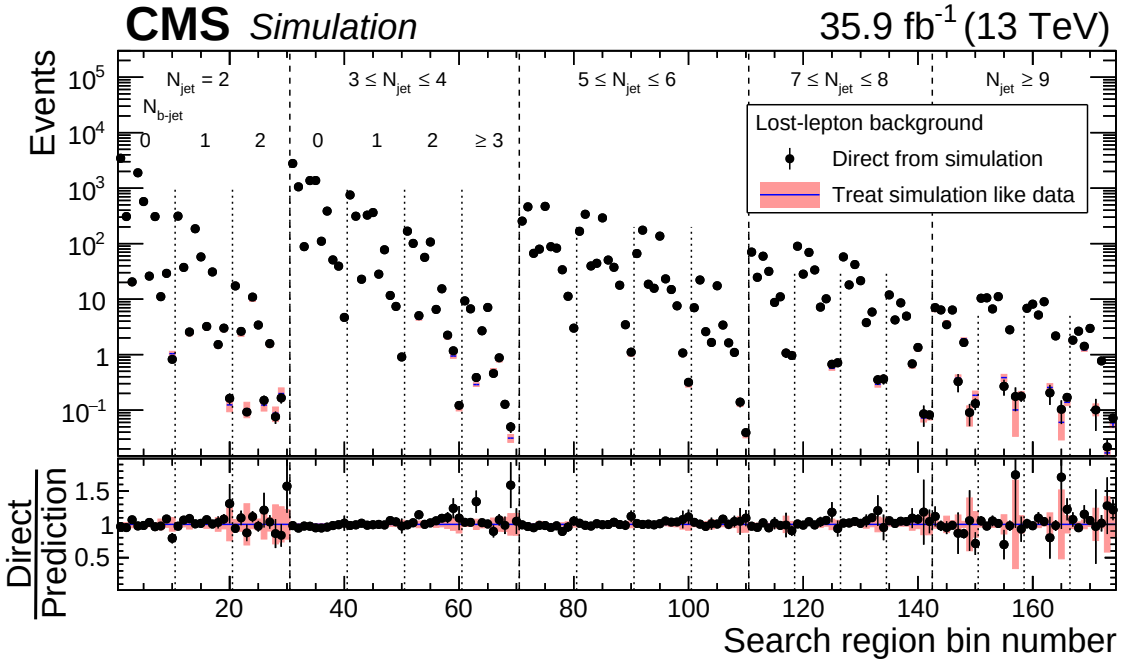

Figure 7.4: Lost lepton background in the search regions taken directly from simulation using truth information (solid points) compared with the prediction of the lost-lepton background estimation method (shaded bars). The lower panel shows the ratio of the two results. The interval numbers are explained in tables C.1-C.5. Figure taken from [52].

7.6.2 Hadronically decaying τ lepton background

Another background that originates from W+jets and top quark events arises when the W boson decays leptonically into a tau lepton $W \to \tau\nu_\tau$, and the tau decays hadronically. The evaluation of this background exploits the similarities between μ + jets and τ + jets events.

The CR events are selected using either a trigger that requires at least one isolated muon candidate with $p_T > 24$GeV, or at least one isolated muon candidate with $p_T > 15$GeV and $H_T > 500$GeV. The standard analysis triggers cannot be used, because the τ_{had} determination method requires no cut on $\not{H}_T$. Furthermore, the events need to include exactly one muon with pseudorapidity $|\eta| < 2.1$ and momentum $p_T > 25$ GeV. The momentum requirement is dropped to $p_T > 15$ GeV for events with scalar momentum sum $H_T > 500$ GeV. The signal contamination is generally at a promiles level $\lesssim 0.1\%$, however, for some of the considered model points it can reach as high as 40% for the high N_{jet}, N_{bjet}, H_T and $\not{H}_T$ values.

The response of the detector is different for muons and hadronic taus. This effect is accounted for by smearing the muons momentum p_T with τ_{had} response templates derived from the simulation of $W \to \tau_{had}\nu_\tau$ events. In the previous iteration of this analysis [136], templates were derived from $t\bar{t}$ and W + jets simulation. In these samples the response templates were contaminated by non-tau particles.

The hadronic tau background estimation method is based on the assumption that the measured momentum p_T of the muon represents the true momentum of tau. The visible spectrum of hadronic tau is then calculated by smearing the muon momentum with the

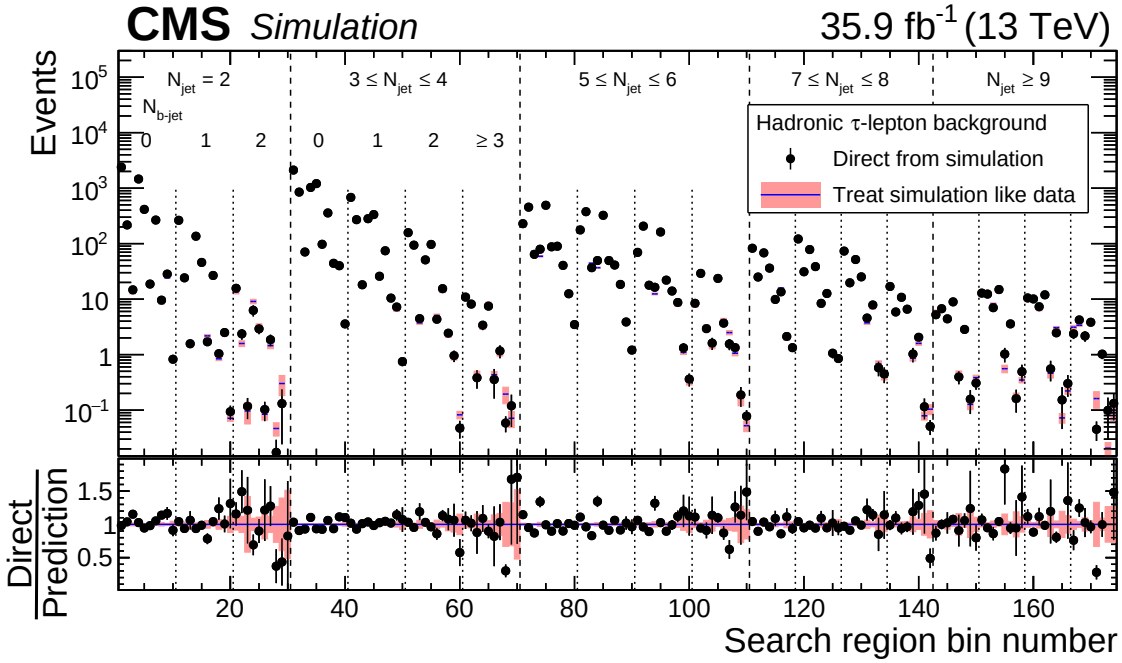

Figure 7.5: Hadronic tau background in the search regions taken directly from simulation using truth information(solid points) compared with the prediction of the hadronically decaying tau background estimation method (shaded bars). The lower panel shows the ratio of the two results. The interval numbers are explained in tables C.1-C.5. Taken from [52].

response template. Following the smearing, the search variables N_{jet}, N_{bjet}, H_T and $\not{H}_T$ are recalculated and the signal region selection is applied to the event. It is important to note here that the event can be smeared to a configuration with higher $\not{H}_T$, and because of these migration effects no $\not{H}_T$ cut can be applied before the smearing procedure. The corrections account for the trigger efficiencies, acceptance and efficiencies of muon selection and branching fractions ratio of $W \to \tau_{had}\nu_\tau$ and $W \to \mu\nu_\mu$.

The validation of the method is shown in figure 7.5, where the event yields taken directly from simulation are compared with the result of applying the hadronic tau background estimation method to the simulation events.

7.6.3 $Z \to \nu\bar{\nu}$ background

The last background discussed in this chapter is the so-called Z-to-invisible background, or the background that originates in the events with Z boson that decays to neutrino-antineutrino pair $Z \to \nu\bar{\nu}$. The method is based on two control regions: one containing γ + jets, and one with Z boson decaying to a pair of charged leptons $Z \to l^+l^-$. The γ or the lepton pair are removed from the event to imitate the missing energy from the neutrino pair.

The γ+jets CR utilizes the similarities between the production of Z boson and direct photon production. This region is highly populated, but the method of extrapolating from it to signal region relies heavily on theoretical modeling. As a result, γ+jets CR is used to calculate the background in 46 bins with $N_{bjet} = 0$. The $Z \to l^+l^-$ CR is less numerous and is used to validate the event counts in $N_{bjet} = 0$ bins and to extrapolate

to $N_{bjet} > 0$. As a result of limited statistics, the extrapolation factors are derived from samples integrated over H_T and $\not{H}_T$.

The $Z \to l^+l^-$ events are selected using one of the four triggers that require i) at least one isolated electron or muon with momentum $p_T > 15$GeV and $H_T > 350$GeV or 400GeV, depending on the instantaneous luminosity of LHC, ii) at least one electron with $p_T > 105, 115$GeV (depending on luminosity), iii) at least one muon with $p_T > 50$GeV, iv) at least one isolated electron (muon) with momentum $p_T > 27$ (24) GeV. The events are required to include exactly one pair of e^+e^- or $\mu^+\mu^-$ with invariant mass within 15GeV of the mass of the Z boson and the momentum of the pair $p_T^{ll} > 200$GeV. To keep both control regions separate, events are vetoed when a photon is identified.

The γ+jets events are selected using the trigger that requires a photon candidate with momentum $p_T > 175$GeV. One well-identified and isolated photon with $p_{T,\gamma} > 200$GeV is required in the event. Approximately 85% of the events contain a direct photon. In the remaining 15% contain either fragmentation photons (initial state radiation, final state radiation, hadronization) or non-prompt photons (i.e. non stable hadron decay). The photon purity β_γ as a fraction of events with prompt photons (direct and fragmentation photons) to the number of events with photons is determined from the control sample.

The number of the $Z \to \nu\bar{\nu}$ background events in bins with no b-tagged jets $N^{pred}_{Z\to\nu\bar{\nu}}\big|_{N_{bjet}=0}$ is calculated using the following formula

$$N^{pred}_{Z\to\nu\bar{\nu}}\Big|_{N_{bjet}=0} = \rho\mathcal{R}^{sim}_{Z\to\nu\bar{\nu}/\gamma}\mathcal{F}^{sim}_{dir}\beta_\gamma N^{obs}_\gamma/\mathcal{C}^{\gamma}_{data/sim}, \tag{7.2}$$

where N^{obs}_γ is the event count in the corresponding N_{jet}, H_T, $\not{H}_T$ bin of the control region, β_γ is the fraction of prompt photons, $\mathcal{F}_{dir}$ is the fraction of the prompt photons that are direct, and $\mathcal{R}^{sim}_{Z\to\nu\bar{\nu}/\gamma}$ is the ratio of the number $Z(\to \nu\bar{\nu}) +$ jets events to the direct-photon $\gamma +$ jets events taken from simulation. $\mathcal{C}^{\gamma}_{data/sim}$ is the correction factor for the efficiency differences in photon reconstruction in data and in simulation, and ρ accounts to differences between simulation and data in the $\mathcal{R}^{sim}_{Z\to\nu\bar{\nu}/\gamma}$.

As mentioned earlier, to calculate the background in bins with $N_{bjet} > 0$, the background count in the corresponding $N_{bjet} > 0$ (same N_{jet}, H_T and $\not{H}_T$) is multiplied with an extrapolation factor

$$\left(N^{pred}_{Z\to\nu\bar{\nu}}\right)_{j,b,k} = \left(N^{pred}_{Z\to\nu\bar{\nu}}\right)_{j,0,k}\mathcal{F}_{j,b}, \tag{7.3}$$

where j, b and k denote the N_{jet}, N_{bjet} and kinematic bin indices. The extrapolation factor $\mathcal{F}_{j,b}$ is derived from data control region for all N_{jet} bins except $N_{jet} \geq 9$. It is obtained from the event counts in $Z \to l^+l^-$ CR, with corrections β^{data}_{ll} that account for the purity of the control region sample:

$$\mathcal{F}_{j,b} = \left(N^{data}_{Z\to l^+l^-}\beta^{data}_{ll}\right)_{j,b}/\left(N^{data}_{Z\to l^+l^-}\beta^{data}_{ll}\right)_{j,0}; \quad j = 0, 1, 2, 3. \tag{7.4}$$

The extrapolation factor for the last N_{jet} bin is calculated from simulation because of low statistics in the data control sample:

$$\mathcal{F}_{4,b} = \mathcal{F}_{3,b}(\mathcal{F}^{sim}_{4,b}/\mathcal{F}^{sim}_{3,b}), \tag{7.5}$$

where $\mathcal{F}^{sim}_{3,b}$ and $\mathcal{F}^{sim}_{4,b}$ are the extrapolation factors derived from simulation for $N_{bjet} = 3,\ 4$ respectively. The validation of the method is presented in figurew 7.6. The prediction for bins with $N_{bjet} = 0$ agree by definition.

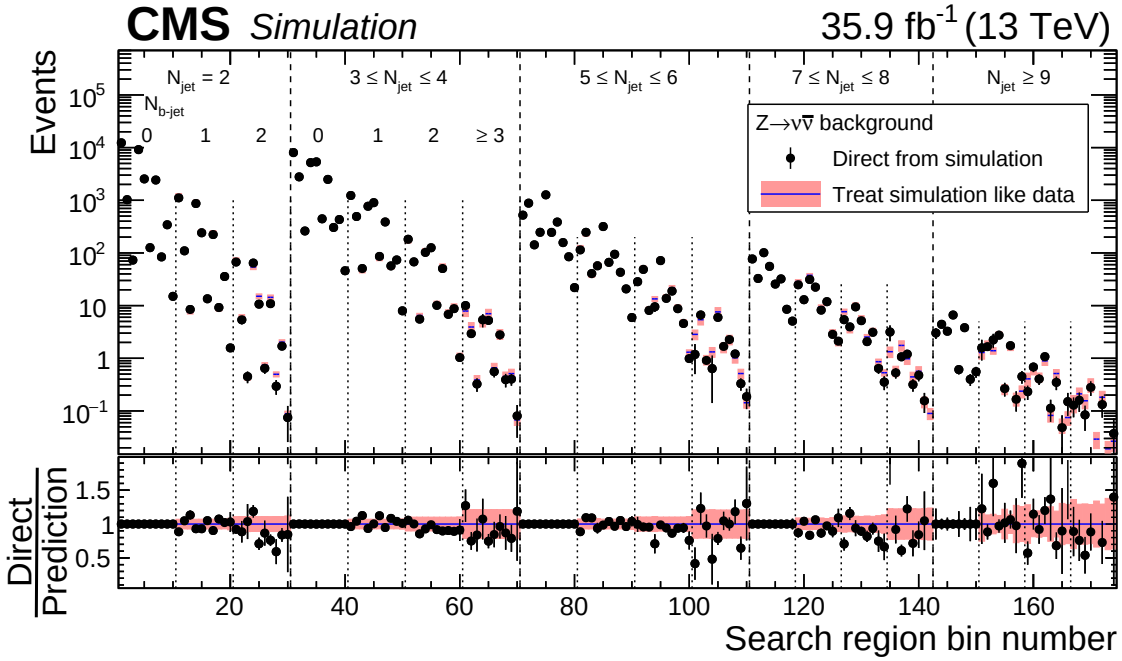

Figure 7.6: The $Z \to \nu\bar{\nu}$ background estimation validation in the simulated sample. Points with statistical uncertainties represent the event counts taken directly from simulation of $Z(\to \nu\bar{\nu}) +$ jets events, the histogram represents the prediction of the method applied to statistically independent $Z(\to l^+l^-) +$jets simulation sample. The lower panel shows the ratio of the two results. For $N_{bjet} = 0$ both results match by definition. The interval numbers are explained in tables C.1-C.5. Figure taken from [52].

8 Rebalance and smear

The background from QCD multi-jet events with jets and missing energy is especially difficult to model in the high-$\not{H}_T$ region. It is not expected to be large, because multi-jet events do not have large genuine $\not{H}_T$. The missing momentum in QCD multi-jet events arises primarily from mismeasurements of the transverse momentum p_T of jets; secondarily, it originates from jets that fall out of acceptance $p_T < 30$GeV, and from neutrinos from heavy flavor jets. The distributions of the missing transverse momentum in QCD simulated events with its three sources distinguished are presented in figure 8.1. As can be seen from the lower panels, the $\not{H}_T$ in QCD events originates mainly from the mismeasurements of the jets. The contribution from neutrinos is at the level of 10% in events with no b-tagged jets, and increases by 5-10% in the case of events with three b-tagged jets. The various origins of the $\not{H}_T$ makes this background difficult to model.

For both the 2015 [136] and 2016 [52] iterations of the supersymmetry searches discussed in chapter 7, two independent methods were used to estimate the QCD background for

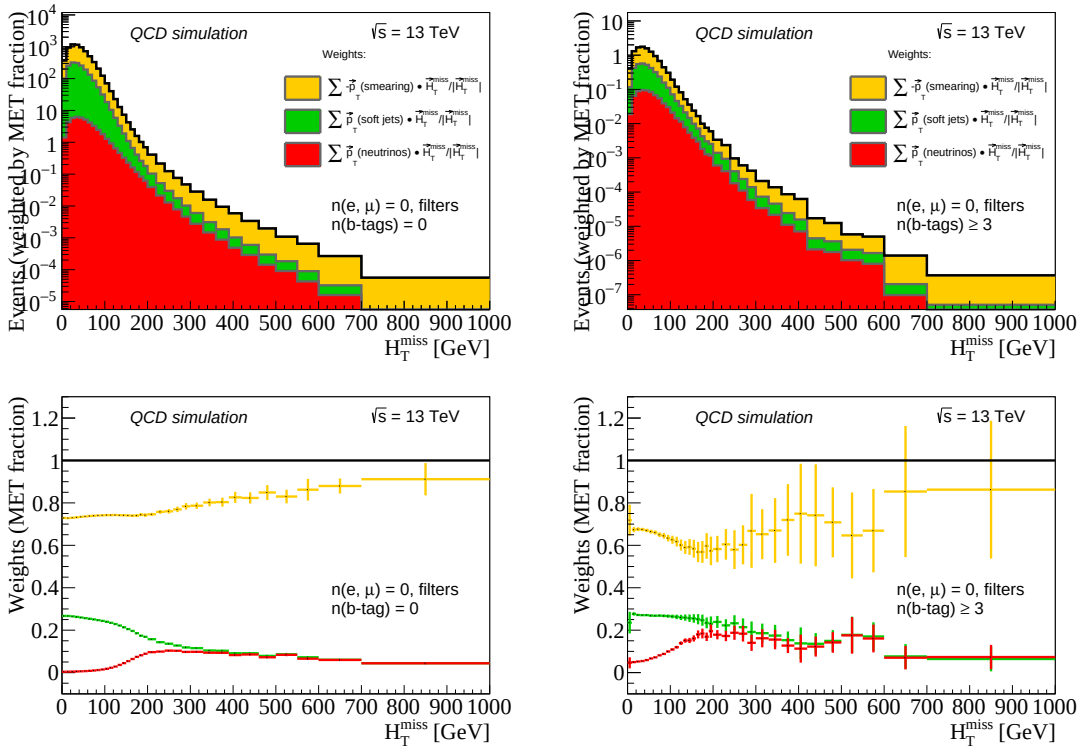

Figure 8.1: The distributions of the $\not{H}_T$ (upper plots) originating from three sources: the neutrinos (red histogram and points), the soft jets (green) and the mismeasurements of the jets (yellow) for events with no b-tagged jets (left) and with three b-tagged jets (right). On the lower plots the fractional contribution of each of the sources to the total $\not{H}_T$ is presented. The distributions were made using QCD simulated events listed in table 8.1.

events with jets and missing energy. The first method, henceforth called $\Delta\phi$ extrapolation, is based on a low-$\Delta\phi$ control region. This region is defined with the same intervals and cuts as the 174 search bins but with an inverted $\Delta\phi$ cut, and a transfer factor from low- to high- $\Delta\phi$ regions modeled from simulation and data. This method has been used as the primary method in the previous iteration of the search, and as a validation of the second method in the latest analysis. The second method is the so-called *rebalance and smear* (RnS) method, in which jets in the QCD events are "rebalanced" to approximately undo the detector effects, and then smeared according to a given jet resolution to a configuration that resembles a detector level QCD event. This method has been developed for and used in 7 and 8 TeV searches [162–164]. It has been used in 13 TeV search for supersymmetry [52], which was discussed in previous chapter, and has been also employed in the previous analysis [136] as a cross check for the $\Delta\phi$ extrapolation method.

The rebalance and smear background estimation method is the main topic of this chapter, and is discussed in detail in section 8. Results and uncertainties are presented and discussed in section 8.2. In section 8.3, $\Delta\phi$ extrapolation method and its results are briefly discussed.

8.1 Rebalance and smear

The rebalance and smear method is used to predict QCD background events with missing transverse momentum $\not{H}_T$ originating from jet mismeasurement, jets out-of-acceptance and neutrinos from heavy-flavored jets. The method can be split into two steps: (1) rebalancing of the selected QCD events to an approximately particle-level configuration, and then (2) smearing them to simulate the detector effects. The events produced in this procedure contain full kinematics information, which allows to verify the background prediction and to derive the contributions of QCD background to various search and validation regions. A schematic of the method is presented in figure 8.2. As can be seen on the sketch, the $\not{H}_T$ distribution for both fake (QCD) and true contributions are pushed to low values by the rebalancing procedure. After smearing, the fake $\not{H}_T$ contribution is recreated and the true contribution stays below the baseline cut. This ensures that possible contamination of the seed sample with the real $\not{H}_T$, originating for example from SUSY signal or non-QCD backgrounds, is removed from the prediction of the QCD background. The procedure is described in more detail below.

8.1.1 Trigger efficiencies and seed sample selection

To select the QCD events from the events recorded by the CMS detector, a set of nine inclusive high level triggers (HLT) is used:

- `HLT_PFHT[x].v* ([x]=250,300,350,400,475,600,650,800,900).`

All of the triggers except the highest H_T one are prescaled, which means that only one in M events that passes the trigger selection is kept. Prescaling of the triggers is necessary to reduce the rate at which the data is being collected. Because processes with high values of H_T have lower cross-sections and at the same time are generally considered more interesting, the higher the H_T of the trigger, the lower the prescale M. These triggers are fired if the online[1] H_T of the event passes the threshold which corresponds to the values

[1] Online H_T is calculated for the high-level trigger calculations. It is reconstructed using simplified version of the particle-flow algorithm.

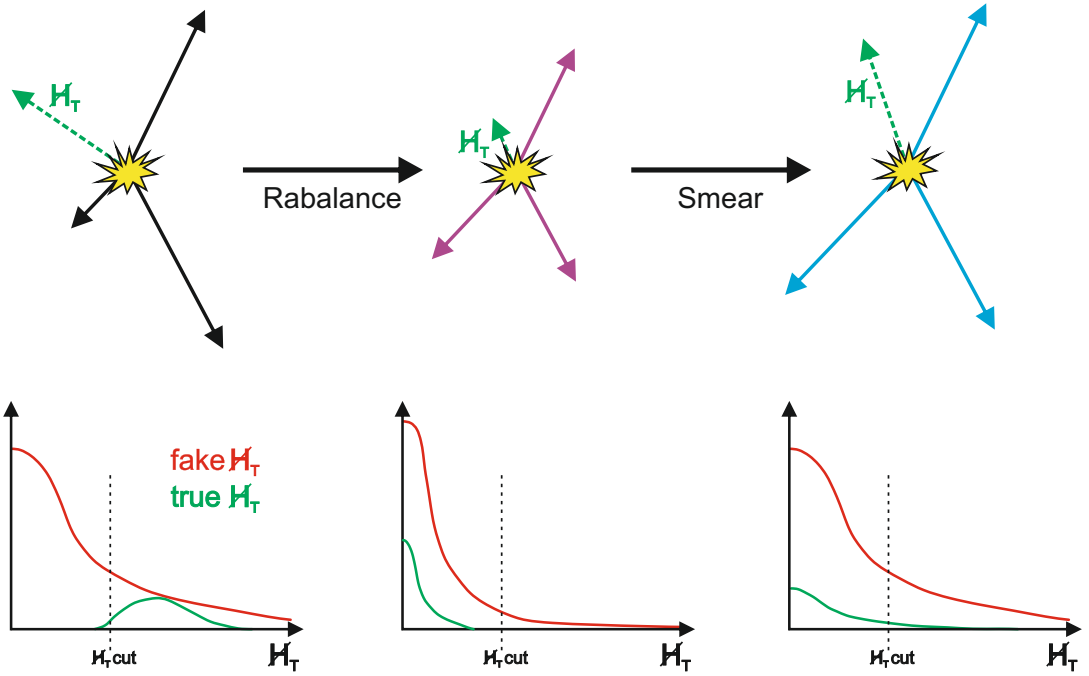

Figure 8.2: A schematic of the two main steps of the rebalance and smear procedure. Below each step, a sketch of the missing transverse momentum $\not{H}_T$ at each stage of the procedure is presented.

in the bracket above. All used triggers are fully efficient at $H_T = 300$ GeV, which is the baseline cut used in this analysis. For a given value of online H_T the corresponding trigger is required to be fired, meaning that for example if $H_T \in (400, 475)$ GeV, the `HLT_PFHT400` trigger is required to fire.

A standard procedure of correcting for the bias introduced by the prescales is to weight the events according to M. This however, in case of rebalance and smear, can lead to a situation where a highly prescaled low-H_T event enters a search region after smearing of the rebalanced jets. This is solved by adjusting the number of smears. As it will be described in section 8.1.4, the smearing of each of the rebalanced events is performed multiple times, and the number of smearings depends on the prescale. For a prescale M, the event is smeared $M \cdot N$ times, where value of N is chosen to produce at maximum 200 smeared events. This allows to populate all search intervals with the QCD background prediction while keeping the computation time practical.

8.1.2 Simulation samples

The simulation samples are used in rebalance and smear method to derive the low-$\not{H}_T$ prior used in rebalancing and the response templates used in both rebalancing and smearing. They are also used to validate the performance of the method. The simulated QCD events were generated with `madgraph` [167] and showered with `pythia8` [160]. The response of the detector is simulated using `Geant4` [92–94].

Table 8.1: Standard model QCD simulation samples used in the rebalance and smear method. All cross sections are calculated to LO. The value in the last column is calculated as $\mathcal{L} = N/\sigma$, where $\mathcal{L}$ is the value presented in the column, N is number of events in the simulated sample, and σ is the cross-section given in second column.

Dataset	σ (pb)	(fb^{-1})
QCD_HT200to300_TuneCUETP8M1_13TeV-madgraphMLM-pythia8	1717000	0.03
QCD_HT300to500_TuneCUETP8M1_13TeV-madgraphMLM-pythia8	351300	0.16
QCD_HT500to700_TuneCUETP8M1_13TeV-madgraphMLM-pythia8	31630	1.97
QCD_HT700to1000_TuneCUETP8M1_13TeV-madgraphMLM-pythia8	6802	6.68
QCD_HT1000to1500_TuneCUETP8M1_13TeV-madgraphMLM-pythia8	1206	12.54
QCD_HT1500to2000_TuneCUETP8M1_13TeV-madgraphMLM-pythia8	120.4	98.23
QCD_HT2000toInf_TuneCUETP8M1_13TeV-madgraphMLM-pythia8	25.42	239.26

8.1.3 Rebalancing

Jets in each of the events from the seed sample are modified to resemble a jet configuration that would be observed if they were measured exactly. In other words, jets are in a configuration that would be observed if the four-momenta of all particles in the event were known. This configuration is often called particle-level configuration. This step, the so-called rebalancing, is performed by maximizing the probability

$$P(\vec{p}_T^{\,rebalanced}|\vec{p}_T^{\,measured}) \tag{8.1}$$

of various configurations of particle-level jet four-momenta $\vec{p}_T^{\,rebalanced}$ given a set of measured jets with four-momenta $\vec{p}_T^{\,measured}$. The rebalancing is performed under kinematic constraints imposed by the responses of the jets and by requiring that the resulting $\not{H}_T$ of the rebalanced jets is either vanishing, or is limited by some particle-level $\not{H}_T$ prior. The momenta of all jets with $p_T \geq 15$ GeV are allowed to float according to the jet responses assigned to each jet based on its momentum p_T and pseudorapidity η, and the softer jets are left unmodified. For a general discussion of the jet transverse momentum response please refer to 6.1. Derivation of the response templates used in the RnS method is discussed in section 8.1.5.

The choice of the threshold below which the jets are not rebalanced is dictated by two effects. During the rebalance procedure, the momenta of the jets can migrate above or below the kinematic threshold $p_T \geq 30$ GeV. To allow migrations in both directions, we also rebalance softer jets. However, rebalancing softer jets increases the computation time of the procedure, so a threshold of 15 GeV has been applied to improve the performance time of the code.

The probability density for a particle-level jet configuration $\vec{p}_T^{\,rebalanced}$ given observed jet collection $\vec{p}_T^{\,measured}$ consists of two components: (1) the responses of the jets involved in the event and (2) low-$\not{H}_T$ prior that contains the information about the kinematics of the particle-level QCD event. It can be described as

$$P(\vec{p}_T^{\,rebalanced}|\vec{p}_T^{\,measured}) \sim \prod_{i=0}^{N_{jet}} \mathcal{R}(p_{T,i}^{measured}|p_{T,i}^{rebalanced}) \cdot \pi(\vec{p}_T), \tag{8.2}$$

where $\mathcal{R}(p_{T,i}^{measured}|p_{T,i}^{rebalanced})$ denotes the response of the jet i. The low-$\not{H}_T$ prior $\pi(\vec{p}_T)$ has two components, and is proportional to:

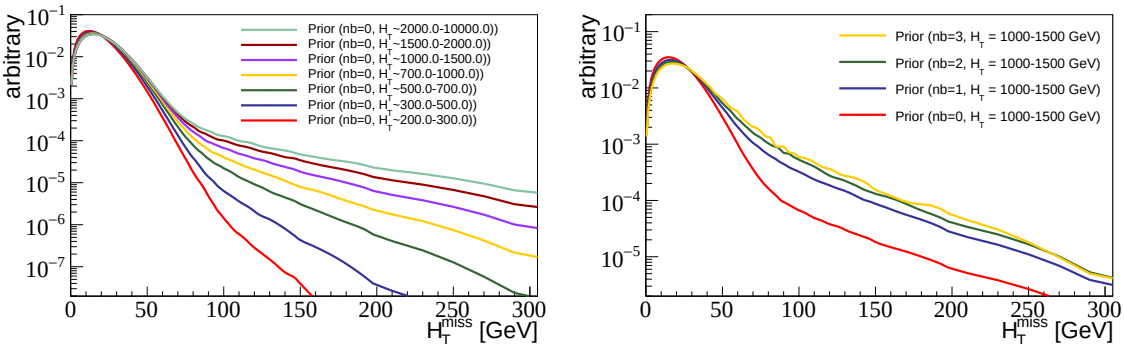

Figure 8.3: Probability distribution of the parton-level $\not{H}_T$ for $N_{b-\text{jet}} = 0$ and varying values of H_T (left); and for $H_T \in (1000 - 1500\text{GeV})$ and varying values of $N_{b-\text{jet}}$ (right).

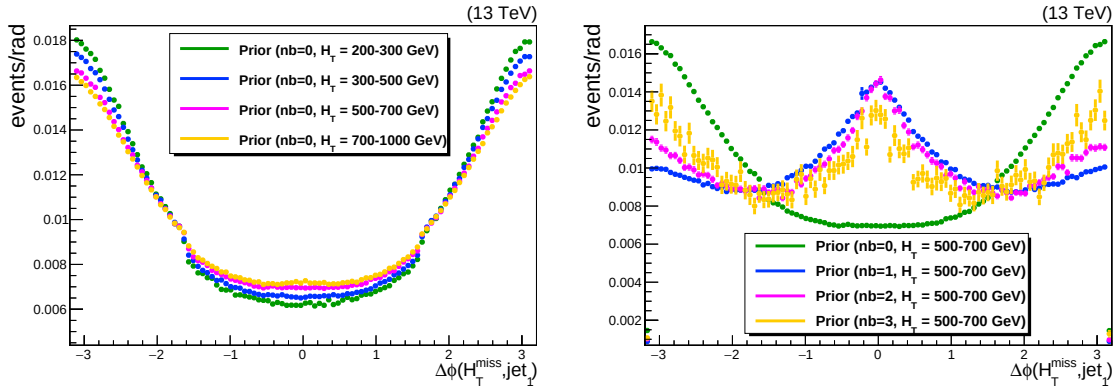

Figure 8.4: Probability distribution of the parton-level $\Delta\phi(\not{H}_T, jet_1)$ for $N_{b-\text{jet}} = 0$ and varying values of H_T (left); and for $H_T \in (500 - 700\text{GeV})$ and varying values of $N_{b-\text{jet}}$ (right).

$$\pi(\vec{p}_T) \sim P(\not{H}_T) \cdot P\big(\Delta\phi(\vec{\not{H}}_T, \vec{p}_T^{\,1^{\text{st}}\text{jet}})\big). \tag{8.3}$$

The first function, $P(\not{H}_T)$, is the probability density of the parton-level missing transverse momentum that is taken as a normalized $\not{H}_T$ distribution in simulation using generator-level jets. It is measured in intervals of b-tagged jet multiplicity, which compensates for genuine missing momentum arising from neutrinos, and in H_T, which accommodates for the missing momentum arising from the jets that fail the kinematic acceptance selection. Examples of $\not{H}_T$ priors for different H_T and N_{b-jet} values are presented in figure 8.3.

The second component of the prior, denoted as $P\big(\Delta\phi(\vec{\not{H}}_T, \vec{p}_T^{\,1^{\text{st}}\text{jet}})\big)$, is the probability distribution of the $\Delta\phi$ between the missing momentum and the leading b-tagged jet in case of $N_{bjet} > 0$ or the leading jet if $N_{bjet} = 0$. As already mentioned in section 7.2, the $\Delta\phi$ between the leading jets and $\vec{\not{H}}_T$ in QCD events is typically low, and this prior component allows for ensuring that the rebalanced jet collection resembles the particle level QCD event. Examples of $\Delta\phi$ priors for different H_T and N_{b-jet} values are presented in figure 8.4.

The rebalancing step has been significantly modified compared to the earlier implemen-

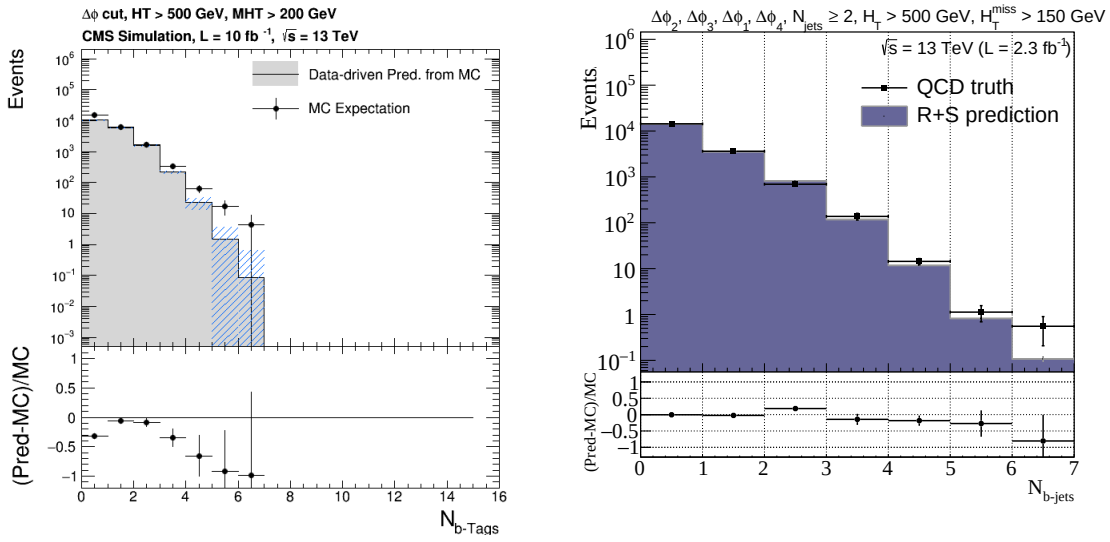

(a) Rebalancing to $\not{H}_T = \Sigma_{\text{soft jets}} p_T$

(b) Rebalancing using $\not{H}_T$ prior.

Figure 8.5: The validation of the prediction of the b-tagged jet multiplicity using simulation. The prediction (grey histogram) is compared directly with simulation (points, MC Expectation). On the left, the result for rebalancing to "soft" jets is shown; on the right, the events are rebalanced to the missing transverse momentum prior defined in equation 8.3.

tations of the rebalance and smear method [136, 152, 153]. Previously, the events were rebalanced to a fixed missing transverse momentum that was either vanishing $\not{H}_T = 0$ or was equal to the sum of momenta of all jets not passing the kinematic selection (the so-called soft jets that fail $p_T < 15$ GeV requirement). With the addition of a number of b-tagged jets as a search variable, this simple approach had to be modified, as it did not accurately predict the b-tagged jet multiplicity. This is due to genuine $\not{H}_T$ component originating from the neutrinos form the decays of B mesons. Previously, this genuine missing transverse momentum was accounted for by adding the neutrinos to the particle level jets used in the construction of the response templates. In current implementation of rebalance and smear, this problem was solved by including the missing transverse momentum prior, which allowed for better modeling of the particle-level QCD events and improved the prediction significantly. On the other hand, it happens that the rebalanced event has a high value of the missing transverse momentum. As this might be caused by substantial amount of genuine $\not{H}_T$, events with $\not{H}_T^{\text{rebalanced}} > 150$ GeV are rejected. First, early results of the modified approach were presented in [168] and the first complete prediction is the result discussed in this thesis. A comparison of the prediction of the number of b-jets for the modified and original rebalancing methods is presented in figure 8.5.

The rebalancing method can be validated with simulations by comparing kinematic distributions of rebalanced jets and generator-level jets (simulation samples listed in table 8.1). Such a comparison of N_{b-jets} and $\not{H}_T$ is presented in figure 8.6. For higher values of both N_{b-jets} and $\not{H}_T$ the distributions of rebalanced and generator-level jets do not agree. However, as it will be shown in figures 8.10 and 8.11, the discrepancies, which are relatively small considering the uncertainties, will be offset after the smearing.

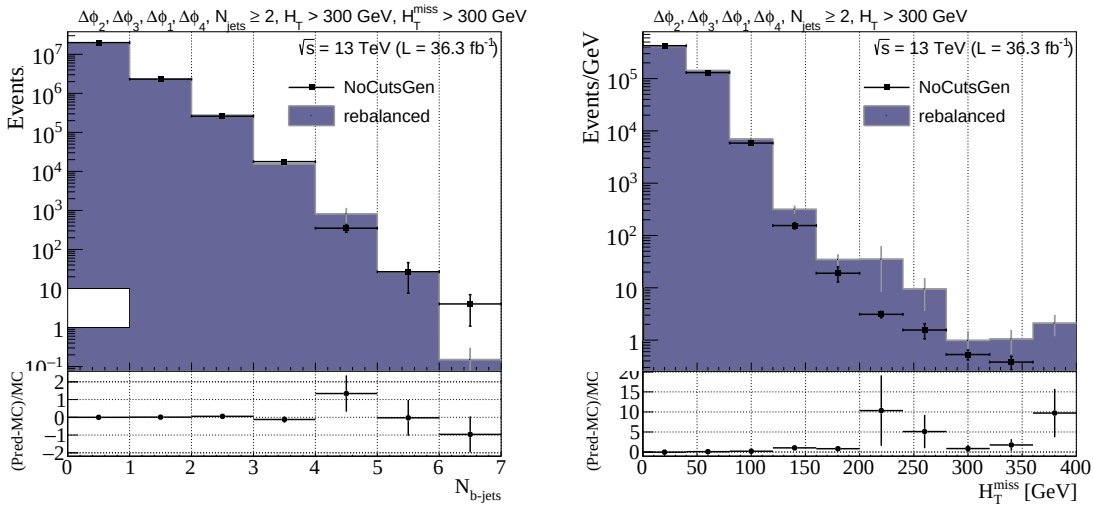

Figure 8.6: The distribution of the N_{b-jets} (left) and $\not{H}_T$ (right) for the rebalanced jets (histograms) and generator-level jets (points).

8.1.4 Smearing

The second step of the rebalance and smear procedure is smearing. The rebalanced jets are smeared according to jet response templates to create jet collections that resemble the kinematics of the QCD event. The smearing is done by modifying each rebalanced jet momentum by a factor obtained by randomly sampling the full jet response distribution corresponding to the transverse momentum and pseudorapidity intervals the rebalanced jet belongs to. To ensure populating all of the search bins, each rebalanced event was used to create up to 200 smeared detector-level events.

The validation of the smearing step is performed in a simulated QCD sample. The generator-level jets are smeared according to the response templates derived from the same sample. Opposite to the templates used in full RnS procedure performed on data, response distributions were not corrected for data to simulation differences. The kinematic distributions of obtained smeared jets are compared with the distributions obtained directly from the simulated sample. A validation of the smearing is presented for N_{bjet} and $\not{H}_T$ distributions in figure 8.7.

8.1.5 Response templates

The jet response is defined as the ratio of the reconstructed p_T and true p_T of a jet. This was discussed in more detail in section 6.1. The response templates, which are the histograms with jet p_T response distributions for a given range of p_T and η, used in the rebalance and smear estimation were obtained from simulation by taking a ratio of the momentum of the reconstructed jet and the corresponding particle-level jet. Response templates are corrected according to jet energy resolution data to simulation ratios, derivation of which has been presented in chapter 6. The templates are stored in fine intervals of p_T and $|\eta|$: the interval edges are listed in table 8.2. The intervals reflect on the dependence of the momentum resolution on the jet energy and on the geometry of the detector. Examples of jet responses for two ranges of p_T and $|\eta|$ are shown in figure 8.8.

The detector- and particle-level jets that are used in the construction of the templates are

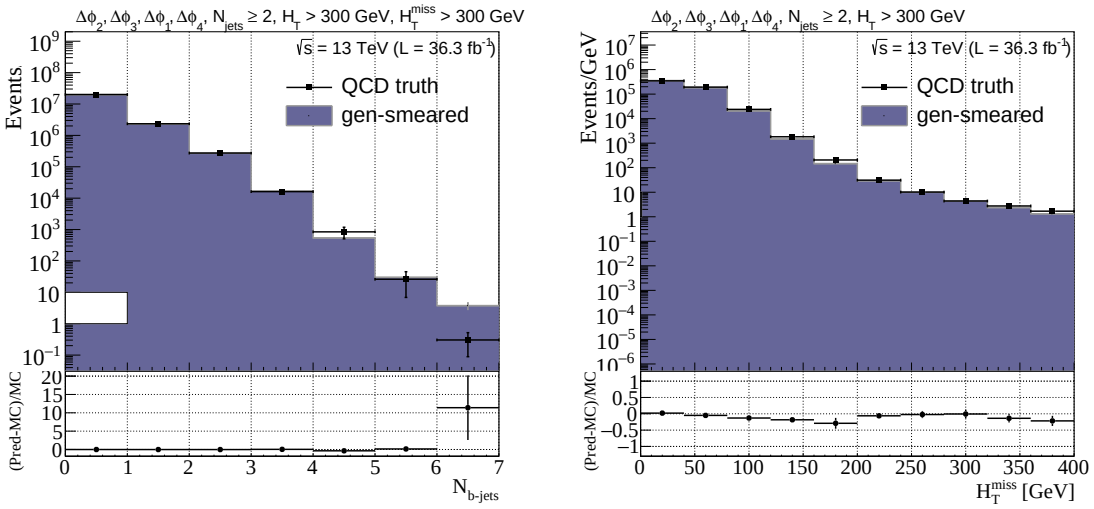

Figure 8.7: The distribution of the N_{b-jets} (left) and $\not{H}_T$ (right) for the smeared generator-level jets (histograms) and detector-level jets (points).

$\lvert\eta\rvert$	0.0, 0.3 ,0.5 ,0.8 ,1.1 ,1.4 ,1.7, 2.0, 2.3, 2.8, 3.2, 4.1, 5.0
p_T(GeV)	0,8,10,12,14,16,18,20,22,24,26,28,30,32,34,36,38,40,44, 48,52,56,60,66,72,78,84,90,100,110,120,130,140,150,160, 170,180,190,200,220,240,260,280,300,330,360,390,420,450, 500,550,600,650,700,750,800,900,1000,1100,1200,1300,1400, 1500,1600,1800,2000,2200,2500,3000,3500,4000,5000,6000

Table 8.2: Transverse momentum and pseudorapidity interval boundaries of the jet response templates.

required to be matched. The matching of the jets ensures that the matched particle- and detector-level jets originate from the same particle. The matching is done by requiring that the spatial distance between the matched jets is not higher than $\Delta R \leq 0.4$. Additionally, jets are required to be isolated to avoid a situation that one particle jet is reconstructed as two detector level jets, sometimes referred to as jet splitting, or the opposite, where two particle level jets are reconstructed as one detector level jet, referred to as jet merging. Isolation is achieved by requiring that at least 98% of the energy in a cone of size $\Delta R = 0.7$ around the jet originates from that jet. Jet splitting and merging would artificially enhance both low and high response tails, the origin of which was discussed in section 6.1. Enhancement of the response tails would increase the number of events predicted from the QCD background.

The jet response templates are derived from simulated QCD events generated with `madgraph` showered with `pythia8` and tuned with `TuneCUETP8M1`. The samples used are listed in table 8.1. As described in detail in chapter 6, the jet responses in simulation and in data differ. To accommodate for these differences, the data to simulation jet response ratios are applied to both the gaussian and non-gaussian part of the response templates. The components of the templates are presented in figure 8.9. The correction is applied as follows: the response distribution is fitted with a gaussian function, which is then subtracted from it. This component of the response distribution is referred to as *core*.

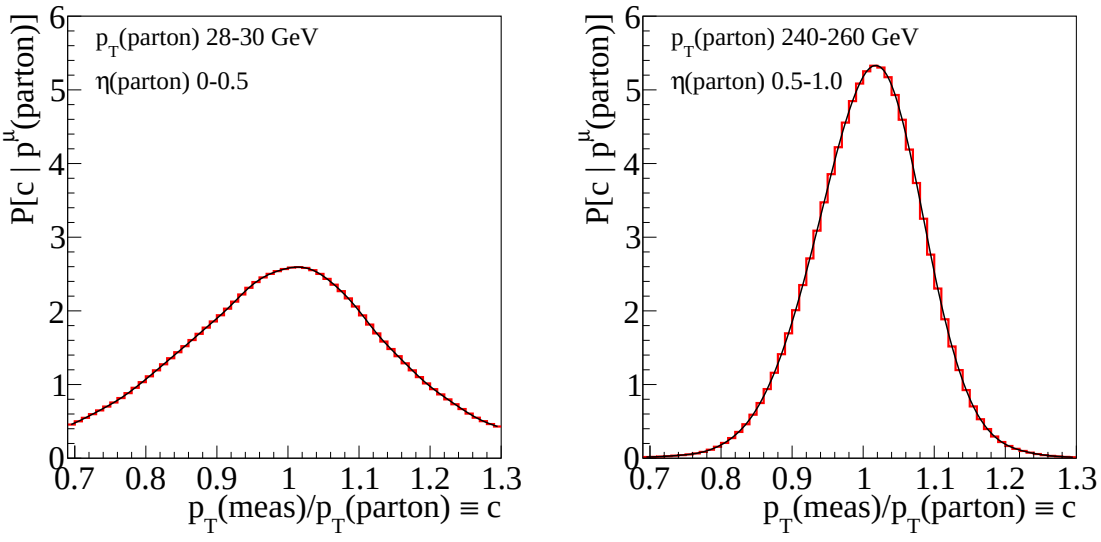

(a) (b)

Figure 8.8: Examples of jet energy response distributions (response templates) for two regions of p_T-$|\eta|$ phase-space. The distribution can be interpreted as unnormalized probability of measuring a jet with transverse momentum $c{\cdot}p_T(parton)$ given a detector-level jet with transverse momentum $p_T(parton)$.

The remaining non-gaussian contribution, referred to as *tails*, is then scaled with the tail scale factors, and the fitted gaussian is scaled with the jet energy resolution scale factors. Derivation of the tail and core scale factors has been presented in chapter 6. The sum of these two contributions constitute the response templates used in both rebalancing, where they are used in the probability density function 8.2, and smearing, where they are randomly sampled to get a correction to the p_T of the smeared jet. To make the response distributions smooth, they are fitted with spline functions, which are then used in the rebalancing and smearing. A spline is a class of piecewise functions defined by polynomials which are used to smooth the data points. Spline interpolation is necessary as the probability density defined in equation 8.2 has to be continuous. The templates used for validation of the rebalance and smear method on simulation are not corrected with the core and tail correction factors, so that the responses reflect the resolution of simulated jets.

8.1.6 Validation of the method

One of the advantages of the rebalance and smear method is that it can be extensively validated in both simulation and data, and that not only the event counts in search and control regions can be investigated, but also the full kinematics of the events can be compared. In figures 8.10, 8.11 and 8.12, the distributions of the prediction from rebalance and smear applied to simulation are compared with predictions taken directly from simulation. As can be seen from the histograms in figures 8.10 and 8.11, the rebalance and smear prediction of all search variables agrees well with prediction from direct simulation. The distributions of $\Delta\phi$ between missing transverse momentum and the two leading jets are presented in fig 8.12. For these distributions the agreement is also good, showing that rebalance and smear reproduces the characteristics of the QCD events.

The validation of the rebalance and smear method in data is performed in the low-$\not{H}_T$

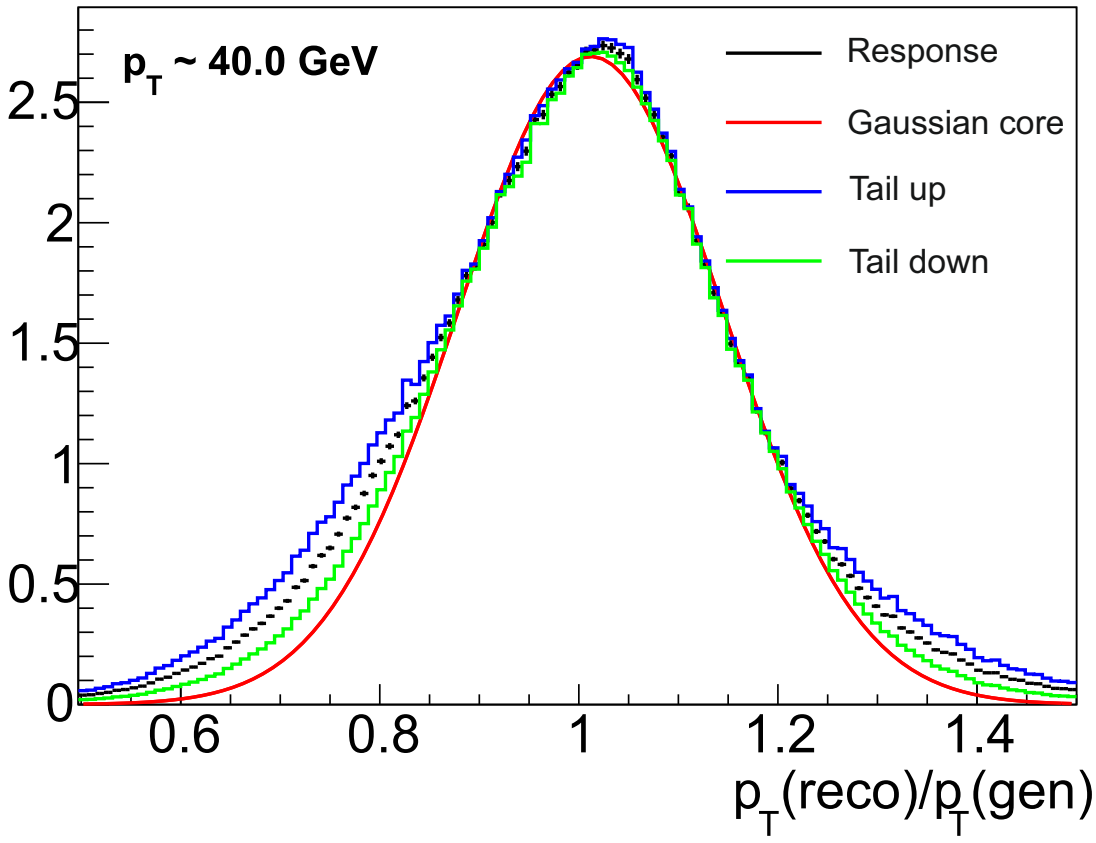

Figure 8.9: An example of the response template. The full response (black points), non-gaussian tails with tail scale factor uncertainty up and down(blue and green lines) and gaussian core (red line).

side band control regions, defined in figure 7.3 as boxes C1-C3, and the inverted $\Delta\phi$-cut region. Both of these regions are dominated by QCD events. The inverted $\Delta\phi$-cut region is defined as 174 control bins with the same search variable intervals and selection, with the exception that at least one of the $\Delta\phi$-cuts is not fulfilled. In all validation plots made for these two control regions, the QCD estimate is shown on top of the non-QCD backgrounds, calculated using the methods described in the previous chapter, and compared to the real data event counts.

The prediction of rebalance and smear in the QCD-enriched inverted $\Delta\phi$-cut low-$\not{H}_T$ high-H_T region (region C3 in 7.3) was observed to be lower than the inferred QCD count. Inferred QCD event counts are calculated by subtracting all non-QCD backgrounds from the observed data. A normalization correction factor of $N = 1.30$ has been applied based on the inferred QCD and rebalance and smear event counts in this region. It has been observed that varying the response tail scale factors by their uncertainties changes the prediction of the rebalance and smear by approximately 40%, values that are used as a systematic uncertainty. The comparison of the nominal prediction of the rebalance and smear and prediction obtained using templates with tail scale factors varied up by their uncertainties is presented in figure 8.13. As can be seen from the plots, both the prediction of number of jets and of missing transverse momentum above the baseline cut of $\not{H}_T > 300$

GeV are shifted by 40%. Because the normalization is smaller than this uncertainty, the change is covered by the uncertainty and no additional systematic uncertainty has been assessed. The comparison of the jet and b-tagged jet multiplicities in the normalized background prediction and data for the low-$\not\!\!H_T$ sideband regions are presented in figures 8.14 and 8.15, respectively. The prediction is consistent with the data.

The rebalance and smear prediction can be further validated by comparing the prediction with data in the search bins with an inverted $\Delta\phi$-cut, namely with requirement that $\mathbf{\Delta\Phi}(\not\!\!\mathbf{H_T}, \mathbf{jet_{1,2}}) < 0.5$ and $\mathbf{\Delta\Phi}(\not\!\!\mathbf{H_T}, \mathbf{jet_{3,4}}) < 0.3$. Such a comparison, with non-QCD backgrounds subtracted from data, is presented in figure 8.16. The event counts are projected to jet and b-tagged jet multiplicities which are presented in figures 8.17 and 8.18 respectively. The prediction seems to be consistent within the uncertainties with the data in nearly all cases. The highest b-tagged jet multiplicity bin seems to show some disagreement. This may be caused by a dependence of the b-tagging efficiency on the p_T of the jet. Further studies would be needed to verify this. The discrepancy in the higher b-jet multiplicity bins has been corrected for by applying the simulation-derived correction factor to $N_{b-jets} \geq 3$ bins. The correction factor is derived from the validation plot for b-tagged jet multiplicity presented in figure 8.11. A systematic uncertainty equal to this correction has been assigned in these bins.

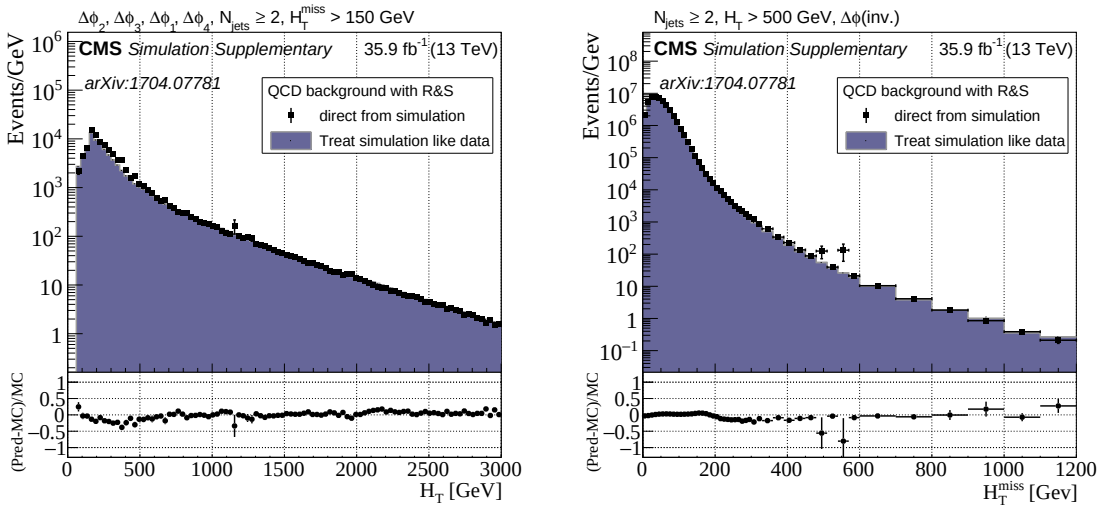

Figure 8.10: Comparisons of the distributions of H_T and $\not\!\!H_T$ between direct simulation (points) and the rebalance and smear method applied to simulation (histograms) in loosened baseline regions (applied cuts are listed above the histograms).

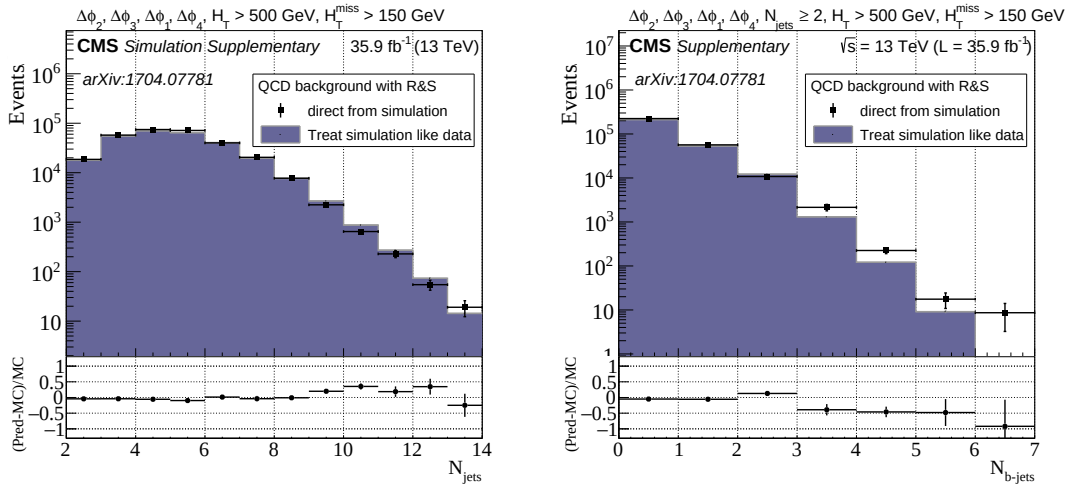

Figure 8.11: Comparison of the distributions of the multiplicities of jets (left) and b-tagged jets (right) between direct simulation prediction (points) and the rebalance and smear method applied to simulation (histograms) with the cuts listed above the histograms applied.

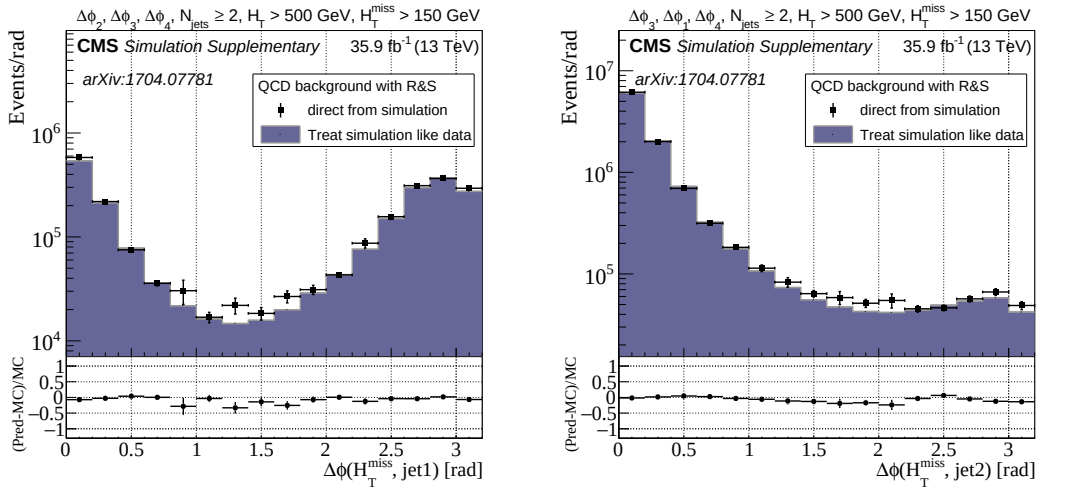

Figure 8.12: Comparison of the distributions of the $\Delta\phi$ angle between the $\not{H}_T$ and the leading jet (left) and sub-leading jet (right) between direct simulation prediction (points) and the rebalance and smear method applied to simulation (histogram).

8.2 The final prediction and systematic uncertainties

The QCD background prediction from the rebalance and smear method is obtained by applying a modified bootstrapping method to the output of the procedure. The bootstrapping is a method of measuring an estimator of a given property of a distribution by calculating the estimator in N randomly drawn subsamples of the considered distribution [169]. In the modified approach the full set of events obtained from rebalance and smear is divided into certain number of independent subsets N, which are then used to

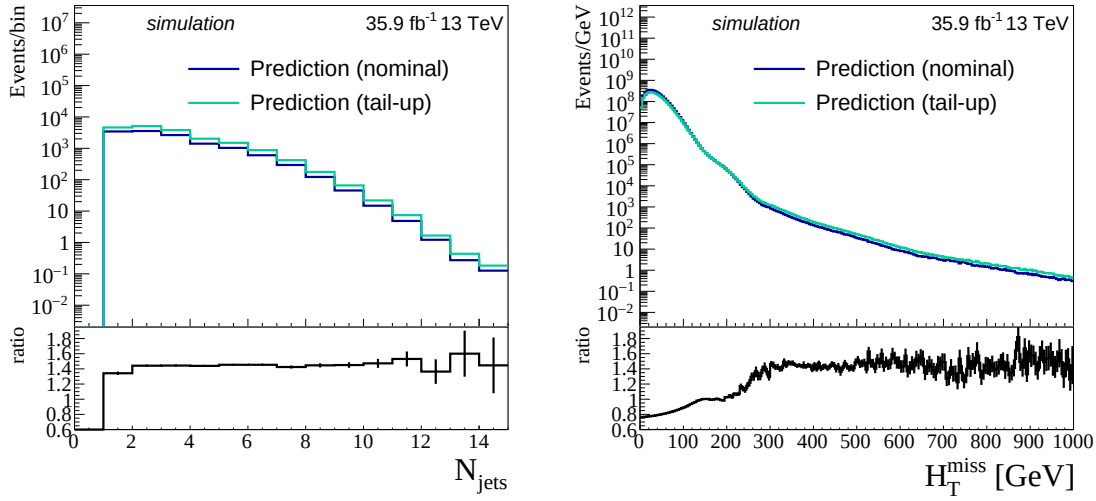

Figure 8.13: The distribution of N_{jet} (left) and $\not{H}_T$ (right) nominal (blue lines) and non-gaussian tail up (green line) prediction obtained using rebalance and smear method. In the bottom panel the ratio of the tail-up to nominal predictions is presented. The distributions were made using QCD simulated events listed in table 8.1.

make N independent predictions for each search bin. The mean values of these predictions are used as the central prediction, and the square root of variance is taken as statistical uncertainty. The number of subsets N has been chosen to be $N = 5$. Unless stated otherwise, the systematical uncertainties are calculated as difference between the prediction calculated using the rebalance and smear method and a prediction calculated using a method modified in a certain way

$$\sigma_i^{syst.} = N_i{}^{nominal} - N_i{}^{modified}, \tag{8.4}$$

where i stands for the search interval number. The sources of the systematic uncertainties are discussed below and the typical values are presented in table 8.3.

Core of the response functions As described in section 8.1.5, the jet response functions used in the procedure are corrected for the differences between the data and simulation using the jet transverse momentum resolution data to simulation ratios, the derivation of which has been presented in chapter 6. The resolution of the jet transverse momentum in data is 10-20% worse than in simulation in the barrel region and 20-80% worse for higher pseudorapidities (see figure 6.14). The uncertainties of these scale factors are propagated to the prediction uncertainty by calculating the QCD background prediction using rebalance and smear method with modified response templates. The templates were modified by correcting them with resolution scale factors plus/minus their uncertainty. The uncertainty is calculated as the mean of the uncertainties obtained from plus and minus modification of the templates. The response core uncertainty in most search intervals is in range of 15-30%.

Non-gaussian tails of the response functions Similar to the core scale factors, the simulation to data tail ratio uncertainties are propagated to the prediction. The response

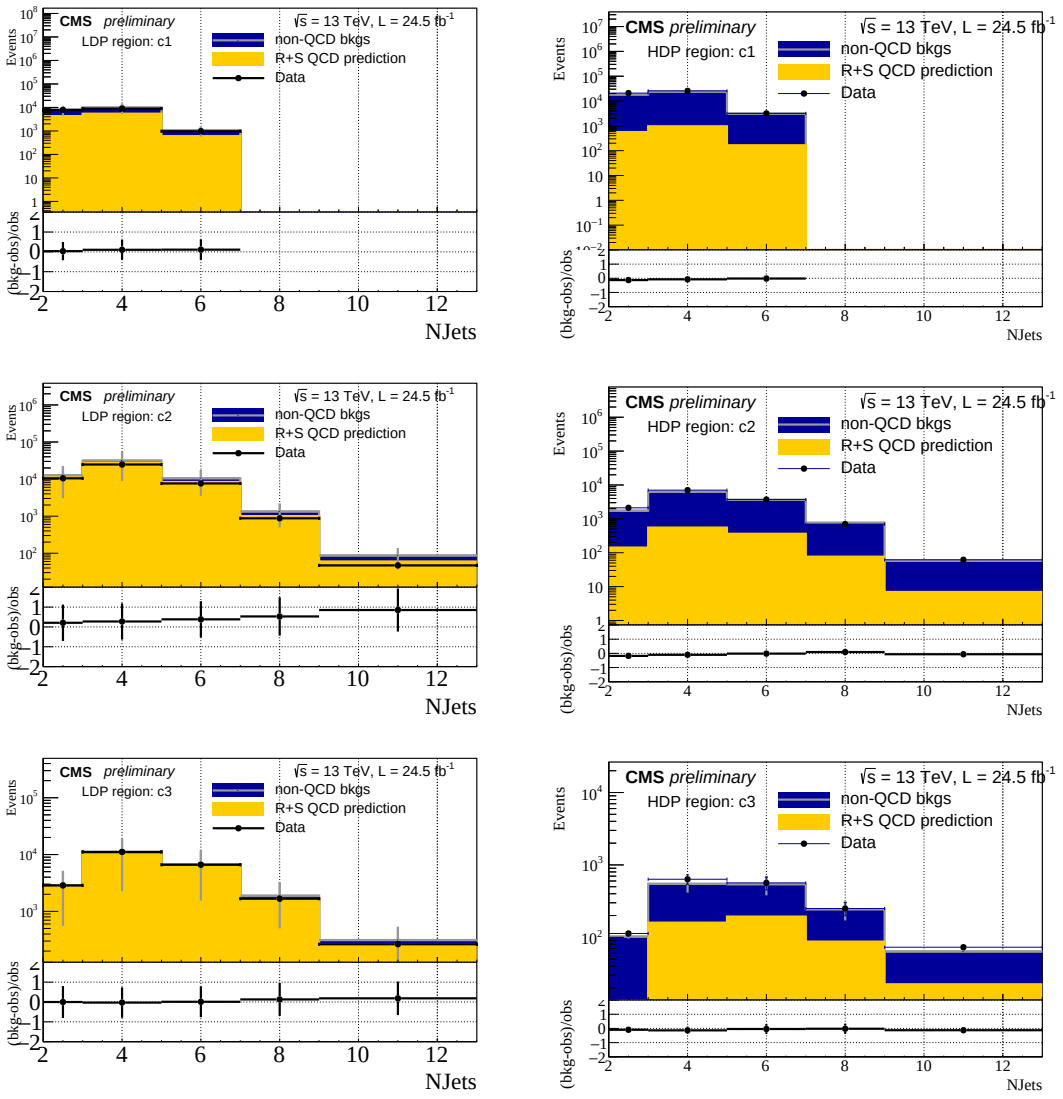

Figure 8.14: The validation in the low-$\not{H}_T$ regions C1-C3 (see figure 7.3) in both low- (left, LDP) and high- (right, HDP) $\Delta\phi$ regions. Non-QCD backgrounds have been estimated using methods presented in section 7.6.

tail uncertainty is around 30% in all search intervals.

Low $\not{H}_T$ prior The rebalancing depends on sufficiently accurate modeling of the particle-level $\not{H}_T$ in simulation. To assess an uncertainty to cover this mismodeling, the low-$\not{H}_T$ prior distribution is reweighted using the ratio of the reconstructed-level $\not{H}_T$ distributions in a QCD-enriched kinematic region in data and in simulation. The prediction is re-derived using the modified prior. The prior uncertainty has a small impact and is typically around 5%.

Trigger efficiencies The signal trigger efficiencies, calculated using the method described in section 8.1.1, are applied to the rebalance and smear prediction. The uncertainties of these efficiencies are propagated to the prediction. Trigger uncertainty is around 2-3%.

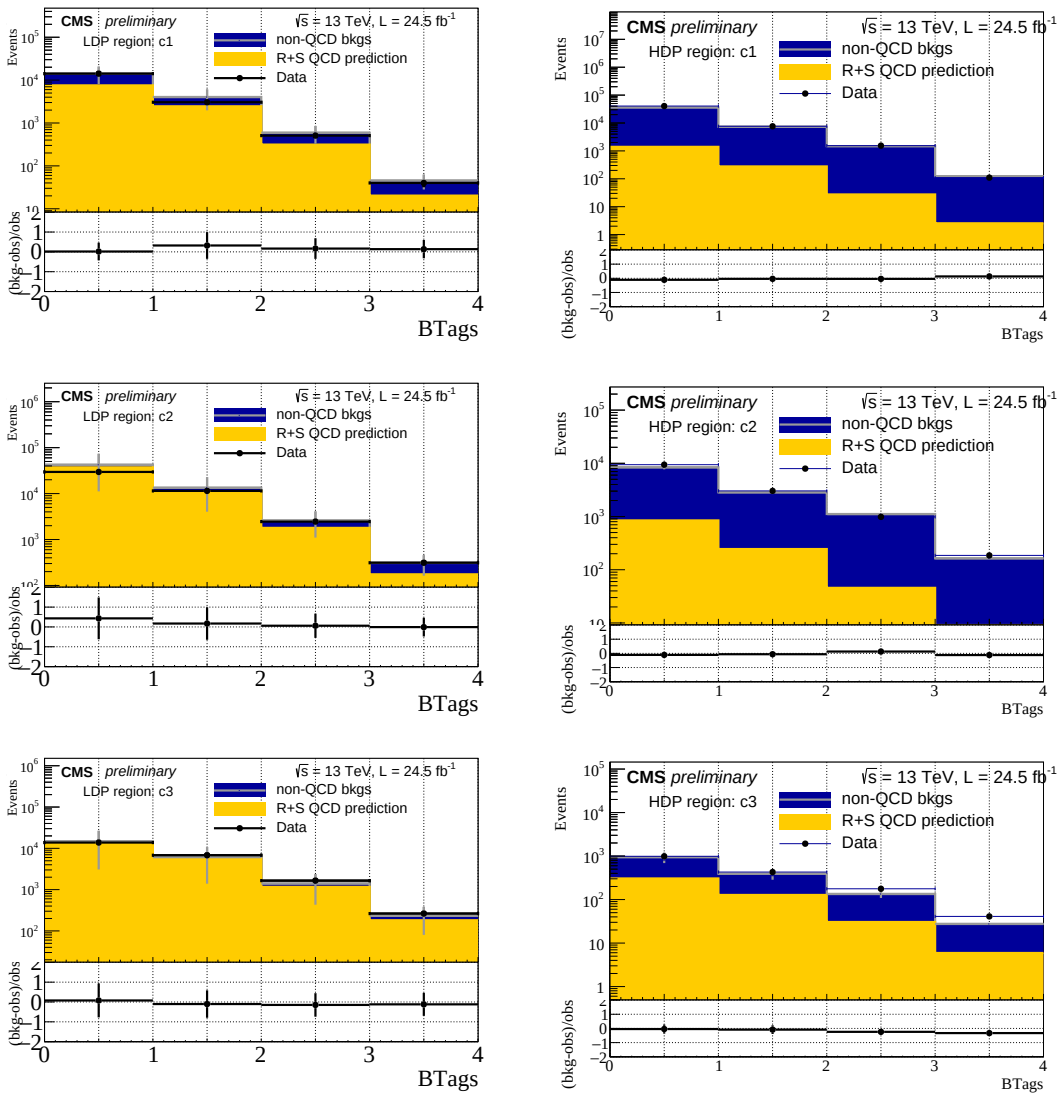

Figure 8.15: The validation of the rebalance and smear method in the low-$\not\!\!H_T$ regions C1-C3 (see figure 7.3) in both low- (left, LDP) and high- (right, HDP) $\Delta\phi$ regions. Non-QCD backgrounds have been estimated using methods presented in section 7.6.

Closure As described in section 8.1.6, the prediction for the bins with highest b-tagged jet multiplicities were systematically lower than the expected counts in the inverted $\Delta\phi$ control region. To account for that difference, the predicted counts in these bins were scaled by a simulation-derived correction factor to match the inferred QCD counts. A 100% non-closure uncertainty was assigned in these bins.

B-tagging The b-tagging efficiency uncertainties that are centrally provided within the CMS collaboration, are propagated to the prediction in a similar fashion to the uncertainties of the jet resolution scale factors. These uncertainties are usually around 20%.

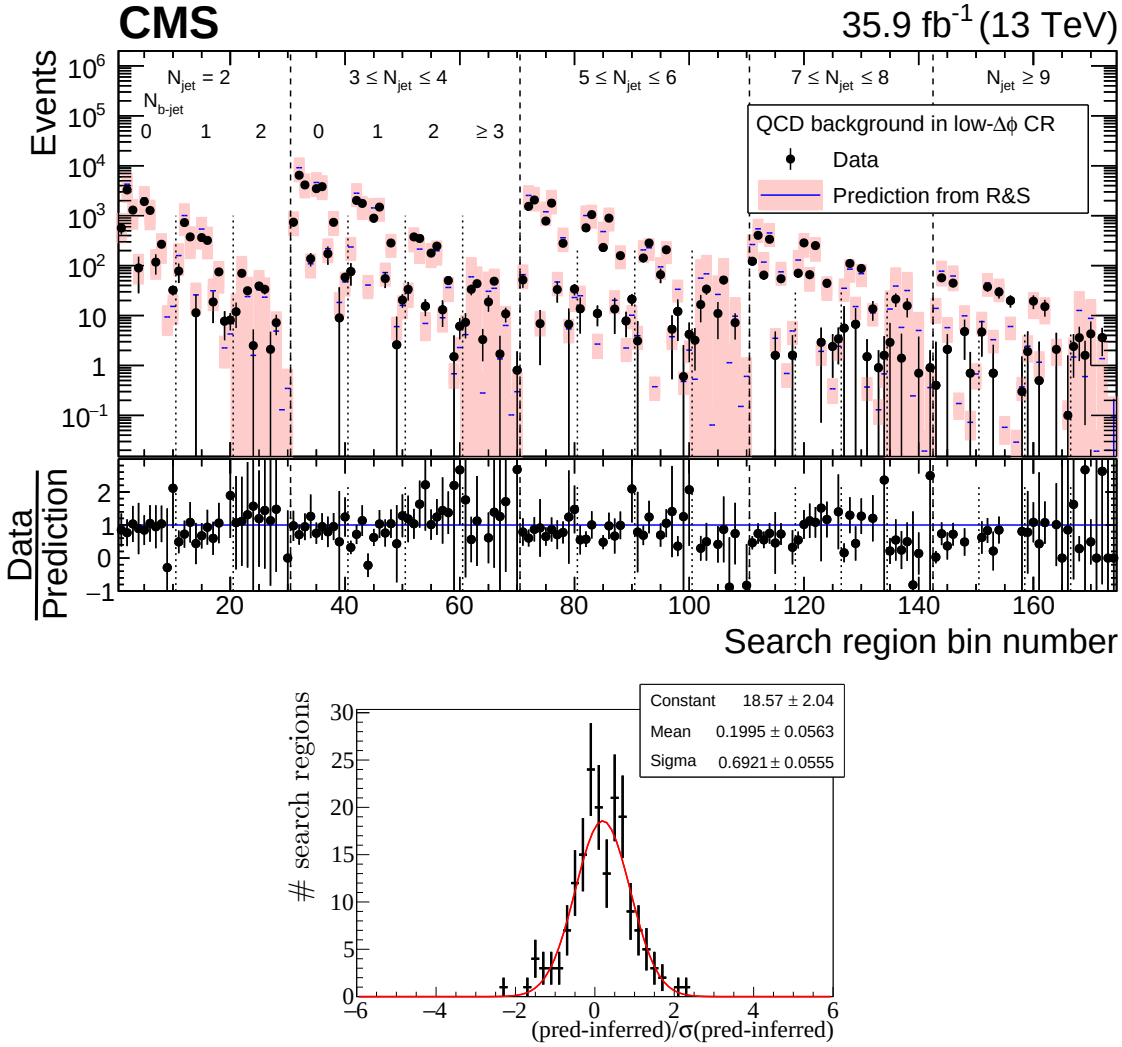

Figure 8.16: Comparison between the rebalance and smear QCD prediction (histogram) and the inferred QCD count (points) in the 174 search intervals in the inverted $\Delta\phi$ control region (top). The inferred QCD count is calculated by subtracting non-QCD background predictions, described in chapter 7, from the observed data event count. The QCD prediction uncertainties include systematic and statistical errors, uncertainties in the data are statistical. The distribution of the uncertainty-normalized difference between predicted and observed QCD event counts (bottom).

Contamination To estimate how likely events with genuine $\not{H}_T$ are to be rebalanced and smeared back to high values of $\not{H}_T$, the RnS procedure has been performed on simulated samples used for the calculations of the other, non-QCD backgrounds. Since the predictions in each of the search intervals obtained from that procedure were tiny, it was decide to use them as the contamination systematic uncertainty.

The final prediction of the rebalance and smear method in 174 search bins is presented in figure 8.21, in which it is compared with an alternative method of calculating background from QCD events called $\Delta\phi$ extrapolation. This alternative method is discussed below in section 8.3.1. The numerical values of the rebalance and smear estimates along with

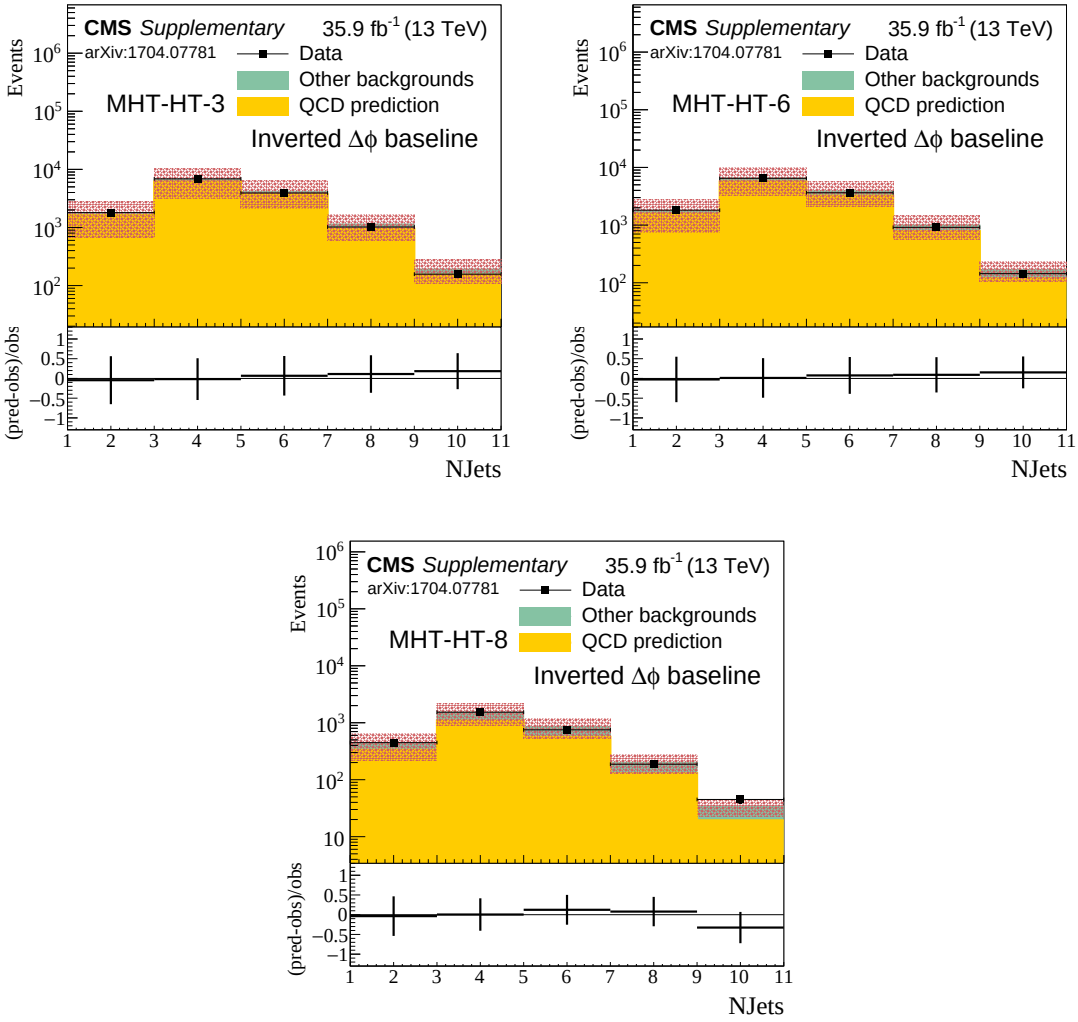

Figure 8.17: Comparison of the jet multiplicity between the rebalance and smear QCD prediction summed with non-QCD backgrounds and observed data in the inverted $\Delta\phi$ control region. The inferred count is defined as the observed count minus the counts for the other backgrounds estimated by the other methods described in section 7. The uncertainties in the QCD prediction are statistical and systematic, and uncertainties in the other background predictions are statistical.

all uncertainties are listed in tables B.1-B.3. Discussion of the prediction is presented in section 8.3.2.

8.3 Results comparison

The estimation of the QCD background for the analysis introduced in chapter 7 has been performed using two independent methods: the rebalance and smear procedure described extensively in this chapter, and the so-called $\Delta\phi$ extrapolation method. In this section the latter will be briefly discussed, and the results of the two estimations will be compared.

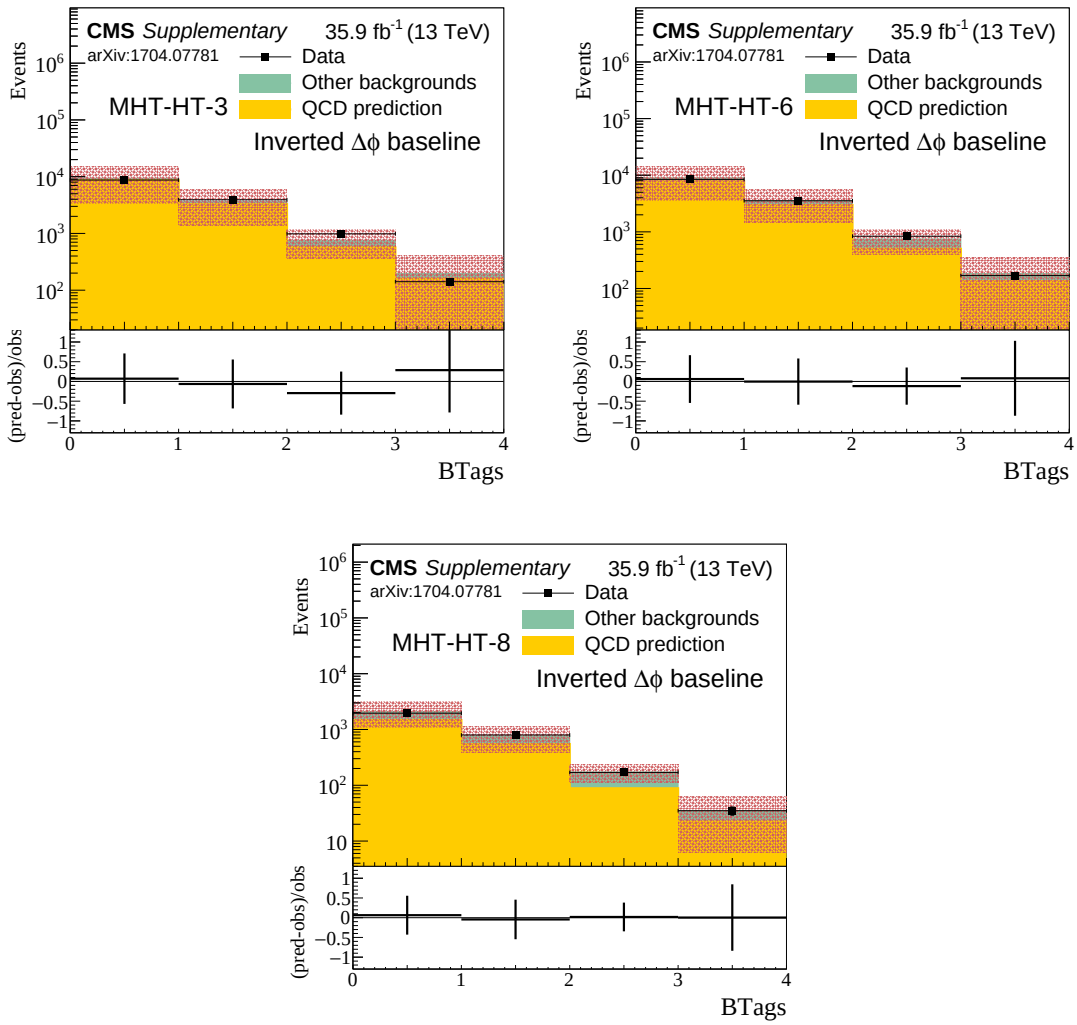

Figure 8.18: Comparison of the b-tagged jet multiplicity between the rebalance and smear QCD prediction summed with non-QCD backgrounds and observed data in the inverted $\Delta\phi$ control region. The inferred count is defined as the observed count minus the counts for the other backgrounds estimated by the other methods described herein. The uncertainties in the QCD prediction are statistical and systematic, and uncertainties in the other background predictions are statistical.

8.3.1 $\Delta\phi$ extrapolation method

Another method of estimating QCD background of the supersymmetry analysis discussed in this thesis is a version of the so-called "ABCD" method. The sketch in figure 8.19 helps to understand the principle behind the procedure. The method uses the low-$\Delta\phi$ control region, meaning a region with an inverted baseline $\Delta\phi$ cut, as a QCD-enriched control sample, and a transfer factor R^{QCD} which allows to predict the number of QCD events in the search region based on the event count in control region. The method is defined in 2 dimensions: in this case these are $\not{H}_T$ and low/high-$\Delta\phi$ (see figure 8.19). It is assumed that the $\not{H}_T$ dependence can be factorized from the low/high-$\Delta\phi$ QCD ratio and that the

Uncertainty	typical values	comments
Response core	15-30%	Higher values up to ≈40% for low N_{jet}, otherwise typically 15-20%
Non-gaussian tails	≈30%	Almost constant across the search intervals
Low $\not{H}_T$ prior	4-5%	
Trigger efficiencies	2-3%	
Closure	100%	Only in $N_{bjets} > 3$ search intervals
B-tagging	≈20%	
Contamination	0.1-1%	For high N_{jet} and N_{bjet} values around 10-20%

Table 8.3: Typical values of the systematic uncertainties.

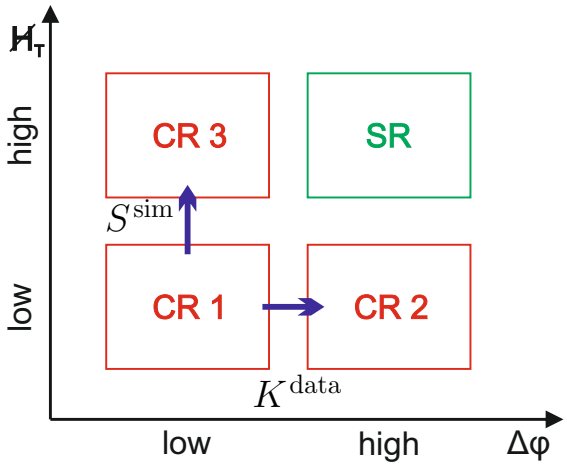

Figure 8.19: Sketch of the $\Delta\phi$-extrapolation method, which is a version of the "ABCD". The method, in general, uses three control regions (CR1-CR3) to calculate the transfer factors, in this case these factors are S^{sim} and K^{data}. Using the transfer factors it is possible to predict the number of expected events in the signal region by multiplying the observed event count in region CR1 and scaling it using both S^{sim}_{ik} and K^{data}_{ij}.

ratio does not depend on the b-tagged jet multiplicity N_{b-jet}. The following equation is used for the transfer factor:

$$R^{QCD}_{ijk} = K^{\text{data}}_{ij} \cdot S^{\text{sim}}_{ik}, \tag{8.5}$$

where i, j, and k are the H_T, N_{jet} and $\not{H}_T$ bin indices, and K^{data}_{ij} and S^{sim}_{ik} are transfer factors from low-$\Delta\phi$ control region to search region. The K^{data}_{ij} parameter is the transfer factor for H_T bin i and N_{jet} bin j, and is derived from data in the low-$\not{H}_T$ sideband region (regions C1-C3 in figure 7.3). To derive it, the QCD contribution in the low-$\not{H}_T$ sideband is estimated in both low- and high- $\Delta\phi$ regions by subtracting the non-QCD backgrounds, calculated using methods presented in chapter 7, from the data. A maximum likelihood fit of the low- and high-$\Delta\phi$ bins is performed in the low-$\not{H}_T$ control region. The fit accounts for the correlated uncertainties of the non-QCD backgrounds in the bins. The S^{sim}_{ik} parameter corrects for the $\not{H}_T$ dependence of the R^{QCD}. It is a transfer factor from the low-$\not{H}_T$ control regions to the high-$\not{H}_T$ search regions and is derived from simulation.

The QCD background in each of the 174 search bins is estimated by applying the R^{QCD} factor to the corresponding control bins, which are defined with the same N_{jet}, N_{b-jet}, H_T and $\not{H}_T$ intervals but have the inverted $\Delta\phi$ cut applied. The validation of the method on

a simulated sample is presented in figure 8.20. The method describes the QCD simulation adequately. To address the limited statistics of the simulated sample used for the derivation of the transfer factors, as well as to cover possible non-closure of the method, a systematic uncertainty on R^{QCD} was applied. This uncertainty is equal to the difference between the direct simulation value and the prediction.

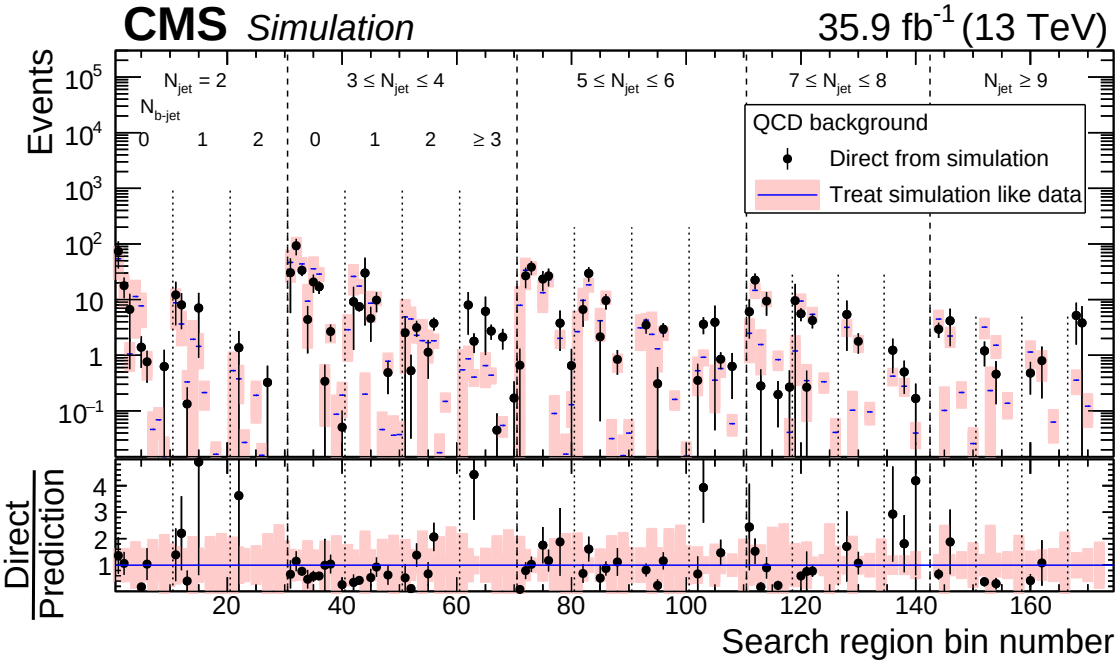

Figure 8.20: Comparison of the prediction of the $\Delta\phi$ extrapolation method applied to simulation (histogram) with the prediction take directly from simulation (points with error bars). The non-closure systematic is not included in the uncertainty of $\Delta\phi$ prediction, because it is applied as the difference between the points and histogram in this plot. The intervals numbers are explained in tables C.1-C.5. Plot taken from [52].

8.3.2 Discussion of QCD background evaluation results

The two QCD background estimation methods described above are independent. The comparison of the full predictions, presented in figure 8.21, and the distributions of the search variables after baseline selection, presented in figures 8.22 and 8.23, show a good agreement between the two methods. This is a good validation of the predictions of a background which is known to be difficult to model. Rebalance and smear has been chosen as the primary method for the estimation of the QCD background in [52]. The first reason is that this method can be extensively validated in the low-$\Delta\phi$ region (see figures 8.14-8.18), while the $\Delta\phi$-extrapolation method relies on this region to normalize the prediction in the search bins. The second reason is that RnS is a first-principle approach because it predicts the fake-$\not{H}_T$ basing on a jet resolution model. The $\Delta\phi$-extrapolation relies on transfer factors derived partially from simulation. Since QCD is not a dominant background in the presented analysis, a combination of the two results would not improve the final physical interpretation of the results.

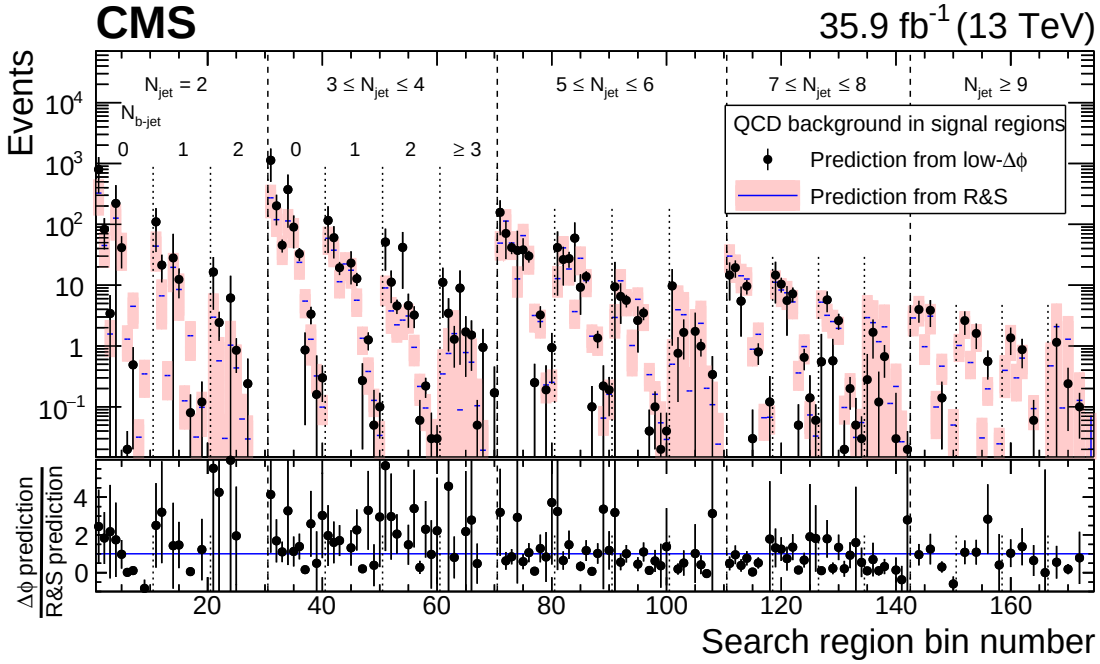

Figure 8.21: Comparison of the $\Delta\phi$ extrapolation and rebalance and smear predictions in the 174 search bins. For both methods full uncertainties are displayed. The interval numbers are explained in tables C.1-C.5. Plot taken from [52].

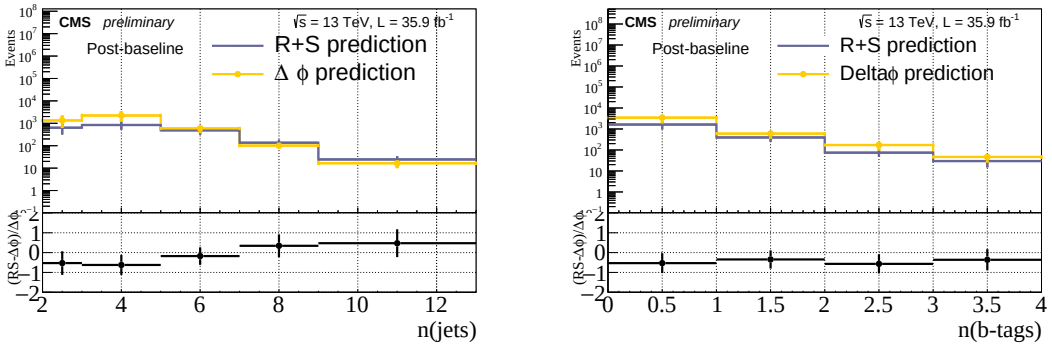

Figure 8.22: Comparison of the predictions of jet (left) and b-jet (right) multiplicities after baseline selection obtained from rebalance and smear (blue lines) and $\Delta\phi$-extrapolation (yellow line). For both methods full uncertainties are displayed.

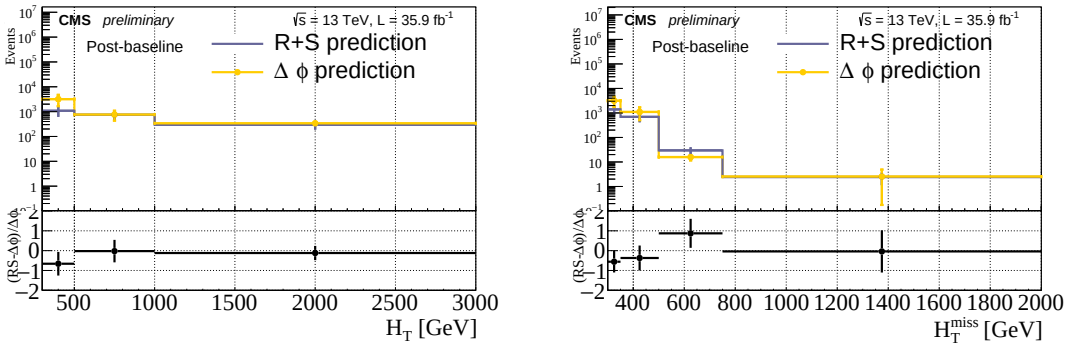

Figure 8.23: Comparison of the predictions of H_T (left) and $\not{H}_T$ (right) after baseline selection obtained from rebalance and smear (blue lines) and $\Delta\phi$-extrapolation (yellow line). For both methods full uncertainties are displayed. The prediction of the $\Delta\phi$-extrapolation depends on the predictions of other backgrounds. In case of the first H_T bin in the left plot it is suspected that the under-prediction of the $Z \to \nu\nu$ background is responsible for the upward fluctuation of the $\Delta\phi$-extrapolation prediction.

9 Results of the supersymmetry search

The observed numbers of events in the 174 search intervals of the supersymmetry search [52] discussed in chapters 7 and 8 are presented in figure 9.1 and the numerical values are listed in tables C.1-C.5 in which also the interval numeration scheme is described. There is a 3.5 standard deviation difference between the observed signal and standard model backgrounds in search region 126 and differences between 2 and 3 standard deviations in signal regions 74, 114 and 151. In all remaining 170 signal regions the background prediction agrees with the observed signal with differences below 2 standard deviations. This is consistent with normal distribution, therefore the prediction of the standard model backgrounds is compatible with the observed data and no evidence for supersymmetry has been observed.

The SM backgrounds have been evaluated in the so-called *aggregate search bins* as well, these are defined in table 7.2. Those search intervals are designed to represent 12 signal topologies and to facilitate interpretation of search results. The observed numbers of

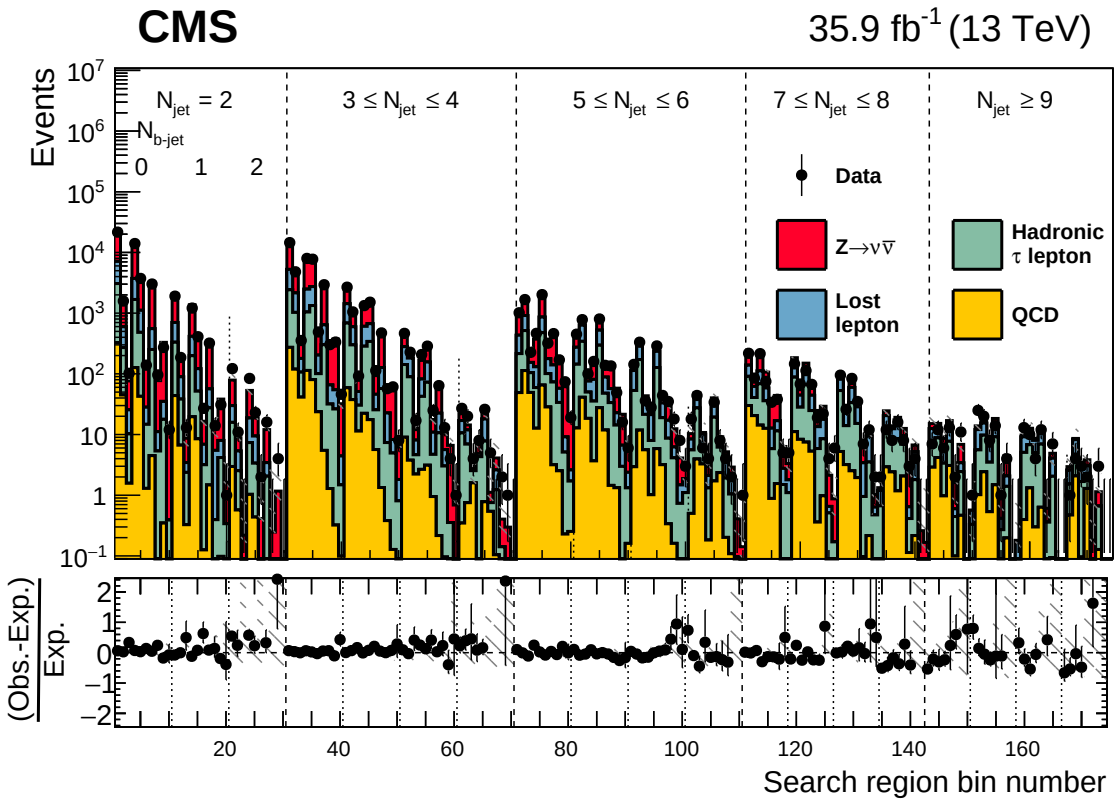

Figure 9.1: The predictions of the standard model backgrounds and the observed number of events in the 174 search regions of the supersymmetry search [52]. The lower plot shows the fractional difference between the data and background predictions. The bin numbers are explained in tables C.1-C.5. Plot taken from [52].

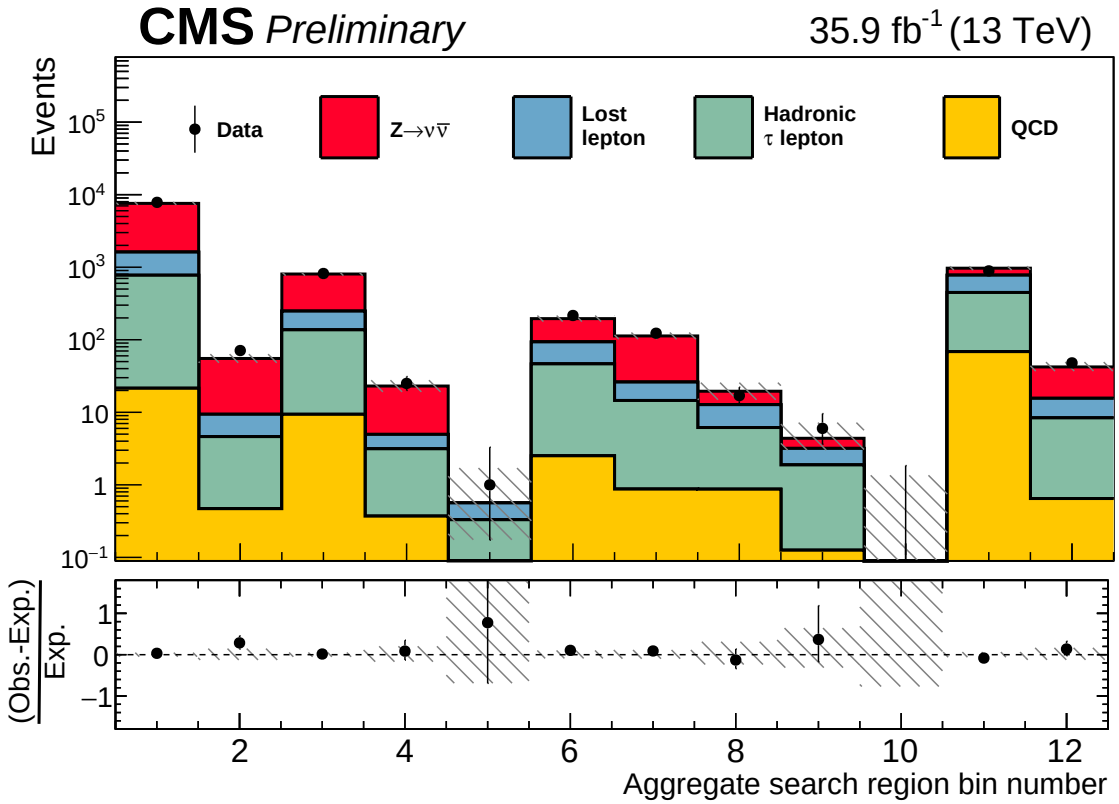

Figure 9.2: The predictions of the standard model backgrounds and the observed number of events in the aggregate search regions. The lower plot shows the fractional difference between the data and background predictions. The interval numbers are explained in table 7.2. Plot taken from [52].

events in the aggregate search intervals are presented in figure 9.2, and the numerical values are listed in table C.6. The limits on the masses of SUSY particles derived from the aggregate search bins do not deviate significantly from the calculations based on the full 174 search regions, as will be discussed in next paragraph. However, they are simpler to use for reinterpretations and investigations of scenarios which were not considered within this analysis.

To calculate the limits on the production cross section for specific SUSY signal scenario, a likelihood fit is used. The limits for the gluino (squark) pair production are calculated as a function of gluino (squark) mass and neutralino mass. For each choice of SUSY particle masses, all 174 search regions are used in the fitting procedure. The fitted function is a product of Poisson probability density functions, one for each search bin, and it is constrained by the uncertainties of the background estimates. The test statistic used is $q_\mu = -2ln(\mathcal{L}_\mu/\mathcal{L}_{max})$, where $\mathcal{L}_\mu$ is the likelihood obtained for a fixed SUSY signal strength and $\mathcal{L}_{max}$ is the maximum likelihood obtained when all parameters of the fit were allowed to vary. In the derivation of the limits, the asymptotic results of the test statistics [170] are used, in conjunction with the CL_s criterion described in references [171, 172].

The 95% confidence level (CL) signal cross section upper limits were sampled using these methods. Exclusion curves were derived using next-to-leading order (NLO) and next-to-leading-logarithm (NLL) signal cross sections [173–177]. In the procedure, the possible contamination of the control regions by signal events is taken into account.

The results of the upper limit calculations for the gluino production for T1tttt, T1bbbb, T1qqqq, T5qqqqVV, T1tbtb, and mixed gluino decay simplified models are presented in figure 9.4. For the first four models listed, the simplified model points with the gluino masses below 1960, 1950, 1825 and 1800 GeV were excluded, depending on the value of $m_{\tilde{\chi}_1^0}$. For the T1tbtb simplified model, points with gluino masses below 1850 to 1880 GeV have been excluded. Note that for this model the acceptance is small for $m_{\tilde{\chi}_1^0} < 25$ GeV. The reason for that is that for very light neutralinos, parent particle, the chargino $\tilde{\chi}_1^{\pm}$ (see figure 7.1b), becomes very light and thus heavily Lorentz boosted. In this case most of the chargino momentum would be transferred to the W boson, which makes the $\not{H}_T$ spectrum softer. Because of that, the search is not sensitive to models with neutralino masses below 25 GeV, for which the charginos $\tilde{\chi}_1^{\pm}$ and neutralino $\tilde{\chi}_1^0$ are nearly mass degenerate.

The upper limits on the squark production cross sections for T2tt, T2bb and T2qq simplified models are presented in figure 9.3. Using the NLO+NLL cross sections [173–177], simplified model points with squark masses below 960, 990 and 1390 GeV, have been excluded, respectively. For the T2tt model, points with small neutralino masses $m_{\tilde{\chi}_1^0}$ and with a mass splitting approximately equal to the mass of the top quark $m_{\tilde{\chi}_1^0}$-$m_{\tilde{g}} \approx m_{top}$, are not included in the calculation. These points correspond to the unshaded region on the diagonal of the plot. The reason is that signal with masses in that region is practically undistinguishable from standard model backgrounds and control regions become dominated by signal.

The same simplified models were targeted by several supersymmetry searches performed within CMS which were based on different final states or used different techniques. The limit plots of these searches are presented in figures 9.5 and 9.6 for the gluino and squark pair production respectively. The limits which were presented in the supersymmetry search discussed in this thesis are denoted on the plots as SUS-16-033. They are compared with other fully hadronic searches denoted as SUS-16-036 [178], SUS-16-032 [179] and SUS-16-049 [180], and with six searches with leptons in the final states: SUS-17-001 [181], SUS-16-037 [182], SUS-16-042 [183], SUS-16-035 [184], SUS-16-041 [185] and SUS-16-051 [186].

In the case of T1qqqq models (figure 9.5), the expected sensitivity of SUS-16-033 is comparable to SUS-16-036. This is because in T1qqqq, at least 4 jets are expected in the final state, and both analyses are sensitive to such scenarios. However, in the case of T1bbbb, at least 8 jets are expected in the final state. In this high multiplicity regime the analysis presented in this thesis is better suited, as it has dedicated search intervals with 7-8 jets and at least 9 jets. For the SUS-16-036 search the highest N_{jets} intervals are $4 \leq N_{jets} \leq 6$ and $N_{jets} \geq 7$, which makes it less sensitive to scenarios with many jets. This is even more visible in the case of T1tttt, in which there are four top quarks in the final state. Considering only fully hadronic events, this corresponds to at least 12 jets. The expected limit of the T1tttt model, in case of light neutralinos, of the search presented in this thesis is around 100 GeV higher than any other search. The advantage over the searches with leptons comes from the fact that the backgrounds with leptons are more difficult to model. Additionally, for the searches with at lest 2 leptons in the final state, the branching ratio of t decaying into leptons plays a significant role, as it is only around 10%.

The limits set by SUS-16-033 on the masses of squarks for the discussed models are competitive compared with other searches which targeted same simplified models. The expected limits presented in figure 9.6 for the T2bb model are very similar for all three searches. For the T2tt, the result presented in this thesis can be directly compared to SUS-16-036, which is also an inclusive, fully hadronic SUSY search. As can be seen from figure

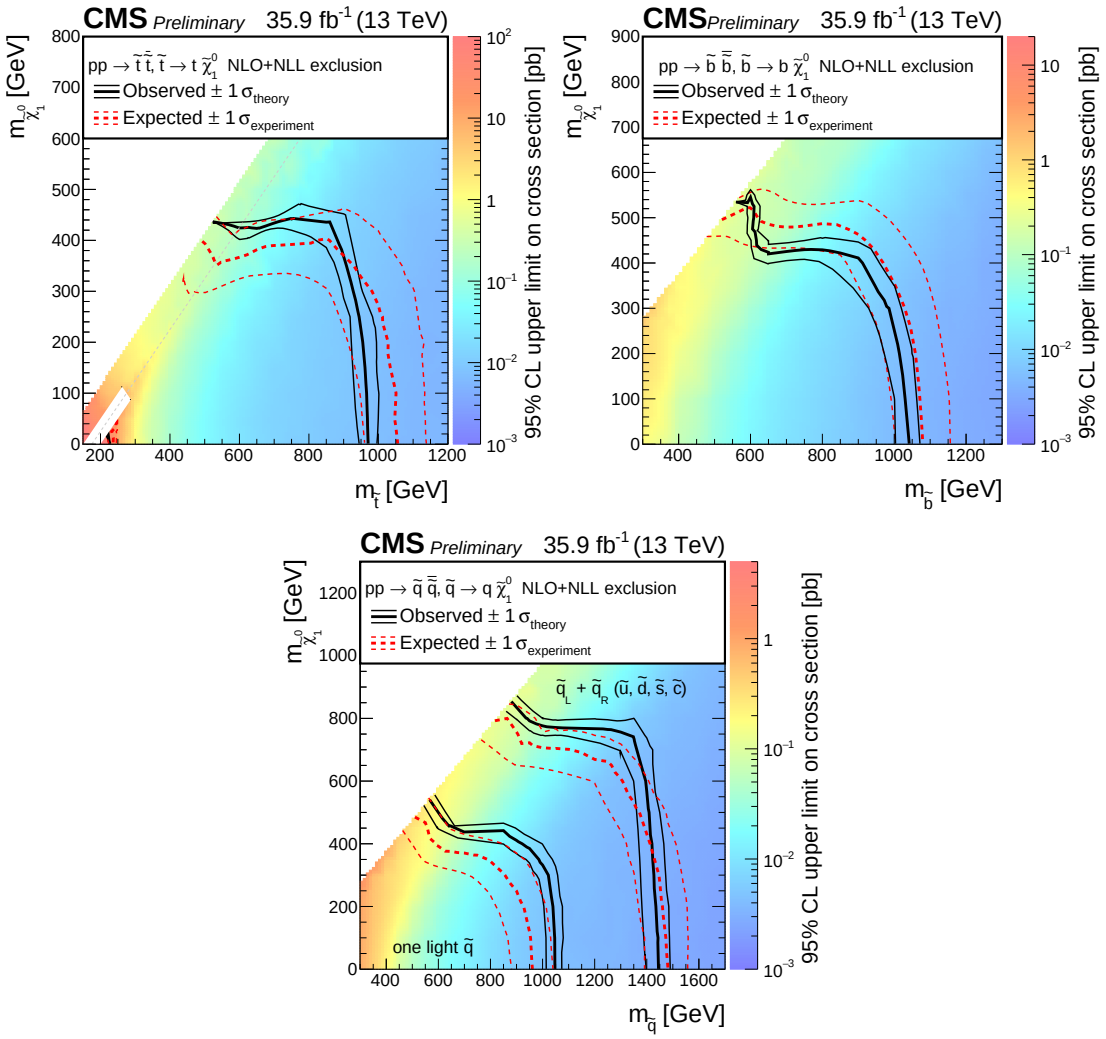

Figure 9.3: The observed 95% CL upper limits on the production cross sections for the T2tt (upper left), T2bb (upper right) and T2qq (lower) simplified models as a function of the squark and LSP masses $m_{\tilde{g}}$ and $m_{\tilde{\chi}_1^0}$. The solid black curves show the observed exclusion limits assuming 100% branching ratios and NLO+NLL cross sections [173–177] and their uncertainties. The thick dashed (red) curves represent the expected limits with uncertainties under the background-only hypothesis. Plot taken from [52].

9.6 in the uncompressed region (high mass difference between the stop and the neutralino), both searches are very competitive. However the SUS-16-033 is much more sensitive in the so-called top corridor, where the mass difference between the neutralino and the stop is close to the value of top quark mass. This is because the M_{T2} variable used in the SUS-16-036 search is not sensitive to model points in the compressed region and does not allow for sufficient background-signal discrimination in the top corridor. The expected limit for the fully hadronic dedicated stop search SUS-16-049 is the strongest because it targets stop production only and uses top-tagging to identify interesting events. On the other hand the search SUS-17-001 with two leptons in the final state is strongly suppressed by the low branching ratio of top quarks decaying into states with leptons.

The limits obtained in ATLAS supersymmetry searches are similar to results presented in this thesis. Simplified models with top squark masses below 1000 GeV were excluded in ATLAS searches (see left plot in figure 9.7), compared to the exclusion of the search presented in this thesis which is 960 GeV. The limit on the gluino mass in T1tttt model from the ATLAS search is around 1950 GeV (pink curve in right plot in figure 9.7). It agrees within the uncertainty with the corresponding mass limit calculated in the SUS-16-033, which is 1960 GeV.

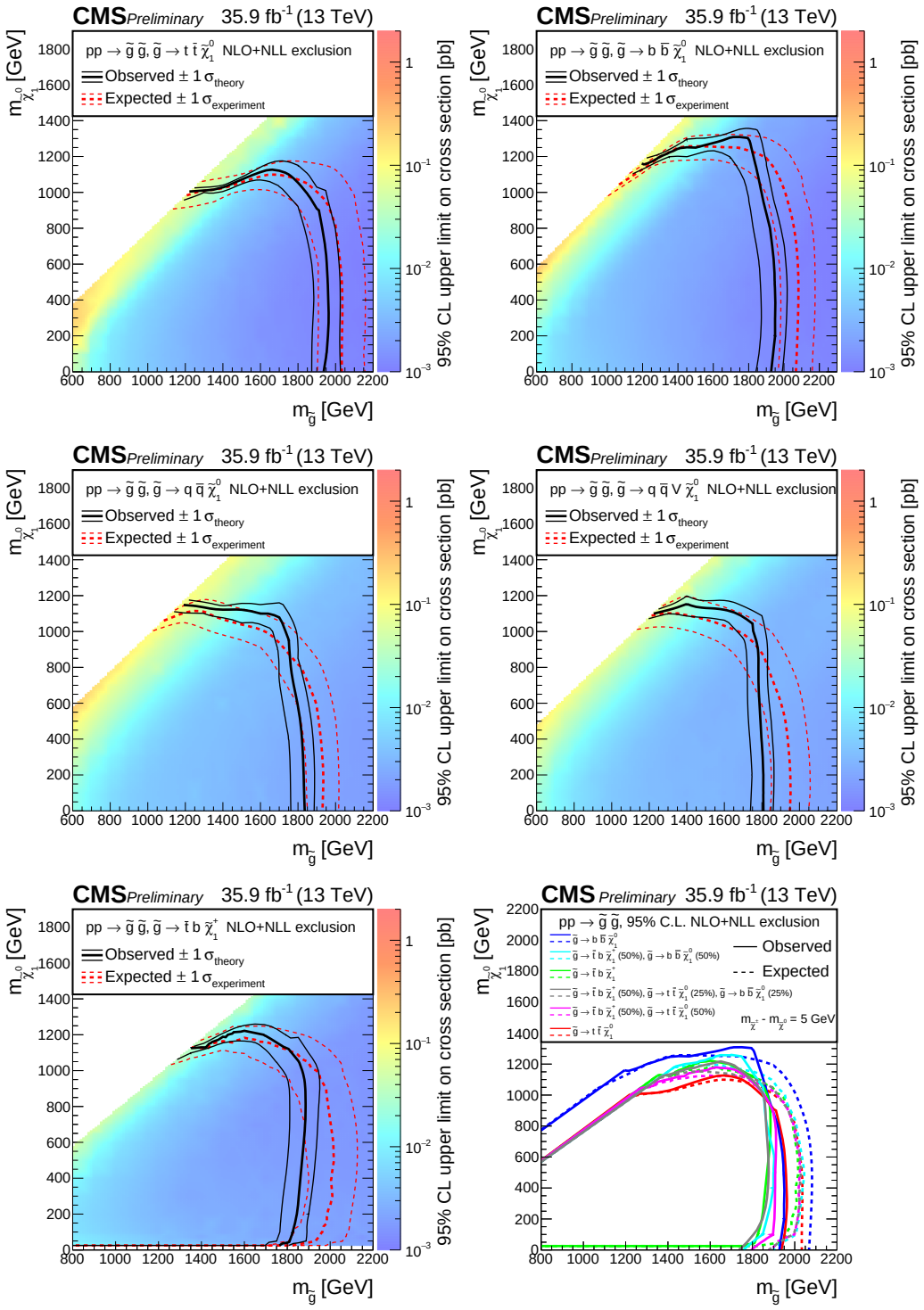

Figure 9.4: The 95% CL upper limits on the production cross sections for the (upper left) T1tttt, (upper right) T1bbbb, (middle left) T1qqqq, (middle right) T5qqqqVV, and (lower left) T1tbtb simplified models as a function of the gluino and LSP masses $m_{\tilde{g}}$ and $m_{\tilde{\chi}_1^0}$. (Lower right) The corresponding 95% NLO+NLL exclusion curves for the mixed models of gluino decays. For the meaning of the solid and dashed lines please refer to figure 9.3. Plot taken from [52].

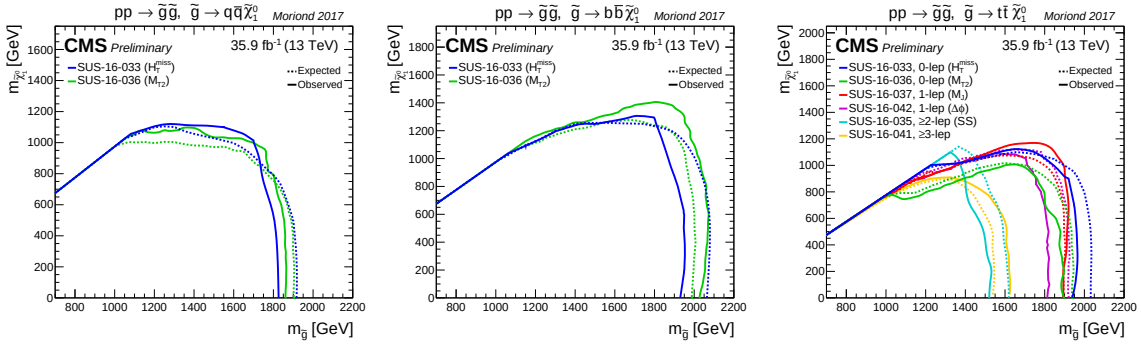

(a) T1qqqq (b) T1bbbb (c) T1tttt

Figure 9.5: The 95% NLO+NLL exclusion curves on the production cross sections for the gluino pair-production simplified models for several CMS supersymmetry searches. [187].

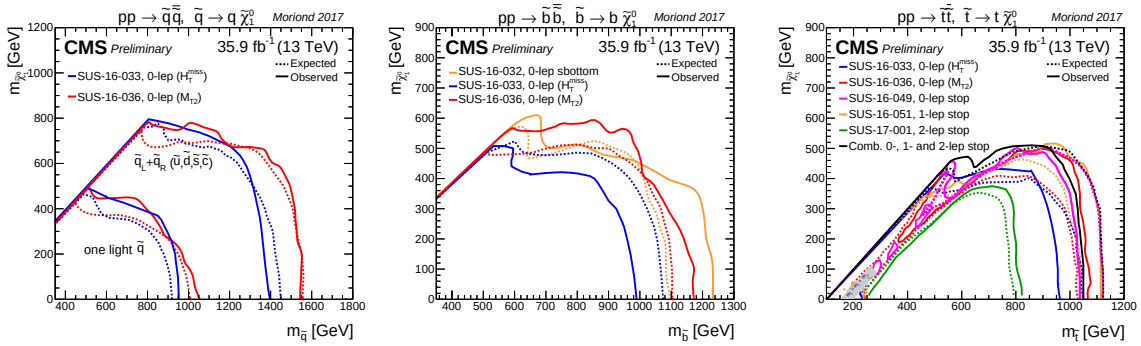

(a) T2qq (b) T2bb (c) T2tt

Figure 9.6: The 95% NLO+NLL exclusion curves on the production cross sections for the squark pair-production simplified models for several CMS supersymmetry searches. [187].

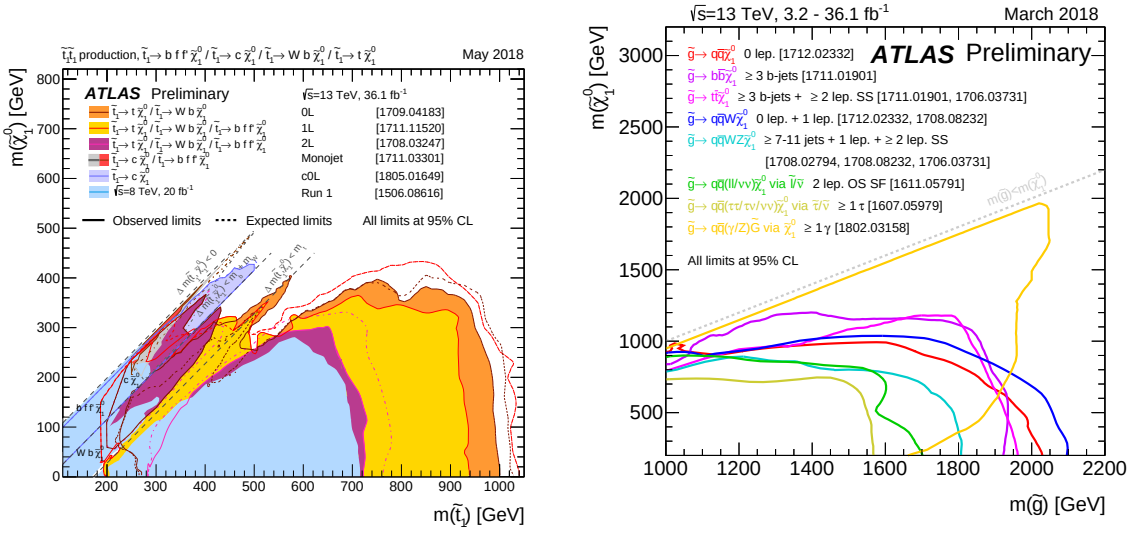

Figure 9.7: The 95% NLO+NLL exclusion curves on the production cross sections for the stop (left) and gluino (right) pair-production simplified models for several ATLAS supersymmetry searches. [188].

10 Conclusions

The year 2016 was very successful for the CMS collaboration. Around 36 fb^{-1} of 13 TeV proton-proton collision data was collected , almost 50% more than expected [60]. The work presented in this thesis focused on two measurements performed using that data. The first was analysis of the resolution of the jet transverse momentum in data and in simulation, presented in chapter 6. The results were used in an estimation of the QCD background for a fully hadronic, inclusive search for supersymmetry using the rebalance and smear method, presented in chapter 8.

The ratios of the jet energy resolution were measured using a dijet method. The volume of the dataset allowed the usage of finer intervals in pseudorapidity $|\eta|$ compared to 7 and 8 TeV measurements, giving the insight into the performance of the detector subcomponents. The resolution in data was observed to be lower compared to simulation. This effect was expected, as the MC only approximates the behavior of the detector and it was observed in the previous measurements [120] that the resolution in simulation is higher.

Four ranges of pseudorapidity can be distinguished based on the geometry of the detector. In range $|\eta| \leq 1.131$ the resolution in data is 15-19% worse than in MC. This $|\eta|$ range corresponds to the coverage of the barrel part of the inner tracking system, and is within the range of the barrel part of ECAL and HCAL. Because of that the values of the scale factors in that range are close to each other. In the range $|\eta| \in (1.131, 2.5)$ the scale factors have values in a similar range as below $|\eta| = 1.131$, however they are showing large fluctuations. This region corresponds to the tracker endcap coverage and the variations of the scale factors is caused by the changing geometry of the calorimeters. The boundary between the barrel and endcap ECAL is at $|\eta| = 1.479$ and the preshower starts only at $|\eta| = 1.653$. The transition between barrel and endcap HCAL occurs at $|\eta| \in (1.2, 1.5)$. Due to these changes the data to simulation ratios vary in the range of 10-30%. The third $|\eta|$ range is $|\eta| \in (2.5, 2.964)$. In this region the scale factors are very high, with resolution in data between 34% and 80% lower than in simulation. This is caused by the fact that there are no tracks reconstructed above $|\eta| = 2.5$ so the jet measurement is based only on calorimeter clusters. The simulation of calorimetry is generally more difficult than that of the tracker. Additionally, the $|\eta|$ intervals used in that range are very narrow, reducing the statistical precision. The last pseudorapidity range is $|\eta| \in (2.964, 5.2)$ which corresponds to the hadronic forward calorimeter coverage. The data resolution in that range is around 19% lower than in simulation, which is an effect very similar to one obtained for 8 TeV jet energy resolution measurement.

Additionally, a measurement of the data to simulation ratios of the jet response non-gaussian tails was presented. A measurement in a wide $|\eta|$ intervals has shown that the tails in data were 14% higher in the barrel region $|\eta| < 1.131$. For higher values of pseudorapidities the tails in data are 10-12% lower than in simulation. However, these scale factors have large uncertainties of around 20%.

The resolution measurement based on the dijet events provides a reach to high values of p_T. However, for low transverse momenta the method is constrained by low trigger rates. A measurement of the resolution with γ/Z + jets could possibly improve the statistical precision for $p_T < 100$ GeV. This perhaps could allow for a measurement of data to simulation ratios not only in intervals of $|\eta|$, but also of p_T.

The knowledge gained through the measurements of the jet transverse momentum response was utilized in the work presented in the second half of this thesis, which was a search for supersymmetry in multijet events with high missing transverse momentum and no leptons. The search was performed on the same data as the jet energy resolution measurement, namely the 13 TeV data recorded by the CMS experiment in the 2016. The search intervals were defined using intervals of N_{jets}, N_{bjets}, H_T and $\not{H}_T$, making the analysis sensitive to multiple supersymmetric models.

The main focus of the work presented in this thesis was the estimation of the background arising from QCD multi-jet events. Though it is not the dominant background, its prediction is especially difficult due to the nature of the missing transverse momentum in QCD events, originating mostly from the jet mismeasurements and neutrinos from the decays of heavy flavored quarks. The QCD background was estimated using the *rebalance and smear* method, which predicts the fake $\not{H}_T$ in multijet events based on a jet resolution model. In this method the jets in multijet events from data are modified to approximately undo the detector effects and then are smeared according to the jet transverse momentum response. The rebalance and smear method has been used in previous searches for supersymmetry performed on fully hadronic events with large missing transverse momentum [162–164] in which the N_{bjets} was not used as a search variable. Inclusion of the number of b-tagged jets in the definitions of search intervals required modification of the method because of additional contribution to the $\not{H}_T$ originating from the neutrinos from decays of B mesons. Previously, the jets were rebalanced to a fixed $\not{H}_T$ which was calculated using the jets below certain p_T threshold. In the modified approach, the $\not{H}_T$ of the rebalanced event is constrained by the particle-level kinematic distributions of missing transverse momentum, calculated using QCD simulation. The prediction of the rebalance and smear method has been compared to the prediction of an alternative QCD background estimation, the $\Delta\phi$-extrapolation, and the two predictions were found to be consistent.

The observed number of events in the 174 search intervals agree with the Standard Model background predictions and no evidence for supersymmetry has been observed [52]. The results were interpreted in the context of simplified models which assume the production and decays of gluinos, and light-flavored, bottom and top squarks. For these models the 95% CL upper limits on the production cross sections and NLO+NLL exclusion curves were calculated. Depending on the simplified model, the production of gluinos with masses in range of 1800-1960 GeV were excluded for LSP masses below around 1 TeV. The top, bottom and light squarks with masses below 960, 1050 and 1450 GeV, respectively, were also excluded for masses of LSP below 400 GeV for the considered simplified models. Furthermore, the results can be re-interpreted for other BSM models which predict final states with jets and missing transverse momentum.

Appendix

A Jet transverse momentum resolution

A.1 Additional jet activity correction

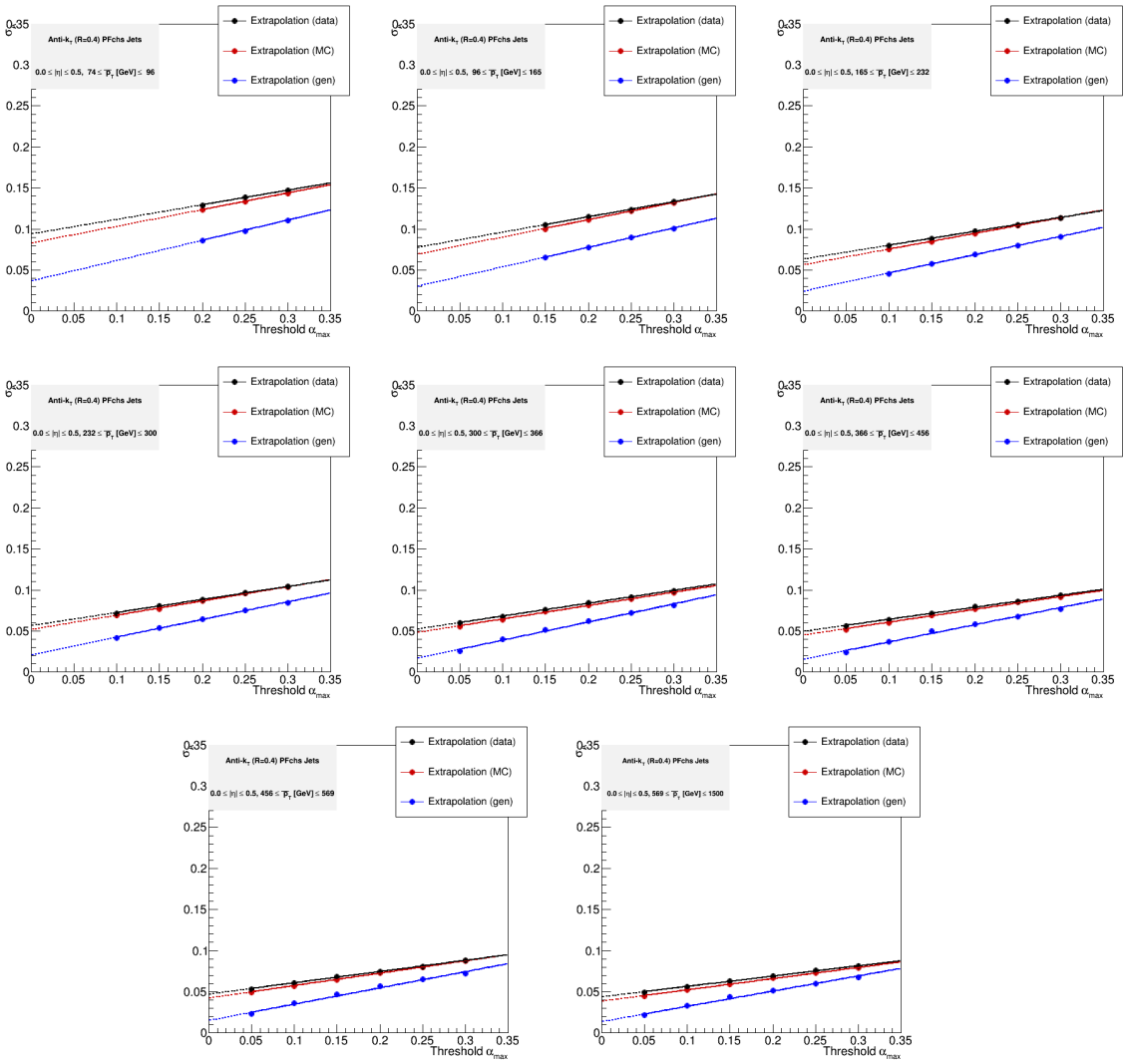

Figure A.1: Plots of the fits to asymmetry widths as a function of additional hadronic activity α_{max} in different p_T bins and $|\eta| \in (0, 0.522)$. The black points and line represent data points, red color represents detector level simulation and blue represents truth level simulation.

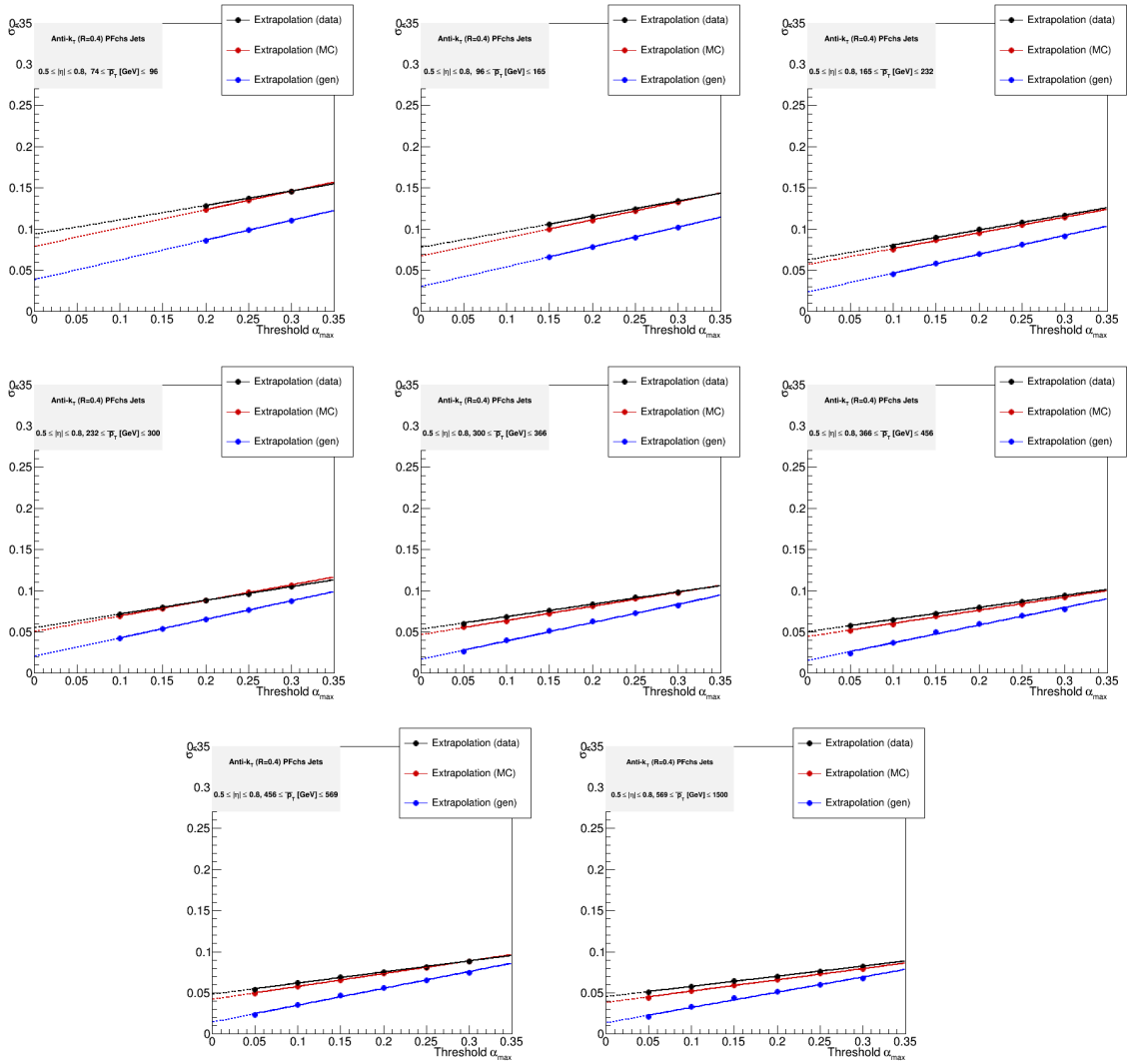

Figure A.2: Plots of the fits to asymmetry widths as a function of additional hadronic activity α_{max} in different p_T bins and $|\eta| \in (0.522, 0.783)$. The black points and line represent data points, red color represents detector level simulation and blue represents truth level simulation.

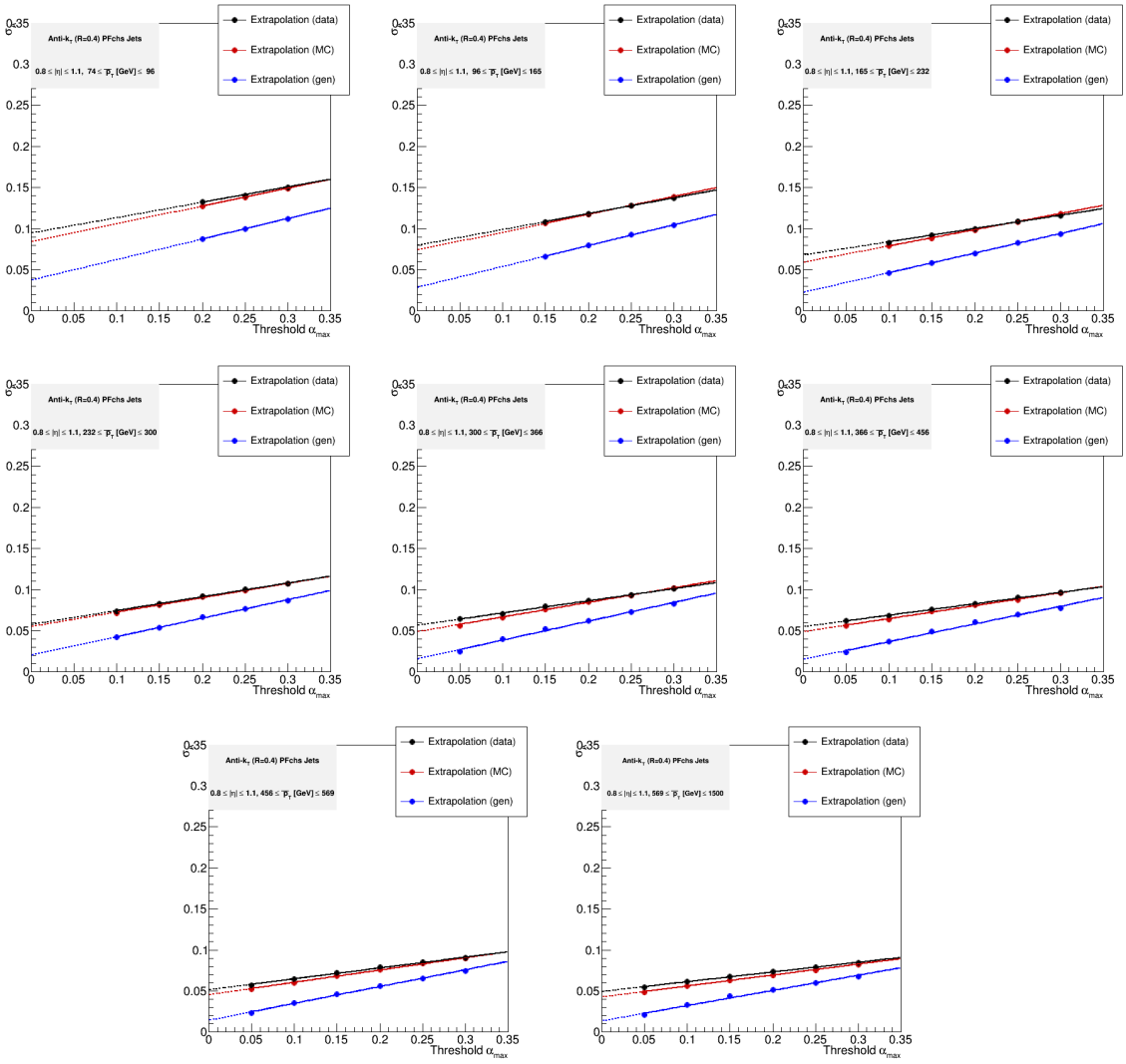

Figure A.3: Plots of the fits to asymmetry widths as a function of additional hadronic activity α_{max} in different p_T bins and $|\eta| \in (0.783, 1.131)$. The black points and line represent data points, red color represents detector level simulation and blue represents truth level simulation.

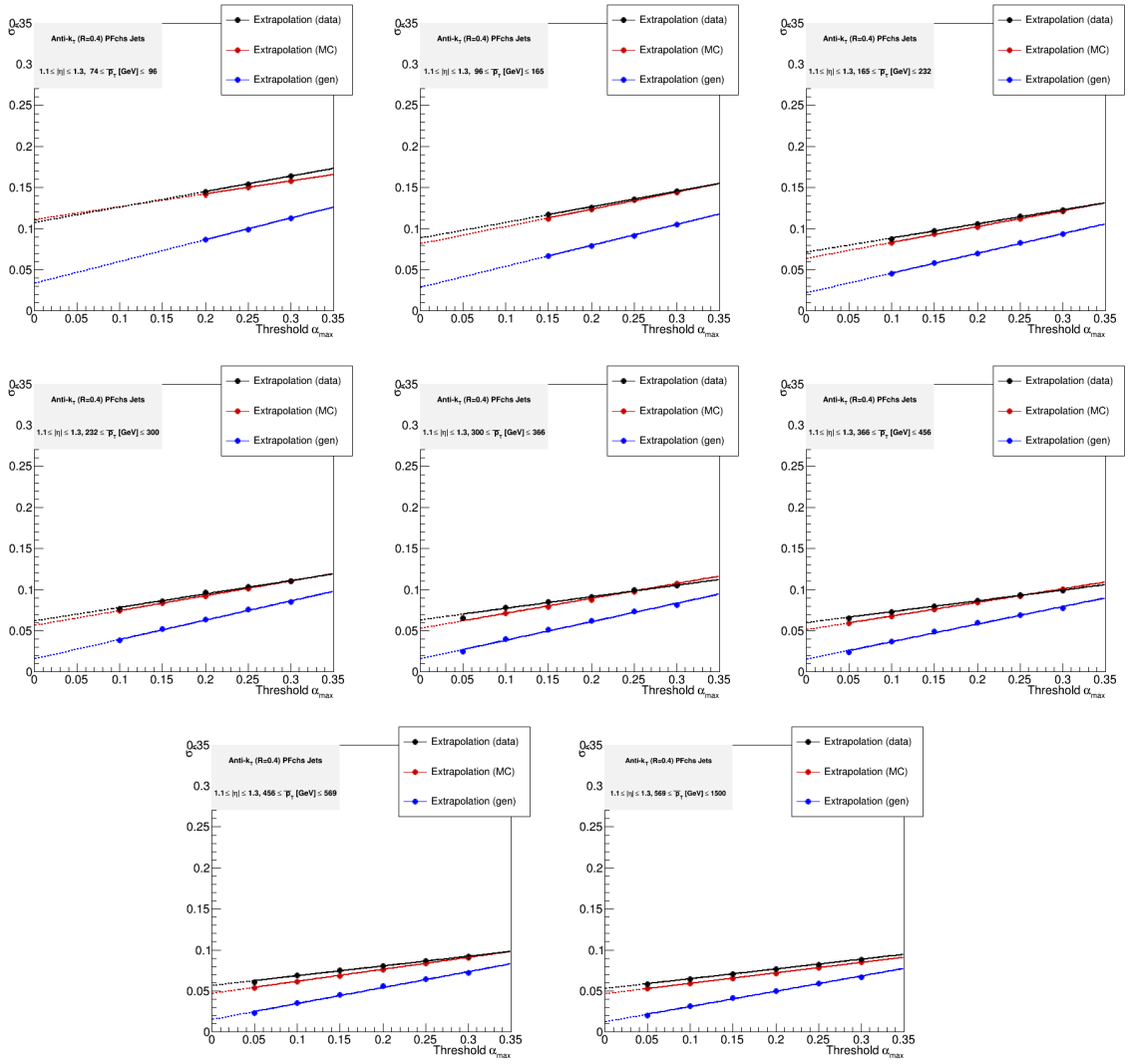

Figure A.4: Plots of the fits to asymmetry widths as a function of additional hadronic activity α_{max} in different p_T bins and $|\eta| \in (1.131, 1.305)$. The black points and line represent data points, red color represents detector level simulation and blue represents truth level simulation.

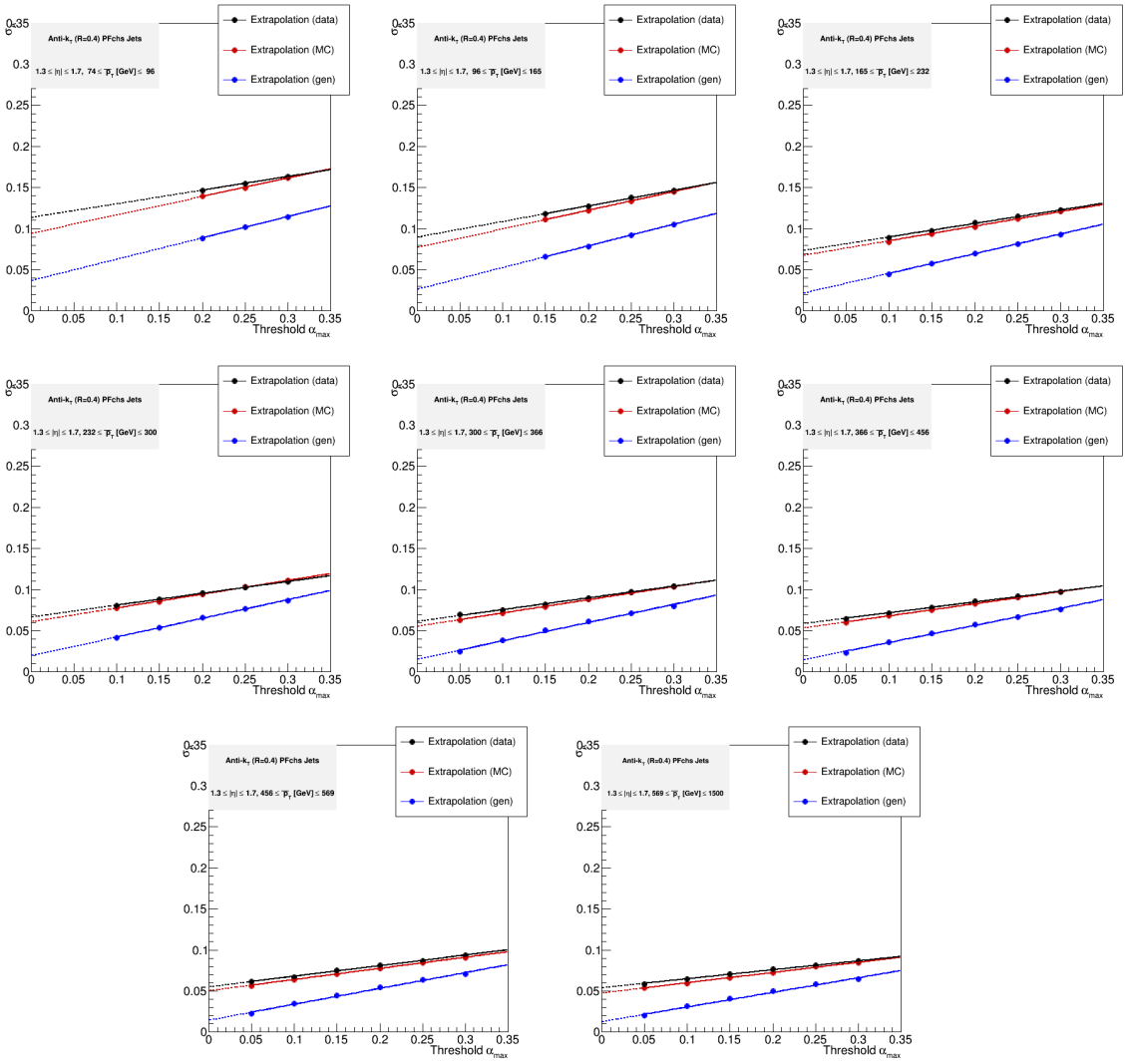

Figure A.5: Plots of the fits to asymmetry widths as a function of additional hadronic activity α_{max} in different p_T bins and $|\eta| \in (1.305, 1.740)$. The black points and line represent data points, red color represents detector level simulation and blue represents truth level simulation.

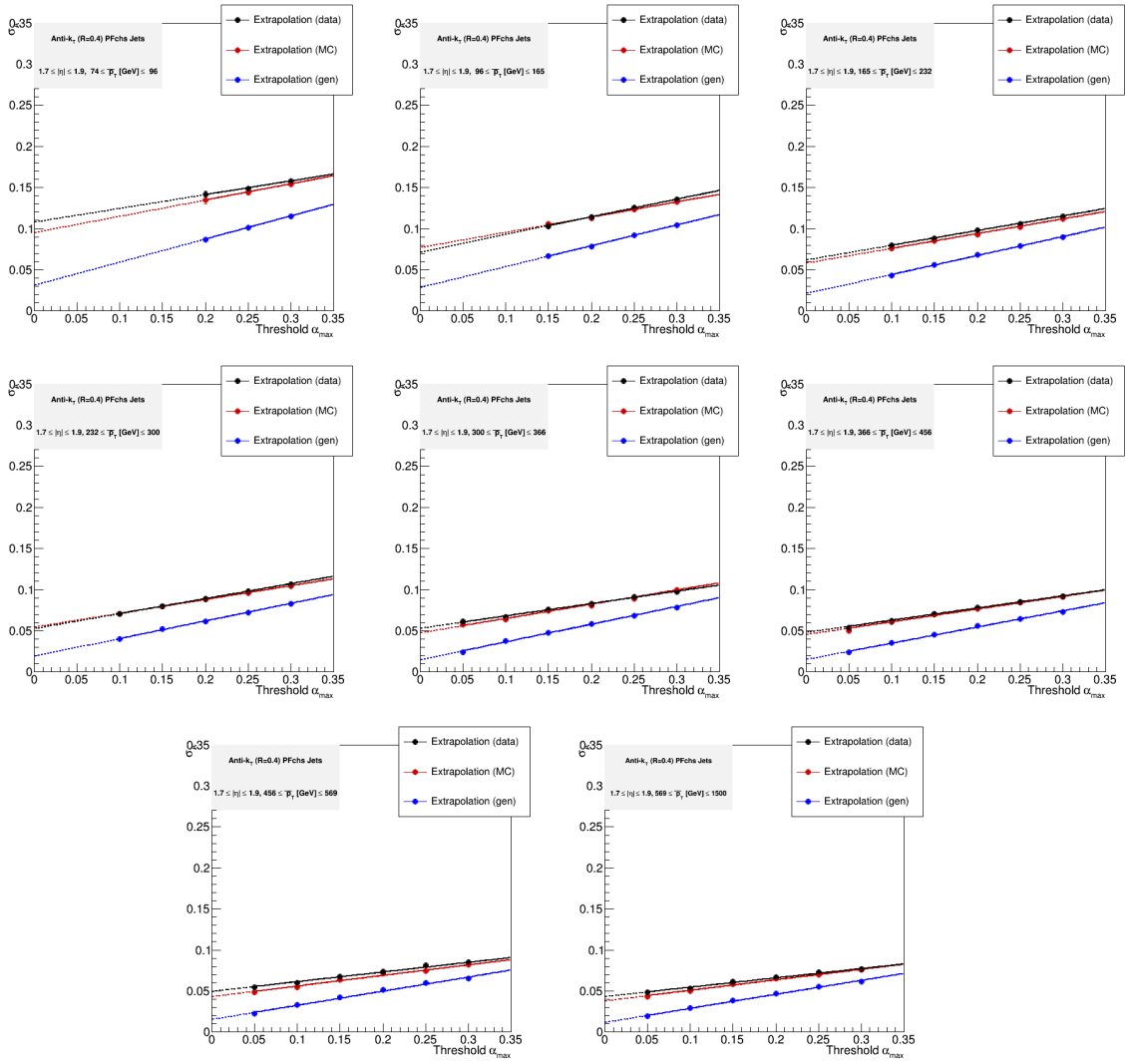

Figure A.6: Plots of the fits to asymmetry widths as a function of additional hadronic activity α_{max} in different p_T bins and $|\eta| \in (1.740, 1.930)$. The black points and line represent data points, red color represents detector level simulation and blue represents truth level simulation.

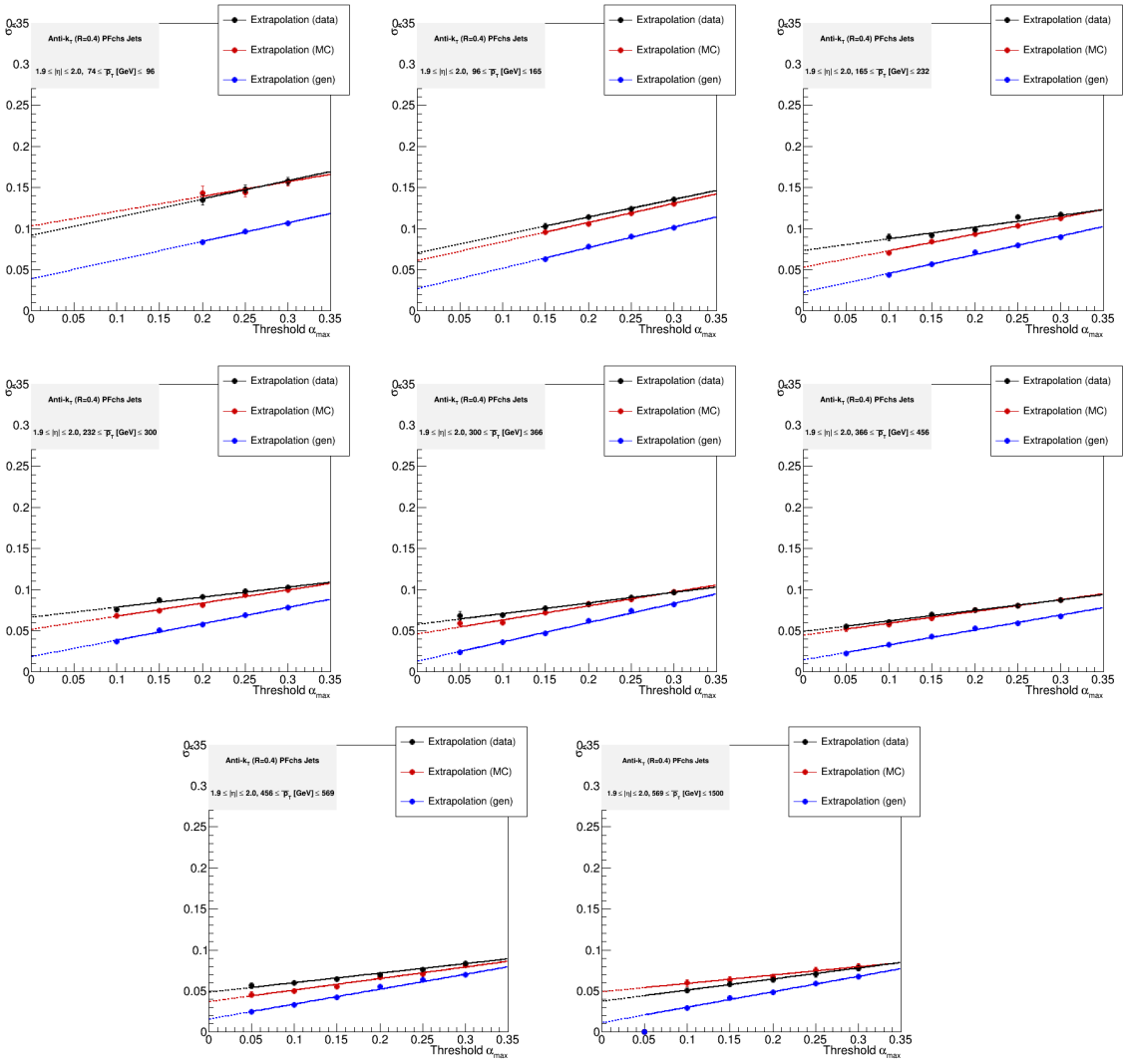

Figure A.7: Plots of the fits to asymmetry widths as a function of additional hadronic activity α_{max} in different p_T bins and $|\eta| \in (1.930, 2.043)$. The black points and line represent data points, red color represents detector level simulation and blue represents truth level simulation.

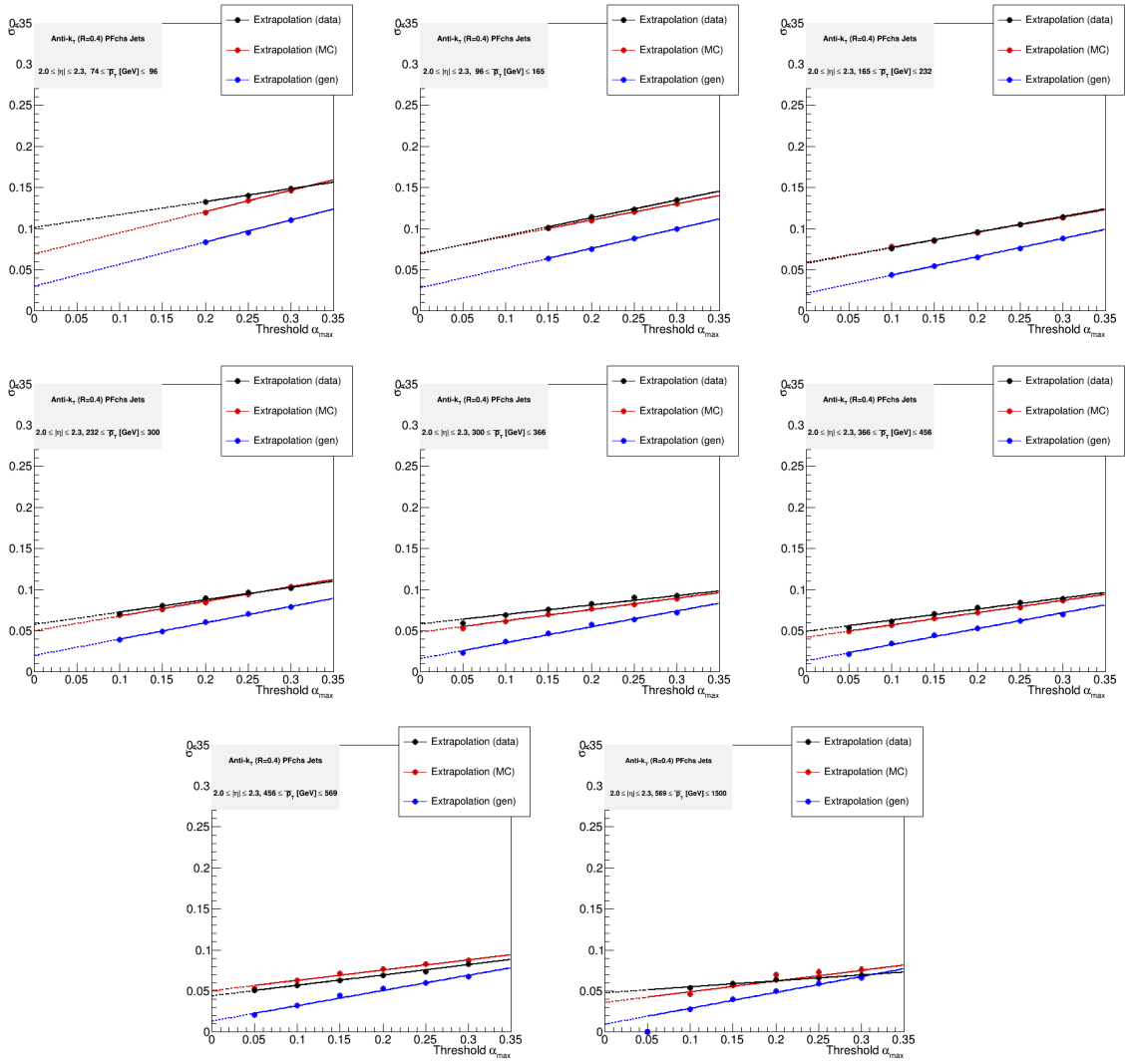

Figure A.8: Plots of the fits to asymmetry widths as a function of additional hadronic activity α_{max} in different p_T bins and $|\eta| \in (2.043, 2.322)$. The black points and line represent data points, red color represents detector level simulation and blue represents truth level simulation.

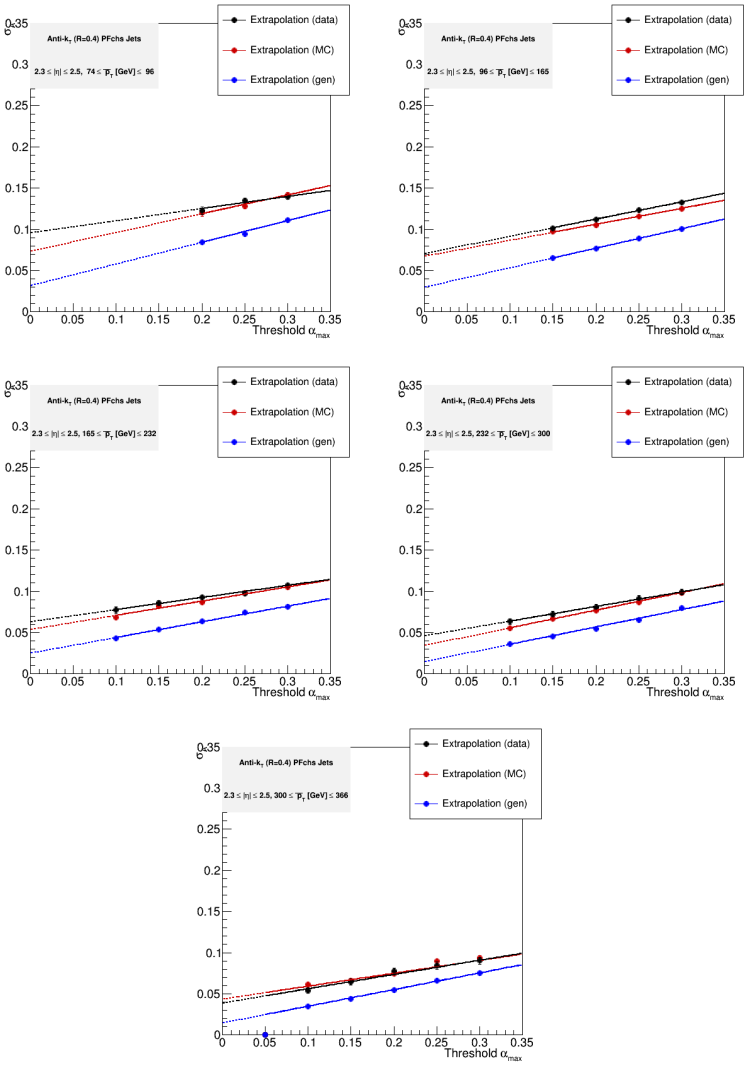

Figure A.9: Plots of the fits to asymmetry widths as a function of additional hadronic activity α_{max} in different p_T bins and $|\eta| \in (2.322.2.5)$. The black points and line represent data points, red color represents detector level simulation and blue represents truth level simulation.

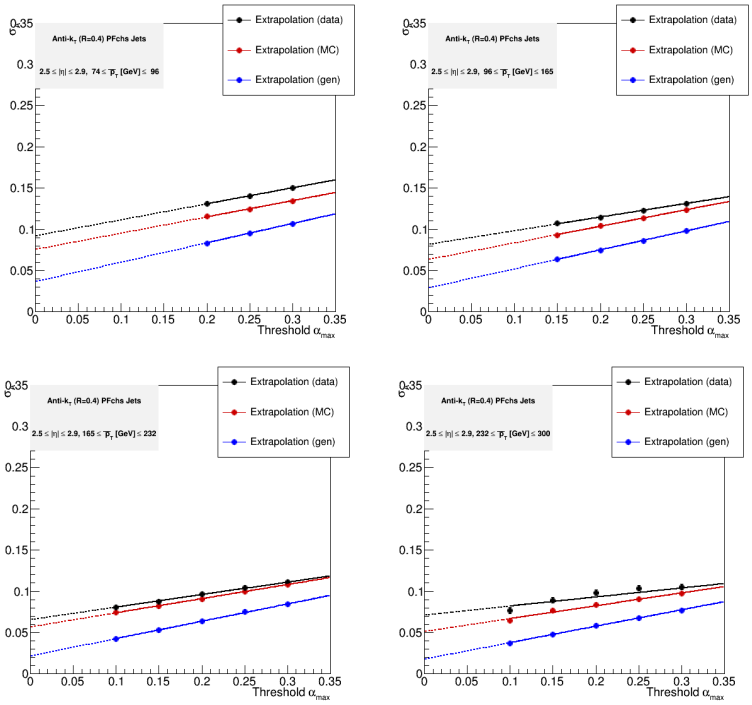

Figure A.10: Plots of the fits to asymmetry widths as a function of additional hadronic activity α_{max} in different p_T bins and $|\eta| \in (2.5, 2.853)$. The black points and line represent data points, red color represents detector level simulation and blue represents truth level simulation.

A.2 Additional jet activity correction for forward extension

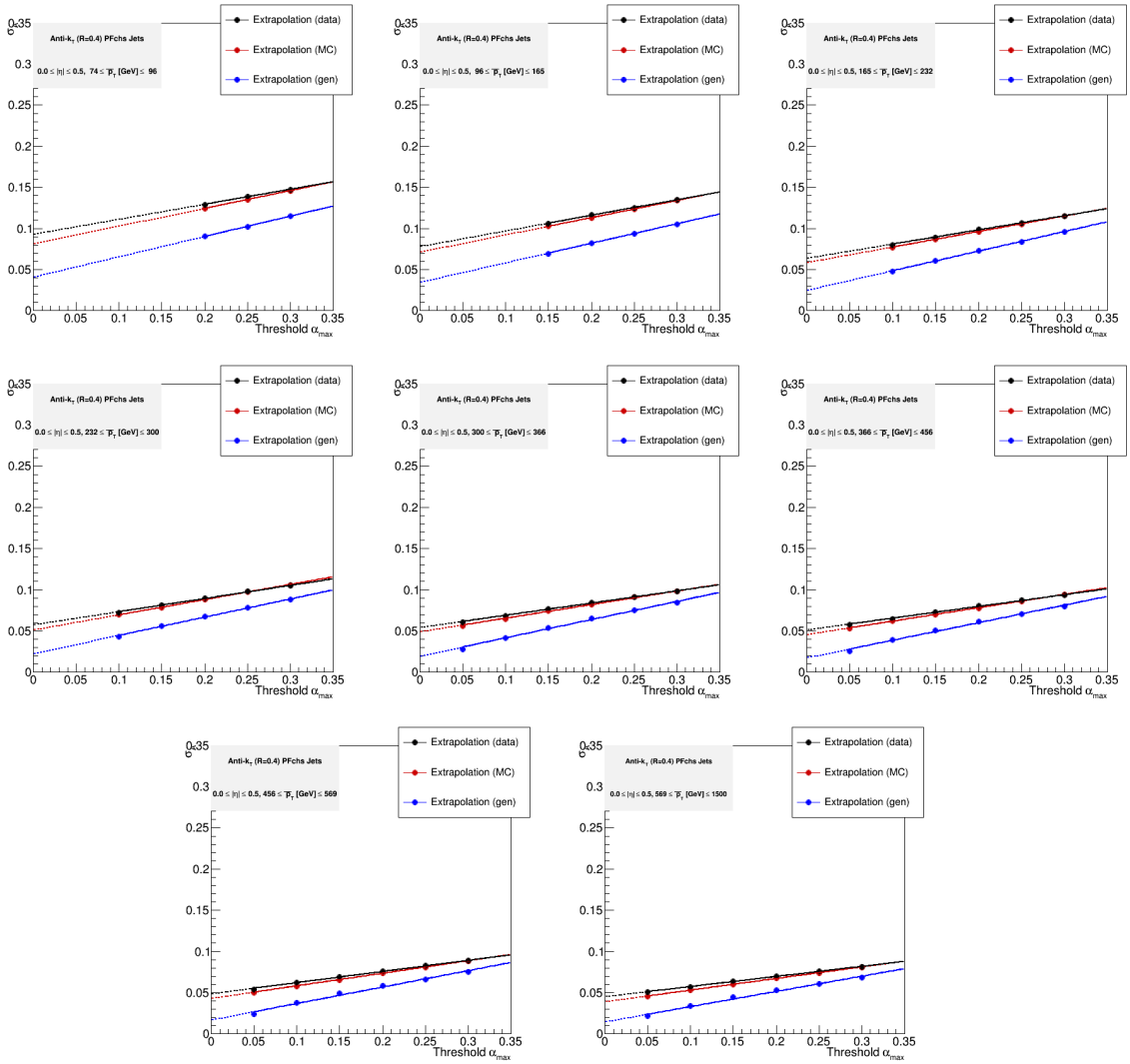

Figure A.11: Plots of the fits to asymmetry widths as a function of additional hadronic activity α_{max} in different p_T bins and $|\eta| \in (0, 1.131)$ for the widths calculated with forward extension. The black points and line represent data points, red color represents detector level simulation and blue represents truth level simulation.

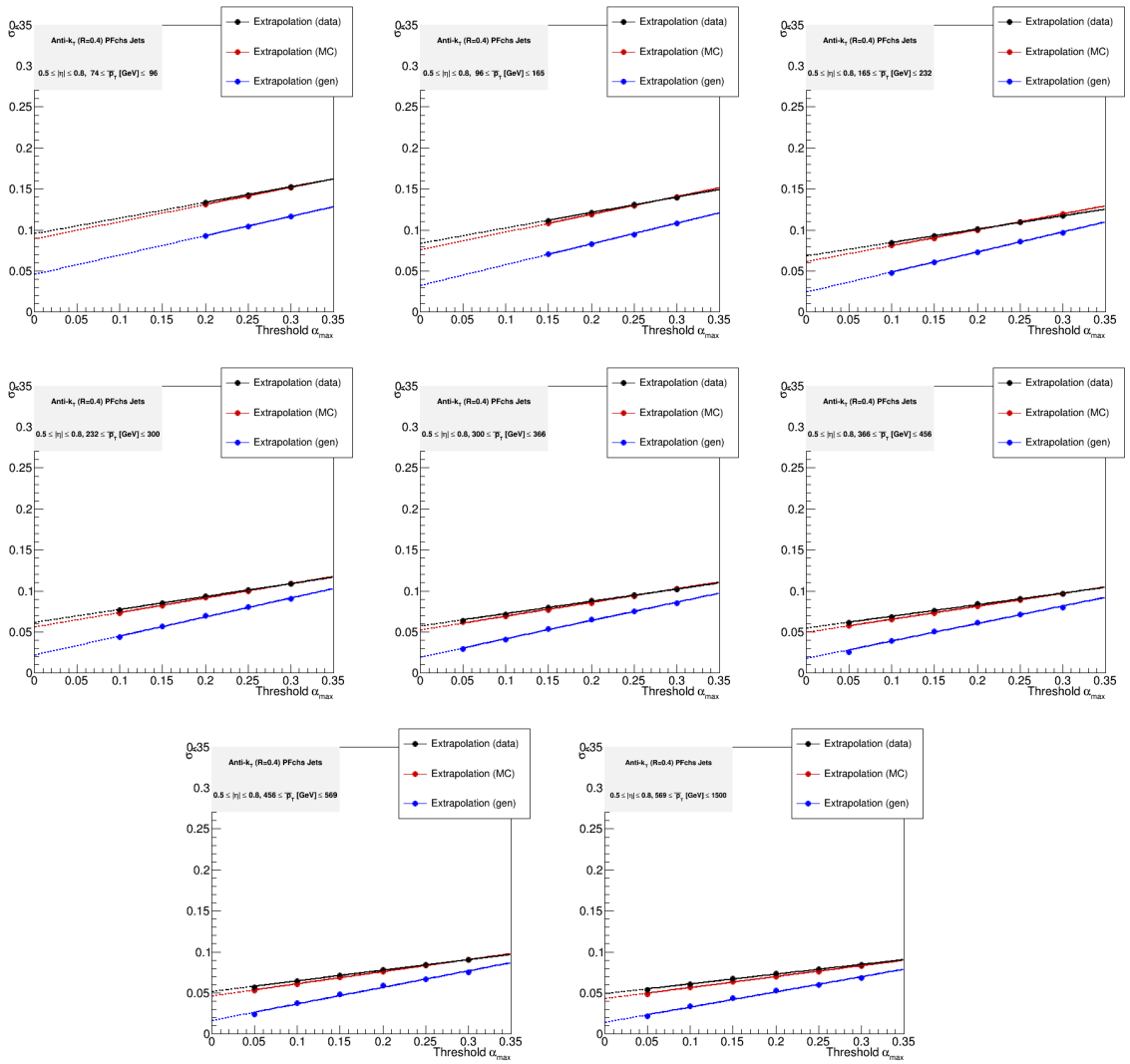

Figure A.12: Plots of the fits to asymmetry widths as a function of additional hadronic activity α_{max} in different p_T bins and $|\eta| \in (1.131, 1.305)$ for the widths calculated with forward extension. The black points and line represent data points, red color represents detector level simulation and blue represents truth level simulation.

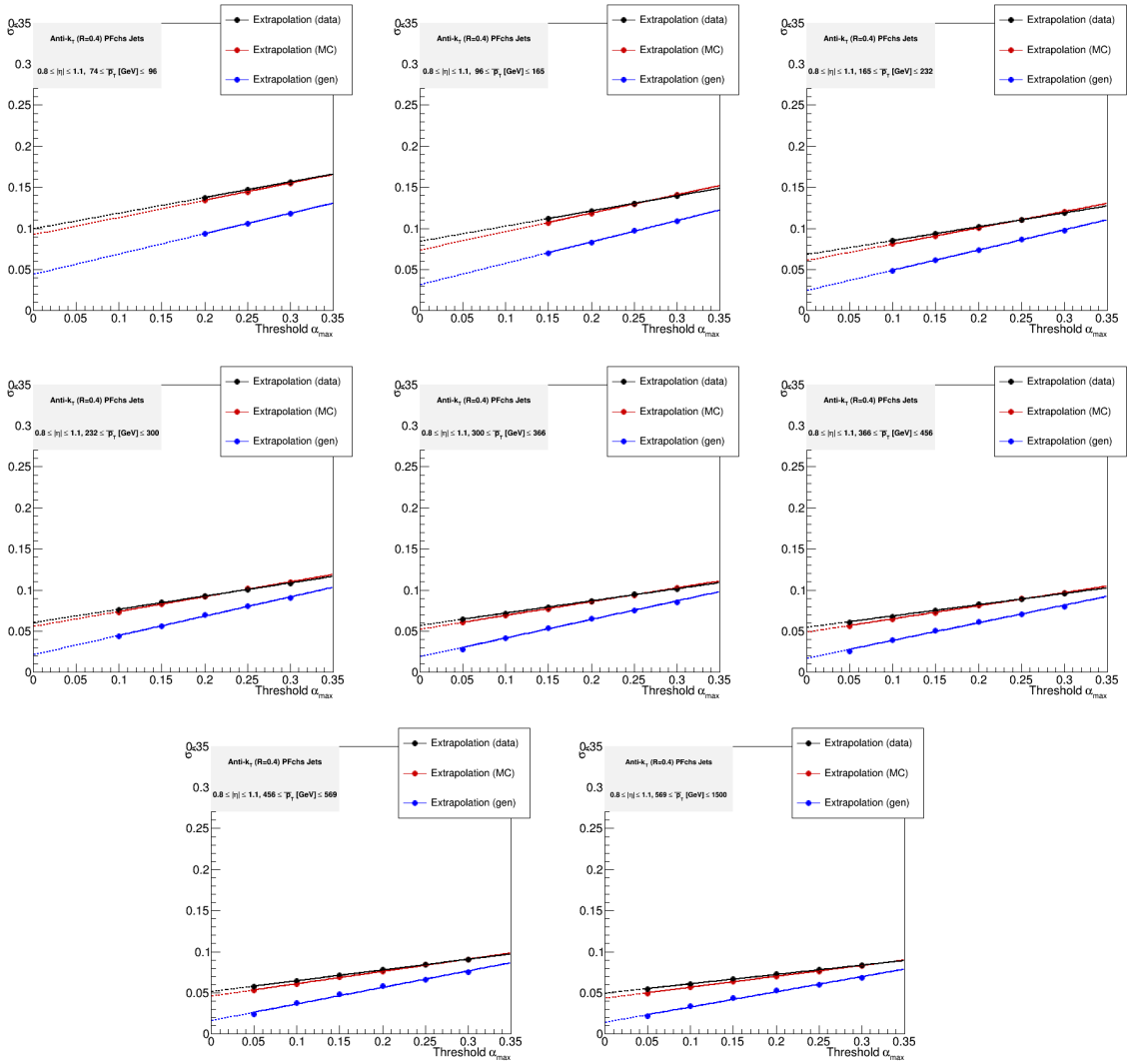

Figure A.13: Plots of the fits to asymmetry widths as a function of additional hadronic activity α_{max} in different p_T bins and $|\eta| \in (1.305, 1.740)$ for the widths calculated with forward extension. The black points and line represent data points, red color represents detector level simulation and blue represents truth level simulation.

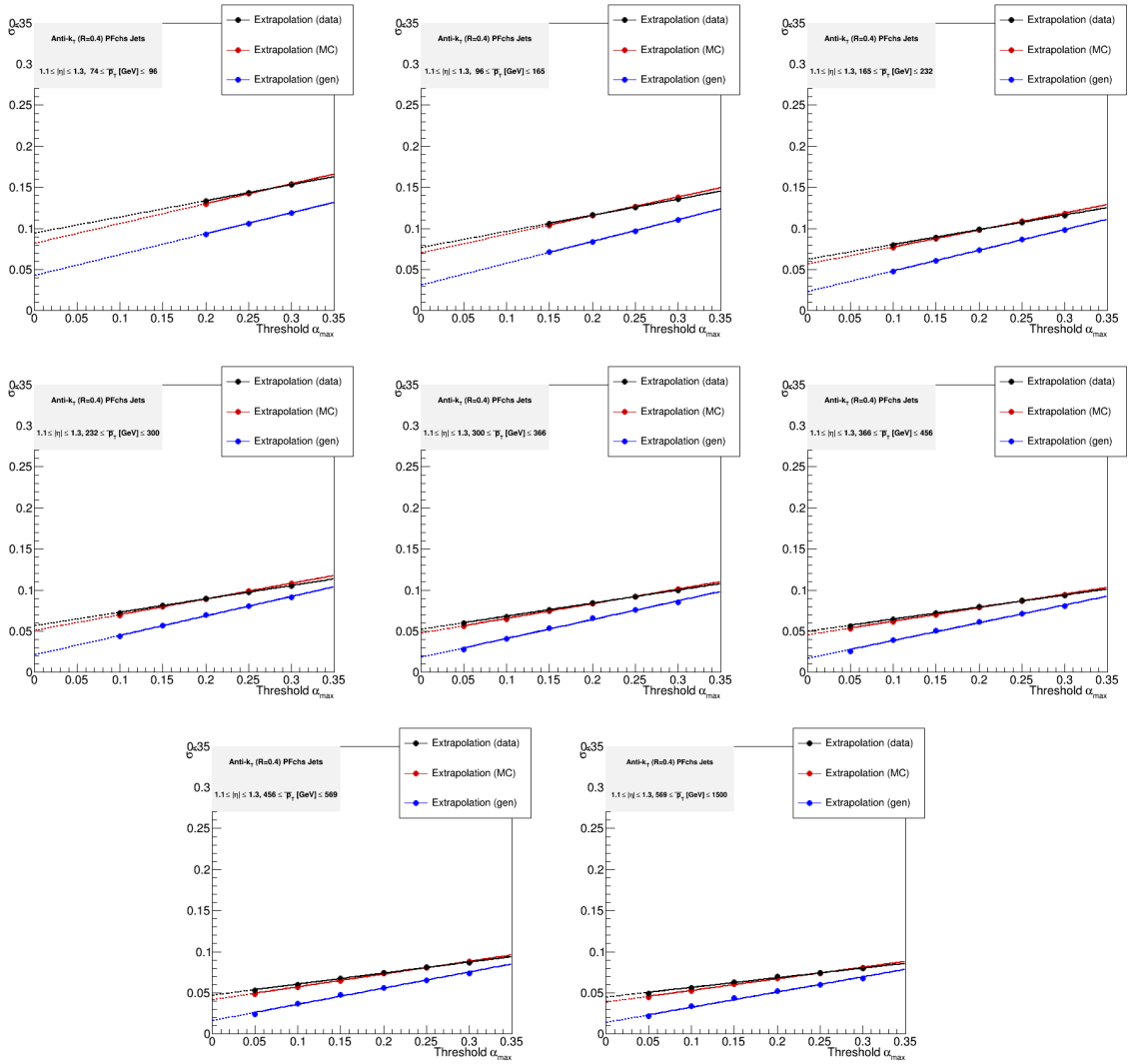

Figure A.14: Plots of the fits to asymmetry widths as a function of additional hadronic activity α_{max} in different p_T bins and $|\eta| \in (1.740, 1.930)$ for the widths calculated with forward extension. The black points and line represent data points, red color represents detector level simulation and blue represents truth level simulation.

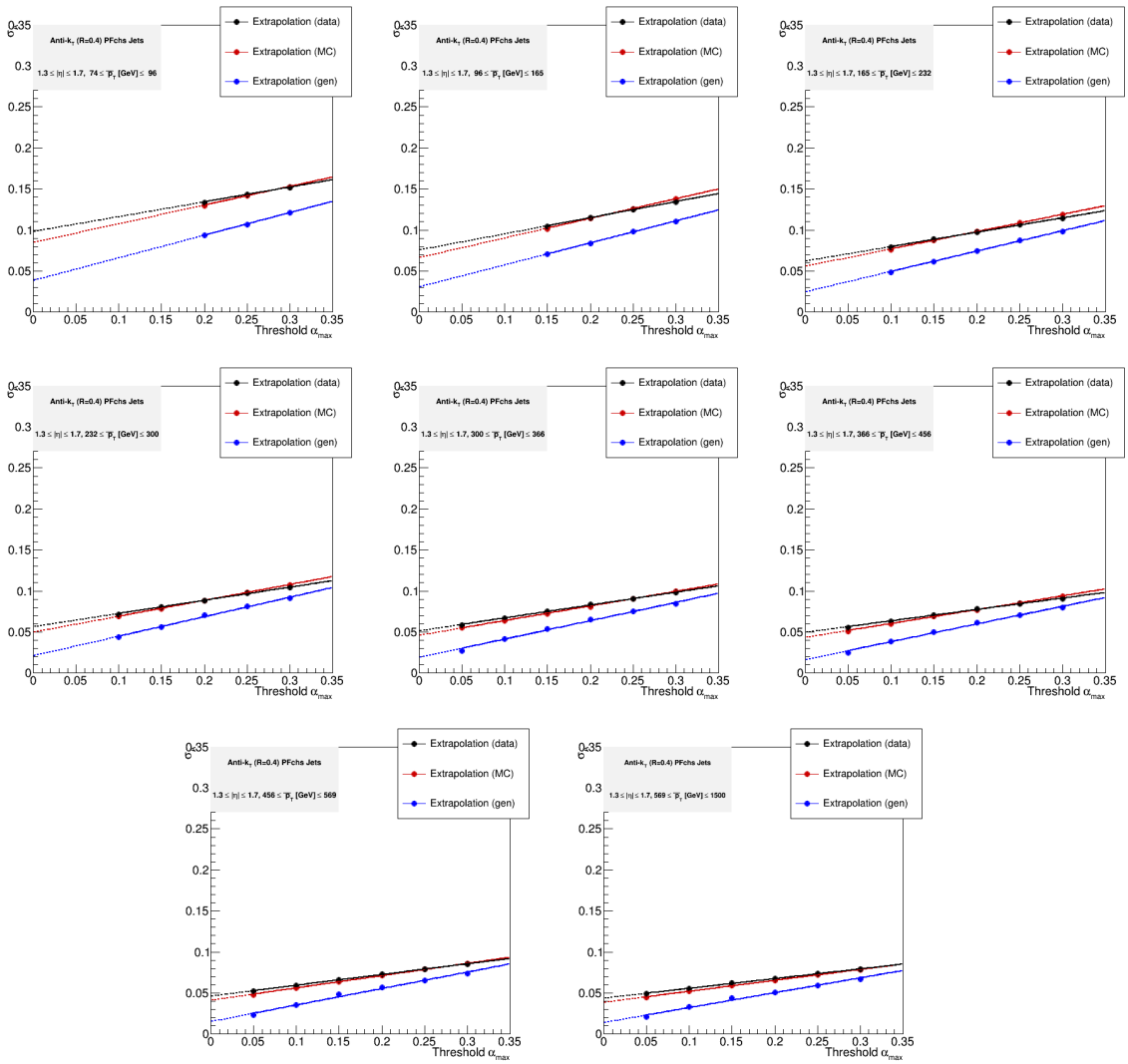

Figure A.15: Plots of the fits to asymmetry widths as a function of additional hadronic activity α_{max} in different p_T bins and $|\eta| \in (1.930, 2.043)$ for the widths calculated with forward extension. The black points and line represent data points, red color represents detector level simulation and blue represents truth level simulation.

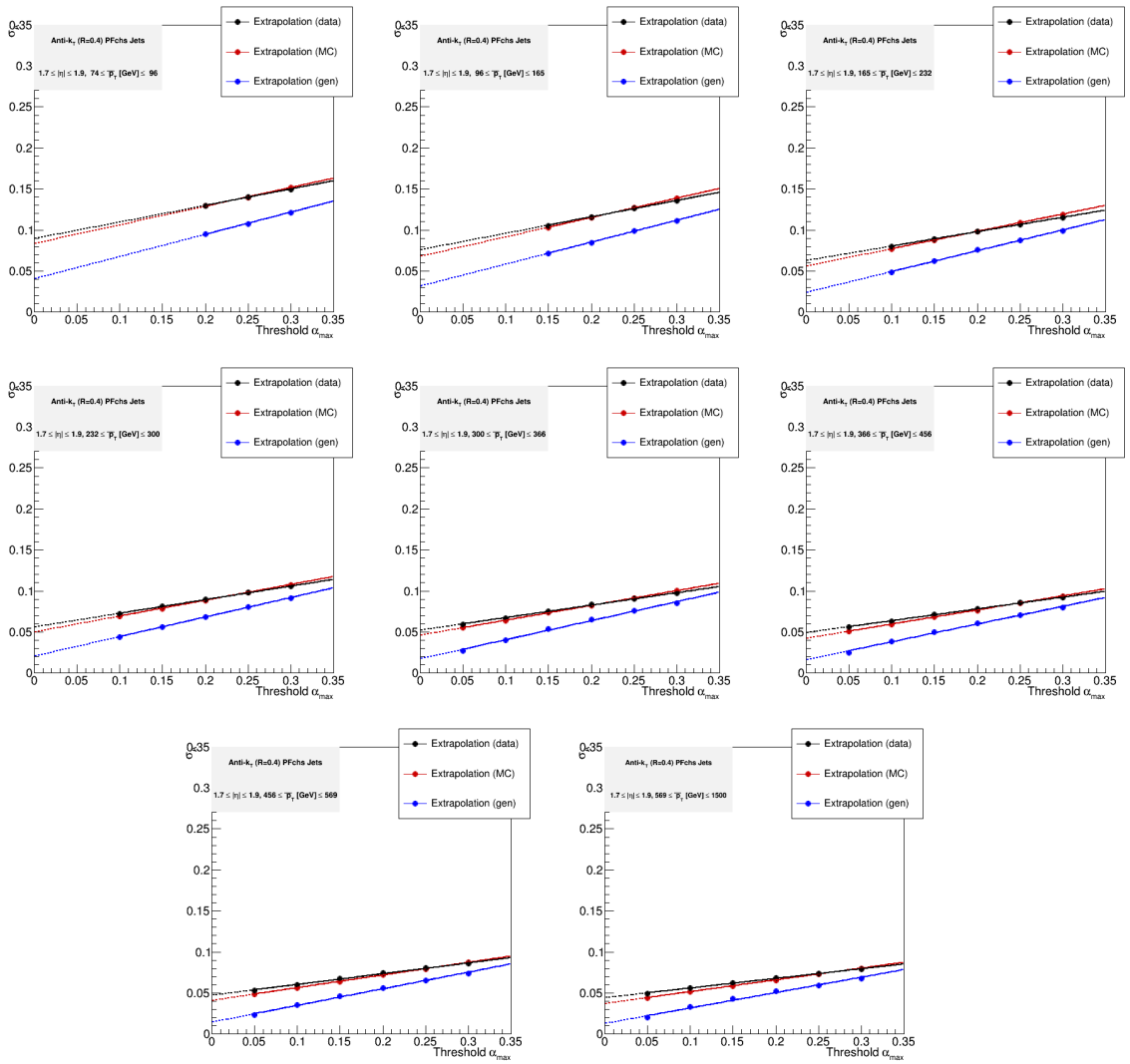

Figure A.16: Plots of the fits to asymmetry widths as a function of additional hadronic activity α_{max} in different p_T bins and $|\eta| \in (2.043, 2.322)$ for the widths calculated with forward extension. The black points and line represent data points, red color represents detector level simulation and blue represents truth level simulation.

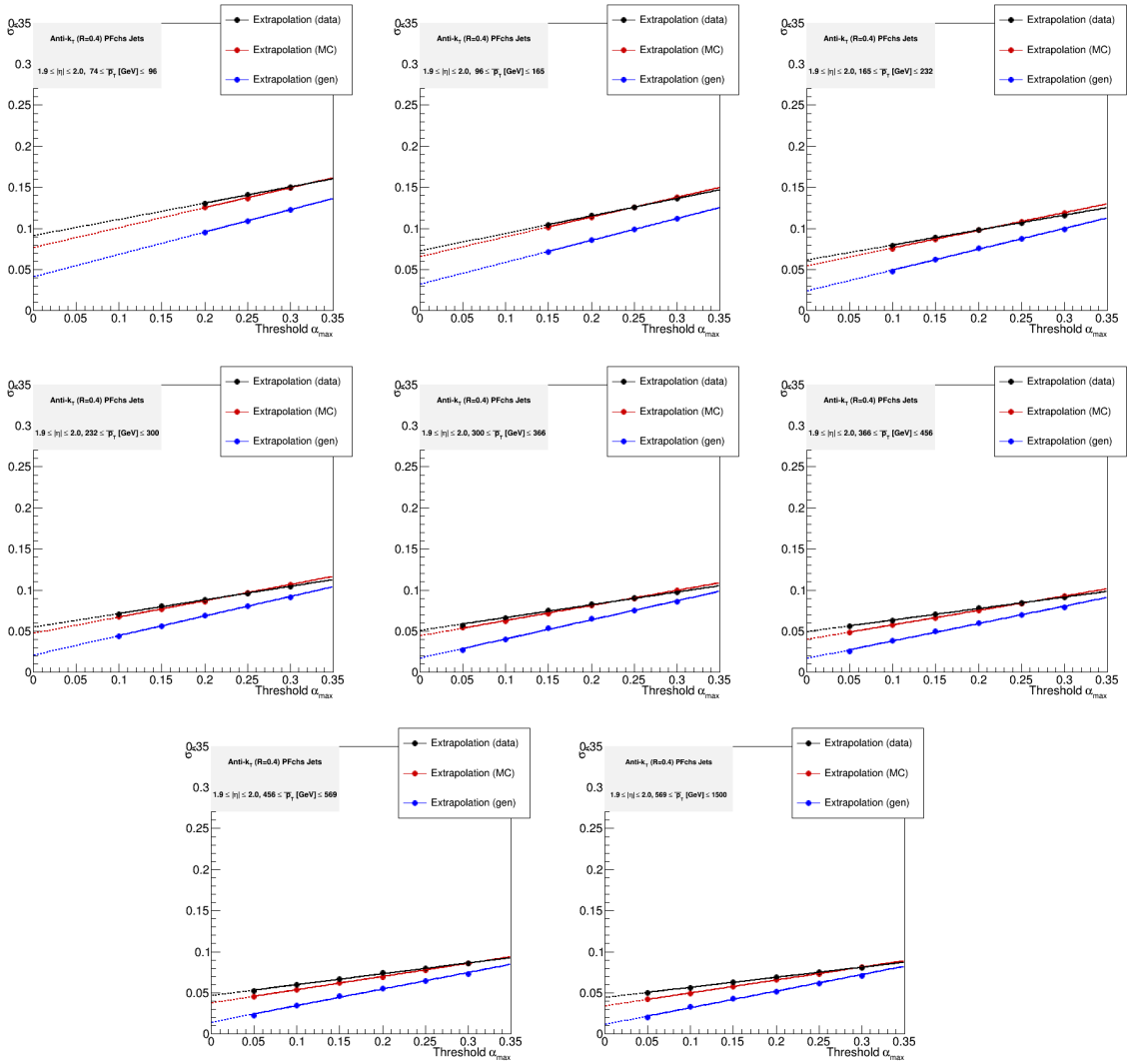

Figure A.17: Plots of the fits to asymmetry widths as a function of additional hadronic activity α_{max} in different p_T bins and $|\eta| \in (2.322, 2.5)$ for the widths calculated with forward extension. The black points and line represent data points, red color represents detector level simulation and blue represents truth level simulation.

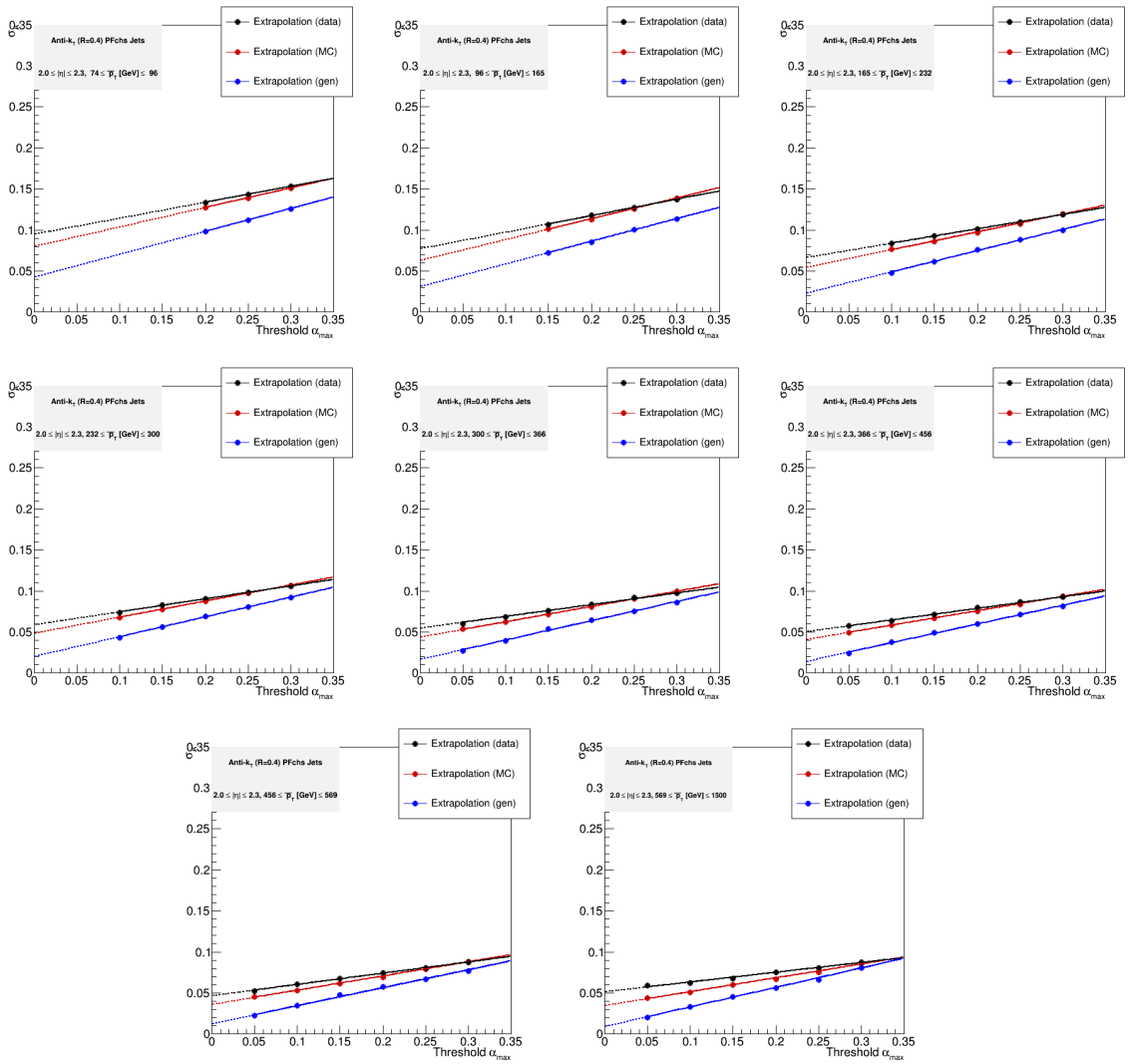

Figure A.18: Plots of the fits to asymmetry widths as a function of additional hadronic activity α_{max} in different p_T bins and $|\eta| \in (2.5, 2.853)$ for the widths calculated with forward extension. The black points and line represent data points, red color represents detector level simulation and blue represents truth level simulation.

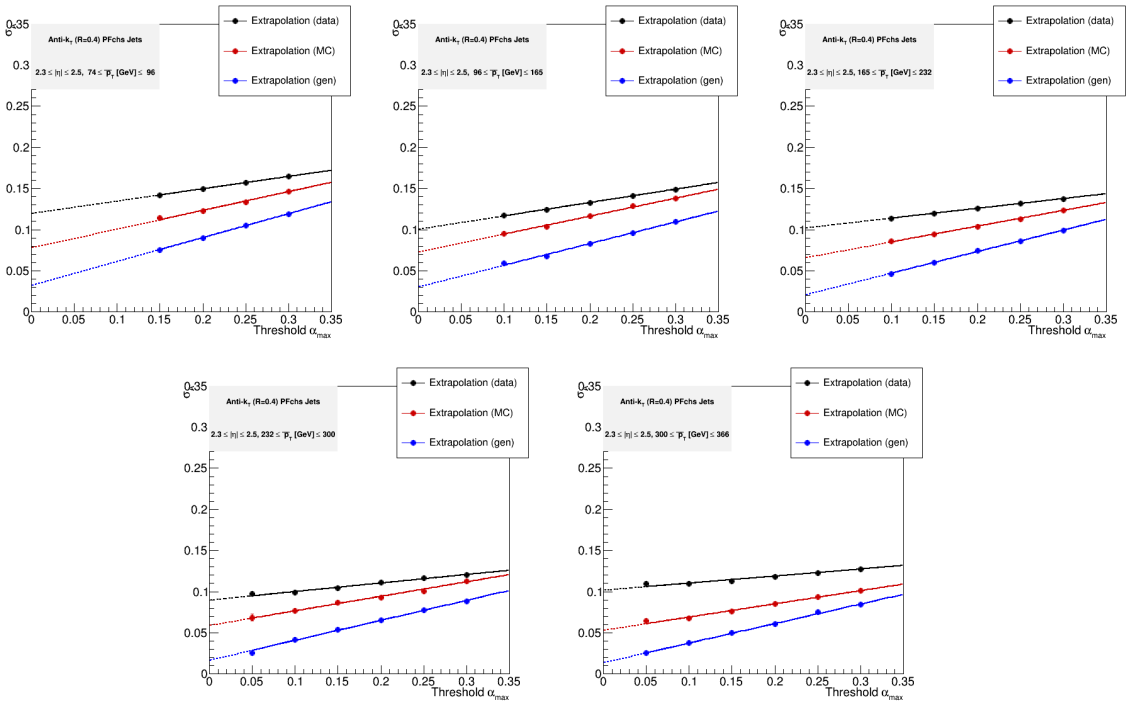

Figure A.19: Plots of the fits to asymmetry widths as a function of additional hadronic activity α_{max} in different p_T bins and $|\eta| \in (2.853, 2.964)$ for the widths calculated with forward extension. The black points and line represent data points, red color represents detector level simulation and blue represents truth level simulation.

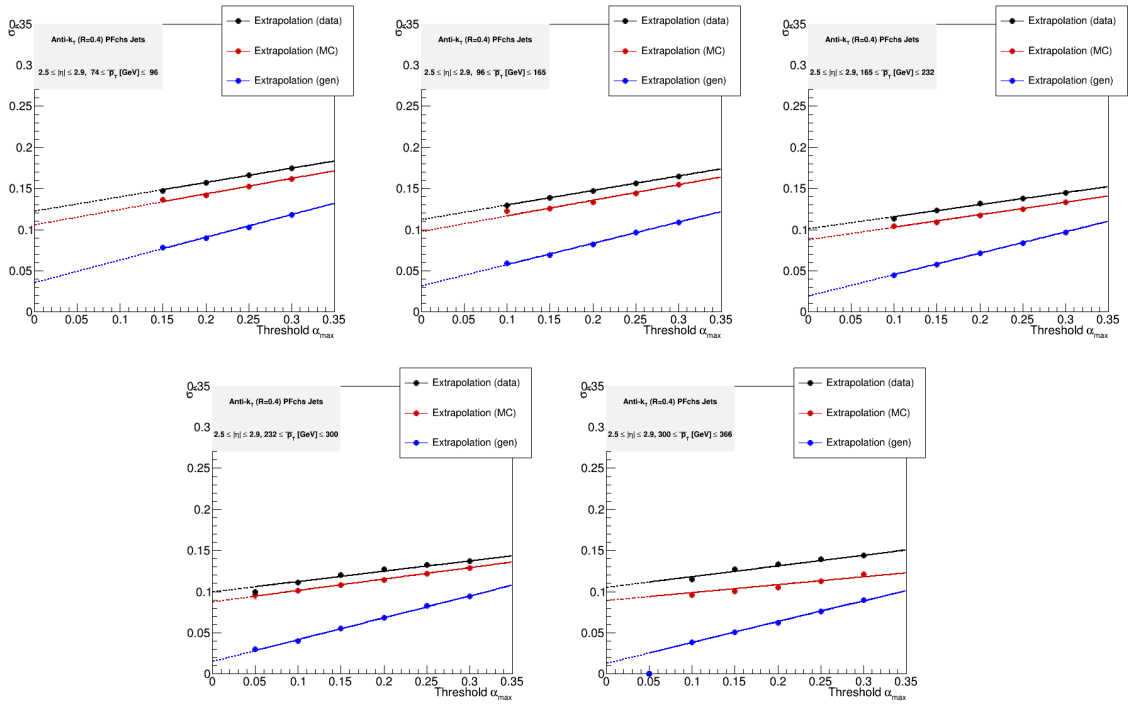

Figure A.20: Plots of the fits to asymmetry widths as a function of additional hadronic activity α_{max} in different p_T bins and $|\eta| \in (2.964, 3.139)$ for the widths calculated with forward extension. The black points and line represent data points, red color represents detector level simulation and blue represents truth level simulation.

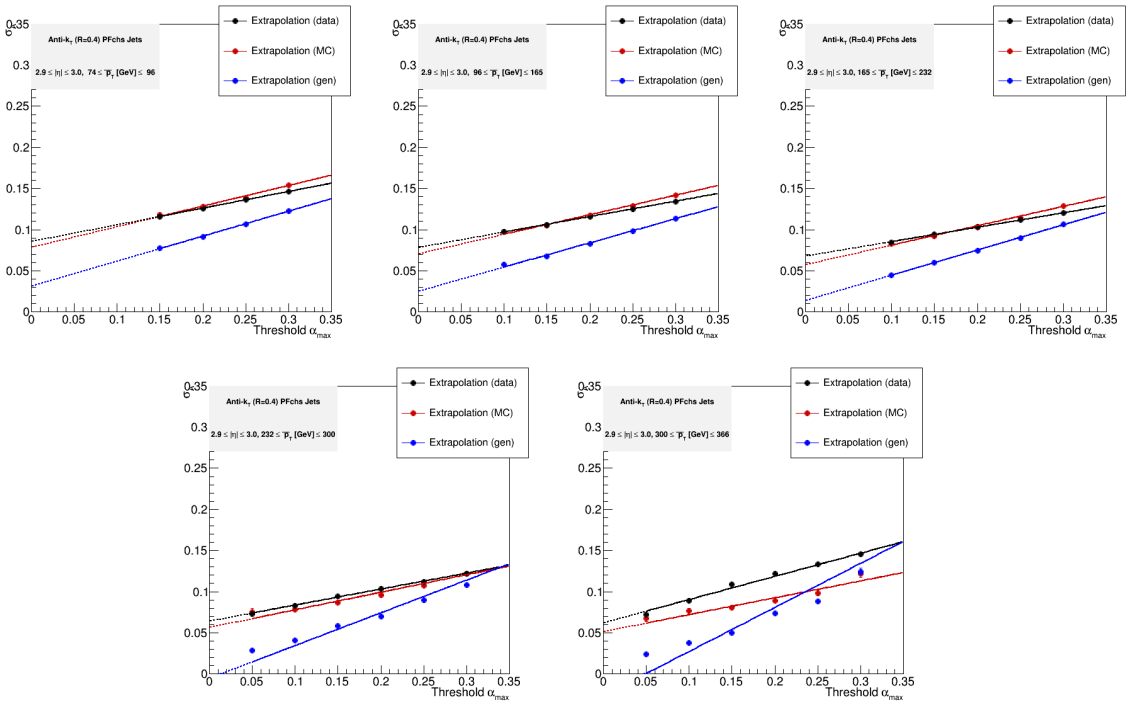

Figure A.21: Plots of the fits to asymmetry widths as a function of additional hadronic activity α_{max} in different p_T bins and $|\eta| \in (3.139, 5.191)$ for the widths calculated with forward extension. The black points and line represent data points, red color represents detector level simulation and blue represents truth level simulation.

B Rebalance and smear

Table B.1: Predicted QCD counts and uncertainties calculated using the rebalance and smear method for search bins 1-47 (L = 35.9 fb^{-1}).

bin	name	n(QCD)	stat	contam	trig	core	tail	prior	closure	btag	tot. syst.
1	Ht300,Mht300,NJets2,BTags0	326.2	±12.4	±0.29	±10.3	±118.9	±104.4	±16.3	±65.2	±0.0	±172.2
2	Ht500,Mht300,NJets2,BTags0	44.9	±1.5	±0.15	±0.95	±16.4	±14.4	±2.2	±9.0	±0.0	±23.7
3	Ht1000,Mht300,NJets2,BTags0	1.6	±0.16	±0.1	±0.04	±0.57	±0.5	±0.08	±0.31	±0.0	±0.84
4	Ht350,Mht350,NJets2,BTags0	126.4	±4.3	±0.12	±3.8	±46.0	±40.4	±6.3	±25.3	±0.0	±66.7
5	Ht500,Mht350,NJets2,BTags0	42.6	±7.2	±0.06	±0.98	±15.5	±13.6	±2.1	±8.5	±0.0	±22.4
6	Ht1000,Mht350,NJets2,BTags0	1.3	±0.06	±0.02	±0.03	±0.47	±0.41	±0.06	±0.26	±0.0	±0.68
7	Ht500,Mht500,NJets2,BTags0	4.5	±0.12	±0.01	±0.12	±1.6	±1.4	±0.22	±0.9	±0.0	±2.4
8	Ht1000,Mht500,NJets2,BTags0	0.03	±0.02	±0.0	±0.0	±0.01	±0.01	±0.0	±0.01	±0.0	±0.02
9	Ht750,Mht750,NJets2,BTags0	0.35	±0.06	±0.0	±0.01	±0.13	±0.11	±0.02	±0.07	±0.0	±0.18
10	Ht1500,Mht750,NJets2,BTags0	0.01	±0.01	±0.0	±0.0	±0.0	±0.0	±0.0	±0.0	±0.0	±0.0
11	Ht300,Mht300,NJets2,BTags1	43.8	±6.1	±0.04	±1.3	±18.1	±14.0	±2.2	±8.8	±0.0	±24.6
12	Ht500,Mht300,NJets2,BTags1	6.7	±2.7	±0.02	±0.14	±2.8	±2.1	±0.33	±1.3	±0.0	±3.7
13	Ht1000,Mht300,NJets2,BTags1	0.33	±0.02	±0.02	±0.01	±0.13	±0.1	±0.02	±0.07	±0.0	±0.18
14	Ht350,Mht350,NJets2,BTags1	19.6	±1.9	±0.02	±0.6	±8.1	±6.3	±0.98	±3.9	±0.0	±11.0
15	Ht500,Mht350,NJets2,BTags1	8.5	±3.0	±0.01	±0.19	±3.5	±2.7	±0.42	±1.7	±0.0	±4.8
16	Ht1000,Mht350,NJets2,BTags1	0.13	±0.04	±0.0	±0.0	±0.05	±0.04	±0.01	±0.03	±0.0	±0.07
17	Ht500,Mht500,NJets2,BTags1	1.5	±0.18	±0.0	±0.04	±0.61	±0.47	±0.07	±0.3	±0.0	±0.83
18	Ht1000,Mht500,NJets2,BTags1	0.03	±0.03	±0.0	±0.0	±0.01	±0.01	±0.0	±0.01	±0.0	±0.02
19	Ht750,Mht750,NJets2,BTags1	0.1	±0.03	±0.0	±0.0	±0.04	±0.03	±0.0	±0.02	±0.0	±0.06
20	Ht1500,Mht750,NJets2,BTags1	0.0	±0.01	±0.0	±0.0	±0.0	±0.0	±0.0	±0.0	±0.0	±0.0
21	Ht300,Mht300,NJets2,BTags2	3.0	±0.85	±0.0	±0.08	±1.6	±0.95	±0.15	±0.59	±3.0	±3.6
22	Ht500,Mht300,NJets2,BTags2	0.57	±0.17	±0.0	±0.01	±0.31	±0.18	±0.03	±0.11	±0.57	±0.69
23	Ht1000,Mht300,NJets2,BTags2	0.03	±0.01	±0.0	±0.0	±0.02	±0.01	±0.0	±0.01	±0.03	±0.04
24	Ht350,Mht350,NJets2,BTags2	1.0	±0.46	±0.0	±0.03	±0.57	±0.33	±0.05	±0.21	±1.0	±1.2
25	Ht500,Mht350,NJets2,BTags2	0.44	±0.05	±0.0	±0.01	±0.24	±0.14	±0.02	±0.09	±0.44	±0.52
26	Ht1000,Mht350,NJets2,BTags2	0.06	±0.04	±0.0	±0.0	±0.03	±0.02	±0.0	±0.01	±0.06	±0.08
27	Ht500,Mht500,NJets2,BTags2	0.03	±0.0	±0.0	±0.0	±0.02	±0.01	±0.0	±0.01	±0.03	±0.04
28	Ht1000,Mht500,NJets2,BTags2	0.0	±0.01	±0.0	±0.0	±0.0	±0.0	±0.0	±0.0	±0.0	±0.0
29	Ht750,Mht750,NJets2,BTags2	0.01	±0.01	±0.0	±0.0	±0.0	±0.0	±0.0	±0.0	±0.01	±0.01
30	Ht1500,Mht750,NJets2,BTags2	0.0	±0.01	±0.0	±0.0	±0.0	±0.0	±0.0	±0.0	±0.0	±0.0
31	Ht300,Mht300,NJets3,BTags0	272.7	±68.0	±0.31	±7.3	±51.0	±87.3	±13.6	±54.5	±0.0	±115.9
32	Ht500,Mht300,NJets3,BTags0	119.3	±7.7	±0.43	±2.2	±22.3	±38.2	±6.0	±23.9	±0.0	±50.7
33	Ht1000,Mht300,NJets3,BTags0	41.3	±2.2	±0.41	±1.7	±7.7	±13.2	±2.1	±8.3	±0.0	±17.6
34	Ht350,Mht350,NJets3,BTags0	113.7	±6.4	±0.13	±3.5	±21.3	±36.4	±5.7	±22.7	±0.0	±48.3
35	Ht500,Mht350,NJets3,BTags0	80.2	±9.1	±0.14	±1.6	±15.0	±25.7	±4.0	±16.0	±0.0	±34.1
36	Ht1000,Mht350,NJets3,BTags0	23.7	±1.1	±0.1	±0.68	±4.4	±7.6	±1.2	±4.7	±0.0	±10.1
37	Ht500,Mht500,NJets3,BTags0	5.5	±0.18	±0.01	±0.15	±1.0	±1.8	±0.27	±1.1	±0.0	±2.3
38	Ht1000,Mht500,NJets3,BTags0	1.3	±0.53	±0.0	±0.03	±0.24	±0.41	±0.06	±0.26	±0.0	±0.55
39	Ht750,Mht750,NJets3,BTags0	0.32	±0.03	±0.0	±0.01	±0.06	±0.1	±0.02	±0.06	±0.0	±0.14
40	Ht1500,Mht750,NJets3,BTags0	0.1	±0.01	±0.0	±0.0	±0.02	±0.03	±0.0	±0.02	±0.0	±0.04
41	Ht300,Mht300,NJets3,BTags1	58.9	±3.6	±0.15	±1.6	±8.4	±18.9	±2.9	±11.8	±0.0	±24.0
42	Ht500,Mht300,NJets3,BTags1	37.6	±4.3	±0.21	±0.73	±5.3	±12.0	±1.9	±7.5	±0.0	±15.3
43	Ht1000,Mht300,NJets3,BTags1	11.4	±0.83	±0.11	±0.5	±1.6	±3.6	±0.57	±2.3	±0.0	±4.7
44	Ht350,Mht350,NJets3,BTags1	22.3	±1.4	±0.05	±0.69	±3.2	±7.1	±1.1	±4.5	±0.0	±9.1
45	Ht500,Mht350,NJets3,BTags1	17.6	±3.4	±0.06	±0.35	±2.5	±5.6	±0.88	±3.5	±0.0	±7.2
46	Ht1000,Mht350,NJets3,BTags1	5.7	±0.45	±0.04	±0.16	±0.8	±1.8	±0.28	±1.1	±0.0	±2.3
47	Ht500,Mht500,NJets3,BTags1	1.3	±0.1	±0.0	±0.04	±0.19	±0.43	±0.07	±0.27	±0.0	±0.55

Table B.2: Predicted QCD counts and uncertainties calculated using the rebalance and smear method for search bins 48-110 (L = 35.9 fb^{-1}).

bin	name	n(QCD)	stat	contam	trig	core	tail	prior	closure	btag	tot. syst.
48	Ht1000,Mht500,NJets3,BTags1	0.38	±0.14	±0.0	±0.01	±0.05	±0.12	±0.02	±0.08	±0.0	±0.16
49	Ht750,Mht750,NJets3,BTags1	0.13	±0.01	±0.0	±0.0	±0.02	±0.04	±0.01	±0.03	±0.0	±0.05
50	Ht1500,Mht750,NJets3,BTags1	0.03	±0.01	±0.0	±0.0	±0.0	±0.01	±0.0	±0.01	±0.0	±0.01
51	Ht300,Mht300,NJets3,BTags2	9.0	±1.1	±0.05	±0.27	±1.8	±2.9	±0.45	±1.8	±0.0	±3.9
52	Ht500,Mht300,NJets3,BTags2	3.8	±1.2	±0.05	±0.07	±0.74	±1.2	±0.19	±0.75	±0.0	±1.6
53	Ht1000,Mht300,NJets3,BTags2	2.2	±0.18	±0.03	±0.11	±0.44	±0.71	±0.11	±0.45	±0.0	±0.96
54	Ht350,Mht350,NJets3,BTags2	2.7	±0.57	±0.01	±0.09	±0.52	±0.85	±0.13	±0.53	±0.0	±1.1
55	Ht500,Mht350,NJets3,BTags2	3.1	±0.23	±0.02	±0.06	±0.61	±1.0	±0.16	±0.62	±0.0	±1.3
56	Ht1000,Mht350,NJets3,BTags2	0.95	±0.16	±0.01	±0.03	±0.19	±0.3	±0.05	±0.19	±0.0	±0.41
57	Ht500,Mht500,NJets3,BTags2	0.22	±0.04	±0.0	±0.01	±0.04	±0.07	±0.01	±0.04	±0.0	±0.09
58	Ht1000,Mht500,NJets3,BTags2	0.1	±0.03	±0.0	±0.0	±0.02	±0.03	±0.0	±0.02	±0.0	±0.04
59	Ht750,Mht750,NJets3,BTags2	0.03	±0.02	±0.0	±0.0	±0.01	±0.01	±0.0	±0.01	±0.0	±0.01
60	Ht1500,Mht750,NJets3,BTags2	0.01	±0.01	±0.0	±0.0	±0.0	±0.0	±0.0	±0.0	±0.0	±0.01
61	Ht300,Mht300,NJets3,BTags3	0.35	±0.18	±0.01	±0.01	±0.19	±0.11	±0.02	±0.07	±0.35	±0.42
62	Ht500,Mht300,NJets3,BTags3	0.75	±0.52	±0.01	±0.01	±0.41	±0.24	±0.04	±0.15	±0.75	±0.9
63	Ht1000,Mht300,NJets3,BTags3	1.6	±0.16	±0.01	±0.07	±0.87	±0.51	±0.08	±0.32	±1.6	±1.9
64	Ht350,Mht350,NJets3,BTags3	0.09	±0.03	±0.01	±0.0	±0.05	±0.03	±0.0	±0.02	±0.09	±0.11
65	Ht500,Mht350,NJets3,BTags3	0.78	±0.18	±0.02	±0.01	±0.42	±0.25	±0.04	±0.16	±0.78	±0.94
66	Ht1000,Mht350,NJets3,BTags3	0.54	±0.15	±0.0	±0.03	±0.29	±0.17	±0.03	±0.11	±0.54	±0.65
67	Ht500,Mht500,NJets3,BTags3	0.1	±0.1	±0.0	±0.0	±0.06	±0.03	±0.01	±0.02	±0.1	±0.13
68	Ht1000,Mht500,NJets3,BTags3	0.02	±0.03	±0.0	±0.0	±0.01	±0.01	±0.0	±0.0	±0.02	±0.02
69	Ht750,Mht750,NJets3,BTags3	0.01	±0.02	±0.0	±0.0	±0.0	±0.0	±0.0	±0.0	±0.01	±0.01
70	Ht1500,Mht750,NJets3,BTags3	0.01	±0.03	±0.0	±0.0	±0.01	±0.0	±0.0	±0.0	±0.01	±0.02
71	Ht300,Mht300,NJets5,BTags0	49.1	±4.8	±0.09	±1.3	±8.6	±15.7	±2.5	±9.8	±0.0	±20.6
72	Ht500,Mht300,NJets5,BTags0	113.1	±4.4	±0.35	±2.1	±19.9	±36.2	±5.7	±22.6	±0.0	±47.5
73	Ht1000,Mht300,NJets5,BTags0	49.3	±0.87	±0.31	±2.0	±8.7	±15.8	±2.5	±9.9	±0.0	±20.8
74	Ht350,Mht350,NJets5,BTags0	12.7	±2.3	±0.03	±0.38	±2.2	±4.1	±0.63	±2.5	±0.0	±5.3
75	Ht500,Mht350,NJets5,BTags0	65.2	±2.3	±0.14	±1.2	±11.5	±20.9	±3.3	±13.0	±0.0	±27.4
76	Ht1000,Mht350,NJets5,BTags0	28.4	±1.3	±0.11	±0.75	±5.0	±9.1	±1.4	±5.7	±0.0	±12.0
77	Ht500,Mht500,NJets5,BTags0	3.2	±0.14	±0.01	±0.07	±0.56	±1.0	±0.16	±0.63	±0.0	±1.3
78	Ht1000,Mht500,NJets5,BTags0	2.5	±0.1	±0.01	±0.04	±0.44	±0.81	±0.13	±0.51	±0.0	±1.1
79	Ht750,Mht750,NJets5,BTags0	0.23	±0.04	±0.0	±0.01	±0.04	±0.07	±0.01	±0.05	±0.0	±0.1
80	Ht1500,Mht750,NJets5,BTags0	0.25	±0.06	±0.0	±0.0	±0.04	±0.08	±0.01	±0.05	±0.0	±0.11
81	Ht300,Mht300,NJets5,BTags1	12.8	±2.8	±0.13	±0.36	±1.8	±4.1	±0.64	±2.6	±0.0	±5.2
82	Ht500,Mht300,NJets5,BTags1	41.0	±3.9	±0.51	±0.71	±5.9	±13.1	±2.1	±8.2	±0.0	±16.7
83	Ht1000,Mht300,NJets5,BTags1	18.4	±0.76	±0.25	±0.75	±2.6	±5.9	±0.92	±3.7	±0.0	±7.5
84	Ht350,Mht350,NJets5,BTags1	3.7	±0.46	±0.03	±0.11	±0.53	±1.2	±0.18	±0.74	±0.0	±1.5
85	Ht500,Mht350,NJets5,BTags1	27.6	±2.9	±0.28	±0.5	±4.0	±8.8	±1.4	±5.5	±0.0	±11.3
86	Ht1000,Mht350,NJets5,BTags1	11.9	±0.66	±0.12	±0.33	±1.7	±3.8	±0.59	±2.4	±0.0	±4.8
87	Ht500,Mht500,NJets5,BTags1	1.4	±0.11	±0.01	±0.03	±0.21	±0.46	±0.07	±0.29	±0.0	±0.59
88	Ht1000,Mht500,NJets5,BTags1	1.3	±0.17	±0.01	±0.02	±0.19	±0.42	±0.07	±0.27	±0.0	±0.54
89	Ht750,Mht750,NJets5,BTags1	0.07	±0.01	±0.0	±0.0	±0.01	±0.02	±0.0	±0.01	±0.0	±0.03
90	Ht1500,Mht750,NJets5,BTags1	0.16	±0.07	±0.0	±0.0	±0.02	±0.05	±0.01	±0.03	±0.0	±0.07
91	Ht300,Mht300,NJets5,BTags2	2.9	±0.95	±0.06	±0.08	±0.19	±0.94	±0.15	±0.59	±0.0	±1.1
92	Ht500,Mht300,NJets5,BTags2	11.8	±1.8	±0.35	±0.21	±0.78	±3.8	±0.59	±2.4	±0.0	±4.6
93	Ht1000,Mht300,NJets5,BTags2	5.6	±0.38	±0.15	±0.26	±0.37	±1.8	±0.28	±1.1	±0.0	±2.2
94	Ht350,Mht350,NJets5,BTags2	1.0	±0.54	±0.02	±0.03	±0.07	±0.33	±0.05	±0.2	±0.0	±0.4
95	Ht500,Mht350,NJets5,BTags2	5.9	±1.0	±0.16	±0.11	±0.39	±1.9	±0.29	±1.2	±0.0	±2.3
96	Ht1000,Mht350,NJets5,BTags2	3.2	±0.15	±0.08	±0.09	±0.21	±1.0	±0.16	±0.64	±0.0	±1.2
97	Ht500,Mht500,NJets5,BTags2	0.34	±0.05	±0.01	±0.01	±0.02	±0.11	±0.02	±0.07	±0.0	±0.13
98	Ht1000,Mht500,NJets5,BTags2	0.16	±0.05	±0.0	±0.0	±0.01	±0.05	±0.01	±0.03	±0.0	±0.06
99	Ht750,Mht750,NJets5,BTags2	0.05	±0.05	±0.0	±0.0	±0.0	±0.02	±0.0	±0.01	±0.0	±0.02
100	Ht1500,Mht750,NJets5,BTags2	0.03	±0.03	±0.0	±0.0	±0.0	±0.01	±0.0	±0.01	±0.0	±0.01
101	Ht300,Mht300,NJets5,BTags3	0.5	±0.37	±0.04	±0.01	±0.19	±0.16	±0.03	±0.1	±0.5	±0.57
102	Ht500,Mht300,NJets5,BTags3	3.9	±2.3	±0.13	±0.06	±1.5	±1.3	±0.2	±0.79	±3.9	±4.5
103	Ht1000,Mht300,NJets5,BTags3	3.3	±0.42	±0.19	±0.15	±1.2	±1.0	±0.0	±0.65	±3.3	±3.7
104	Ht350,Mht350,NJets5,BTags3	0.18	±0.08	±0.01	±0.0	±0.07	±0.06	±0.01	±0.04	±0.18	±0.21
105	Ht500,Mht350,NJets5,BTags3	1.7	±0.13	±0.07	±0.03	±0.64	±0.55	±0.09	±0.34	±1.7	±1.9
106	Ht1000,Mht350,NJets5,BTags3	2.4	±0.29	±0.12	±0.09	±0.87	±0.75	±0.12	±0.47	±2.4	±2.7
107	Ht500,Mht500,NJets5,BTags3	0.2	±0.03	±0.01	±0.0	±0.07	±0.06	±0.01	±0.04	±0.2	±0.23
108	Ht1000,Mht500,NJets5,BTags3	0.11	±0.03	±0.0	±0.0	±0.04	±0.03	±0.01	±0.02	±0.11	±0.12
109	Ht750,Mht750,NJets5,BTags3	0.02	±0.04	±0.0	±0.0	±0.01	±0.01	±0.0	±0.0	±0.02	±0.03
110	Ht1500,Mht750,NJets5,BTags3	0.0	±0.02	±0.0	±0.0	±0.0	±0.0	±0.0	±0.0	±0.0	±0.01

Table B.3: Predicted QCD counts and uncertainties calculated using the rebalance and smear method for search bins 111-174 (L = 35.9 fb^{-1}).

bin	name	n(QCD)	stat	contam	trig	core	tail	prior	closure	btag	tot. syst.
111	Ht500,Mht300,NJets7,BTags0	30.0	±2.0	±0.13	±0.53	±4.7	±9.6	±1.5	±6.0	±0.0	±12.4
112	Ht1000,Mht300,NJets7,BTags0	20.5	±0.54	±0.14	±0.68	±3.2	±6.6	±1.0	±4.1	±0.0	±8.5
113	Ht500,Mht350,NJets7,BTags0	14.3	±1.9	±0.06	±0.21	±2.2	±4.6	±0.71	±2.9	±0.0	±5.9
114	Ht1000,Mht350,NJets7,BTags0	12.6	±0.68	±0.07	±0.26	±2.0	±4.0	±0.63	±2.5	±0.0	±5.2
115	Ht500,Mht500,NJets7,BTags0	0.88	±0.1	±0.0	±0.01	±0.14	±0.28	±0.04	±0.18	±0.0	±0.36
116	Ht1000,Mht500,NJets7,BTags0	1.6	±0.12	±0.01	±0.02	±0.24	±0.5	±0.08	±0.31	±0.0	±0.64
117	Ht750,Mht750,NJets7,BTags0	0.07	±0.02	±0.0	±0.0	±0.01	±0.02	±0.0	±0.01	±0.0	±0.03
118	Ht1500,Mht750,NJets7,BTags0	0.07	±0.01	±0.0	±0.0	±0.01	±0.02	±0.0	±0.01	±0.0	±0.03
119	Ht500,Mht300,NJets7,BTags1	11.2	±0.48	±0.32	±0.19	±2.0	±3.6	±0.56	±2.2	±0.0	±4.7
120	Ht1000,Mht300,NJets7,BTags1	8.3	±0.16	±0.23	±0.29	±1.5	±2.7	±0.42	±1.7	±0.0	±3.5
121	Ht500,Mht350,NJets7,BTags1	7.5	±0.4	±0.19	±0.11	±1.3	±2.4	±0.37	±1.5	±0.0	±3.2
122	Ht1000,Mht350,NJets7,BTags1	5.3	±0.45	±0.1	±0.12	±0.95	±1.7	±0.27	±1.1	±0.0	±2.2
123	Ht500,Mht500,NJets7,BTags1	0.36	±0.04	±0.0	±0.01	±0.06	±0.12	±0.02	±0.07	±0.0	±0.15
124	Ht1000,Mht500,NJets7,BTags1	0.98	±0.12	±0.02	±0.01	±0.17	±0.31	±0.05	±0.2	±0.0	±0.41
125	Ht750,Mht750,NJets7,BTags1	0.07	±0.03	±0.0	±0.0	±0.01	±0.02	±0.0	±0.01	±0.0	±0.03
126	Ht1500,Mht750,NJets7,BTags1	0.03	±0.01	±0.0	±0.0	±0.01	±0.01	±0.0	±0.01	±0.0	±0.01
127	Ht500,Mht300,NJets7,BTags2	5.3	±0.49	±0.44	±0.09	±0.59	±1.7	±0.26	±1.1	±0.0	±2.1
128	Ht1000,Mht300,NJets7,BTags2	3.2	±0.09	±0.27	±0.12	±0.36	±1.0	±0.16	±0.64	±0.0	±1.3
129	Ht500,Mht350,NJets7,BTags2	2.5	±0.25	±0.23	±0.04	±0.28	±0.81	±0.13	±0.5	±0.0	±1.0
130	Ht1000,Mht350,NJets7,BTags2	1.9	±0.13	±0.12	±0.04	±0.22	±0.62	±0.1	±0.39	±0.0	±0.78
131	Ht500,Mht500,NJets7,BTags2	0.1	±0.01	±0.0	±0.0	±0.01	±0.03	±0.0	±0.02	±0.0	±0.04
132	Ht1000,Mht500,NJets7,BTags2	0.22	±0.06	±0.02	±0.0	±0.02	±0.07	±0.01	±0.04	±0.0	±0.09
133	Ht750,Mht750,NJets7,BTags2	0.03	±0.01	±0.0	±0.0	±0.0	±0.01	±0.0	±0.01	±0.0	±0.01
134	Ht1500,Mht750,NJets7,BTags2	0.06	±0.02	±0.0	±0.0	±0.01	±0.02	±0.0	±0.01	±0.0	±0.02
135	Ht500,Mht300,NJets7,BTags3	2.9	±0.63	±0.48	±0.05	±0.74	±0.94	±0.15	±0.59	±2.9	±3.3
136	Ht1000,Mht300,NJets7,BTags3	2.4	±0.3	±0.31	±0.09	±0.61	±0.77	±0.12	±0.48	±2.4	±2.7
137	Ht500,Mht350,NJets7,BTags3	1.2	±0.12	±0.16	±0.02	±0.3	±0.38	±0.06	±0.24	±1.2	±1.3
138	Ht1000,Mht350,NJets7,BTags3	2.1	±0.31	±0.17	±0.04	±0.52	±0.66	±0.1	±0.41	±2.1	±2.3
139	Ht500,Mht500,NJets7,BTags3	0.11	±0.03	±0.0	±0.0	±0.03	±0.04	±0.01	±0.02	±0.11	±0.12
140	Ht1000,Mht500,NJets7,BTags3	0.22	±0.08	±0.01	±0.0	±0.05	±0.07	±0.01	±0.04	±0.22	±0.24
141	Ht750,Mht750,NJets7,BTags3	0.03	±0.04	±0.0	±0.0	±0.01	±0.01	±0.0	±0.01	±0.03	±0.03
142	Ht1500,Mht750,NJets7,BTags3	0.01	±0.02	±0.01	±0.0	±0.0	±0.0	±0.0	±0.0	±0.01	±0.01
143	Ht500,Mht300,NJets9,BTags0	2.9	±0.26	±0.02	±0.05	±0.65	±0.93	±0.14	±0.58	±0.0	±1.3
144	Ht1000,Mht300,NJets9,BTags0	4.2	±0.28	±0.05	±0.14	±0.94	±1.3	±0.21	±0.84	±0.0	±1.9
145	Ht500,Mht350,NJets9,BTags0	0.97	±0.08	±0.01	±0.01	±0.22	±0.31	±0.05	±0.19	±0.0	±0.43
146	Ht1000,Mht350,NJets9,BTags0	3.1	±0.2	±0.03	±0.07	±0.69	±0.99	±0.15	±0.62	±0.0	±1.4
147	Ht500,Mht500,NJets9,BTags0	0.1	±0.05	±0.0	±0.0	±0.02	±0.03	±0.0	±0.02	±0.0	±0.04
148	Ht1000,Mht500,NJets9,BTags0	0.47	±0.05	±0.01	±0.01	±0.1	±0.15	±0.02	±0.09	±0.0	±0.21
149	Ht750,Mht750,NJets9,BTags0	0.01	±0.02	±0.0	±0.0	±0.0	±0.0	±0.0	±0.0	±0.0	±0.0
150	Ht1500,Mht750,NJets9,BTags0	0.05	±0.02	±0.0	±0.0	±0.01	±0.02	±0.0	±0.01	±0.0	±0.02
151	Ht500,Mht300,NJets9,BTags1	1.0	±0.06	±0.07	±0.02	±0.13	±0.33	±0.05	±0.2	±0.0	±0.42
152	Ht1000,Mht300,NJets9,BTags1	2.4	±0.06	±0.12	±0.08	±0.3	±0.78	±0.12	±0.49	±0.0	±0.99
153	Ht500,Mht350,NJets9,BTags1	0.53	±0.05	±0.02	±0.01	±0.07	±0.17	±0.03	±0.11	±0.0	±0.22
154	Ht1000,Mht350,NJets9,BTags1	1.5	±0.05	±0.07	±0.04	±0.19	±0.47	±0.07	±0.3	±0.0	±0.6
155	Ht500,Mht500,NJets9,BTags1	0.03	±0.03	±0.0	±0.0	±0.0	±0.01	±0.0	±0.01	±0.0	±0.01
156	Ht1000,Mht500,NJets9,BTags1	0.2	±0.02	±0.0	±0.0	±0.02	±0.06	±0.01	±0.04	±0.0	±0.08
157	Ht750,Mht750,NJets9,BTags1	0.01	±0.01	±0.0	±0.0	±0.0	±0.0	±0.0	±0.0	±0.0	±0.0
158	Ht1500,Mht750,NJets9,BTags1	0.02	±0.01	±0.0	±0.0	±0.0	±0.01	±0.0	±0.0	±0.0	±0.01
159	Ht500,Mht300,NJets9,BTags2	0.4	±0.05	±0.15	±0.01	±0.11	±0.13	±0.02	±0.08	±0.0	±0.24
160	Ht1000,Mht300,NJets9,BTags2	1.3	±0.15	±0.28	±0.05	±0.36	±0.42	±0.07	±0.26	±0.0	±0.68
161	Ht500,Mht350,NJets9,BTags2	0.3	±0.08	±0.03	±0.0	±0.08	±0.1	±0.01	±0.06	±0.0	±0.14
162	Ht1000,Mht350,NJets9,BTags2	0.63	±0.02	±0.12	±0.01	±0.17	±0.2	±0.03	±0.13	±0.0	±0.32
163	Ht500,Mht500,NJets9,BTags2	0.01	±0.01	±0.0	±0.0	±0.0	±0.0	±0.0	±0.0	±0.0	±0.01
164	Ht1000,Mht500,NJets9,BTags2	0.09	±0.02	±0.01	±0.0	±0.03	±0.03	±0.0	±0.02	±0.0	±0.04
165	Ht750,Mht750,NJets9,BTags2	0.0	±0.01	±0.0	±0.0	±0.0	±0.0	±0.0	±0.0	±0.0	±0.0
166	Ht1500,Mht750,NJets9,BTags2	0.01	±0.02	±0.0	±0.0	±0.0	±0.0	±0.0	±0.0	±0.0	±0.0
167	Ht500,Mht300,NJets9,BTags3	0.47	±0.13	±0.07	±0.01	±0.22	±0.15	±0.02	±0.09	±0.47	±0.56
168	Ht1000,Mht300,NJets9,BTags3	2.1	±0.3	±0.27	±0.07	±0.96	±0.67	±0.1	±0.42	±2.1	±2.4
169	Ht500,Mht350,NJets9,BTags3	0.1	±0.03	±0.02	±0.0	±0.04	±0.03	±0.0	±0.02	±0.1	±0.11
170	Ht1000,Mht350,NJets9,BTags3	1.3	±0.18	±0.25	±0.03	±0.6	±0.41	±0.0	±0.26	±1.3	±1.5
171	Ht500,Mht500,NJets9,BTags3	0.01	±0.02	±0.0	±0.0	±0.0	±0.0	±0.0	±0.0	±0.01	±0.01
172	Ht1000,Mht500,NJets9,BTags3	0.13	±0.14	±0.03	±0.0	±0.06	±0.04	±0.01	±0.03	±0.13	±0.15
173	Ht750,Mht750,NJets9,BTags3	0.01	±0.05	±0.0	±0.0	±0.01	±0.0	±0.0	±0.0	±0.01	±0.02
174	Ht1500,Mht750,NJets9,BTags3	0.02	±0.05	±0.0	±0.0	±0.01	±0.01	±0.0	±0.0	±0.02	±0.02

C Supersymmetry search

Table C.1: Observed number of events and pre-fit background predictions in the $N_{jets} = 2$ search bins.

Bin	$\not{H}_T$ [GeV]	H_T [GeV]	N_{jets}	N_{b-jets}	Lost-e/μ	$\tau \to$ had	$Z \to \nu\bar{\nu}$	QCD	Total Pred.	Obs.
1	300–350	300–500	2	0	$4069^{+67+320}_{-67-320}$	$2744^{+37+510}_{-37-500}$	$13231^{+67+760}_{-66-740}$	$326^{+12+170}_{-12-120}$	$20370^{+120+980}_{-120-960}$	21626
2	300–350	500–1000	2	0	326^{+22+36}_{-22-36}	226^{+11+43}_{-11-42}	944^{+18+55}_{-18-54}	45^{+2+24}_{-2-17}	1541^{+37+82}_{-37-79}	1583
3	300–350	>1000	2	0	$15.2^{+5.8+2.3}_{-5.1-2.3}$	$8.7^{+2.1+2.1}_{-2.0-2.1}$	$50.9^{+4.5+4.4}_{-4.1-3.8}$	$1.57^{+0.16+0.84}_{-0.16-0.61}$	$76.3^{+9.1+5.5}_{-8.2-5.0}$	102
4	350–500	350–500	2	0	$2049^{+46+160}_{-46-160}$	$1553^{+27+290}_{-27-290}$	$9347^{+57+540}_{-57-520}$	126^{+4+67}_{-4-48}	$13076^{+93+630}_{-93-620}$	14019
5	350–500	500–1000	2	0	631^{+25+54}_{-25-54}	439^{+14+84}_{-14-84}	$2502^{+30+150}_{-30-140}$	43^{+7+22}_{-7-16}	$3615^{+49+180}_{-49-170}$	3730
6	350–500	>1000	2	0	$13.5^{+4.9+1.9}_{-4.3-1.9}$	$13.4^{+2.4+2.6}_{-2.3-2.6}$	$94.0^{+6.2+7.9}_{-5.8-6.9}$	$1.30^{+0.06+0.68}_{-0.06-0.49}$	$122.1^{+9.5+8.6}_{-8.8-7.6}$	139
7	500–750	500–1000	2	0	303^{+17+29}_{-17-29}	247^{+10+48}_{-10-47}	$2328^{+30+170}_{-29-160}$	$4.5^{+0.1+2.4}_{-0.1-1.7}$	$2883^{+40+180}_{-40-170}$	3018
8	500–750	>1000	2	0	$5.8^{+2.7+1.5}_{-2.2-1.5}$	$5.3^{+1.4+1.3}_{-1.3-1.3}$	$66.2^{+5.4+5.3}_{-5.0-5.1}$	$0.03^{+0.02+0.02}_{-0.02-0.01}$	$77.3^{+6.8+5.7}_{-6.1-5.4}$	96
9	>750	750–1500	2	0	$17.3^{+4.5+3.0}_{-4.1-3.0}$	$17.4^{+2.5+4.5}_{-2.4-4.5}$	295^{+11+41}_{-11-38}	$0.35^{+0.06+0.18}_{-0.06-0.13}$	330^{+13+42}_{-12-38}	272
10	>750	>1500	2	0	$0.0^{+1.8+0.0}_{-0.0-0.0}$	$0.38^{+0.54+0.09}_{-0.29-0.09}$	$12.6^{+3.0+2.1}_{-2.4-1.9}$	$0.01^{+0.01+0.00}_{-0.01-0.00}$	$13.0^{+3.8+2.1}_{-2.5-1.9}$	12
11	300–350	300–500	2	1	370^{+21+31}_{-21-31}	288^{+11+63}_{-11-63}	1361^{+7+140}_{-7-140}	44^{+6+25}_{-6-17}	$2063^{+33+160}_{-33-160}$	1904
12	300–350	500–1000	2	1	51^{+10+7}_{-10-7}	$31.6^{+4.2+7.2}_{-4.2-7.2}$	97^{+2+10}_{-2-10}	$6.7^{+2.7+3.7}_{-2.7-2.5}$	186^{+15+15}_{-14-14}	186
13	300–350	>1000	2	1	$1.1^{+2.3+0.2}_{-1.1-0.0}$	$2.0^{+1.1+0.5}_{-1.0-0.5}$	$5.23^{+0.46+0.63}_{-0.42-0.59}$	$0.33^{+0.02+0.18}_{-0.02-0.13}$	$8.7^{+3.4+0.9}_{-2.1-0.8}$	13
14	350–500	350–500	2	1	215^{+16+19}_{-16-19}	179^{+9+39}_{-9-39}	962^{+6+99}_{-6-98}	20^{+2+11}_{-2-8}	$1376^{+26+110}_{-26-110}$	1212
15	350–500	500–1000	2	1	$69.8^{+9.9+7.5}_{-9.8-7.5}$	$43.3^{+4.4+9.7}_{-4.4-9.6}$	257^{+3+27}_{-3-26}	$8.5^{+3.0+4.8}_{-3.0-3.2}$	379^{+15+30}_{-15-29}	409
16	350–500	>1000	2	1	$3.7^{+2.5+0.7}_{-1.9-0.7}$	$3.1^{+1.1+0.9}_{-1.0-0.9}$	$9.7^{+0.6+1.2}_{-0.6-1.1}$	$0.13^{+0.04+0.07}_{-0.04-0.05}$	$16.6^{+3.7+1.6}_{-3.0-1.6}$	27
17	500–750	500–1000	2	1	$28.9^{+5.8+3.3}_{-5.6-3.3}$	$26.0^{+2.9+5.8}_{-2.9-5.8}$	240^{+3+27}_{-3-26}	$1.48^{+0.18+0.83}_{-0.18-0.56}$	296^{+9+28}_{-9-27}	321
18	500–750	>1000	2	1	$5.1^{+6.2+1.6}_{-4.1-1.6}$	$0.36^{+0.55+0.12}_{-0.30-0.12}$	$6.81^{+0.56+0.80}_{-0.52-0.78}$	$0.03^{+0.03+0.02}_{-0.03-0.00}$	$12.3^{+6.8+1.8}_{-4.5-1.7}$	14
19	>750	750–1500	2	1	$3.8^{+2.2+0.8}_{-1.7-0.8}$	$4.1^{+1.5+1.1}_{-1.4-1.1}$	$30.4^{+1.1+5.0}_{-1.1-4.7}$	$0.10^{+0.03+0.06}_{-0.03-0.04}$	$38.4^{+3.9+5.1}_{-3.3-4.8}$	31
20	>750	>1500	2	1	$0.0^{+1.4+0.0}_{-0.0-0.0}$	$0.34^{+0.51+0.13}_{-0.22-0.13}$	$1.29^{+0.31+0.24}_{-0.25-0.23}$	$0.00^{+0.01+0.00}_{-0.00-0.00}$	$1.6^{+2.0+0.3}_{-0.3-0.3}$	1
21	300–350	300–500	2	2	$14.1^{+4.5+2.6}_{-4.0-2.6}$	$12.9^{+2.3+2.8}_{-2.2-2.8}$	49^{+0+17}_{-0-17}	$3.0^{+0.8+3.6}_{-0.8-2.1}$	79^{+7+18}_{-6-18}	122
22	300–350	500–1000	2	2	$2.8^{+2.4+0.9}_{-1.7-0.9}$	$2.0^{+1.1+1.0}_{-0.9-1.0}$	$3.5^{+0.1+1.2}_{-0.1-1.2}$	$0.57^{+0.17+0.69}_{-0.17-0.40}$	$8.9^{+3.5+2.0}_{-2.6-1.9}$	11
23	300–350	>1000	2	2	$0.0^{+2.2+0.0}_{-0.0-0.0}$	$0.00^{+0.46+0.00}_{-0.00-0.00}$	$0.19^{+0.02+0.07}_{-0.01-0.07}$	$0.03^{+0.01+0.04}_{-0.01-0.02}$	$0.2^{+2.6+0.1}_{-0.0-0.1}$	0
24	350–500	350–500	2	2	$11.4^{+4.5+2.5}_{-3.9-2.5}$	$6.3^{+1.7+2.1}_{-1.6-2.1}$	35^{+0+12}_{-0-12}	$1.0^{+0.5+1.2}_{-0.5-0.6}$	53^{+6+13}_{-6-13}	84
25	350–500	500–1000	2	2	$6.1^{+2.9+1.5}_{-2.4-1.5}$	$2.9^{+1.2+0.8}_{-1.1-0.8}$	$9.3^{+0.1+3.3}_{-0.1-3.3}$	$0.44^{+0.05+0.52}_{-0.05-0.39}$	$18.7^{+4.1+3.8}_{-3.5-3.7}$	23
26	350–500	>1000	2	2	$0.0^{+1.1+0.0}_{-0.0-0.0}$	$0.00^{+0.46+0.00}_{-0.00-0.00}$	$0.35^{+0.02+0.13}_{-0.02-0.13}$	$0.06^{+0.04+0.08}_{-0.04-0.02}$	$0.4^{+1.5+0.1}_{-0.0-0.1}$	2
27	500–750	500–1000	2	2	$1.4^{+2.9+0.4}_{-1.4-0.0}$	$2.03^{+0.84+0.61}_{-0.70-0.61}$	$8.6^{+0.1+3.1}_{-0.1-3.1}$	$0.03^{+0.01+0.04}_{-0.01-0.03}$	$12.1^{+3.7+3.2}_{-2.1-3.2}$	16
28	500–750	>1000	2	2	$0.0^{+2.2+0.0}_{-0.0-0.0}$	$0.00^{+0.46+0.00}_{-0.00-0.00}$	$0.24^{+0.02+0.09}_{-0.02-0.09}$	$0.00^{+0.01+0.00}_{-0.00-0.00}$	$0.2^{+2.7+0.1}_{-0.0-0.1}$	0
29	>750	750–1500	2	2	$0.0^{+1.6+0.0}_{-0.0-0.0}$	$0.07^{+0.46+0.07}_{-0.04-0.06}$	$1.09^{+0.04+0.41}_{-0.04-0.41}$	$0.01^{+0.01+0.01}_{-0.01-0.00}$	$1.2^{+2.1+0.4}_{-0.1-0.4}$	4
30	>750	>1500	2	2	$0.0^{+2.0+0.0}_{-0.0-0.0}$	$0.00^{+0.46+0.00}_{-0.00-0.00}$	$0.05^{+0.01+0.02}_{-0.01-0.02}$	$0.00^{+0.01+0.00}_{-0.00-0.00}$	$0.0^{+2.5+0.0}_{-0.0-0.0}$	0

Table C.2: Observed number of events and pre-fit background predictions in the $3 \leq N_{jets} \leq 4$ search bins.

Bin	$\not{H}_T$ [GeV]	H_T [GeV]	N_{jets}	N_{b-jets}	Lost-e/μ	$\tau \to$ had	$Z \to \nu\bar{\nu}$	QCD	Total Pred.	Obs.
31	300–350	300–500	3–4	0	$2830^{+45+200}_{-45-200}$	$2152^{+29+160}_{-29-150}$	$8353^{+52+480}_{-52-470}$	$273^{+68+120}_{-68-100}$	$13608^{+110+560}_{-110-540}$	14520
32	300–350	500–1000	3–4	0	$1125^{+25+120}_{-25-120}$	$909^{+18+100}_{-18-100}$	$2487^{+29+140}_{-28-140}$	119^{+8+51}_{-8-45}	$4640^{+52+220}_{-52-210}$	4799
33	300–350	>1000	3–4	0	$72.7^{+7.1+6.1}_{-7.1-6.1}$	$65.3^{+5.2+6.4}_{-5.2-6.3}$	176^{+8+14}_{-8-12}	41^{+2+18}_{-2-16}	356^{+15+24}_{-15-22}	354
34	350–500	350–500	3–4	0	$1439^{+37+110}_{-37-110}$	$930^{+19+120}_{-19-110}$	$5014^{+41+280}_{-41-280}$	114^{+6+48}_{-6-43}	$7496^{+70+330}_{-69-320}$	7973
35	350–500	500–1000	3–4	0	$1402^{+27+140}_{-27-140}$	$1253^{+22+120}_{-22-120}$	$4811^{+40+270}_{-40-260}$	80^{+9+34}_{-9-31}	$7547^{+65+330}_{-64-320}$	7735
36	350–500	>1000	3–4	0	103^{+8+11}_{-8-11}	$77.0^{+5.9+7.6}_{-5.9-7.5}$	303^{+11+24}_{-10-21}	24^{+1+10}_{-1-9}	506^{+18+30}_{-17-26}	490
37	500–750	500–1000	3–4	0	339^{+15+33}_{-15-33}	297^{+10+26}_{-10-26}	$2143^{+28+150}_{-28-140}$	$5.5^{+0.2+2.3}_{-0.2-2.1}$	$2785^{+37+160}_{-37-150}$	2938
38	500–750	>1000	3–4	0	$33.8^{+4.4+3.6}_{-4.3-3.6}$	$30.5^{+3.4+2.9}_{-3.4-2.9}$	219^{+10+16}_{-9-15}	$1.29^{+0.53+0.55}_{-0.53-0.49}$	284^{+12+17}_{-12-16}	303
39	>750	750–1500	3–4	0	$28.2^{+4.4+3.7}_{-4.3-3.7}$	$26.0^{+2.9+3.4}_{-2.9-3.4}$	319^{+11+44}_{-11-40}	$0.32^{+0.03+0.14}_{-0.03-0.12}$	373^{+14+44}_{-13-41}	334
40	>750	>1500	3–4	0	$2.9^{+2.0+0.7}_{-1.5-0.7}$	$1.38^{+0.66+0.17}_{-0.48-0.17}$	$27.8^{+3.9+4.1}_{-3.5-3.8}$	$0.10^{+0.01+0.04}_{-0.01-0.04}$	$32.2^{+4.8+4.2}_{-4.0-3.9}$	46
41	300–350	300–500	3–4	1	746^{+25+55}_{-25-55}	627^{+15+48}_{-15-47}	1235^{+8+130}_{-8-120}	59^{+4+24}_{-4-22}	$2667^{+41+150}_{-41-150}$	2677
42	300–350	500–1000	3–4	1	296^{+15+25}_{-15-25}	262^{+9+27}_{-9-27}	385^{+4+39}_{-4-39}	38^{+4+15}_{-4-14}	981^{+24+56}_{-24-56}	1048
43	300–350	>1000	3–4	1	$20.8^{+4.1+2.1}_{-4.0-2.1}$	$19.0^{+2.6+1.8}_{-2.5-1.8}$	$27.6^{+1.3+3.2}_{-1.2-3.0}$	$11.4^{+0.8+4.7}_{-0.8-4.4}$	$78.8^{+6.9+6.3}_{-6.6-6.0}$	92
44	350–500	350–500	3–4	1	321^{+17+25}_{-17-25}	263^{+10+22}_{-10-21}	738^{+6+74}_{-6-74}	$22.3^{+1.4+9.1}_{-1.4-8.5}$	1343^{+28+82}_{-28-81}	1332
45	350–500	500–1000	3–4	1	329^{+14+26}_{-14-26}	324^{+11+26}_{-11-26}	737^{+6+74}_{-6-74}	$17.6^{+3.4+7.2}_{-3.4-6.7}$	1407^{+26+83}_{-26-83}	1515
46	350–500	>1000	3–4	1	$20.4^{+4.0+2.0}_{-3.8-2.0}$	$19.9^{+2.9+1.8}_{-2.9-1.7}$	$47.5^{+1.7+5.5}_{-1.6-5.1}$	$5.7^{+0.5+2.3}_{-0.5-2.2}$	$93.4^{+7.1+6.5}_{-6.9-6.2}$	113
47	500–750	500–1000	3–4	1	$69.7^{+7.4+6.6}_{-7.3-6.6}$	$56.0^{+4.1+5.0}_{-4.1-4.9}$	322^{+4+35}_{-4-35}	$1.34^{+0.10+0.55}_{-0.10-0.51}$	449^{+12+36}_{-12-36}	472
48	500–750	>1000	3–4	1	$15.3^{+3.4+1.9}_{-3.3-1.9}$	$7.0^{+1.4+0.7}_{-1.4-0.7}$	$34.4^{+1.5+3.8}_{-1.4-3.8}$	$0.38^{+0.14+0.16}_{-0.14-0.15}$	$57.0^{+5.1+4.4}_{-4.9-4.3}$	57
49	>750	750–1500	3–4	1	$3.3^{+1.5+0.5}_{-1.3-0.5}$	$4.8^{+1.3+0.8}_{-1.2-0.8}$	$48.5^{+1.7+7.9}_{-1.7-7.3}$	$0.13^{+0.01+0.05}_{-0.01-0.05}$	$56.8^{+3.3+7.9}_{-3.0-7.4}$	61
50	>750	>1500	3–4	1	$1.0^{+1.2+0.3}_{-0.7-0.3}$	$0.77^{+0.75+0.16}_{-0.59-0.16}$	$4.40^{+0.62+0.75}_{-0.55-0.71}$	$0.03^{+0.01+0.01}_{-0.01-0.01}$	$6.2^{+2.0+0.8}_{-1.4-0.8}$	8
51	300–350	300–500	3–4	2	137^{+11+11}_{-11-11}	133^{+7+11}_{-7-11}	145^{+1+26}_{-1-26}	$9.0^{+1.1+3.9}_{-1.1-3.4}$	424^{+18+31}_{-17-31}	464
52	300–350	500–1000	3–4	2	$92.3^{+9.1+9.5}_{-9.0-9.5}$	$85.6^{+5.7+7.5}_{-5.7-7.4}$	$53.0^{+0.6+9.6}_{-0.6-9.6}$	$3.8^{+1.2+1.6}_{-1.2-1.4}$	235^{+15+16}_{-15-15}	227
53	300–350	>1000	3–4	2	$3.4^{+2.2+0.8}_{-1.7-0.8}$	$2.41^{+0.91+0.50}_{-0.78-0.50}$	$3.95^{+0.18+0.75}_{-0.17-0.73}$	$2.23^{+0.18+0.96}_{-0.18-0.86}$	$12.0^{+3.1+1.6}_{-2.5-1.5}$	17
54	350–500	350–500	3–4	2	$39.6^{+6.1+3.8}_{-5.9-3.8}$	$39.8^{+3.9+3.8}_{-3.8-3.8}$	84^{+1+15}_{-1-15}	$2.7^{+0.6+1.1}_{-0.6-1.0}$	166^{+10+16}_{-10-16}	208
55	350–500	500–1000	3–4	2	$83.9^{+8.2+7.8}_{-8.1-7.8}$	$69.4^{+4.9+5.9}_{-4.9-5.8}$	97^{+1+18}_{-1-17}	$3.1^{+0.2+1.3}_{-0.2-1.2}$	254^{+13+20}_{-13-20}	286
56	350–500	>1000	3–4	2	$6.2^{+4.0+1.0}_{-3.6-1.0}$	$3.8^{+1.1+0.6}_{-1.0-0.6}$	$6.8^{+0.2+1.3}_{-0.2-1.3}$	$0.95^{+0.16+0.41}_{-0.16-0.36}$	$17.7^{+5.2+1.8}_{-4.6-1.8}$	25
57	500–750	500–1000	3–4	2	$11.8^{+3.3+2.0}_{-3.1-2.0}$	$10.5^{+1.8+1.6}_{-1.7-1.6}$	$39.7^{+0.5+7.4}_{-0.5-7.3}$	$0.22^{+0.04+0.09}_{-0.04-0.08}$	$62.1^{+5.1+7.8}_{-4.8-7.7}$	64
58	500–750	>1000	3–4	2	$2.6^{+2.3+0.6}_{-1.6-0.6}$	$2.9^{+1.5+0.6}_{-1.5-0.6}$	$4.90^{+0.21+0.92}_{-0.21-0.91}$	$0.10^{+0.03+0.04}_{-0.03-0.04}$	$10.5^{+3.8+1.2}_{-3.1-1.2}$	13
59	>750	750–1500	3–4	2	$0.0^{+1.1+0.0}_{-0.0-0.0}$	$0.32^{+0.48+0.09}_{-0.13-0.09}$	$6.3^{+0.2+1.4}_{-0.2-1.3}$	$0.03^{+0.02+0.01}_{-0.02-0.01}$	$6.6^{+1.6+1.4}_{-0.3-1.3}$	4
60	>750	>1500	3–4	2	$0.0^{+1.1+0.0}_{-0.0-0.0}$	$0.03^{+0.46+0.01}_{-0.02-0.01}$	$0.65^{+0.09+0.15}_{-0.08-0.14}$	$0.01^{+0.01+0.01}_{-0.01-0.00}$	$0.7^{+1.6+0.1}_{-0.1-0.1}$	1
61	300–350	300–500	3–4	≥3	$6.4^{+2.8+0.7}_{-2.3-0.7}$	$10.3^{+1.9+2.7}_{-1.9-2.7}$	$5.0^{+0.0+2.8}_{-0.0-2.8}$	$0.35^{+0.18+0.42}_{-0.18-0.16}$	$22.0^{+4.7+3.9}_{-4.2-3.9}$	27
62	300–350	500–1000	3–4	≥3	$4.9^{+2.7+0.6}_{-2.2-0.6}$	$6.2^{+1.4+1.7}_{-1.3-1.7}$	$2.5^{+0.0+1.4}_{-0.0-1.4}$	$0.75^{+0.52+0.90}_{-0.52-0.24}$	$14.4^{+4.2+2.4}_{-3.6-2.2}$	20
63	300–350	>1000	3–4	≥3	$0.0^{+1.1+0.0}_{-0.0-0.0}$	$0.94^{+0.87+0.44}_{-0.74-0.44}$	$0.21^{+0.01+0.12}_{-0.01-0.12}$	$1.6^{+0.2+1.9}_{-0.2-1.4}$	$2.7^{+2.0+2.0}_{-0.8-1.5}$	4
64	350–500	350–500	3–4	≥3	$0.6^{+1.2+0.1}_{-0.6-0.0}$	$4.2^{+1.5+1.3}_{-1.4-1.3}$	$2.5^{+0.0+1.4}_{-0.0-1.4}$	$0.09^{+0.04+0.11}_{-0.04-0.05}$	$7.4^{+2.6+1.9}_{-1.9-1.9}$	8
65	350–500	500–1000	3–4	≥3	$10.2^{+6.3+2.1}_{-5.7-2.1}$	$7.0^{+1.5+1.9}_{-1.5-1.9}$	$4.3^{+0.0+2.4}_{-0.0-2.4}$	$0.78^{+0.18+0.94}_{-0.18-0.60}$	$22.3^{+7.9+3.8}_{-7.2-3.7}$	26
66	350–500	>1000	3–4	≥3	$0.0^{+1.1+0.0}_{-0.0-0.0}$	$0.21^{+0.49+0.13}_{-0.16-0.13}$	$0.36^{+0.01+0.20}_{-0.01-0.20}$	$0.54^{+0.15+0.65}_{-0.15-0.39}$	$1.1^{+1.6+0.7}_{-0.2-0.5}$	5
67	500–750	500–1000	3–4	≥3	$1.4^{+2.9+0.4}_{-1.4-0.0}$	$1.13^{+0.74+0.45}_{-0.58-0.45}$	$1.50^{+0.02+0.83}_{-0.02-0.83}$	$0.10^{+0.10+0.13}_{-0.10-0.00}$	$4.1^{+3.6+1.0}_{-2.0-0.9}$	0
68	500–750	>1000	3–4	≥3	$0.00^{+0.95+0.00}_{-0.00-0.00}$	$0.12^{+0.46+0.09}_{-0.06-0.09}$	$0.26^{+0.01+0.15}_{-0.01-0.15}$	$0.02^{+0.03+0.02}_{-0.02-0.00}$	$0.4^{+1.4+0.2}_{-0.1-0.2}$	2
69	>750	750–1500	3–4	≥3	$0.00^{+0.97+0.00}_{-0.00-0.00}$	$0.00^{+0.46+0.00}_{-0.00-0.00}$	$0.29^{+0.01+0.16}_{-0.01-0.16}$	$0.01^{+0.02+0.01}_{-0.01-0.00}$	$0.3^{+1.4+0.2}_{-0.0-0.2}$	1
70	>750	>1500	3–4	≥3	$0.0^{+1.4+0.0}_{-0.0-0.0}$	$0.00^{+0.46+0.00}_{-0.00-0.00}$	$0.04^{+0.01+0.02}_{-0.00-0.02}$	$0.01^{+0.03+0.02}_{-0.01-0.00}$	$0.0^{+1.8+0.0}_{-0.0-0.0}$	0

Table C.3: Observed number of events and pre-fit background predictions in the $5 \leq N_{jets} \leq 6$ search bins.

Bin	$\not{H}_T$ [GeV]	H_T [GeV]	N_{jets}	N_{b-jets}	Lost-e/μ	$\tau \to$ had	$Z \to \nu\bar{\nu}$	QCD	Total Pred.	Obs.
71	300–350	300–500	5–6	0	217^{+11+22}_{-11-22}	166^{+6+27}_{-6-27}	489^{+12+42}_{-12-39}	49^{+5+21}_{-5-19}	922^{+21+58}_{-21-56}	1015
72	300–350	500–1000	5–6	0	397^{+13+37}_{-13-37}	403^{+9+36}_{-9-36}	772^{+16+61}_{-15-57}	113^{+4+47}_{-4-43}	1686^{+27+93}_{-27-88}	1673
73	300–350	>1000	5–6	0	$49.6^{+4.5+5.4}_{-4.5-5.4}$	$55.1^{+3.8+8.3}_{-3.8-8.3}$	$100.0^{+6.4+8.2}_{-6.0-7.1}$	49^{+1+21}_{-1-19}	254^{+11+24}_{-10-22}	226
74	350–500	350–500	5–6	0	71^{+7+11}_{-6-11}	47^{+3+16}_{-3-16}	242^{+9+20}_{-9-19}	$12.7^{+2.3+5.3}_{-2.3-4.8}$	372^{+13+29}_{-13-28}	464
75	350–500	500–1000	5–6	0	384^{+12+33}_{-12-33}	412^{+11+32}_{-11-32}	1110^{+19+84}_{-19-78}	65^{+2+27}_{-2-25}	1971^{+30+99}_{-29-93}	2018
76	350–500	>1000	5–6	0	$76.9^{+6.4+8.9}_{-6.4-8.9}$	$72.4^{+4.8+9.3}_{-4.8-9.3}$	170^{+8+14}_{-8-12}	28^{+1+12}_{-1-11}	347^{+14+22}_{-14-21}	320
77	500–750	500–1000	5–6	0	$66.7^{+5.1+7.3}_{-5.0-7.3}$	$70.1^{+4.3+6.1}_{-4.2-6.0}$	302^{+10+23}_{-10-22}	$3.2^{+0.1+1.3}_{-0.1-1.2}$	442^{+14+25}_{-14-24}	460
78	500–750	>1000	5–6	0	$23.9^{+2.9+4.5}_{-2.9-4.5}$	$31.2^{+3.1+4.0}_{-3.1-4.0}$	$123.5^{+7.3+9.4}_{-6.9-8.9}$	$2.5^{+0.1+1.1}_{-0.1-1.0}$	181^{+10+11}_{-9-11}	170
79	>750	750–1500	5–6	0	$4.0^{+1.2+0.7}_{-1.1-0.7}$	$4.90^{+0.89+0.52}_{-0.76-0.52}$	$52.2^{+4.6+7.5}_{-4.2-6.8}$	$0.23^{+0.04+0.10}_{-0.04-0.09}$	$61.3^{+5.0+7.5}_{-4.6-6.9}$	74
80	>750	>1500	5–6	0	$0.90^{+0.61+0.19}_{-0.45-0.19}$	$1.46^{+0.67+0.16}_{-0.49-0.16}$	$16.5^{+2.9+2.7}_{-2.5-2.5}$	$0.25^{+0.06+0.11}_{-0.06-0.10}$	$19.1^{+3.2+2.7}_{-2.7-2.5}$	19
81	300–350	300–500	5–6	1	130^{+8+11}_{-8-11}	131^{+6+17}_{-6-17}	133^{+3+19}_{-3-19}	$12.8^{+2.8+5.2}_{-2.8-4.9}$	407^{+15+29}_{-15-28}	450
82	300–350	500–1000	5–6	1	290^{+11+25}_{-11-25}	302^{+8+25}_{-8-25}	218^{+4+31}_{-4-30}	41^{+4+17}_{-4-16}	851^{+20+50}_{-20-49}	781
83	300–350	>1000	5–6	1	$25.8^{+3.4+2.5}_{-3.4-2.5}$	$31.6^{+2.9+5.9}_{-2.9-5.9}$	$29.0^{+1.8+4.1}_{-1.7-4.0}$	$18.4^{+0.8+7.5}_{-0.8-7.1}$	105^{+7+11}_{-6-10}	100
84	350–500	350–500	5–6	1	$45.4^{+5.5+5.4}_{-5.4-5.4}$	32^{+3+11}_{-3-11}	$65.1^{+2.4+9.3}_{-2.3-9.1}$	$3.7^{+0.5+1.5}_{-0.5-1.4}$	146^{+9+16}_{-8-16}	160
85	350–500	500–1000	5–6	1	228^{+10+20}_{-10-20}	269^{+8+21}_{-8-21}	310^{+5+43}_{-5-42}	28^{+3+11}_{-3-11}	834^{+19+53}_{-19-52}	801
86	350–500	>1000	5–6	1	$40.5^{+5.5+4.2}_{-5.4-4.2}$	$36.0^{+3.3+4.3}_{-3.3-4.2}$	$49.4^{+2.3+7.0}_{-2.2-6.7}$	$11.9^{+0.7+4.8}_{-0.7-4.5}$	138^{+9+10}_{-9-10}	138
87	500–750	500–1000	5–6	1	$23.4^{+3.5+2.6}_{-3.4-2.6}$	$32.1^{+2.8+3.3}_{-2.8-3.3}$	84^{+3+12}_{-3-12}	$1.45^{+0.11+0.59}_{-0.11-0.55}$	141^{+7+13}_{-7-12}	135
88	500–750	>1000	5–6	1	$8.5^{+1.8+1.1}_{-1.7-1.1}$	$13.0^{+1.8+1.5}_{-1.7-1.5}$	$35.3^{+2.1+4.9}_{-2.0-4.8}$	$1.33^{+0.17+0.54}_{-0.17-0.51}$	$58.0^{+4.1+5.3}_{-3.9-5.2}$	49
89	>750	750–1500	5–6	1	$3.7^{+1.4+0.7}_{-1.2-0.7}$	$2.9^{+1.0+0.4}_{-0.9-0.4}$	$14.9^{+1.3+2.8}_{-1.2-2.6}$	$0.07^{+0.01+0.03}_{-0.01-0.03}$	$21.6^{+2.8+2.9}_{-2.5-2.7}$	16
90	>750	>1500	5–6	1	$1.06^{+0.74+0.26}_{-0.56-0.26}$	$1.16^{+0.73+0.18}_{-0.57-0.18}$	$4.79^{+0.85+0.96}_{-0.73-0.92}$	$0.16^{+0.07+0.07}_{-0.07-0.06}$	$7.2^{+1.7+1.0}_{-1.3-1.0}$	6
91	300–350	300–500	5–6	2	$60.1^{+7.1+6.0}_{-7.0-6.0}$	$50.2^{+3.3+4.9}_{-3.3-4.9}$	$23.8^{+0.6+7.1}_{-0.6-7.1}$	$2.9^{+0.9+1.1}_{-0.9-1.1}$	137^{+10+11}_{-10-11}	143
92	300–350	500–1000	5–6	2	137^{+9+13}_{-9-13}	160^{+6+14}_{-6-14}	39^{+1+12}_{-1-11}	$11.8^{+1.8+4.6}_{-1.8-4.5}$	347^{+15+22}_{-15-22}	332
93	300–350	>1000	5–6	2	$16.9^{+3.8+2.0}_{-3.7-2.0}$	$15.9^{+2.1+2.1}_{-2.1-2.1}$	$5.1^{+0.3+1.5}_{-0.3-1.5}$	$5.6^{+0.4+2.2}_{-0.4-2.2}$	$43.5^{+5.9+3.9}_{-5.8-3.9}$	36
94	350–500	350–500	5–6	2	$13.3^{+3.1+1.9}_{-2.9-1.9}$	$7.0^{+1.1+2.3}_{-1.0-2.3}$	$11.7^{+0.4+3.5}_{-0.4-3.5}$	$1.02^{+0.54+0.40}_{-0.54-0.39}$	$32.9^{+4.3+4.6}_{-4.0-4.6}$	28
95	350–500	500–1000	5–6	2	$107.5^{+7.6+9.6}_{-7.6-9.6}$	$121.2^{+5.8+9.9}_{-5.8-9.8}$	55^{+1+16}_{-1-16}	$5.9^{+1.0+2.3}_{-1.0-2.2}$	290^{+14+22}_{-13-21}	288
96	350–500	>1000	5–6	2	$14.2^{+2.8+1.8}_{-2.7-1.8}$	$15.7^{+2.2+2.0}_{-2.1-2.0}$	$8.7^{+0.4+2.6}_{-0.4-2.6}$	$3.2^{+0.1+1.2}_{-0.1-1.2}$	$41.8^{+5.0+4.0}_{-4.8-3.9}$	44
97	500–750	500–1000	5–6	2	$8.4^{+2.3+1.1}_{-2.2-1.1}$	$8.3^{+1.3+1.0}_{-1.2-1.0}$	$15.0^{+0.5+4.4}_{-0.5-4.4}$	$0.34^{+0.05+0.13}_{-0.05-0.13}$	$32.1^{+3.7+4.7}_{-3.4-4.7}$	35
98	500–750	>1000	5–6	2	$2.1^{+1.3+0.3}_{-1.0-0.3}$	$4.0^{+1.1+0.6}_{-1.0-0.6}$	$6.2^{+0.4+1.9}_{-0.3-1.8}$	$0.16^{+0.05+0.06}_{-0.05-0.06}$	$12.5^{+2.4+2.0}_{-2.0-2.0}$	18
99	>750	750–1500	5–6	2	$0.74^{+0.87+0.22}_{-0.53-0.22}$	$0.68^{+0.64+0.16}_{-0.45-0.16}$	$2.64^{+0.23+0.85}_{-0.21-0.83}$	$0.05^{+0.05+0.02}_{-0.05-0.00}$	$4.1^{+1.5+0.9}_{-1.0-0.9}$	8
100	>750	>1500	5–6	2	$0.77^{+0.65+0.24}_{-0.45-0.24}$	$1.07^{+0.72+0.33}_{-0.56-0.33}$	$0.84^{+0.15+0.28}_{-0.13-0.27}$	$0.03^{+0.03+0.01}_{-0.03-0.00}$	$2.7^{+1.4+0.5}_{-1.0-0.5}$	3
101	300–350	300–500	5–6	≥3	$2.8^{+1.5+0.3}_{-1.2-0.3}$	$5.1^{+1.0+0.8}_{-0.9-0.8}$	$2.0^{+0.0+1.1}_{-0.0-1.1}$	$0.50^{+0.37+0.57}_{-0.37-0.13}$	$10.4^{+2.5+1.5}_{-2.1-1.4}$	18
102	300–350	500–1000	5–6	≥3	$17.0^{+3.2+1.6}_{-3.1-1.6}$	$23.5^{+2.4+3.2}_{-2.3-3.2}$	$4.2^{+0.1+2.3}_{-0.1-2.3}$	$3.9^{+2.3+4.5}_{-2.3-1.6}$	$48.7^{+6.0+6.2}_{-5.9-4.5}$	44
103	300–350	>1000	5–6	≥3	$4.4^{+2.1+0.6}_{-1.8-0.6}$	$2.50^{+0.86+0.47}_{-0.73-0.47}$	$0.65^{+0.04+0.35}_{-0.04-0.35}$	$3.3^{+0.4+3.7}_{-0.4-2.8}$	$10.8^{+3.0+3.8}_{-2.6-3.0}$	6
104	350–500	350–500	5–6	≥3	$0.8^{+1.7+0.2}_{-0.8-0.0}$	$1.14^{+0.75+0.33}_{-0.59-0.33}$	$0.87^{+0.03+0.47}_{-0.03-0.47}$	$0.18^{+0.08+0.21}_{-0.08-0.10}$	$3.0^{+2.4+0.6}_{-1.4-0.6}$	4
105	350–500	500–1000	5–6	≥3	$15.2^{+2.6+1.5}_{-2.6-1.5}$	$17.6^{+2.2+2.7}_{-2.1-2.7}$	$5.7^{+0.1+3.1}_{-0.1-3.1}$	$1.7^{+0.1+1.9}_{-0.1-1.6}$	$40.2^{+4.8+4.8}_{-4.7-4.6}$	34
106	350–500	>1000	5–6	≥3	$1.9^{+1.1+0.3}_{-0.8-0.3}$	$3.8^{+1.1+0.7}_{-1.0-0.7}$	$1.14^{+0.05+0.62}_{-0.05-0.62}$	$2.4^{+0.3+2.7}_{-0.3-2.1}$	$9.2^{+2.2+2.8}_{-1.9-2.3}$	8
107	500–750	500–1000	5–6	≥3	$1.8^{+1.1+0.3}_{-0.8-0.3}$	$1.71^{+0.77+0.67}_{-0.61-0.67}$	$1.48^{+0.05+0.81}_{-0.05-0.80}$	$0.20^{+0.04+0.23}_{-0.04-0.17}$	$5.2^{+1.8+1.1}_{-1.5-1.1}$	4
108	500–750	>1000	5–6	≥3	$1.13^{+0.96+0.25}_{-0.66-0.25}$	$0.94^{+0.67+0.27}_{-0.49-0.27}$	$0.73^{+0.04+0.40}_{-0.04-0.40}$	$0.11^{+0.03+0.12}_{-0.03-0.08}$	$2.9^{+1.6+0.6}_{-1.1-0.6}$	2
109	>750	750–1500	5–6	≥3	$0.00^{+0.72+0.00}_{-0.00-0.00}$	$0.07^{+0.46+0.04}_{-0.06-0.04}$	$0.31^{+0.03+0.17}_{-0.03-0.17}$	$0.02^{+0.04+0.03}_{-0.02-0.00}$	$0.4^{+1.2+0.2}_{-0.1-0.2}$	0
110	>750	>1500	5–6	≥3	$0.00^{+0.63+0.00}_{-0.00-0.00}$	$0.03^{+0.46+0.01}_{-0.02-0.01}$	$0.11^{+0.02+0.06}_{-0.02-0.06}$	$0.00^{+0.02+0.01}_{-0.00-0.00}$	$0.1^{+1.1+0.1}_{-0.0-0.1}$	1

Table C.4: Observed number of events and pre-fit background predictions in the $7 \leq N_{jets} \leq 8$ search bins.

Bin	$\not{H}_T$ [GeV]	H_T [GeV]	N_{jets}	N_{b-jets}	Lost-e/μ	$\tau \to$ had	$Z \to \nu\bar{\nu}$	QCD	Total Pred.	Obs.
111	300–350	500–1000	7–8	0	$48.0^{+3.9+5.4}_{-3.8-5.4}$	$60.8^{+3.4+6.0}_{-3.4-6.0}$	76^{+5+11}_{-5-10}	30^{+2+12}_{-2-11}	215^{+9+18}_{-9-17}	218
112	300–350	>1000	7–8	0	$21.2^{+2.9+2.3}_{-2.9-2.3}$	$20.3^{+2.2+2.8}_{-2.1-2.8}$	$23.9^{+3.3+2.8}_{-2.9-2.5}$	$20.5^{+0.5+8.5}_{-0.5-7.8}$	$85.9^{+6.1+9.6}_{-5.8-9.0}$	85
113	350–500	500–1000	7–8	0	$43.2^{+3.9+4.9}_{-3.9-4.9}$	$54.2^{+3.6+5.7}_{-3.5-5.7}$	89^{+6+11}_{-5-10}	$14.3^{+1.9+5.9}_{-1.9-5.4}$	201^{+10+14}_{-9-14}	215
114	350–500	>1000	7–8	0	$22.5^{+2.8+2.7}_{-2.7-2.7}$	$23.3^{+2.5+2.3}_{-2.4-2.3}$	$48.3^{+4.7+5.4}_{-4.3-4.8}$	$12.6^{+0.7+5.2}_{-0.7-4.8}$	$106.7^{+7.1+8.3}_{-6.7-7.7}$	75
115	500–750	500–1000	7–8	0	$6.9^{+1.8+1.4}_{-1.7-1.4}$	$4.96^{+0.95+0.77}_{-0.84-0.77}$	$26.5^{+3.6+3.3}_{-3.2-3.0}$	$0.88^{+0.10+0.36}_{-0.10-0.34}$	$39.2^{+4.5+3.7}_{-4.1-3.5}$	34
116	500–750	>1000	7–8	0	$5.4^{+1.1+0.9}_{-1.0-0.9}$	$9.9^{+1.6+1.7}_{-1.5-1.7}$	$27.2^{+3.7+3.1}_{-3.2-2.8}$	$1.56^{+0.12+0.64}_{-0.12-0.59}$	$44.1^{+4.5+3.7}_{-4.1-3.5}$	38
117	>750	750–1500	7–8	0	$1.26^{+0.70+0.50}_{-0.58-0.50}$	$1.44^{+0.74+0.24}_{-0.57-0.24}$	$3.6^{+1.4+0.7}_{-1.0-0.6}$	$0.07^{+0.02+0.03}_{-0.02-0.03}$	$6.4^{+2.0+0.9}_{-1.5-0.8}$	5
118	>750	>1500	7–8	0	$0.69^{+0.47+0.16}_{-0.35-0.16}$	$1.03^{+0.69+0.15}_{-0.51-0.15}$	$1.5^{+1.2+0.3}_{-0.7-0.3}$	$0.07^{+0.01+0.03}_{-0.01-0.03}$	$3.3^{+1.7+0.4}_{-1.1-0.4}$	5
119	300–350	500–1000	7–8	1	$64.7^{+5.1+6.4}_{-5.1-6.4}$	$77.0^{+3.9+7.5}_{-3.8-7.4}$	$31.7^{+2.1+8.6}_{-1.9-8.4}$	$11.2^{+0.5+4.7}_{-0.5-4.3}$	184^{+9+14}_{-9-14}	146
120	300–350	>1000	7–8	1	$16.3^{+2.4+1.7}_{-2.4-1.7}$	$19.9^{+2.2+2.1}_{-2.1-2.1}$	$10.3^{+1.4+2.7}_{-1.2-2.6}$	$8.3^{+0.2+3.5}_{-0.2-3.2}$	$54.8^{+4.8+5.2}_{-4.7-5.0}$	68
121	350–500	500–1000	7–8	1	$46.9^{+4.4+5.0}_{-4.4-5.0}$	$58.6^{+3.7+5.7}_{-3.7-5.7}$	$37.0^{+2.4+9.7}_{-2.2-9.5}$	$7.5^{+0.4+3.2}_{-0.4-2.9}$	150^{+8+13}_{-8-12}	113
122	350–500	>1000	7–8	1	$19.5^{+2.5+2.1}_{-2.4-2.1}$	$19.5^{+2.3+2.0}_{-2.3-2.0}$	$21.0^{+2.0+5.4}_{-1.9-5.3}$	$5.3^{+0.5+2.2}_{-0.5-2.0}$	$65.3^{+5.2+6.5}_{-5.1-6.4}$	67
123	500–750	500–1000	7–8	1	$7.6^{+2.0+1.4}_{-1.9-1.4}$	$5.5^{+1.1+0.8}_{-1.1-0.8}$	$11.5^{+1.6+3.0}_{-1.4-3.0}$	$0.36^{+0.04+0.15}_{-0.04-0.14}$	$24.9^{+3.5+3.4}_{-3.3-3.4}$	19
124	500–750	>1000	7–8	1	$9.3^{+2.1+1.3}_{-2.0-1.3}$	$7.5^{+1.5+0.8}_{-1.4-0.8}$	$11.4^{+1.5+3.0}_{-1.4-2.9}$	$0.98^{+0.12+0.41}_{-0.12-0.37}$	$29.2^{+3.9+3.3}_{-3.7-3.3}$	22
125	>750	750–1500	7–8	1	$0.14^{+0.30+0.05}_{-0.14-0.00}$	$0.44^{+0.51+0.10}_{-0.22-0.10}$	$1.48^{+0.56+0.44}_{-0.42-0.43}$	$0.07^{+0.03+0.03}_{-0.03-0.03}$	$2.14^{+0.99+0.46}_{-0.56-0.45}$	4
126	>750	>1500	7–8	1	$0.00^{+0.47+0.00}_{-0.00-0.00}$	$0.14^{+0.47+0.02}_{-0.08-0.02}$	$0.70^{+0.55+0.22}_{-0.34-0.21}$	$0.03^{+0.01+0.01}_{-0.01-0.01}$	$0.9^{+1.1+0.2}_{-0.3-0.2}$	6
127	300–350	500–1000	7–8	2	$34.7^{+3.5+3.6}_{-3.5-3.6}$	$47.7^{+3.0+4.4}_{-3.0-4.4}$	$8.1^{+0.5+3.6}_{-0.5-3.5}$	$5.3^{+0.5+2.1}_{-0.5-2.1}$	$95.8^{+6.6+7.1}_{-6.5-7.0}$	95
128	300–350	>1000	7–8	2	$9.0^{+2.1+1.2}_{-2.1-1.2}$	$10.8^{+1.4+1.3}_{-1.4-1.3}$	$2.4^{+0.3+1.0}_{-0.3-1.0}$	$3.2^{+0.1+1.3}_{-0.1-1.3}$	$25.4^{+3.6+2.4}_{-3.4-2.4}$	26
129	350–500	500–1000	7–8	2	$26.2^{+3.0+2.9}_{-3.0-2.9}$	$31.0^{+2.5+3.3}_{-2.5-3.2}$	$9.6^{+0.6+4.1}_{-0.6-4.1}$	$2.5^{+0.2+1.0}_{-0.2-1.0}$	$69.3^{+5.6+6.1}_{-5.5-6.1}$	84
130	350–500	>1000	7–8	2	$13.3^{+2.5+1.5}_{-2.4-1.5}$	$13.3^{+1.8+1.3}_{-1.7-1.3}$	$4.7^{+0.5+2.0}_{-0.4-2.0}$	$1.95^{+0.13+0.78}_{-0.13-0.75}$	$33.3^{+4.3+3.0}_{-4.2-2.9}$	35
131	500–750	500–1000	7–8	2	$2.5^{+1.4+0.5}_{-1.2-0.5}$	$0.86^{+0.50+0.21}_{-0.18-0.21}$	$2.6^{+0.3+1.1}_{-0.3-1.1}$	$0.10^{+0.01+0.04}_{-0.01-0.04}$	$6.0^{+1.9+1.3}_{-1.4-1.3}$	7
132	500–750	>1000	7–8	2	$6.0^{+2.3+1.0}_{-2.2-1.0}$	$3.3^{+1.0+0.6}_{-0.9-0.6}$	$2.9^{+0.4+1.2}_{-0.3-1.2}$	$0.22^{+0.06+0.09}_{-0.06-0.08}$	$12.4^{+3.4+1.7}_{-3.1-1.7}$	12
133	>750	750–1500	7–8	2	$0.16^{+0.34+0.08}_{-0.16-0.00}$	$0.44^{+0.56+0.15}_{-0.32-0.15}$	$0.39^{+0.15+0.18}_{-0.11-0.18}$	$0.03^{+0.01+0.01}_{-0.01-0.01}$	$1.03^{+0.91+0.25}_{-0.49-0.23}$	2
134	>750	>1500	7–8	2	$0.53^{+0.62+0.20}_{-0.38-0.20}$	$0.61^{+0.57+0.22}_{-0.33-0.22}$	$0.13^{+0.10+0.06}_{-0.06-0.06}$	$0.06^{+0.02+0.02}_{-0.02-0.02}$	$1.3^{+1.2+0.3}_{-0.7-0.3}$	2
135	300–350	500–1000	7–8	≥3	$8.1^{+1.8+1.0}_{-1.7-1.0}$	$9.4^{+1.4+1.3}_{-1.3-1.3}$	$4.1^{+0.3+2.3}_{-0.2-2.3}$	$2.9^{+0.6+3.3}_{-0.6-2.3}$	$24.6^{+3.2+4.3}_{-3.1-3.7}$	12
136	300–350	>1000	7–8	≥3	$4.7^{+2.0+0.7}_{-1.8-0.7}$	$5.4^{+1.2+0.8}_{-1.1-0.8}$	$1.51^{+0.21+0.85}_{-0.18-0.84}$	$2.4^{+0.3+2.7}_{-0.3-2.1}$	$13.9^{+3.2+3.0}_{-2.9-2.5}$	8
137	350–500	500–1000	7–8	≥3	$5.9^{+1.9+0.8}_{-1.7-0.8}$	$7.4^{+1.4+1.2}_{-1.3-1.2}$	$4.7^{+0.3+2.7}_{-0.3-2.7}$	$1.2^{+0.1+1.3}_{-0.1-1.1}$	$19.2^{+3.2+3.3}_{-3.1-3.2}$	16
138	350–500	>1000	7–8	≥3	$2.6^{+1.1+0.3}_{-1.0-0.3}$	$4.8^{+1.3+0.7}_{-1.2-0.7}$	$3.1^{+0.3+1.8}_{-0.3-1.8}$	$2.1^{+0.3+2.3}_{-0.3-1.8}$	$12.6^{+2.5+3.0}_{-2.2-2.6}$	8
139	500–750	500–1000	7–8	≥3	$0.23^{+0.48+0.08}_{-0.23-0.00}$	$0.30^{+0.48+0.10}_{-0.13-0.10}$	$1.70^{+0.23+0.96}_{-0.20-0.96}$	$0.11^{+0.04+0.12}_{-0.04-0.08}$	$2.34^{+0.99+0.98}_{-0.41-0.96}$	3
140	500–750	>1000	7–8	≥3	$3.4^{+2.4+0.7}_{-2.1-0.7}$	$1.59^{+0.83+0.49}_{-0.69-0.49}$	$1.51^{+0.20+0.85}_{-0.18-0.85}$	$0.22^{+0.08+0.24}_{-0.08-0.14}$	$6.7^{+3.2+1.2}_{-2.7-1.2}$	4
141	>750	750–1500	7–8	≥3	$0.00^{+0.56+0.00}_{-0.00-0.00}$	$0.05^{+0.46+0.02}_{-0.03-0.02}$	$0.19^{+0.07+0.11}_{-0.05-0.11}$	$0.03^{+0.04+0.03}_{-0.03-0.00}$	$0.3^{+1.0+0.1}_{-0.1-0.1}$	0
142	>750	>1500	7–8	≥3	$0.00^{+0.72+0.00}_{-0.00-0.00}$	$0.04^{+0.46+0.02}_{-0.02-0.02}$	$0.12^{+0.10+0.07}_{-0.06-0.07}$	$0.01^{+0.03+0.01}_{-0.01-0.00}$	$0.2^{+1.2+0.1}_{-0.1-0.1}$	0

Table C.5: Observed number of events and pre-fit background predictions in the $N_{jets} \geq 9$ search bins.

Bin	$\not{H}_T$ [GeV]	H_T [GeV]	N_{jets}	N_{b-jets}	Lost-e/μ	$\tau \to$ had	$Z \to \nu\bar{\nu}$	QCD	Total Pred.	Obs.
143	300–350	500–1000	≥9	0	$6.2^{+2.7+1.7}_{-2.6-1.7}$	$3.46^{+0.89+0.59}_{-0.77-0.59}$	$2.6^{+1.2+0.7}_{-0.9-0.7}$	$2.9^{+0.3+1.3}_{-0.3-1.1}$	$15.1^{+3.8+2.3}_{-3.5-2.2}$	7
144	300–350	>1000	≥9	0	$3.5^{+1.2+0.6}_{-1.1-0.6}$	$4.6^{+1.0+0.6}_{-0.9-0.6}$	$3.0^{+1.4+0.6}_{-1.0-0.6}$	$4.2^{+0.3+1.9}_{-0.3-1.6}$	$15.2^{+2.7+2.1}_{-2.3-1.9}$	12
145	350–500	500–1000	≥9	0	$2.39^{+0.99+0.69}_{-0.89-0.69}$	$2.39^{+0.86+0.48}_{-0.73-0.48}$	$2.9^{+1.3+0.7}_{-0.9-0.6}$	$0.97^{+0.08+0.43}_{-0.08-0.37}$	$8.6^{+2.3+1.2}_{-1.9-1.1}$	6
146	350–500	>1000	≥9	0	$3.7^{+1.1+0.6}_{-1.1-0.6}$	$4.6^{+1.0+0.6}_{-0.9-0.6}$	$5.5^{+1.9+1.0}_{-1.5-0.9}$	$3.1^{+0.2+1.4}_{-0.2-1.2}$	$17.0^{+2.9+1.9}_{-2.5-1.7}$	13
147	500–750	500–1000	≥9	0	$0.15^{+0.32+0.10}_{-0.15-0.00}$	$0.35^{+0.55+0.12}_{-0.30-0.12}$	$1.0^{+1.3+0.4}_{-0.7-0.4}$	$0.10^{+0.05+0.04}_{-0.05-0.04}$	$1.6^{+1.6+0.5}_{-0.8-0.4}$	2
148	500–750	>1000	≥9	0	$0.98^{+0.50+0.26}_{-0.41-0.26}$	$1.98^{+0.74+0.30}_{-0.58-0.30}$	$3.5^{+1.6+0.7}_{-1.1-0.7}$	$0.47^{+0.05+0.21}_{-0.05-0.18}$	$6.9^{+2.0+0.8}_{-1.5-0.8}$	11
149	>750	750–1500	≥9	0	$0.00^{+0.44+0.00}_{-0.00-0.00}$	$0.00^{+0.46+0.00}_{-0.00-0.00}$	$0.00^{+0.64+0.00}_{-0.00-0.00}$	$0.01^{+0.02+0.00}_{-0.01-0.00}$	$0.0^{+1.1+0.0}_{-0.0-0.0}$	0
150	>750	>1500	≥9	0	$0.23^{+0.27+0.16}_{-0.17-0.16}$	$0.28^{+0.50+0.08}_{-0.21-0.08}$	$0.00^{+0.82+0.00}_{-0.00-0.00}$	$0.05^{+0.03+0.02}_{-0.03-0.02}$	$0.6^{+1.1+0.2}_{-0.4-0.2}$	1
151	300–350	500–1000	≥9	1	$6.5^{+1.8+1.1}_{-1.7-1.1}$	$4.57^{+0.93+0.77}_{-0.81-0.77}$	$1.83^{+0.84+0.68}_{-0.60-0.74}$	$1.02^{+0.06+0.42}_{-0.06-0.40}$	$13.9^{+2.8+1.5}_{-2.6-1.6}$	25
152	300–350	>1000	≥9	1	$5.7^{+1.6+0.7}_{-1.5-0.7}$	$7.3^{+1.3+1.1}_{-1.2-1.1}$	$2.08^{+0.95+0.69}_{-0.68-0.77}$	$2.43^{+0.06+0.99}_{-0.06-0.94}$	$17.5^{+3.0+1.8}_{-2.8-1.8}$	20
153	350–500	500–1000	≥9	1	$2.92^{+0.94+0.57}_{-0.84-0.57}$	$2.96^{+0.77+0.60}_{-0.61-0.60}$	$2.00^{+0.91+0.71}_{-0.65-0.78}$	$0.53^{+0.05+0.22}_{-0.05-0.21}$	$8.4^{+1.9+1.1}_{-1.6-1.2}$	8
154	350–500	>1000	≥9	1	$5.4^{+1.4+0.7}_{-1.3-0.7}$	$7.7^{+1.4+1.1}_{-1.3-1.1}$	$3.9^{+1.3+1.3}_{-1.0-1.4}$	$1.48^{+0.05+0.60}_{-0.05-0.57}$	$18.4^{+3.1+1.9}_{-2.8-2.0}$	14
155	500–750	500–1000	≥9	1	$0.14^{+0.30+0.08}_{-0.14-0.00}$	$0.24^{+0.49+0.21}_{-0.18-0.16}$	$0.71^{+0.94+0.35}_{-0.46-0.36}$	$0.03^{+0.03+0.01}_{-0.03-0.00}$	$1.1^{+1.2+0.4}_{-0.6-0.4}$	1
156	500–750	>1000	≥9	1	$0.68^{+0.58+0.12}_{-0.41-0.12}$	$1.20^{+0.64+0.21}_{-0.44-0.21}$	$2.4^{+1.1+0.8}_{-0.8-0.9}$	$0.20^{+0.02+0.08}_{-0.02-0.07}$	$4.5^{+1.6+0.8}_{-1.2-0.9}$	4
157	>750	750–1500	≥9	1	$0.00^{+0.73+0.00}_{-0.00-0.00}$	$0.04^{+0.46+0.02}_{-0.04-0.00}$	$0.00^{+0.45+0.00}_{-0.00-0.00}$	$0.01^{+0.01+0.00}_{-0.01-0.00}$	$0.1^{+1.3+0.0}_{-0.0-0.0}$	0
158	>750	>1500	≥9	1	$0.13^{+0.27+0.06}_{-0.13-0.00}$	$0.03^{+0.46+0.01}_{-0.02-0.01}$	$0.00^{+0.57+0.00}_{-0.00-0.00}$	$0.02^{+0.01+0.01}_{-0.01-0.01}$	$0.18^{+0.93+0.06}_{-0.15-0.01}$	0
159	300–350	500–1000	≥9	2	$4.1^{+1.3+0.7}_{-1.2-0.7}$	$4.68^{+0.92+0.85}_{-0.80-0.85}$	$0.64^{+0.29+0.34}_{-0.21-0.36}$	$0.40^{+0.06+0.24}_{-0.06-0.21}$	$9.8^{+2.2+1.2}_{-2.0-1.2}$	13
160	300–350	>1000	≥9	2	$5.2^{+1.6+0.7}_{-1.5-0.7}$	$5.5^{+1.2+1.0}_{-1.1-1.0}$	$0.73^{+0.33+0.37}_{-0.24-0.39}$	$1.32^{+0.15+0.68}_{-0.15-0.58}$	$12.7^{+2.8+1.4}_{-2.6-1.4}$	10
161	350–500	500–1000	≥9	2	$3.01^{+0.91+0.63}_{-0.82-0.63}$	$4.7^{+1.1+0.9}_{-1.0-0.9}$	$0.70^{+0.32+0.36}_{-0.23-0.39}$	$0.30^{+0.08+0.14}_{-0.08-0.12}$	$8.7^{+2.0+1.1}_{-1.8-1.1}$	4
162	350–500	>1000	≥9	2	$4.4^{+1.1+0.6}_{-1.1-0.6}$	$6.3^{+1.4+0.8}_{-1.3-0.8}$	$1.35^{+0.47+0.67}_{-0.36-0.72}$	$0.63^{+0.03+0.32}_{-0.03-0.27}$	$12.7^{+2.6+1.3}_{-2.4-1.3}$	12
163	500–750	500–1000	≥9	2	$0.00^{+0.39+0.00}_{-0.00-0.00}$	$0.35^{+0.49+0.17}_{-0.18-0.17}$	$0.25^{+0.33+0.15}_{-0.16-0.16}$	$0.01^{+0.01+0.01}_{-0.01-0.00}$	$0.61^{+0.95+0.23}_{-0.24-0.23}$	0
164	500–750	>1000	≥9	2	$2.0^{+1.1+0.4}_{-0.9-0.4}$	$1.95^{+0.87+0.45}_{-0.73-0.45}$	$0.84^{+0.39+0.43}_{-0.28-0.46}$	$0.09^{+0.02+0.04}_{-0.02-0.04}$	$4.9^{+2.0+0.7}_{-1.7-0.7}$	7
165	>750	750–1500	≥9	2	$0.00^{+0.60+0.00}_{-0.00-0.00}$	$0.01^{+0.46+0.01}_{-0.00-0.00}$	$0.00^{+0.16+0.00}_{-0.00-0.00}$	$0.00^{+0.01+0.00}_{-0.00-0.00}$	$0.0^{+1.1+0.0}_{-0.0-0.0}$	0
166	>750	>1500	≥9	2	$0.00^{+0.38+0.00}_{-0.00-0.00}$	$0.00^{+0.46+0.00}_{-0.00-0.00}$	$0.00^{+0.20+0.00}_{-0.00-0.00}$	$0.01^{+0.02+0.00}_{-0.01-0.00}$	$0.01^{+0.87+0.00}_{-0.01-0.00}$	0
167	300–350	500–1000	≥9	≥3	$1.06^{+0.63+0.27}_{-0.50-0.27}$	$1.06^{+0.57+0.29}_{-0.34-0.29}$	$0.37^{+0.17+0.26}_{-0.12-0.28}$	$0.47^{+0.13+0.56}_{-0.13-0.34}$	$3.0^{+1.2+0.7}_{-0.9-0.6}$	1
168	300–350	>1000	≥9	≥3	$3.5^{+1.7+0.5}_{-1.5-0.5}$	$2.6^{+1.0+0.7}_{-0.9-0.7}$	$0.42^{+0.19+0.29}_{-0.14-0.31}$	$2.1^{+0.3+2.4}_{-0.3-1.8}$	$8.6^{+2.7+2.6}_{-2.4-2.0}$	4
169	350–500	500–1000	≥9	≥3	$1.03^{+0.60+0.30}_{-0.47-0.30}$	$1.58^{+0.71+0.43}_{-0.55-0.43}$	$0.40^{+0.18+0.28}_{-0.13-0.31}$	$0.10^{+0.03+0.11}_{-0.03-0.07}$	$3.1^{+1.3+0.6}_{-1.0-0.6}$	3
170	350–500	>1000	≥9	≥3	$0.81^{+0.56+0.14}_{-0.41-0.14}$	$0.96^{+0.54+0.16}_{-0.27-0.16}$	$0.77^{+0.27+0.53}_{-0.20-0.58}$	$1.3^{+0.2+1.5}_{-0.2-1.1}$	$3.8^{+1.1+1.6}_{-0.7-1.3}$	2
171	500–750	500–1000	≥9	≥3	$0.00^{+0.43+0.00}_{-0.00-0.00}$	$0.03^{+0.46+0.03}_{-0.02-0.03}$	$0.14^{+0.19+0.11}_{-0.09-0.11}$	$0.01^{+0.02+0.01}_{-0.01-0.00}$	$0.18^{+0.91+0.11}_{-0.09-0.11}$	0
172	500–750	>1000	≥9	≥3	$0.00^{+0.48+0.00}_{-0.00-0.00}$	$0.53^{+0.56+0.13}_{-0.31-0.13}$	$0.48^{+0.22+0.33}_{-0.16-0.37}$	$0.13^{+0.14+0.15}_{-0.13-0.00}$	$1.1^{+1.1+0.4}_{-0.4-0.4}$	3
173	>750	750–1500	≥9	≥3	$0.00^{+0.50+0.00}_{-0.00-0.00}$	$0.00^{+0.46+0.00}_{-0.00-0.00}$	$0.00^{+0.09+0.00}_{-0.00-0.00}$	$0.01^{+0.05+0.02}_{-0.01-0.00}$	$0.01^{+0.97+0.02}_{-0.01-0.00}$	0
174	>750	>1500	≥9	≥3	$0.00^{+0.42+0.00}_{-0.00-0.00}$	$0.00^{+0.46+0.00}_{-0.00-0.00}$	$0.00^{+0.11+0.00}_{-0.00-0.00}$	$0.02^{+0.05+0.02}_{-0.02-0.00}$	$0.02^{+0.89+0.02}_{-0.02-0.00}$	0

Table C.6: Observed number of events and pre-fit background predictions in the aggregate search regions.

Bin	$\not{H}_T$ [GeV]	H_T [GeV]	N_{jets}	N_{b-jets}	Lost-e/μ	$\tau \to$ had	$Z \to \nu\bar{\nu}$	QCD	Total Pred.	Obs.
1	>500	>500	≥2	0	842^{+25+48}_{-25-46}	753^{+16+65}_{-16-65}	$5968^{+48+360}_{-47-350}$	$21.4^{+0.6+8.5}_{-0.6-7.1}$	$7584^{+63+370}_{-62-360}$	7838
2	>750	>1500	≥3	0	$4.8^{+2.2+0.6}_{-1.6-0.6}$	$4.2^{+1.3+0.3}_{-0.9-0.3}$	$45.8^{+5.1+5.2}_{-4.3-4.9}$	$0.47^{+0.06+0.18}_{-0.06-0.16}$	$55.2^{+6.2+5.3}_{-5.0-4.9}$	71
3	>500	>500	≥5	0	$111.0^{+6.4+8.3}_{-6.3-7.9}$	$127.6^{+5.9+8.5}_{-5.7-8.6}$	558^{+15+36}_{-14-34}	$9.4^{+0.2+3.5}_{-0.2-3.1}$	806^{+19+38}_{-18-37}	819
4	>750	>1500	≥5	0	$1.82^{+0.82+0.26}_{-0.59-0.21}$	$2.8^{+1.1+0.2}_{-0.7-0.2}$	$18.1^{+3.3+2.7}_{-2.6-2.6}$	$0.37^{+0.06+0.15}_{-0.06-0.13}$	$23.0^{+3.8+2.7}_{-2.9-2.6}$	25
5	>750	>1500	≥9	0	$0.23^{+0.27+0.14}_{-0.17-0.07}$	$0.28^{+0.50+0.08}_{-0.21-0.07}$	$0.00^{+0.82+0.00}_{-0.00-0.00}$	$0.05^{+0.03+0.02}_{-0.03-0.02}$	$0.6^{+1.1+0.2}_{-0.4-0.1}$	1
6	>500	>500	≥2	≥2	$46.9^{+8.9+3.1}_{-5.9-3.0}$	$44.0^{+4.4+3.2}_{-3.4-3.2}$	102^{+2+14}_{-1-14}	$2.5^{+0.3+1.5}_{-0.2-1.3}$	196^{+13+15}_{-9-15}	216
7	>750	>750	≥3	≥1	$11.5^{+4.1+1.0}_{-2.2-0.9}$	$13.7^{+3.0+1.2}_{-2.0-1.2}$	87^{+3+10}_{-3-10}	$0.87^{+0.15+0.34}_{-0.11-0.31}$	113^{+8+10}_{-5-10}	123
8	>500	>500	≥5	≥3	$6.6^{+3.3+0.6}_{-2.3-0.6}$	$5.3^{+1.9+0.9}_{-1.1-0.9}$	$6.8^{+0.5+2.8}_{-0.3-2.8}$	$0.87^{+0.20+0.96}_{-0.17-0.70}$	$19.5^{+5.2+3.2}_{-3.4-3.1}$	17
9	>750	>1500	≥5	≥2	$1.3^{+1.4+0.2}_{-0.6-0.2}$	$1.8^{+1.3+0.4}_{-0.7-0.4}$	$1.20^{+0.41+0.33}_{-0.19-0.33}$	$0.13^{+0.07+0.06}_{-0.04-0.05}$	$4.4^{+2.8+0.6}_{-1.3-0.6}$	6
10	>750	>750	≥9	≥3	$0.00^{+0.66+0.00}_{-0.00-0.00}$	$0.00^{+0.65+0.00}_{-0.00-0.00}$	$0.00^{+0.15+0.00}_{-0.00-0.00}$	$0.03^{+0.07+0.04}_{-0.02-0.01}$	$0.0^{+1.3+0.0}_{-0.0-0.0}$	0
11	>300	>300	≥7	≥1	328^{+12+21}_{-12-20}	380^{+10+22}_{-9-22}	193^{+8+38}_{-6-38}	69^{+1+29}_{-1-26}	969^{+23+57}_{-22-55}	890
12	>750	>750	≥5	≥1	$7.2^{+2.8+0.8}_{-1.6-0.7}$	$7.7^{+2.4+0.8}_{-1.4-0.8}$	$26.6^{+2.4+3.9}_{-1.8-3.7}$	$0.65^{+0.14+0.26}_{-0.11-0.23}$	$42.2^{+5.7+4.0}_{-3.5-3.9}$	48

Bibliography

[1] S. Weinberg, "A Model of Leptons", *Phys. Rev. Lett.* **1**9 (Nov, 1967) 1264–1266. doi:10.1103/PhysRevLett.19.1264.

[2] S. L. Glashow, "Partial-symmetries of weak interactions", *Nuclear Physics* **2**2 (1961), no. 4, 579 – 588. doi:https://doi.org/10.1016/0029-5582(61)90469-2.

[3] P. W. Higgs, "Broken Symmetries and the Masses of Gauge Bosons", *Phys. Rev. Lett.* **1**3 (Oct, 1964) 508–509. doi:10.1103/PhysRevLett.13.508.

[4] F. Englert and R. Brout, "Broken Symmetry and the Mass of Gauge Vector Mesons", *Phys. Rev. Lett.* **1**3 (Aug, 1964) 321–323. doi:10.1103/PhysRevLett.13.321.

[5] G. S. Guralnik, C. R. Hagen, and T. W. B. Kibble, "Global Conservation Laws and Massless Particles", *Phys. Rev. Lett.* **1**3 (Nov, 1964) 585–587. doi:10.1103/PhysRevLett.13.585.

[6] M. E. Peskin and D. V. Schroeder, "An introduction to quantum field theory". Westview, Boulder, CO, 1995. Includes exercises.

[7] Particle Data Group. Berkeley Collaboration, "Review of Particle Physics, 2014-2015. Review of Particle Properties", *Chin. Phys. C* **3**8 (2014) 090001. All tables, listings, and reviews (and errata) are also available on the Particle Data Group website: http://pdg.lbl.gov.

[8] E. Drexler, "Elementary particle interactions in the Standard Model", 2014.

[9] A. D. Martin, "Proton structure, Partons, QCD, DGLAP and beyond", *Acta Phys. Polon.* **B**39 (2008) 2025–2062, arXiv:0802.0161.

[10] N. Cabibbo, "Unitary Symmetry and Leptonic Decays", *Phys. Rev. Lett.* **1**0 (Jun, 1963) 531–533. doi:10.1103/PhysRevLett.10.531.

[11] M. Kobayashi and T. Maskawa, "CP-Violation in the Renormalizable Theory of Weak Interaction", *Progress of Theoretical Physics* **4**9 (1973), no. 2, 652–657. doi:10.1143/PTP.49.652.

[12] B. Pontecorvo, "Neutrino Experiments and the Problem of Conservation of Leptonic Charge",. [Zh. Eksp. Teor. Fiz.53,1717(1967)].

[13] F. Close, "Neutrino". OUP Oxford, 2010.

[14] B. Pontecorvo, "Inverse beta processes and nonconservation of lepton charge", *Sov. Phys. JETP* **7** (1958) 172–173. [Zh. Eksp. Teor. Fiz.34,247(1957)].

[15] Z. Maki, M. Nakagawa, and S. Sakata, "Remarks on the Unified Model of Elementary Particles", *Progress of Theoretical Physics* **2**8 (1962), no. 5, 870–880. doi:10.1143/PTP.28.870.

[16] C. S. Wu, E. Ambler, R. W. Hayward et al., "Experimental Test of Parity Conservation in Beta Decay", *Phys. Rev.* **1**05 (Feb, 1957) 1413–1415. doi:10.1103/PhysRev.105.1413.

[17] T. D. Lee and C. N. Yang, "Question of Parity Conservation in Weak Interactions", *Phys. Rev.* **1**04 (Oct, 1956) 254–258. doi:10.1103/PhysRev.104.254.

[18] B. Naroska, "e+e physics with the jade detector at petra", *Physics Reports* **1**48 (1987), no. 2, 67 – 215. doi:https://doi.org/10.1016/0370-1573(87)90031-7.

[19] SLD Electroweak Group, DELPHI, ALEPH, SLD, SLD Heavy Flavour Group, OPAL, LEP Electroweak Working Group, L3 Collaboration, "Precision electroweak measurements on the Z resonance", *Phys. Rept.* **4**27 (2006) 257–454, arXiv:hep-ex/0509008. doi:10.1016/j.physrep.2005.12.006.

[20] F. Hasert, H. Faissner, W. Krenz et al., "Search for elastic muon-neutrino electron scattering", *Physics Letters B* **4**6 (1973), no. 1, 121 – 124. doi:https://doi.org/10.1016/0370-2693(73)90494-2.

[21] F. Hasert, S. Kabe, W. Krenz et al., "Observation of neutrino-like interactions without muon or electron in the gargamelle neutrino experiment", *Physics Letters B* **4**6 (1973), no. 1, 138 – 140. doi:https://doi.org/10.1016/0370-2693(73)90499-1.

[22] G. Arnison, A. Astbury, B. Aubert et al., "Experimental observation of lepton pairs of invariant mass around 95 GeV/c2 at the CERN SPS collider", *Physics Letters B* **1**26 (1983), no. 5, 398 – 410. doi:https://doi.org/10.1016/0370-2693(83)90188-0.

[23] G. Arnison, A. Astbury, B. Aubert et al., "Experimental observation of isolated large transverse energy electrons with associated missing energy at s=540 GeV", *Physics Letters B* **1**22 (1983), no. 1, 103 – 116. doi:https://doi.org/10.1016/0370-2693(83)91177-2.

[24] O. W. Greenberg, "Spin and Unitary Spin Independence in a Paraquark Model of Baryons and Mesons", *Phys. Rev. Lett.* **1**3 (1964) 598–602. doi:10.1103/PhysRevLett.13.598.

[25] M. Y. Han and Y. Nambu, "Three-Triplet Model with Double SU(3) Symmetry", *Phys. Rev.* **1**39 (Aug, 1965) B1006–B1010. doi:10.1103/PhysRev.139.B1006.

[26] C. Berger, W. Lackas, F. Raupach et al., "Jet analysis of the (9.46) decay into charged hadrons", *Physics Letters B* **8**2 (1979), no. 3, 449 – 455. doi:https://doi.org/10.1016/0370-2693(79)90265-X.

[27] C. Berger, W. Lackas, F. Raupach et al., "Topology of the Υ-decay", *Zeitschrift für Physik C Particles and Fields* **8** (Jun, 1981) 101–114. doi:10.1007/BF01547873.

[28] D. J. Gross and F. Wilczek, "Ultraviolet Behavior of Non-Abelian Gauge Theories", *Phys. Rev. Lett.* **3**0 (Jun, 1973) 1343–1346. doi:10.1103/PhysRevLett.30.1343.

[29] H. D. Politzer, "Reliable Perturbative Results for Strong Interactions?", *Phys. Rev. Lett.* **3**0 (Jun, 1973) 1346–1349. doi:10.1103/PhysRevLett.30.1346.

[30] ATLAS Collaboration, "Observation of a new particle in the search for the Standard Model Higgs boson with the ATLAS detector at the LHC", *Phys. Lett.* **B**716 (2012) 1–29, arXiv:1207.7214. doi:10.1016/j.physletb.2012.08.020.

[31] S. Chatrchyan, V. Khachatryan, A. Sirunyan et al., "Observation of a new boson at a mass of 125 GeV with the CMS experiment at the LHC", *Physics Letters B* **7**16 (2012), no. 1, 30 – 61. doi:https://doi.org/10.1016/j.physletb.2012.08.021.

[32] Planck Collaboration, "Planck 2015 results. I. Overview of products and scientific results", *Astron. Astrophys.* **5**94 (2016) A1, arXiv:1502.01582. doi:10.1051/0004-6361/201527101.

[33] Planck Collaboration, "Planck 2015 results. XIII. Cosmological parameters", *Astron. Astrophys.* **5**94 (2016) A13, arXiv:1502.01589. doi:10.1051/0004-6361/201525830.

[34] K. G. Begeman, A. H. Broeils, and R. H. Sanders, "Extended rotation curves of spiral galaxies: dark haloes and modified dynamics", *Monthly Notices of the Royal Astronomical Society* **2**49 (1991), no. 3, 523–537. doi:10.1093/mnras/249.3.523.

[35] E. Corbelli and P. Salucci, "The Extended Rotation Curve and the Dark Matter Halo of M33", *Mon. Not. Roy. Astron. Soc.* **3**11 (2000) 441–447, arXiv:astro-ph/9909252. doi:10.1046/j.1365-8711.2000.03075.x.

[36] A. Refregier, "Weak gravitational lensing by large scale structure", *Ann. Rev. Astron. Astrophys.* **4**1 (2003) 645–668, arXiv:astro-ph/0307212. doi:10.1146/annurev.astro.41.111302.102207.

[37] G. Bertone and D. Hooper, "A History of Dark Matter", *Submitted to: Rev. Mod. Phys.* (2016) arXiv:1605.04909.

[38] L. Canetti, M. Drewes, and M. Shaposhnikov, "Matter and Antimatter in the Universe", *New J. Phys.* **1**4 (2012) 095012, arXiv:1204.4186. doi:10.1088/1367-2630/14/9/095012.

[39] G. Ross, "Grand Unified Theories (Frontiers in Physics)". Westview Press, 2003.

[40] R. Haag, J. T. Lopuszanski, and M. Sohnius, "All possible generators of supersymmetries of the S-matrix", *Nuclear Physics B* **8**8 (1975), no. 2, 257 – 274. doi:https://doi.org/10.1016/0550-3213(75)90279-5.

[41] J. Wess and B. Zumino, "Supergauge transformations in four dimensions", *Nuclear Physics B* **7**0 (1974), no. 1, 39 – 50. doi:https://doi.org/10.1016/0550-3213(74)90355-1.

[42] S. Dimopoulos and H. Georgi, "Softly Broken Supersymmetry and SU(5)", *Nucl. Phys.* **B**193 (1981) 150–162. doi:10.1016/0550-3213(81)90522-8.

[43] S. P. Martin, "A Supersymmetry primer", arXiv:hep-ph/9709356.

[44] I. Aitchison, "Supersymmetry in Particle Physics: An Elementary Introduction". Cambridge University Press, 2007.

[45] Particle Data Group Collaboration, "Review of Particle Physics", *Chin. Phys.* **C**40 (2016), no. 10, 100001. doi:10.1088/1674-1137/40/10/100001.

[46] G. L. Kane and J. P. Leveille, "Experimental Constraints on Gluino Masses and Supersymmetric Theories", *Phys. Lett.* **1**12B (1982) 227–232. doi:10.1016/0370-2693(82)90968-6.

[47] P. R. Harrison and C. H. Llewellyn Smith, "Hadroproduction of Supersymmetric Particles", *Nucl. Phys.* **B**213 (1983) 223. [Erratum: Nucl. Phys.B223,542(1983)]. doi:10.1016/0550-3213(83)90510-2,10.1016/0550-3213(83)90070-6.

[48] E. Reya and D. P. Roy, "SUPERSYMMETRIC PARTICLE PRODUCTION AT p anti-p COLLIDER ENERGIES", *Phys. Rev.* **D**32 (1985) 645. doi:10.1103/PhysRevD.32.645.

[49] S. Dawson, E. Eichten, and C. Quigg, "Search for Supersymmetric Particles in Hadron - Hadron Collisions", *Phys. Rev.* **D**31 (1985) 1581. doi:10.1103/PhysRevD.31.1581.

[50] H. Baer and X. Tata, "Component Formulae for Hadroproduction of Left-handed and Right-handed Squarks", *Phys. Lett.* **1**60B (1985) 159–162. doi:10.1016/0370-2693(85)91484-4.

[51] CMS Collaboration, "Interpretation of Searches for Supersymmetry with simplified Models", *Phys. Rev.* **D**88 (2013), no. 5, 052017, arXiv:1301.2175. doi:10.1103/PhysRevD.88.052017.

[52] CMS Collaboration, "Search for supersymmetry in multijet events with missing transverse momentum in proton-proton collisions at 13 TeV", *Phys. Rev.* **D**96 (2017), no. 3, 032003, arXiv:1704.07781. doi:10.1103/PhysRevD.96.032003.

[53] LHC New Physics Working Group Collaboration, "Simplified Models for LHC New Physics Searches", *J. Phys.* **G**39 (2012) 105005, arXiv:1105.2838. doi:10.1088/0954-3899/39/10/105005.

[54] L. Evans and P. Bryant, "LHC Machine", *JINST* **3** (2008) S08001. doi:10.1088/1748-0221/3/08/S08001.

[55] O. S. Brning, P. Collier, P. Lebrun et al., "LHC Design Report". CERN Yellow Reports: Monographs. CERN, Geneva, 2004.

[56] M. Brice, "Aerial View of the CERN taken in 2008.". Jul, 2008.

[57] E. Mobs, "The CERN accelerator complex. Complexe des acclrateurs du CERN",. General Photo.

[58] "Restarting the LHC: Why 13 Tev?",.

[59] by Frdrick Bordry and C. Pralavorio, " LHC smashes targets for 2016 run",.

[60] by Corinne Pralavorio and C. Pralavorio, "2016: an exceptional year for the LHC ",.

[61] by Corinne Pralavorio and C. Pralavorio, "Record luminosity: well done LHC",.

[62] W. J. Stirling, "private communication".

[63] J. M. Campbell, J. W. Huston, and W. J. Stirling, "Hard Interactions of Quarks and Gluons: A Primer for LHC Physics", *Rept. Prog. Phys.* **7**0 (2007) 89, arXiv:hep-ph/0611148. doi:10.1088/0034-4885/70/1/R02.

[64] CMS Collaboration, "CMS physics: Technical design report",.

[65] CMS Collaboration Collaboration, G. L. Bayatian et al., "CMS Physics: Technical Design Report Volume 1: Detector Performance and Software". Technical Design Report CMS. CERN, Geneva, 2006. There is an error on cover due to a technical problem for some items.

[66] CMS Collaboration Collaboration, "Description and performance of track and primary-vertex reconstruction with the CMS tracker", *JINST* **9** (May, 2014) P10009. 80 p. Comments: Replaced with published version. Added journal reference and DOI.

[67] A. Dominguez, D. Abbaneo, K. Arndt et al., "CMS Technical Design Report for the Pixel Detector Upgrade", CERN-LHCC-2012-016. CMS-TDR-11, Sep, 2012. Additional contacts: Jeffrey Spalding, Fermilab, Jeffrey.Spalding@cern.ch Didier Contardo, Universite Claude Bernard-Lyon I, didier.claude.contardo@cern.ch.

[68] CMS Collaboration Collaboration, "The CMS electromagnetic calorimeter project: Technical Design Report". Technical Design Report CMS. CERN, Geneva, 1997.

[69] CMS Collaboration, "Particle-flow reconstruction and global event description with the CMS detector", *JINST* **1**2 (2017), no. 10, P10003, arXiv:1706.04965. pf reference 2. doi:10.1088/1748-0221/12/10/P10003.

[70] CMS Collaboration Collaboration, A. Benaglia, "The CMS ECAL performance with examples", CMS-CR-2013-430, CERN, Geneva, Nov, 2013.

[71] P. Adzic, "Energy resolution of the barrel of the CMS Electromagnetic Calorimeter", *Journal of Instrumentation* **2** (2007), no. 04, P04004.

[72] CMS Collaboration Collaboration, "The CMS hadron calorimeter project: Technical Design Report". Technical Design Report CMS. CERN, Geneva, 1997.

[73] T. C. collaboration, "The CMS barrel calorimeter response to particle beams from2to350 GeV/c", *The European Physical Journal C* **6**0 (Apr, 2009) 359–373. ecal reference. doi:10.1140/epjc/s10052-009-0959-5.

[74] M. Dobbs and J. B. Hansen, "The HepMC C++ Monte Carlo Event Record for High Energy Physics", ATL-SOFT-2000-001, CERN, Geneva, Jun, 2000. revised version number 1 submitted on 2001-02-27 09:54:32.

[75] S. D. Drell and T.-M. Yan, "Partons and their Applications at High-Energies", *Annals Phys.* **6**6 (1971) 578. [Annals Phys.281,450(2000)]. doi:10.1016/0003-4916(71)90071-6.

[76] L. N. Lipatov, "The parton model and perturbation theory", *Sov. J. Nucl. Phys.* **2**0 (1975) 94–102. [Yad. Fiz.20,181(1974)].

[77] V. N. Gribov and L. N. Lipatov, "Deep inelastic e p scattering in perturbation theory", *Sov. J. Nucl. Phys.* **1**5 (1972) 438–450. [Yad. Fiz.15,781(1972)].

[78] Y. L. Dokshitzer, "Calculation of the Structure Functions for Deep Inelastic Scattering and e+ e- Annihilation by Perturbation Theory in Quantum Chromodynamics.", *Sov. Phys. JETP* **4**6 (1977) 641–653. [Zh. Eksp. Teor. Fiz.73,1216(1977)].

[79] G. Altarelli and G. Parisi, "Asymptotic Freedom in Parton Language", *Nucl. Phys.* **B**126 (1977) 298–318. doi:10.1016/0550-3213(77)90384-4.

[80] ZEUS, H1 Collaboration, "Combined Measurement and QCD Analysis of the Inclusive e+- p Scattering Cross Sections at HERA", *JHEP* **0**1 (2010) 109, arXiv:0911.0884. doi:10.1007/JHEP01(2010)109.

[81] B. Andersson, G. Gustafson, G. Ingelman et al., "Parton Fragmentation and String Dynamics", *Phys. Rept.* **9**7 (1983) 31–145. doi:10.1016/0370-1573(83)90080-7.

[82] D. Amati and G. Veneziano, "Preconfinement as a Property of Perturbative QCD", *Phys. Lett.* **8**3B (1979) 87–92. doi:10.1016/0370-2693(79)90896-7.

[83] A. Bassetto, M. Ciafaloni, and G. Marchesini, "Color Singlet Distributions and Mass Damping in Perturbative QCD", *Phys. Lett.* **8**3B (1979) 207–212. doi:10.1016/0370-2693(79)90687-7.

[84] J. Alwall, M. Herquet, F. Maltoni et al., "MadGraph 5 : Going Beyond", *JHEP* **0**6 (2011) 128, arXiv:1106.0522. doi:10.1007/JHEP06(2011)128.

[85] J. Alwall et al., "Comparative study of various algorithms for the merging of parton showers and matrix elements in hadronic collisions", *Eur. Phys. J.* **C**53 (2008) 473–500, arXiv:0706.2569. doi:10.1140/epjc/s10052-007-0490-5.

[86] P. Nason, "A New method for combining NLO QCD with shower Monte Carlo algorithms", *JHEP* **1**1 (2004) 040, arXiv:hep-ph/0409146. doi:10.1088/1126-6708/2004/11/040.

[87] S. Frixione, P. Nason, and C. Oleari, "Matching NLO QCD computations with Parton Shower simulations: the POWHEG method", *JHEP* **1**1 (2007) 070, arXiv:0709.2092. doi:10.1088/1126-6708/2007/11/070.

[88] S. Alioli, P. Nason, C. Oleari et al., "A general framework for implementing NLO calculations in shower Monte Carlo programs: the POWHEG BOX", *JHEP* **0**6 (2010) 043, arXiv:1002.2581. doi:10.1007/JHEP06(2010)043.

[89] T. Sjostrand, S. Mrenna, and P. Z. Skands, "PYTHIA 6.4 Physics and Manual", *JHEP* **0**5 (2006) 026, arXiv:hep-ph/0603175. doi:10.1088/1126-6708/2006/05/026.

[90] T. Sjostrand, S. Mrenna, and P. Z. Skands, "A Brief Introduction to PYTHIA 8.1", *Comput. Phys. Commun.* **1**78 (2008) 852–867, arXiv:0710.3820. doi:10.1016/j.cpc.2008.01.036.

[91] M. Bahr et al., "Herwig++ Physics and Manual", *Eur. Phys. J.* **C**58 (2008) 639–707, arXiv:0803.0883. doi:10.1140/epjc/s10052-008-0798-9.

[92] J. Allison, K. Amako, J. Apostolakis et al., "Geant4 developments and applications", *IEEE Transactions on Nuclear Science* **5**3 (Feb, 2006) 270–278. doi:10.1109/TNS.2006.869826.

[93] S. Agostinelli, J. Allison, K. Amako et al., "Geant4a simulation toolkit", *Nuclear Instruments and Methods in Physics Research Section A: Accelerators, Spectrometers, Detectors and Associated Equipment* **5**06 (2003), no. 3, 250 – 303. doi:https://doi.org/10.1016/S0168-9002(03)01368-8.

[94] J. Allison, K. Amako, J. Apostolakis et al., "Recent developments in Geant4", *Nuclear Instruments and Methods in Physics Research Section A: Accelerators, Spectrometers, Detectors and Associated Equipment* **8**35 (2016) 186 – 225. doi:https://doi.org/10.1016/j.nima.2016.06.125.

[95] CMS Collaboration, "The fast simulation of the CMS detector at LHC", *J. Phys. Conf. Ser.* **3**31 (2011) 032049. doi:10.1088/1742-6596/331/3/032049.

[96] ALEPH Collaboration, "Performance of the ALEPH detector at LEP", *Nucl. Instrum. Meth.* **A**360 (1995) 481–506. doi:10.1016/0168-9002(95)00138-7.

[97] M. A. Thomson, "Particle Flow Calorimetry and the PandoraPFA Algorithm", *Nucl. Instrum. Meth.* **A**611 (2009) 25–40, arXiv:0907.3577. doi:10.1016/j.nima.2009.09.009.

[98] M. Ruan and H. Videau, "Arbor, a new approach of the Particle Flow Algorithm", in *Proceedings, International Conference on Calorimetry for the High Energy Frontier (CHEF 2013): Paris, France, April 22-25, 2013*, pp. 316–324. 2013. arXiv:1403.4784.

[99] CMS Collaboration, "Description and performance of track and primary-vertex reconstruction with the CMS tracker", *JINST* **9** (2014), no. 10, P10009, arXiv:1405.6569. doi:10.1088/1748-0221/9/10/P10009.

[100] W. Adam, B. Mangano, T. Speer et al., "Track Reconstruction in the CMS tracker", CMS-NOTE-2006-041, CERN, Geneva, Dec, 2006.

[101] CMS Collaboration, "The performance of the CMS muon detector in proton-proton collisions at sqrt(s) = 7 TeV at the LHC", *JINST* **8** (2013) P11002, arXiv:1306.6905. doi:10.1088/1748-0221/8/11/P11002.

[102] W. Adam, R. Frhwirth, A. Strandlie et al., "Reconstruction of Electrons with the Gaussian-Sum Filter in the CMS Tracker at the LHC",.

[103] CMS Collaboration, "Performance of Electron Reconstruction and Selection with the CMS Detector in Proton-Proton Collisions at s = 8 TeV", *JINST* **1**0 (2015), no. 06, P06005, arXiv:1502.02701. doi:10.1088/1748-0221/10/06/P06005.

[104] F. Bloch and A. Nordsieck, "Note on the Radiation Field of the electron", *Phys. Rev.* **5**2 (1937) 54–59. doi:10.1103/PhysRev.52.54.

[105] T. Kinoshita, "Mass singularities of Feynman amplitudes", *J. Math. Phys.* **3** (1962) 650–677. doi:10.1063/1.1724268.

[106] T. D. Lee and M. Nauenberg, "Degenerate Systems and Mass Singularities", *Phys. Rev.* **1**33 (1964) B1549–B1562. [,25(1964)]. doi:10.1103/PhysRev.133.B1549.

[107] G. P. Salam, "Towards Jetography", *Eur. Phys. J.* **C**67 (2010) 637–686, arXiv:0906.1833. doi:10.1140/epjc/s10052-010-1314-6.

[108] G. F. Sterman and S. Weinberg, "Jets from Quantum Chromodynamics", *Phys. Rev. Lett.* **3**9 (1977) 1436. doi:10.1103/PhysRevLett.39.1436.

[109] G. P. Salam and G. Soyez, "A Practical Seedless Infrared-Safe Cone jet algorithm", *JHEP* **0**5 (2007) 086, arXiv:0704.0292. doi:10.1088/1126-6708/2007/05/086.

[110] JADE Collaboration, "Experimental Investigation of the Energy Dependence of the Strong Coupling Strength", *Phys. Lett.* **B**213 (1988) 235–241. doi:10.1016/0370-2693(88)91032-5.

[111] JADE Collaboration, "Experimental Studies on Multi-Jet Production in e+ e- Annihilation at PETRA Energies", *Z. Phys.* **C**33 (1986) 23. [,53(1986)]. doi:10.1007/BF01410449.

[112] S. D. Ellis and D. E. Soper, "Successive combination jet algorithm for hadron collisions", *Phys. Rev.* **D**48 (1993) 3160–3166, arXiv:hep-ph/9305266. doi:10.1103/PhysRevD.48.3160.

[113] Y. L. Dokshitzer, G. D. Leder, S. Moretti et al., "Better jet clustering algorithms", *JHEP* **0**8 (1997) 001, arXiv:hep-ph/9707323. doi:10.1088/1126-6708/1997/08/001.

[114] M. Wobisch and T. Wengler, "Hadronization corrections to jet cross-sections in deep inelastic scattering", in *Monte Carlo generators for HERA physics. Proceedings, Workshop, Hamburg, Germany, 1998-1999*, pp. 270–279. 1998. arXiv:hep-ph/9907280.

[115] M. Wobisch, "Measurement and QCD analysis of jet cross-sections in deep inelastic positron proton collisions at $\sqrt{s} = 300$ GeV". PhD thesis, Aachen, Tech. Hochsch., 2000.

[116] M. Cacciari, G. P. Salam, and G. Soyez, "The Anti-k(t) jet clustering algorithm", *JHEP* **0**4 (2008) 063, arXiv:0802.1189. doi:10.1088/1126-6708/2008/04/063.

[117] G. Marchesini, B. R. Webber, G. Abbiendi et al., "HERWIG: A Monte Carlo event generator for simulating hadron emission reactions with interfering gluons. Version 5.1 - April 1991", *Comput. Phys. Commun.* **6**7 (1992) 465–508. doi:10.1016/0010-4655(92)90055-4.

[118] D. Bertolini, P. Harris, M. Low et al., "Pileup Per Particle Identification", *JHEP* **1**0 (2014) 059, arXiv:1407.6013. doi:10.1007/JHEP10(2014)059.

[119] CMS Collaboration Collaboration, "Determination of Jet Energy Calibration and Transverse Momentum Resolution in CMS", *JINST* **6** (Jul, 2011) P11002. 67 p.

[120] CMS Collaboration, "Jet energy scale and resolution in the CMS experiment in pp collisions at 8 TeV", *JINST* **1**2 (2017), no. 02, P02014, arXiv:1607.03663. doi:10.1088/1748-0221/12/02/P02014.

[121] M. Cacciari and G. P. Salam, "Dispelling the N^3 myth for the k_t jet-finder", *Phys. Lett.* **B**641 (2006) 57–61, arXiv:hep-ph/0512210. doi:10.1016/j.physletb.2006.08.037.

[122] M. Cacciari, G. P. Salam, and G. Soyez, "FastJet User Manual", *Eur. Phys. J.* **C**72 (2012) 1896, arXiv:1111.6097. doi:10.1140/epjc/s10052-012-1896-2.

[123] P. Skands, S. Carrazza, and J. Rojo, "Tuning PYTHIA 8.1: the Monash 2013 Tune", *Eur. Phys. J.* **C**74 (2014), no. 8, 3024, arXiv:1404.5630. doi:10.1140/epjc/s10052-014-3024-y.

[124] CMS, "Jet energy scale and resolution performances with 13TeV data",.

[125] N. Kovalchuk, "Top quark mass measurement and color effects at the LHC". PhD thesis, U. Hamburg, Dept. Phys., Hamburg, 2018.

[126] CMS Collaboration, "Measurement of the top quark mass with lepton+jets final states using pp collisions at $\sqrt{s} = 13$ TeV", arXiv:1805.01428. doi:10.3204/PUBDB-2018-02205.

[127] ATLAS Collaboration, "Measurements of top-quark pair differential cross-sections in the lepton+jets channel in *pp* collisions at $\sqrt{s} = 8$ TeV using the ATLAS detector", *Eur. Phys. J.* **C**76 (2016), no. 10, 538, arXiv:1511.04716. doi:10.1140/epjc/s10052-016-4366-4.

[128] CMS Collaboration, "Measurement of the differential cross section for top quark pair production in pp collisions at $\sqrt{s} = 8\,\text{TeV}$", *Eur. Phys. J.* **C**75 (2015), no. 11, 542, arXiv:1505.04480. doi:10.1140/epjc/s10052-015-3709-x.

[129] ATLAS Collaboration, "Evidence for the $H \to b\bar{b}$ decay with the ATLAS detector", *JHEP* **1**2 (2017) 024, arXiv:1708.03299. doi:10.1007/JHEP12(2017)024.

[130] CMS Collaboration, "Observation of the Higgs boson decay to a pair of τ leptons with the CMS detector", *Phys. Lett.* **B**779 (2018) 283–316, arXiv:1708.00373. doi:10.1016/j.physletb.2018.02.004.

[131] ATLAS Collaboration, "Evidence for the Higgs-boson Yukawa coupling to tau leptons with the ATLAS detector", *JHEP* **0**4 (2015) 117, arXiv:1501.04943. doi:10.1007/JHEP04(2015)117.

[132] CMS Collaboration, "Evidence for the direct decay of the 125 GeV Higgs boson to fermions", *Nature Phys.* **1**0 (2014) 557–560, arXiv:1401.6527. doi:10.1038/nphys3005.

[133] CMS Collaboration, "Search for $\mathrm{t\bar{t}H}$ production in the $H \to \mathrm{b\bar{b}}$ decay channel with leptonic $\mathrm{t\bar{t}}$ decays in proton-proton collisions at $\sqrt{s} = 13$ TeV", arXiv:1804.03682.

[134] ATLAS Collaboration, "Summary of the searches for squarks and gluinos using $\sqrt{s} = 8$ TeV pp collisions with the ATLAS experiment at the LHC", *JHEP* **1**0 (2015) 054, arXiv:1507.05525. doi:10.1007/JHEP10(2015)054.

[135] CMS Collaboration, "Searches for Supersymmetry using the M_{T2} Variable in Hadronic Events Produced in pp Collisions at 8 TeV", *JHEP* **0**5 (2015) 078, arXiv:1502.04358. doi:10.1007/JHEP05(2015)078.

[136] CMS Collaboration, "Search for supersymmetry in the multijet and missing transverse momentum final state in pp collisions at 13 TeV", *Phys. Lett.* **B**758 (2016) 152–180, arXiv:1602.06581. doi:10.1016/j.physletb.2016.05.002.

[137] ATLAS Collaboration, "Performance of *b*-Jet Identification in the ATLAS Experiment", *JINST* **1**1 (2016), no. 04, P04008, arXiv:1512.01094. doi:10.1088/1748-0221/11/04/P04008.

[138] CMS Collaboration, "Identification of b-quark jets with the CMS experiment", *JINST* **8** (2013) P04013, arXiv:1211.4462. doi:10.1088/1748-0221/8/04/P04013.

[139] CMS Collaboration, "Identification of b quark jets at the CMS Experiment in the LHC Run 2",.

[140] ATLAS, CMS Collaboration, L. Scodellaro, "b tagging in ATLAS and CMS", in *5th Large Hadron Collider Physics Conference (LHCP 2017) Shanghai, China, May 15-20, 2017*. 2017. arXiv:1709.01290.

[141] CMS Collaboration, "Measurement of $B\bar{B}$ Angular Correlations based on Secondary Vertex Reconstruction at $\sqrt{s} = 7$ TeV", *JHEP* **0**3 (2011) 136, arXiv:1102.3194. doi:10.1007/JHEP03(2011)136.

[142] CMS Collaboration Collaboration, "Heavy flavor identification at CMS with deep neural networks",.

[143] F. Pedregosa, G. Varoquaux, A. Gramfort et al., "Scikit-learn: Machine Learning in Python", *CoRR* **a**bs/1201.0490 (2012) arXiv:1201.0490.

[144] CMS Collaboration, "Performance of the CMS missing transverse momentum reconstruction in pp data at $\sqrt{s} = 8$ TeV", *JINST* **1**0 (2015), no. 02, P02006, arXiv:1411.0511. doi:10.1088/1748-0221/10/02/P02006.

[145] CMS, "Introduction to missing transverse momentum (MET) in CMSSW", 2018.

[146] CMS Collaboration, "Performance of missing energy reconstruction in 13 TeV pp collision data using the CMS detector",.

[147] CMS Collaboration, "Measurement and QCD analysis of double-differential inclusive jet cross sections in pp collisions at $\sqrt{s} = 8$ TeV and cross section ratios to 2.76 and 7 TeV", *JHEP* **0**3 (2017) 156, arXiv:1609.05331. doi:10.1007/JHEP03(2017)156.

[148] CMS Collaboration, "Measurement of the weak mixing angle with the Drell-Yan process in proton-proton collisions at the LHC", *Phys. Rev.* **D**84 (2011) 112002, arXiv:1110.2682. doi:10.1103/PhysRevD.84.112002.

[149] CMS Collaboration, "Measurement of the double-differential inclusive jet cross section in protonproton collisions at $\sqrt{s} = 13\,\text{TeV}$", *Eur. Phys. J.* **C**76 (2016), no. 8, 451, arXiv:1605.04436. doi:10.1140/epjc/s10052-016-4286-3.

[150] J. S. Anastasia Karavdina, Marek Niedziela, "Jet Transverse Momentum Resolution Measurement using Dijet Events at $\sqrt{s} = 13$ GeV", *CMS Analysis Note* (2018).

[151] T. C. collaboration, "Determination of jet energy calibration and transverse momentum resolution in CMS", *Journal of Instrumentation* **6** (2011), no. 11, P11002.

[152] M. Schroeder, "Quality of Jet Measurements and Impact on a Search for New Physics at CMS". Dr., Universitt Hamburg, 2012. Universitt Hamburg, Diss., 2012.

[153] K. Goebel, "Probing supersymmetry based on precise jet measurements at the CMS experiment". PhD thesis, Universitt Hamburg, August, 2015.

[154] CMS Collaboration Collaboration, "CMS ECAL with 2017 data",.

[155] CMS Collaboration, "Performance of Photon Reconstruction and Identification with the CMS Detector in Proton-Proton Collisions at sqrt(s) = 8 TeV", *JINST* **10** (2015), no. 08, P08010, arXiv:1502.02702. doi:10.1088/1748-0221/10/08/P08010.

[156] D0 Collaboration, "High-p_T jets in $\bar{p}p$ collisions at $\sqrt{s} = 630$ GeV and 1800 GeV", *Phys. Rev.* **D**64 (2001) 032003, arXiv:hep-ex/0012046. doi:10.1103/PhysRevD.64.032003.

[157] D0 Collaboration, "Measurement of the inclusive jet cross section in $p\bar{p}$ collisions at $\sqrt{s} = 1.96$ TeV", *Phys. Rev.* **D**85 (2012) 052006, arXiv:1110.3771. doi:10.1103/PhysRevD.85.052006.

[158] ATLAS Collaboration, "Jet energy resolution in proton-proton collisions at $\sqrt{s} = 7$ TeV recorded in 2010 with the ATLAS detector", *Eur. Phys. J.* **C**73 (2013), no. 3, 2306, arXiv:1210.6210. doi:10.1140/epjc/s10052-013-2306-0.

[159] CMS collaboration Collaboration, A. Massironi, "Evolution studies of the CMS ECAL endcap response and upgrade design options for High-Luminosity LHC", arXiv:1409.2985, Sep, 2014.

[160] T. Sjstrand, S. Ask, J. R. Christiansen et al., "An Introduction to PYTHIA 8.2", *Comput. Phys. Commun.* **1**91 (2015) 159–177, arXiv:1410.3012. doi:10.1016/j.cpc.2015.01.024.

[161] J. energy resolution scale factor measurement (Internal CMS documentation).

[162] CMS Collaboration, "Search for New Physics with Jets and Missing Transverse Momentum in pp collisions at $\sqrt{s} = 7$ TeV", *JHEP* **0**8 (2011) 155, arXiv:1106.4503. doi:10.1007/JHEP08(2011)155.

[163] CMS Collaboration, "Search for new physics in the multijet and missing transverse momentum final state in proton-proton collisions at $\sqrt{s} = 7$ TeV", *Phys. Rev. Lett.* **1**09 (2012) 171803, arXiv:1207.1898. doi:10.1103/PhysRevLett.109.171803.

[164] CMS Collaboration, "Search for new physics in the multijet and missing transverse momentum final state in proton-proton collisions at $\sqrt{s}$= 8 TeV", *JHEP* **0**6 (2014) 055, arXiv:1402.4770. doi:10.1007/JHEP06(2014)055.

[165] N. M.Diamantopoulou and E.Tziaferi, "Performance of the Particle-Flow jet identification criteria using proton-proton collisions at 13 TeV". CMS Draft Analysis Note, 2016.

[166] "BAYESIAN NEURAL NETWORKS". 2005.

[167] J. Alwall, R. Frederix, S. Frixione et al., "The automated computation of tree-level and next-to-leading order differential cross sections, and their matching to parton shower simulations", *JHEP* **0**7 (2014) 079, arXiv:1405.0301. doi:10.1007/JHEP07(2014)079.

[168] S. L. Bein, "Targeting the minimal supersymmetric standard model with the compact muon solenoid experiment". PhD thesis, The Florida State University, 2016.

[169] B. Efron, "Bootstrap Methods: Another Look at the Jackknife", *Ann. Statist.* **7** (01, 1979) 1–26. doi:10.1214/aos/1176344552.

[170] G. Cowan, K. Cranmer, E. Gross et al., "Asymptotic formulae for likelihood-based tests of new physics", *Eur. Phys. J.* **C**71 (2011) 1554, arXiv:1007.1727. [Erratum: Eur. Phys. J.C73,2501(2013)]. doi:10.1140/epjc/s10052-011-1554-0, 10.1140/epjc/s10052-013-2501-z.

[171] T. Junk, "Confidence level computation for combining searches with small statistics", *Nucl. Instrum. Meth.* **A**434 (1999) 435–443, arXiv:hep-ex/9902006. doi:10.1016/S0168-9002(99)00498-2.

[172] A. L. Read, "Presentation of search results: the CL s technique", *Journal of Physics G: Nuclear and Particle Physics* **2**8 (2002), no. 10, 2693.

[173] W. Beenakker, R. Hopker, M. Spira et al., "Squark and gluino production at hadron colliders", *Nucl. Phys.* **B**492 (1997) 51–103, arXiv:hep-ph/9610490. doi:10.1016/S0550-3213(97)80027-2.

[174] A. Kulesza and L. Motyka, "Threshold resummation for squark-antisquark and gluino-pair production at the LHC", *Phys. Rev. Lett.* **1**02 (2009) 111802, arXiv:0807.2405. doi:10.1103/PhysRevLett.102.111802.

[175] A. Kulesza and L. Motyka, "Soft gluon resummation for the production of gluino-gluino and squark-antisquark pairs at the LHC", *Phys. Rev.* **D**80 (2009) 095004, arXiv:0905.4749. doi:10.1103/PhysRevD.80.095004.

[176] W. Beenakker, S. Brensing, M. Kramer et al., "Soft-gluon resummation for squark and gluino hadroproduction", *JHEP* **1**2 (2009) 041, arXiv:0909.4418. doi:10.1088/1126-6708/2009/12/041.

[177] W. Beenakker, S. Brensing, M. n. Kramer et al., "Squark and Gluino Hadroproduction", *Int. J. Mod. Phys.* **A**26 (2011) 2637–2664, arXiv:1105.1110. doi:10.1142/S0217751X11053560.

[178] CMS Collaboration, "Search for new phenomena with the M_{T2} variable in the all-hadronic final state produced in protonproton collisions at $\sqrt{s} = 13$ TeV", *Eur. Phys. J.* **C**77 (2017), no. 10, 710, arXiv:1705.04650. doi:10.1140/epjc/s10052-017-5267-x.

[179] CMS Collaboration, "Search for the pair production of third-generation squarks with two-body decays to a bottom or charm quark and a neutralino in protonproton collisions at $\sqrt{s} = 13$ TeV", *Phys. Lett.* **B**778 (2018) 263–291, arXiv:1707.07274. doi:10.1016/j.physletb.2018.01.012.

[180] CMS Collaboration, "Search for direct production of supersymmetric partners of the top quark in the all-jets final state in proton-proton collisions at $\sqrt{s} = 13$ TeV", *JHEP* **1**0 (2017) 005, arXiv:1707.03316. doi:10.1007/JHEP10(2017)005.

[181] CMS Collaboration, "Search for top squarks and dark matter particles in opposite-charge dilepton final states at $\sqrt{s} = 13$ TeV", *Phys. Rev.* **D**97 (2018), no. 3, 032009, arXiv:1711.00752. doi:10.1103/PhysRevD.97.032009.

[182] CMS Collaboration, "Search for Supersymmetry in pp Collisions at $\sqrt{s} = 13$ TeV in the Single-Lepton Final State Using the Sum of Masses of Large-Radius Jets", *Phys. Rev. Lett.* **1**19 (2017), no. 15, 151802, arXiv:1705.04673. doi:10.1103/PhysRevLett.119.151802.

[183] CMS Collaboration, "Search for supersymmetry in events with one lepton and multiple jets exploiting the angular correlation between the lepton and the missing transverse momentum in proton-proton collisions at $\sqrt{s} = 13$ TeV", *Phys. Lett.* **B**780 (2018) 384–409, arXiv:1709.09814. doi:10.1016/j.physletb.2018.03.028.

[184] CMS Collaboration, "Search for physics beyond the standard model in events with two leptons of same sign, missing transverse momentum, and jets in protonproton collisions at $\sqrt{s} = 13\,\text{TeV}$", *Eur. Phys. J.* **C**77 (2017), no. 9, 578, arXiv:1704.07323. doi:10.1140/epjc/s10052-017-5079-z.

[185] CMS Collaboration, "Search for supersymmetry in events with at least three electrons or muons, jets, and missing transverse momentum in proton-proton collisions at $\sqrt{s} = 13$ TeV", *JHEP* **0**2 (2018) 067, arXiv:1710.09154. doi:10.1007/JHEP02(2018)067.

[186] CMS Collaboration, "Search for top squark pair production in pp collisions at $\sqrt{s} = 13$ TeV using single lepton events", *JHEP* **1**0 (2017) 019, arXiv:1706.04402. doi:10.1007/JHEP10(2017)019.

[187] CMS, "CMS Supersymmetry Physics Results", 2018.

[188] ATLAS, "Summary plots from the ATLAS Supersymmetry physics group", 2018.

Acknowledgements

The work presented in this thesis would not have been made possible without my parents. Their stubbornness and persistence in encouraging me to learn and study is what led me to science and eventually to this PhD project. I greatly appreciate their support, care and love. I am equally grateful to the Love of my life, Ola. Besides being my life companion for almost a decade already, she made sure I don't miss any exams and I prepare for all of them. Without her I would probably be a mess and this project would never happen. My brother claims not to be sentimental, so I will only write here that he always motivated me to push forward and advance and I am very grateful for that.

I wanted to thank Christian who got me into CMS and supervised me throughout my years at Uni Hamburg. I am grateful for the confidence he had in me and his help and teachings. I also wanted to thank Peter. I've always been amazed by how he manages to keep an eye on all students and all projects while he is so busy with running the group.

Jory and Sam also played a very significant part in my particle physics education. They not only thought me a lot about SUSY, but also about the functioning of science. And they both became my great friends. I will miss all the discussions we had and I am hoping for more.

Furthermore, I wanted to thank Simon. We had so much fun, and we visited so many places together, but I also have learned a lot from him. He helped me with so many things related to living in Germany, that they would probably fill another 100 pages here. I hope there's still some fun ahead of us!

I can't miss here Deniele, Lukas and Malte, great friends and probably the best lunch buddies ever! Thanks for your friendship.

And last but not least, I would like to thank the whole Uni Hamburg CMS group. It's been a pleasure and I always felt welcome here.

Thank you.